TECHNISCHE
UNIVERSITÄT
DRESDEN

Studies on Organic Solar Cells Composed of Fullerenes and Zinc-Phthalocyanines

Dissertation
zur Erlangung des
Doktorgrades der Naturwissenschaften
(Doctor rerum naturalium)

vorgelegt von

Steffen Pfützner

geboren am 23. November 1981 in Leipzig

Institut für Angewandte Photophysik
Fachrichtung Physik
Fakultät Mathematik und Naturwissenschaften
Technische Universität Dresden

Dresden 2011

Eingereicht am 8th August 2011

1. Gutachter: Prof. Dr. Karl Leo

2. Gutachter: Prof. Dr. Masahiro Hiramoto

Verteidigt am 30th January 2012

Abstract

This work deals with the investigation and research on organic solar cells.

In the first part of this work we focus on the spectroscopical and electrical characterization of the acceptor molecule and fullerene derivative C_{70}. In combination with the donor molecule zinc-phthalocyanines (ZnPc) we investigate C_{70} in flat and bulk heterojunction solar cells and compare the results with C_{60} as acceptor. The stronger and spectral broader thin film absorption of C_{70} and thus enhanced contribution to photocurrent as well as the similar electrical properties with respect to C_{60} result in higher power conversion efficiencies.

In the second part, modifications of the blend layer morphology of a C_{60}:ZnPc bulk heterojunction solar cell are considered. Using substrate heating during co-deposition of acceptor and donor, the molecular arrangement is influenced. Due to the additional thermal energy at the substrate the blend layer morphology is improved and optimized for a substrate heating temperature of 110°C. With transmission electron microscopy, molecular phase separation of C_{60} and ZnPc and the formation of polycrystalline ZnPc domains in a lateral dimension on the order of 50 nm are detected. Mobility measurements show an increased ZnPc hole mobility in the heated blend layer. The improved charge carrier percolation and transport are confirmed by the enhanced performance of such bulk heterojunction solar cells. Furthermore, we show a strong influence of the pre-deposited p-doped hole transport layer on the molecular phase separation.

In the third part, we study the dependency of the open circuit voltage on the mixing ratio of C_{60} and ZnPc in bulk heterojunction solar cells. For the different mixing ratios we determine the ionization potentials of C_{60} and ZnPc. Over the various C_{60}:ZnPc blends from 1:3 - 6:1, the ionization potentials change linearly, but different from each other and exhibit a correlation to the change in open circuit voltage.

Depending on the mixing ratio an intrinsic ZnPc layer adjacent to the blend leads to injection barriers which result in reduced open circuit voltage. We hence determine a voltage loss dependent on ZnPc layer thickness and barrier height.

Kurzfassung

Diese Arbeit beschäftigt sich mit der Untersuchung und Forschung an organischen Solarzellen und gliedert sich in drei Teile. Im ersten Teil wird auf die spektroskopische und elektrische Charakerisierung des Fullerenderivates C_{70} eingegangen, welches als Akzeptormolekül in Kombination mit dem Donormolekül Zink-Phthalocyanin (ZnPc) in Flach- und Mischschichtheteroübergänge organischer Solarzellen Anwendung findet. Dabei wird das Molekül mit dem bisherigen Standard Akzeptormolekül C_{60} verglichen. Die deutlich stärkere und spektral verbreiterte Dünnschichtabsorption von C_{70}, sowie die vergleichbaren elektrischen Eigenschaften zu C_{60} führen zu einer Effizienzsteigerung in den Flach- und Mischschichtsolarzellen, welche maßgeblich durch die Erhöhung des Kurzschlussstromes erreicht wird. Im zweiten Teil widmet sich diese Arbeit der Morphologiemodifizierung des Mischschichtsystems C_{60}:ZnPc, welche durch Heizen des Substrates während der Mischverdampfung von Akzeptor- und Donormolekülen in organischen Mischschichtsolarzellen erreicht werden kann. Es wird gezeigt, dass mit der zusätzlichen Zufuhr thermischer Energie über das Substrat die Anordnung der Moleküle in der Mischschicht beeinflusst werden kann. Unter Verwendung eines Transmissionselektronmikroskops lässt sich für die Mischschicht mit der optimalen Solarzellensubstrattemperatur von 110°C eine Phasenseparation von C_{60} und ZnPc unter Ausbildung von polykristallinen ZnPc Domänen in der lateralen Dimension von 50 nm nachweisen. Mit zusätzlichen Messungen der Ladungsträgerbeweglichkeiten des Mischschichtsystems kann die verbesserte Perkolation und Löcherbeweglichkeit von ZnPc für die Steigerung der Performance geheizter Solarzellen bestätigt werden. Desweiteren wird gezeigt, dass die Ausbildung einer Phasenseparation sehr stark von der darunter liegenden Molekülschicht z.B. der p-dotierte Löchertransportschicht abhängig ist. Im letzten und dritten Teil geht die Arbeit auf die Abhängigkeit der Klemmspannung von der Mischschichtkonzentration von C_{60} und ZnPc ein. Für die unterschiedlichen Volumenkonzentrationen von C_{60}:ZnPc zwishen 6:1 und 1:6 kann gezeigt werden, dass sich die Ionisationspotentiale von C_{60} und ZnPc über einen großen Bereich linear und voneinander verschieden verändern und mit den absoluten Änderung der offenenen Klemmspannung korrelieren. Desweiteren wird gezeigt, dass sich durch eine zusätzlich an die Mischschicht angrenzende intrinsische ZnPc Schicht, abhängig von der Mischschichtkonzentration, Injektionsbarrieren ausbilden, welche nachweislich einen Spannungsverlust bedingen. Dabei kann gezeigt werden, dass der Spannungsverlust mit der ZnPc Schichtdicke und der Barrierenhöhe korreliert.

Phantasie ist wichtiger als Wissen,
denn Wissen ist begrenzt.

Albert Einstein

Contents

Publications

Articles

1. S. Pfuetzner, A. Petrich, C. Malbrich, J. Meiss, M. Koch, M. K. Riede, M. Pfeiffer, and K. Leo. Characterisation of different hole transport materials as used in organic p-i-n solar cells. *Proc. of SPIE* **6999**, 69991M (2008).

2. S. Pfuetzner, J. Meiss, A. Petrich, M. Riede, and K. Leo. Improved bulk heterojunction organic solar cells employing C_{70} fullerenes. *Appl. Phys. Lett.* **94**, 223307 (2009).

3. S. Pfuetzner, J. Meiss, A. Petrich, M. Riede, and K. Leo. Thick C_{60}:ZnPc bulk heterojunction solar cells with improved performance by film deposition on heated substrates. *Appl. Phys. Lett.* **94**, 253303 (2009).

4. S. Pfuetzner, J. Meiss, S. Olthof, M. P. Hein, A. Petrich, L. Dunsch, K. Leo, and M. Riede. Improved photon harvesting by employing C_{70} in bulk heterojunction solar cells. *Proc. of SPIE* **7725**, 77250E (2010).

5. S. Pfuetzner, C. Mickel, J. Jankowski, M. Hein, J. Meiss, C. Schuenemann, C. Elschner, A. A. Levin, B. Rellinghaus, K. Leo, and M. Riede. The influence of substrate heating on morphology and layer growth in C_{60}:ZnPc bulk heterojunction solar cells. *Organic Electronics* **12**, 435 (2011).

6. J. Drechsel, A. Petrich, M. Koch, S. Pfützner, R. Meerheim, S. Scholz, J. Drechsel, K. Walzer, M. Pfeiffer, and K. Leo. 53.3: Influence of material purification by vacuum sublimation on organic optoelectronic device performance. *SID Symposium Digest of Technical Papers.* **37**, 1692 (2006).

7. J. Meiss, C. L. Uhrich, K. Fehse, S. Pfuetzner, M. K. Riede, and K. Leo. Transparent electrode materials for solar cells. *Proceedings of SPIE* **7002**, 700210 (2008).

8. J. Meiss, M. Furno, S. Pfuetzner, K. Leo, and M. Riede. Selective absorption enhancement in organic solar cells using light incoupling layers. *J. Appl. Phys.* **107**, 053117 (2010).

9. J. Meiss, M. Hummert, A. Petrich, S. Pfuetzner, K. Leo, and M. Riede. Tetrabutyl-tetraphenyl-diindenoperylene derivatives as alternative green donor in bulk heterojunction organic solar cells. *Sol. Energy Mater. Sol. Cells* **95**, 630 (2011).

10. J. Meiss, S. Pfuetzner, M. Hummert, T. Menke, K. Leo, and M. Riede. ITO-free, semitransparent small-molecule organic solar cells with dibenzoperiflanthene as absorber, *EU PVSEC Proceedings* **25**, 303 (2010).

11. W. Tress, S. Pfuetzner, K. Leo, and M. Riede. Open circuit voltage and IV curve shape of ZnPc:C_{60} solar cells with varied mixing ratio and hole transport layer. *submitted to JPE* (2010)

Talks

1. DPG Frühjahrstagung, Regensburg (Germany), 21 - 26 March 2010. *Improved transport properties of p-i-i small molecule solar cells deposited on heated substrate.* Session DS 3.2.

2. SPIE Photonics Europe 2010, Brussels (Belgium), 12 - 16 April 2010. *Improved photon harvesting by employing C_{70} in bulk heterojunction solar cells.* Paper 7725-13.

3. MRS Spring Meeting 2011, San Francisco (USA), 25 - 29 April 2011. *Effect of mixing ratio on open circuit voltage in ZnPc:C_{60} bulk heterojunction organic solar cells.* Paper number OO8.7.

Posters

1. DPG - Physics School, Bad Honnef (Germany), 23 - 28 September 2007. *Characterisation of different hole transport materials as used in organic p-i-n solar cells.*

2. DPG Fühjahrstagung, Berlin (Germany), 25 - 29 February 2008. *Characterisation of different hole transport materials as used in organic p-i-n solar cells.* Session HL 36.16.

3. SPIE Photonics Europe 2008, Strasbourg (France) 7 - 10 April 2008. *Characterisation of different hole transport materials as used in organic p-i-n solar cells.* Paper 6999-58.

4. DPG Fühjahrstagung, Dresden (Germany), 22 - 17 March 2009. *Improved morphology of* C_{60}*:ZnPc blend solar cells by using heated substrates.* Session SYOP 4.67.
5. Vth International Krutyn Summer School 2009, Krutyn (Poland), 2 - 8 June 2009. *Improved morphology of* C_{60}*:ZnPc blend solar cells by using heated substrates.*
6. European Conference on Molecular Electronics 2009, Copenhagen (Denmark), 9 - 12 September 2009. *Improved morphology of* C_{60}*:ZnPc blend solar cells by using heated substrates.*
7. Plastic Electronics, Dresden (Germany), 27 - 29 October 2009. *Improved photon harvesting by employing* C_{70} *in small molecules solar cells.*

1 Introduction

The energy provided by the sun is the most abundant and permanent energy resource on earth and it is available for use in its direct (solar radiation) and indirect (e.g. wind, biomass, tidal power plant) forms.
The sun emits energy of $3.8\text{x}10^{26}$ W. Approximately only $1.8\text{x}10^{17}$ W is irradiated on earth, which is located about 150 million km from the sun. From that, $1.08\text{x}10^{17}$ W (60 % of this amount) or approx. 210 W/m^2 is irradiated on the surface of the earth. The rest is absorbed by the atmosphere or reflected back into space. A simple calculation shows that the sun provides enough energy to cover world energy consumption. A conversion of only 0.1 % of the irradiated solar energy on earth with an efficiency of 10 % would lead to a four times world's total generating capacity of about 3000 GW [1]. However, around 80 % of the worldwide primary energy use in 2006 was based on fossil fuels (gas, oil, and coal) as sketched in Fig. 1.1 [1, 2]. Unfortunately, the usage of energy implies also high risk concerning adverse weather conditions or human acts on infrastructures e.g. power plants, transmission lines and substations, and gas and oil pipelines. Recent examples for environmental disasters are the explosion on the British Petrol (BP p.l.c.) oil platform "Deepwater Horizon" close to the US gulf coast or the damaged nuclear power plants in Fukushima in Japan by the earthquake and tsunami. World demand for fossil fuels (begin with oil) is expected to exceed annual production

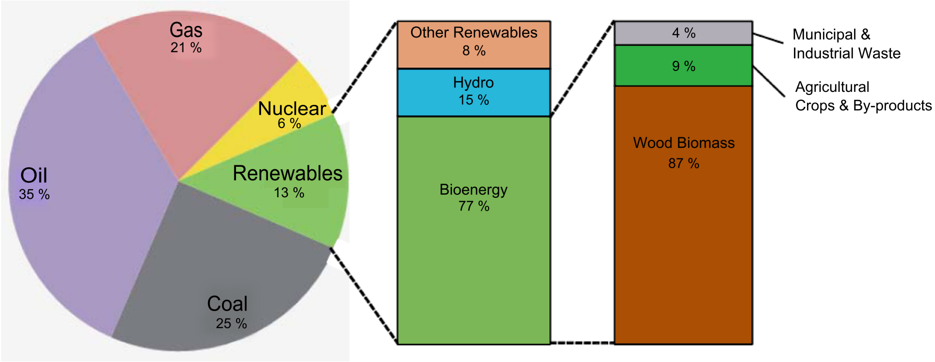

Figure 1.1: *Worldwide energy consumption in 2006. Over 80 % is based on fossil fuels (gas, oil, and coal) after [1, 2].*

within the next two decades [1]. Furthermore, according to estimates by the World Energy Council, the world's demand for electricity will double within the next forty years [1]. At the same time prices for scarce resources such as oil and natural gas will rise and can trigger international economic and political crises and conflicts. Moreover, burning fossil fuels releases emissions such as carbon dioxide, nitrogen oxides, aerosols, etc. which affect the local, regional and global environment [1].

All these factors lead to a reconsideration and a global demand for alternative energy sources such as solar energy. Thus, the photovoltaic industry will become more and more important in the next few years [1]. Photovoltaic means direct conversion of sunlight into electricity with no step via a heat engine.

The European goal of 20 % reduction in carbon dioxide emissions by 2020, based on 2008 levels, may be achieved by supplying 20 % of energy demand from renewable resources [3]. According to a recent report published by the European Photovoltaic Industry Association (EPIA) a 12 % market share of the EU electricity demand from photovoltaics in 2020 is an achievable objective [4]. The total energy production in the EU of 0.5 % in 2010 generated from solar power must rise if solar energy is to contribute to sustainable development. A prediction of global energy demand is made by the World Energy Council and shown in Fig. 1.2 [1, 5].

Photovoltaic devices are robust and simple in design and require very little maintenance

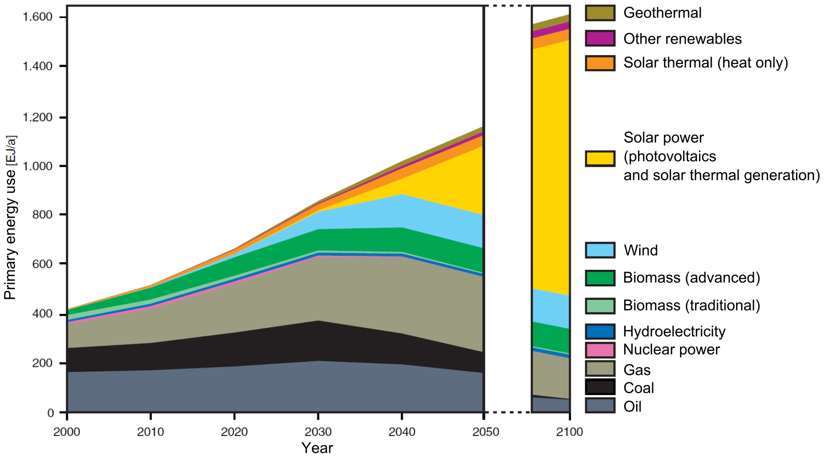

Figure 1.2: *The prediction of the global energy mix until 2050/2100 taken from [1, 5].*

in comparison to other energy providing systems. A big advantage of photovoltaic devices is that they can be constructed as stand-alone systems to give outputs from microwatts to megawatts and offer a huge potential for applications of power sources, e.g. calculators, remote building, and even megawatt-scale power plants. Due to the vast array of applications the demand for photovoltaics is increasing. Solarbuzz reported in March 2011 that a world photovoltaic installations record of 18.2 GW was

obtained in 2010, representing a growth of 139 % over the previous year [6]. European countries accounted for 14.7 GW, or 81 % of world demand in 2010 and the world solar photovoltaic market grew. The top three countries for solar energy production in Europe are Germany, Italy and Czech Republic, which collectively accounted for 12.9 GW. All three countries experienced soaring demand, with Italy becoming the second largest market in the world. All those installed photovoltaics are based on inorganic solar cells (e.g. silicon, CiGs, CdTe, and GaAs).
The question is why do we spend much effort on research and development of organic solar cells based on semiconductors?
Organic materials and in particular organic solar cells have high attractiveness and potential in comparison to inorganics as listed in the following points:

1. Organic chemistry allows modifications to molecular structures or to even create new compounds and material classes with desired electrical and optical properties. Furthermore, there is potential with respect to low synthesis costs and higher performance of organic compounds.

2. Cost-efficient production methods (e.g. roll-to-roll production [7], inject print technique [8]) and low material costs are favorable for large area and niche applications.

3. Organic molecules can have high absorption coefficients ($10^5\,\mathrm{cm}^{-1}$ which allow high efficiencies of thin film device architectures (several 100 nm) [9].

4. Using plastic foils (e.g. PET or PEN) instead of glass as substrates, the organic thin film solar cells can produce light weight, flexible, and adaptable surfaces which enables a large application field (e.g. foldable solar cells and integration in clothing) [10–12].

5. With new concepts of semitransparent electrodes [13, 14] and new materials, absorbing in the near-infrared or infrared spectral region, highly transparent organic solar cells are realizable and are interesting for building integration (e.g. windows, solar protection) [13].

6. Due to the usage of organic compounds, the devices can be made environmental friendly and harmless.

   Of course organic photovoltaic struggle has some disadvantages (e.g. narrow absorption bands, low charge carrier mobilities, and low dielectric constants), leading to lower power conversion efficiencies than inorganic solar cells. While the inorganic single crystal silicon solar cells have p.c. efficiencies around 25 %, the organic based solar cells show efficiencies up to 8.3 % as reported in the solar cell efficiency table in reference [15]. Theoretical calculations predict achievable power conversion efficiencies of 15 % for tandem bulk heterojunctions solar cells [16, 17]. Thus, much effort is spent on research to investigate and understand the physics of such devices to further improve performance and power conversion efficiencies.

This work deals with the investigation of organic solar cells composed of fullerenes and zinc-phtalocynines with the focus on the characterization of the fullerene C_{70} as acceptor, morphology modifications of bulk heterojunctions, and the dependency of the blend layer ratio and related adjacent layers on the open circuit voltage.
The thesis is organized as follows. The basic physics needed for the later discussion are introduced in chapter 2. The properties of organic semiconductors are presented and the photovoltaic princple is described. Chapter 3 presents the properties of the organic materials, the experimental details, and data evaluation of the characterization tools and measurement techniques. The results are presented throughout the chapters 4 - 6 and starts with the electrical and optical characterization of the fullerene C_{70} as alternative to replace the acceptor C_{60}. Furthermore, the integration and the performance of C_{70} in organic solar cells is discussed with respect to C_{60}. Morphology related improvements of bulk heterojunction solar cells are discussed in chapter 5 by detailed investigations of the morphology, depending on the substrate temperature, which is applied during deposition of the fullerene:ZnPc bulk heterojunctions. Additionally, sublayer dependent cluster formations of the mixed layers are discussed. Chapter 6 is dedicated to the investigation of the dependency of the open circuit voltage on the mixing ratio of the bulk heterojunction and implementation of thin ZnPc layers between mixed and hole transport layer. Several measurement techniques are applied. By using mainly photoelectron spectroscopy, measuring the ionization potentials, the origins of these effects are explained.

2 History, Fundamentals, and Motivation

2.1 History

The first studies on organic semiconductors concerning dark and photoconductivity (e.g. anthracene) were done in the early 20th century [18]). In the 1960s, motivated by the discovery of the electroluminescence of thin films [19,20], molecular crystals were intensely investigated (e.g. optical excitation and charge carrier transport) by many groups, see reviews [21–23]. In spite of the demonstration of the working principle of organic electroluminescent diodes, researchers had to struggle with many drawbacks (e.g. insufficient current, high operating voltage, low light output, and device stability) which prevented early success and commercial device application.

In the 1970s, a second important class of organic semiconducters was established by the successful synthesis and controlled doping of conjugated polymers, and honored later with the Nobel Prize in chemistry in 2000 for Alan J. Heeger, Alan G. MacDiarmid und Hideki Shirakawa [24]. The conducting polymers initiated the first applications of organic materials (e.g. organic photoconductors, conductive coating, and photoreceptors in electrophotography [18]).

Although photovoltaic effects have been observed a long time ago. The breakthrough of the first thin film organic heterojunction solar cell was achieved in 1986 by Tang and van Slyke. The basic principle is that two materials (n- and p- conducting) in a double layer structure are sandwiched between two electrodes.

In 1991 Hiramoto [25] invented the bulk heterojunction solar cell by mixing both materials to a blend layer. This approach was then further improved by Pfeiffer et al. [26] through the possibility of organic doping of wide gap transport materials, leading to a real p-i-n structure [27]. Using this method, efficient p-i-n tandem solar cells have been realized [28].

Organic solar cells can be classified into two major classes according to their working principle, the dye sensitized solar cells (DSSCs) firstly shown by Grätzel [29] in 1991 and heterojunction solar cells (HJSCs). The DSSCs achieved quite high power conversion efficiencies of around 12 % [30], but they still suffer from corrosive nature and complex two-electron redox chemistry [31] achieving long term stable devices.

The HJSCs can further split up into solution [32] and vacuum processed devices [33,34]. Currently standard materials for solution processing are polythiophenes as electron donor and fullerene derivatives as electron acceptor. The standard materials for small molecule heterojunction cells are phthalocyanines as donor and fullerene C_{60} as acceptor.

Concerning the HJSCs, a competition is currently going on between polymer based (solution processed) and small molecule (vacuum and thermal evaporation processed) solar cells. The Heliatek GmbH (http://www.heliatek.com) and IAPP (Dresden, Germany) achieve production-relevant efficiency record of 8.3 % [35, 36] for organic photovoltaic cells in 2010 [15].

Later in the same year Konarka Technologies Inc. (http://www.konarka.com) (Lowell, USA) achieved the same power convesion efficiency for a polymer based single-junction solar cell.

While Konarka is already selling products on the market, Heliatek is planning to produce in the start of 2012.

However, through the huge potential of chemical syntheses, in the future we will have materials absorbing in the near or infrared sun spectrum allowing new niche applications and design studies.

2.2 Fundamentals

2.2.1 Organic semiconductors

What are organic semiconductors? "Organic" means compounds made from hydrocarbons. Around 19 million organic compounds are known. All building blocks of life known so far are based on hydrocarbons.

Organic semiconductors are hydrocarbon compounds with a saturated π-electron system. Organic solids and crystals are only weakly bound through the Van-der-Waals interaction and do not form covalent bonds. The Van-der-Waals interaction [37], also called dispersion force, is an attraction force between two neutral and non-polar molecules with a polarization α and is given by:

$$F = \frac{1}{(4\pi\epsilon_0)^2}\frac{A'\alpha^2}{r^7}, \tag{2.1}$$

A' is a molecule specific factor, which accounts that the interacting molecules do not necessarily have spherical symmetry and that their distance in a crystal is not much larger than their extension. The dispersion force is of very short range due to the r^7 dependency and proportionality to the square of α.

Van-der-Waals binding energies are typically on the order of 0.01-0.001 eV and much smaller compared to those of covalent bonds with 2-8 eV [38]. Through the relatively small overlap of the π-orbitals, only narrow transport bands are formed in organic crystals. Therefore, a strong localization of the charge carriers occurs on the molecule. In case of amorphous organic solids, the band model is not applicable anymore and other models have to be found to describe the transport mechanism. The transport states in organics are now denoted as "transport levels". Properties of such solids are low charge carrier mobilities, melting, and boiling points. However, huge dipole interactions allow extremely high absorption coefficients ($>10^5\,\mathrm{cm}^{-1}$) [39].

The intermolecular compared to the intramolecular interaction is lower for organic solids and contrary to covalent or ionic bound crystals. Hence, most of the organic materials are found to be amorphous or anisotropic. The properties of the single molecule remain and significantly influence the properties of the organic solid. Not only the electrical and optical characteristics of the single molecules are crucial, but also the molecular orientation and arrangement in the solids. Due to the typically low symmetry of molecules (except of the fullerene C_{60}), no isotropic structures are formed. Thus, macroscopic properties in organic solids, e.g. charge carrier mobilities or light absorption, are typically anisotropic.

The aromatic molecule benzene as one possible basic molecule among, e.g. polyacetylene or thiophene rings, is discussed following.

2.2.1.1 Aromatic molecules

The major component of aromatic molecules was successfully isolated by Michael Faraday [40] in 1825 from compressed illuminating gas. Today, this hydrocarbon is known as benzene C_6H_6. Benzene is the model substance for a huge class of compounds, which are referred to as "aromatics" due to their particular properties. Because of its unusual stability (aromaticity) and inertness it attracted attention. The explanation was found in the electronic, regular hexagonal structure of the benzene ring, which is created by six sp^2-hybridized carbon atoms, as shown in Fig. 2.1. Each p-orbital overlaps equally with its neighbor and forms a π-cloud (delocalized π-electrons) above and below the ring plane, respectively, visualized in Fig. 2.2. The molecule benzene is a symmetrical hexagon with a C-C bond (139 pm). This length is between a single bond (147 pm) and a double bond (134 pm) and shows no alternating single and double bonds (mesomerism) [41]. In contrast, the instable cyclohexatrien with its alternating single and double bonds is just a theoretical model and does not exist [41]. The difference between them is the hybridization heat of 124 kJ/mol and is a degree of stability (resonance energy or aromaticity).

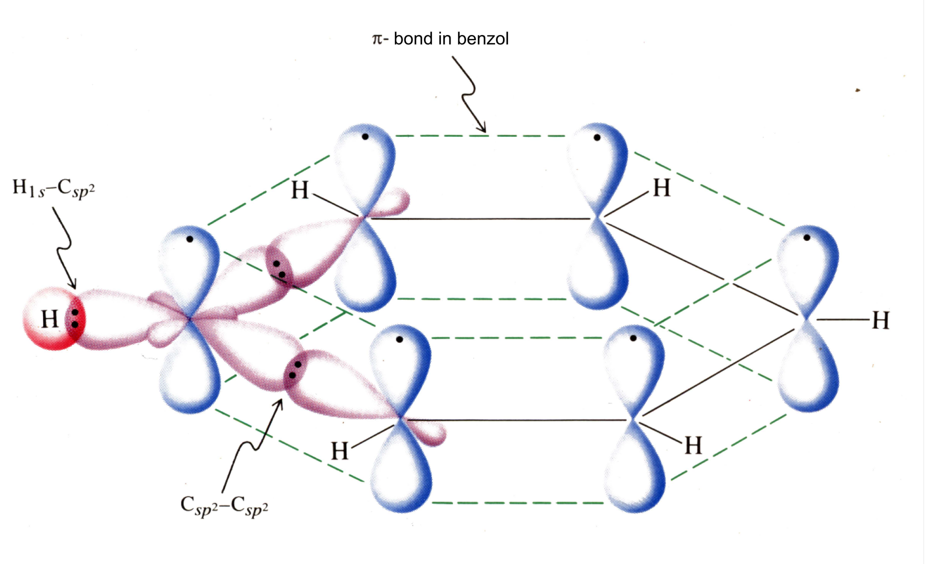

Figure 2.1: *Orbital illustration of σ- and π- bonds in benzene, which form sp^2 hybrid orbitals [41].*

By a transition from atoms to a molecule, Fig 2.3(a) a smaller splitting of the p_z orbitals and formations of the π-molecule orbitals occur, which are caused by a smaller overlap of the p_z orbitals in the π-bonds, compared to the sp^2 orbitals in the σ-bonds, Fig 2.3(b). Therefore, the π-electrons determine fundamentally the solid properties of the organic semiconductor. Here, we differentiate between the HOMO (highest occupied molecular orbital) and the LUMO (lowest unoccupied molecular orbital). The

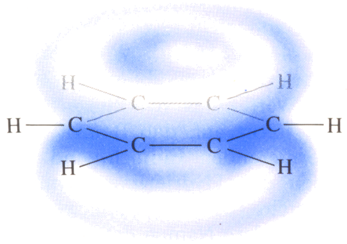

Figure 2.2:π*-electron cloud is formed due to the overlap of* π*-bonds in benzene [41].*

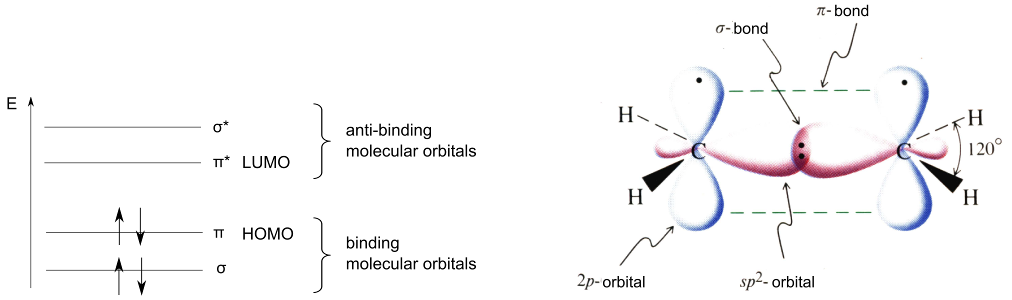

(a) binding and non-binding hybrid orbitals

(b) sp^2 hybrid orbitals

Figure 2.3: *a) energetic depiction of the splitting of binding and anti-binding* π*- and* σ*- molecular orbitals [41]; b) depiction of* π*- and* σ*-bonds in a* sp^2*-hybrid orbital.*

π-π^* (HOMO-LUMO) is the lowest electronic transition, where π represents the binding and π^* the anti-binding molecular orbital, schematically shown Fig. 2.3(a). The difference between the molecular orbitals is called energy band gap (E_g) and confers the properties of a semiconductor to aromatic molecules. The π-electron systems allows the charge transfer between molecules, if their π-systems overlap.

Typical representatives of this molecular class depicted in Fig. 2.4 are the polycondensed hydrocarbons, which consist basically of a number of benzene rings, composed to flat molecules like naphtaline, antracene, tetracene, or pentacene. Fundamental studies with this material class have been carried out [43]. A general rule is that adding with benzene rings, the different molecular π-orbitals are coming closer and closer and lead to an increased number of molecular p_z orbitals which take part in the π-conjugation. Accordingly, both the optical and the electrical gap decrease with the size of the molecule [44]. To obtain molecules with absorption properties in the visible part of the sun spectrum, rather large molecules like phthalocyanines (e.g. ZnPc [45]) or perylene derivatives (e.g. Bu4-Ph4-DIP [46, 47]) are needed. Such large molecules are heavier and need more thermal energy for sublimation. Consequently, they are easier to handle in vacuum as long as they have high glass transition temperature. Going to even larger molecules for near infrared and infrared absorbers, which are also required in the application field of solar cells, the probability rises that the molecules

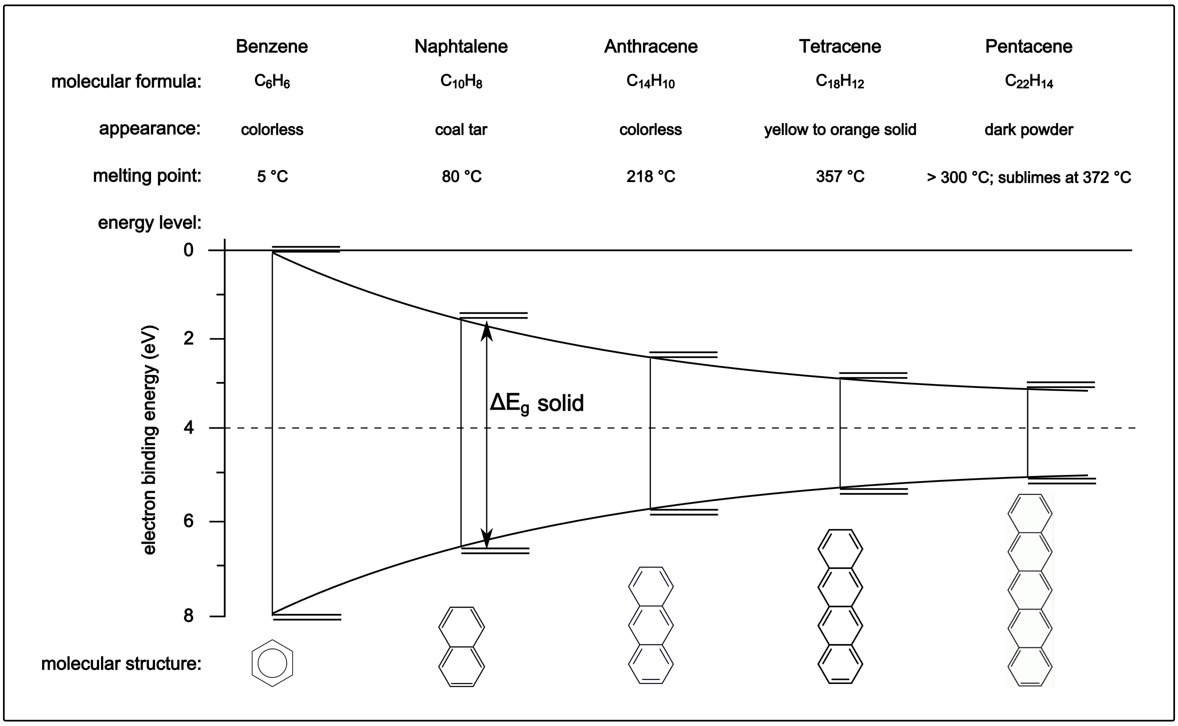

Figure 2.4: *Ionization energies and electron affinities of linear polyacenes in solid state, after [42].*

are not vaporable anymore and decompose before sublimation due to a too high supply of thermal energy. With the possibility to create molecules with desired properties, the organic materials have huge potential for various thin film applications. The characteristics of molecules can also be influenced by adding functional endgroups (e.g. fluoridation [48]). Currently, much effort is put into synthesizing organic compounds for organic solar cells.

2.2.1.2 From a single molecule to an organic solid

In Fig. 2.5 the change of energy levels for a transition from a single molecule to a Van-der-Waals bound organic solid is shown [37]. The ionization potential IP_s of the solid is decreased by the polarization energy P_h compared to the ionization potential of the molecule IP_m. Due to a small molecular interaction (overlap of the π-orbitals) in the organic solid, the charge carrier transport level for holes E_h (HOMO) is only weakly broadened. The LUMO corresponds to the electron transport level E_e in organic solids. The HOMO (M^-) (molecular anion) is shifted downwards by the polarization energy P_e in organic solids to E_e. The first excited singlet state S_1 is broadened in an organic solid due to intramolecular dipole-dipole interaction and is called exciton band. The energetic difference between the first excited singlet state S_1 and the HOMO corresponds to the first optical transition of the molecule. In the solid state, optical transitions may be allowed or forbidden.

Due to an often undifferentiated usage of HOMO and ionization potential (*IP*) in the organic semiconductor community, we set HOMO equal to the ionization potential and the LUMO to the electron affinity (*EA*) in this work.

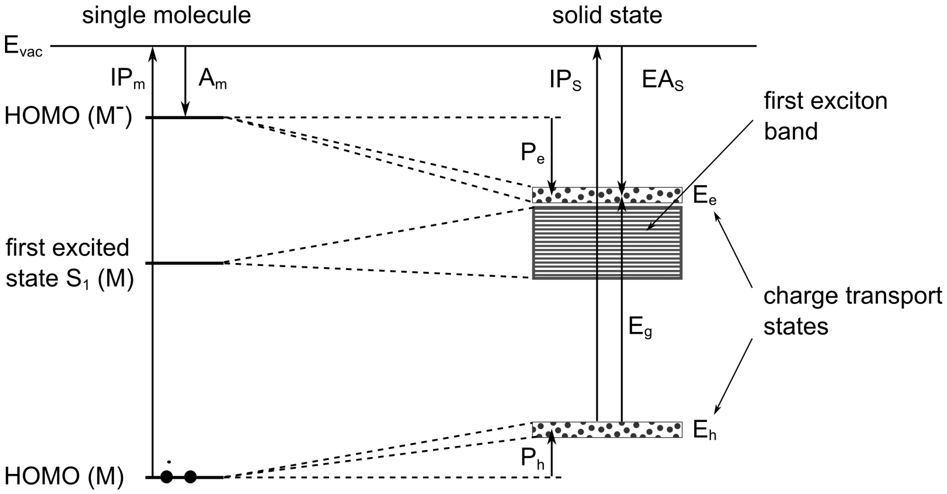

Figure 2.5: *Evolution of the π-electron state upon formation of a Van-der-Waals solid of organic molecules M with saturated π-electron systems, after [37].*

2.2.1.3 Excitons

An exciton is a quasiparticle consisting of a bound state of an electron and hole in semiconductors. It is a Coulomb-correlated electron-hole pair with no net charge and an elementary excitation of condensed matter. The bound electron and hole pairs provide a means to transport energy without transporting net charge. The concept of excitons was first proposed by Yakov Frenkel in 1931 [49], when he described the excitation of atoms in a lattice of insulators. He proposed that this excited state would be able to travel in a particle-like fashion through the lattice without the net transfer of charge [50].

An exciton may be created when a photon is absorbed by a semiconductor. Different kinds of excitons exist, depending on the material properties.

Wannier-Mott-Excitons

This type of exciton was named after Gregory Wannier and Nevill Francis Mott. Wannier-Mott excitons [51] are typically found in semiconductor crystals with small energy gaps and high dielectric constant ϵ, e.g. Si $\epsilon_{\text{silicon}} = 11.7$ [52]. In inorganics, exciting an electron from the valence band into the conduction band, a localized hole of opposite electric charge is created, to which the electron is attracted by the Coulomb force. This attraction provides a stabilized state. Therefore, the exciton has a lower energy than the unbound electron and hole. The wave function of the bound state is hydrogenic. However, the binding energy in these systems is much smaller and the particle size much larger than a hydrogen atom because of the screening of the Coulomb force due to the presence of other surrounding electrons in the semiconductor and the small effective masses of the excited electron and hole. Therefore, a Wannier-Mott exciton schematically shown in Fig. 2.6 a) is created, which has a radius larger than the lattice spacing. Due to the lower masses and the screened Coulomb interaction, the binding energy is much less than that of a hydrogen atom, typically on the order of 0.01 eV. At ambient conditions the thermal energy is on the order of 25 meV and is well above the binding energy of the Wannier-Mott exciton and leads to free charge carriers in inorganic semiconductors, e.g. silicon solar cells [52]. The recombination of the electron and hole, i.e. the decay of the exciton, depends on the overlap of the electron and hole wave functions.

Frenkel excitons

The Frenkel exciton [49, 53], named after Yakov Frenkel, has a typical binding energy on the order of 0.1 - 1.0 eV. Frenkel excitons are found in alkali halide crystals and in organic molecular crystals composed of aromatic molecules, where they are electrostatically bound with a binding energy much higher than $k_\mathrm{B}T$ at room temperature. In materials with small dielectric constants, e.g. organic molecules (benzol $\epsilon_\mathrm{benzol} = 2.28$ [54]), the Coulomb interaction between electron and hole may be strong and the excitons tend to be small compared to the size of the unit cell, see Fig. 2.6 b), or, in the case of molecular excitons, even on the same molecule. Thus, the electron and hole are located in the same cell. If the electron is found in the LUMO and a hole in the HOMO, and since they are within the same molecular orbital manifold, the electron-hole state is bound. Molecular excitons typically have characteristic lifetimes on the order of nanoseconds (1 - 10 ns [18], after which the excited electron decays radiatively (photoluminescence) or non-radiatively (energy of the excitation is transferred to vibrations (phonons)) in the electronic ground state of the molecule.

The average distance in a given material that an exciton can travel before annihilation is defined as the material-specific exciton diffusion length L_D, given by

$$L_\mathrm{D} = \sqrt{D\tau}, \tag{2.2}$$

where τ is the exciton lifetime and D the diffusion coefficient. L_D can vary from 1 nm to more than 50 nm, dependent on the material and structure [55–59]. The diffusion coefficient of charge carriers in typical molecular crystals is on the order of $10^{-2}\,\mathrm{cm}^2/\mathrm{s}$ corresponding to a mobility around $1\,\mathrm{cm}^2/\mathrm{Vs}$ [60], whereas the diffusion coefficient of singlet [61] and triplet [62] excitons is 10^{-3}-$10^{-4}\,\mathrm{cm}^2/\mathrm{s}$ and 10^{-4}-$10^{-5}\,\mathrm{cm}^2/\mathrm{s}$ [63].

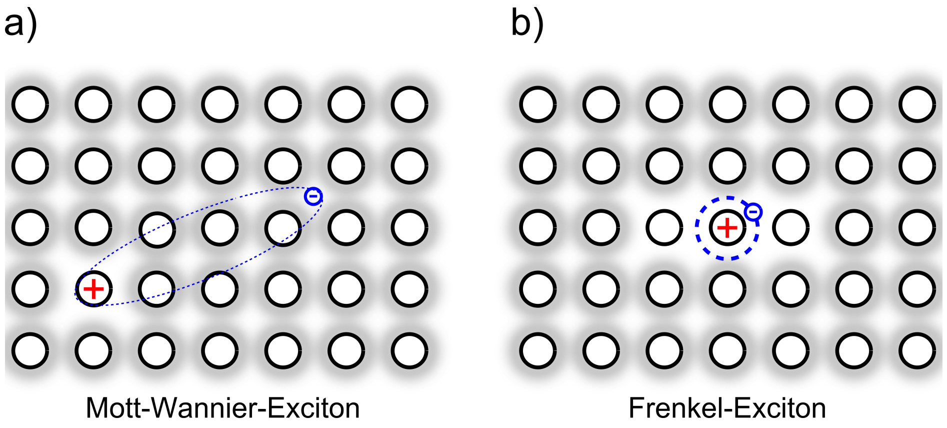

Figure 2.6: *a) Wannier-Mott exciton and b) Frenkel exciton.*

Molecular excitons have several interesting properties, one is the Förster resonance energy transfer [64]. If a molecular exciton has good energetic matching to a second molecule's absorption spectrum, the energy is may be transferred from one molecule to another. The crucial parameter for this process is the intermolecular distance, which is on the order of 2 - 5 nm [65]. Furthermore, there is another energy transfer assisted by Coulomb interaction over a distance of 1 - 1.5 nm called Dexter transfer [66,67].

However, the excitation process in organic solids is not fully understood yet. The group of Knupfer et al. [68,69] determined by employing inelastic electron scattering the exciton dispersion in pentacene. They claim: *"the failure of the applied tight-binding description provides strong evidence for a necessary reconsideration of the traditional, Frenkel exciton based, understanding of the lowest-lying electronic transitions in organic semiconductors"* [70].

2.2.1.4 Charge carrier mobility

The charge carrier mobility μ

$$\vec{\nu} = \overline{\overline{\mu}}\vec{E}, \tag{2.3}$$

links two vector variables, the macroscopic electrical field ($\vec{E}$) and the microscopic drift velocity of the charge carriers ($\vec{\nu}$). Therefore, the mobility is a second order tensor. Simplified, the mobility can be described as scalar, when both vector variables point in the same direction. Accordingly, the mobility can be determined from the quotient of the absolute values of the vector variables to

$$\mu = \frac{\nu}{E} = \frac{d}{E \cdot \tau_t}. \tag{2.4}$$

τ_t is the transit time and d the layer thickness. Equation 2.4 can be applied to simplified structures like the flat heterojunctions in organic solar cells.

For electrons n as well as for holes h, the specific material variable can be determined. In organic materials the mobility is on the order of 10^{-9}-10^{1} cm^2/Vs [71–73] and is low compared to inorganic materials, e.g. Si 480 and 1350 cm^2/Vs [74] for holes and electrons, respectively. Using the mobility, given by formula 2.3 for the electrons (μ_n) and holes (μ_h), the elementary charge e, and the charge carrier densities (n, p), the conductivity which is defined by Ohm´s law can be expressed using the microscopic variables:

$$\sigma = e \cdot (n\mu_n + p\mu_p). \tag{2.5}$$

2.2.1.5 Band and hopping transport

The application of the band model after applying Bloch's theorem has been proven for inorganic crystalline semiconductors [75]. A strong interaction between the lattice components is caused by the small distances and strong covalent bonds. Due to the lattice structure periodic potentials are formed $V(\vec{r} + \vec{R}_i) = V(\vec{r})$ (i count index; $\vec{R}_i$ lattice vector). After solving the one electron - Schrödinger equation

$$H(\vec{r})\Psi_{\vec{k}}(\vec{r}) = \left(-\frac{\hbar^2\nabla^2}{2m} + V(\vec{r})\right)\Psi_{\vec{k}}(\vec{r}) = E(\vec{k})\Psi_{\vec{k}}(\vec{r}) \tag{2.6}$$

and using the Bloch theorem

$$\Psi_{\vec{k}}(\vec{r} + \vec{R}_i) = \Psi_{\vec{k}}(\vec{r})e^{(i\vec{k}\vec{R}_i)} \tag{2.7}$$

the formation and splitting of bands at the edge of the Brillouin zone is obtained. For band transport the charge carriers behave like strongly delocalized plane waves in a distinct charge carrier band. Such materials show mobilities larger than 1 cm^2/Vs [74] with a mean free path larger than the distance between two neighboring molecules. The band model can be applied for organic solids in just a few cases (e.g. C_{60} single crystals [76], naphthalene, and perylene [77, 78]). Due to the weak Van-der-Waals interaction in amorphous organic solids, where the overlap of neighboring molecules is very small, no band structures are formed.

The charge transport in organic semiconductors is mostly dominated by hopping and not by band transport. In this case the charge carriers are located in localized states on the molecule and hop from one molecule to another as illustrated in Fig. 2.7 b). Thereby, existing barriers can be overcome either by hopping or by tunneling. Charge carrier mobilities for such organic semiconductors are typically $<<$ 1 cm^2/Vs [79–81].

If a charge carrier remains longer than the electrical relaxation time (τ_e=10^{-16}-10^{-15} s) on the molecule, a polarization is built up. The polarization energies in organic semiconductors are large, contrary to inorganic semiconductors, and range between

1-3 eV [82]. The polarization induces dipoles in the neighboring molecules, which provides an energetic stabilization of the charge carrier. Since the charge carriers remain much longer on the molecule than the relaxation time, the charge carriers can be considered as polarons before they hop. The polarization cloud moves with the charge carrier from one molecule to another. This system can not be described with the one electron approach [52] of the classical band model anymore. In principle, polarons can also form bands, whereas the band width is reduced in comparison to free charge carriers [83]. However, above room temperature the hopping process is the predominant transport mechanism, due to a thermally activated onward hopping, which happens faster than the delocalization in a polaron band. In a disordered layer the statistic scattering of the polarization energy is accompanied by the delocalization [84–86]. As mentioned above, there are different possibilities to describe the hopping process. On the one hand, there is the tunneling model; on the other hand, there are the thermally activated hopping transport models [75,87,88]. The tunneling model describes an electron transfer through the intermolecular potential barrier, which takes place quantum mechanically. Thereby, the thickness and the shape of the barrier play a crucial role. However, the thermal activation is also of importance, because the molecular distances can get smaller than the mean distance due to vibrionic states which allows a preferential tunneling.

During the thermally activated hopping an energy transfer of the lattice vibrations (phonons) occurs at the initial and and final state, but not during the electron transfer. In a first step, the states "A^-A" and "AA^-" are generated through thermal activation. In the second step, an electron transfer k_{ET} takes place to the "activated complex" without any energy transfer [89].

$$A^-A \rightleftharpoons \text{"}A^-A\text{"} \overset{k_{\mathrm{ET}}}{\leftrightarrow} \text{"}AA^-\text{"} \rightleftharpoons AA^- \tag{2.8}$$

A^- defines the state of a molecule with a negative charge, which was induced by thermal activation and A the neutral state. The electron transfer rate k_{ET} depends on the overlap of the involved molecular orbitals. Note that there is no generally accepted model to describe the charge transport in organic semiconductors. To determine the predominant transport mechanism, the mobility value can be used as indication.

Knowledge concerning the mechanism of charge carrier generation and transportation is required to improve the properties of organic devices. This recognition has recently led to an increased effort, both experimentally and theoretically, by different groups [63, 90, 91] to clarify the fundamental aspects of charge transport in organic solids. Usually, a disordered solid will exhibit both diagonal (fluctuation of electron energies) and off-diagonal (fluctuation of hopping integrals) disorder. However, it is

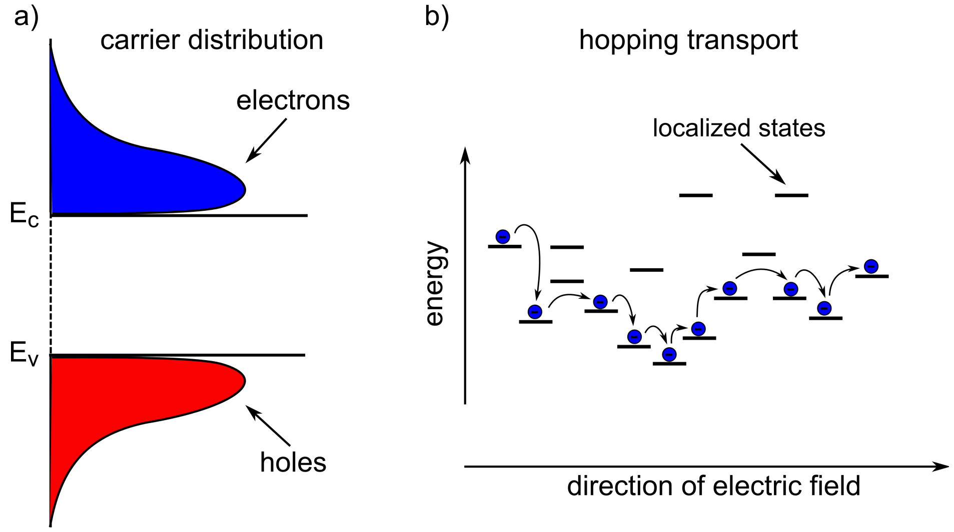

Figure 2.7: *Charge distribution for electrons (blue) and holes (red) and hopping transport from one localized state to another, shown here for electrons.*

difficult to separate both effects on electronic transport phenomena. Exceptions are isotropically mixed crystals, like naphthalene/perdeutero naphthalene. The present treatment is focused on electronic transport processes in disordered single component organic solids prepared by methods like vapor condensation or solvent evaporation.

Bässler disorder model

Bässler and co-workers [63] have used Monte Carlo techniques to understand the transport mechanism in organic materials, achieving quite good fits of field and temperature dependency of the mobility determined by e.g. transient electroluminescence measurements. The Gaussian shape of the density of states (DOS) is assumed since the polarization energy is determined by a large number of internal coordinates, each varying randomly by small amounts. Therefore, the proposed function $g(E)$ [63] of DOS distribution, implying that all states are localized is:

$$g(E) = \frac{N_{\mathrm{HOMO}}}{\sqrt{2\pi\sigma^2}} \exp\left(-\frac{E^2}{2\sigma^2}\right), \tag{2.9}$$

where N_{HOMO} is the total density of states on the order of $10^{21}\,\mathrm{cm}^{-3}$, σ the Gaussian width of the distribution, and E is the shift between these distributions.

The jump rate among sites n and m is assumed to be of Miller-Abrahams type [92]: jumps to higher site energies $\nu_{\mathrm{nm}}(\uparrow)$ scale by Boltzmann factor by neglecting the polaronic effects, while the respective factor is unity for hops to lower energies $\nu_{\mathrm{nm}}(\downarrow)$:

$$\nu_{\mathrm{nm}(\uparrow\downarrow)} = \nu_0 \exp\left(-2\gamma_{\mathrm{d}} \cdot a \frac{\Delta R_{\mathrm{nm}}}{a}\right) \begin{cases} (\uparrow) & \exp\left(-\frac{E_{\mathrm{n}}-E_{\mathrm{m}}}{k_{\mathrm{B}}T}\right); \; E_{\mathrm{n}} > E_{\mathrm{m}}, \\ (\downarrow) & \quad 1; \qquad E_{\mathrm{n}} < E_{\mathrm{m}}, \end{cases} \tag{2.10}$$

where ν_0 is a prefactor which considers the overlap of the wave functions, a is the average lattice constant, γ_{d} denotes the dimensionless random variable describing the off diagonal disorder effects, E_{n} and E_{m} are the energies of the transport states of the localized states within the distribution $g(E)$ in the zero field, and ΔR is the intersite distance between transport sites located at lattice site R_{n} and R_{m}. Equation 2.10 implies that for a thermally activated hopping process $\nu_{\mathrm{nm}}(\uparrow)$ to an energetically higher state, an additional activation energy is needed than the energy difference of the transport states, which is a function of the field strength. Hopping processes $\nu_{\mathrm{nm}}(\downarrow)$ to energetically deeper lying localized states do not need any activation. Thus, $\nu_{\mathrm{nm}}(\uparrow) \neq \nu_{\mathrm{nm}}(\downarrow)$. A universal law from the Monte Carlo simulation of the Gaussian formulation is established, relating μ to the degree of both diagonal and off-diagonal disorder in the high field ($E > 10^5$ V/cm) and can be given as dependency of the energetic scale $\hat{\sigma}$, spatial disorder parameter Σ, electric field E, and pre-exponential factor μ_0:

$$\mu(\hat{\sigma}, \Sigma, E) = \mu_0 \exp(-(\frac{2}{3}\hat{\sigma})^2) \begin{cases} \exp C(\hat{\sigma}^2 - \Sigma^2)E^{1/2}; & \Sigma \leqq 1.5, \\ \exp C(\hat{\sigma}^2 - 2.25)E^{1/2}; & \Sigma < 1.5, \end{cases} \tag{2.11}$$

where the empirical constant C depends on the distance between adjacent hopping sites and is $3.9\times10^{-4}\sqrt{\mathrm{cm/V}}$. Accordingly, the interplay between the Boltzmann factors and the Gaussian distribution of states can determine the equilibrium energetic distribution of the charge carriers and the average transport energy.

Poole-Frenkel model

Another empirical approach is the Poole-Frenkel formula [37], where the field dependent mobility can be described as:

$$\mu(E, T) = \mu_\infty \exp\left(-\frac{\Delta_0 - \beta_{\mathrm{PF}}\sqrt{E}}{k_{\mathrm{B}} T_{\mathrm{eff}}}\right), \tag{2.12}$$

where μ_∞, Δ_0, β_{PF}, and T_{eff} are constants. The fundamental assumption (Poole-Frenkel-effect) is that charged trap states exist which become neutral after trapping a charge carrier. The trap states have Coulomb-potentials which superpose with the external potential. In the direction of the electric field E a maximum of the potential Φ_{m} is established at $x_{\mathrm{m}} = \sqrt{e/4\pi\epsilon\epsilon_0 E}$, as shown in Fig. 2.8. The decrease of the energetic barrier at x_{m} adverse to the field-free case is:

$$\Delta\Phi \equiv \beta_{\mathrm{PF}}\sqrt{E} = \sqrt{\frac{e^3}{\pi\epsilon\epsilon_0}}\sqrt{E}, \tag{2.13}$$

where the probability to overcome the barrier increases with exp($-\Delta\Phi/k_\mathrm{B}T$) and the mobility can be given as:

$$\mu(E,T) = \mu_\infty \mathrm{exp}\left(-\frac{\Delta_0 - e\sqrt{eE/\pi\epsilon\epsilon_0}}{k_\mathrm{B}T}\right). \tag{2.14}$$

The derivation from the Poole-Frenkel-effect is formally possible, but there are some reasons which contradict the model picture, e.g. the distance of the potential maximum x_m to the trap state at typical field intensity is one order of magnitude larger as the typical hopping distance between two molecules of 0.5-1 nm ($x_\mathrm{m} = 6$ nm at E=10^5 V/cm, and $\epsilon = 4.0$). Therefore, the $\sqrt{E}$ dependency in the exponent of the mobility can not easily be described by the Poole-Frenkel-effect. Pautmeier et al. [94] have shown by Monte Carlo simulation techniques that inclusion of random variations of the wave function overlap parameter ("off-diagonal" disorder) generates Poole-Frenkel behavior of the charge-carrier mobility in random organic solids within an experimentally relevant range.

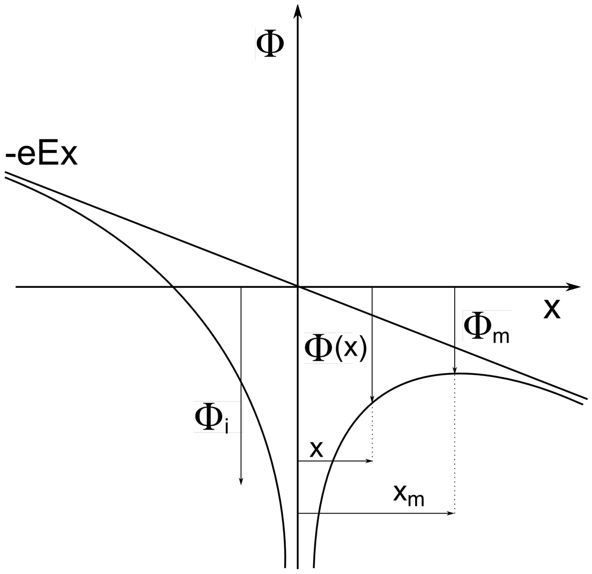

Figure 2.8: *Superposition of the Coulomb potential of the traps with the external potential (Poole-Frenkel effect). A maximum of the potential* Φ_m *is established at* x_m *[after [93]].*

Transport in doped organic materials

Doping of organic semiconductors is essential for improved charge carrier injection and reduction of Ohmic losses for thick layers. Arkhipov et al. [95] considered the charge carrier transport in such doped disordered organic layers. Since the HOMO level is deep in most organic solids and the gap separating LUMO and HOMO states is wide, energies of donor and acceptor molecules are normally well below LUMO and above

HOMO, respectively. Therefore, a double peak Gaussian function is supposed to be a realistic model for the DOS distribution $g(E)$:

$$g(E) = \frac{N_\mathrm{i}}{\sqrt{2\pi}\sigma_\mathrm{i}} \exp\left(-\frac{E^2}{2\sigma_\mathrm{i}^2}\right) + \frac{N_\mathrm{d}}{\sqrt{2\pi}\sigma_\mathrm{d}} \exp\left(-\frac{(E+E_\mathrm{d})^2}{2\sigma_\mathrm{d}^2}\right) \quad [95], \tag{2.15}$$

where N_i and N_d are the total densities of intrinsic states and dopants, σ_i and σ_d the Gaussian widths of the intrinsic and dopant DOS distributions, and E_d is the energy shift between these distributions. Both analytic consideration and Monte-Carlo simulation have shown that a carrier will most probably jump from a currently occupied state to a hopping site that belongs to a so-called effective transport level with the energy E_tr. At higher temperatures, E_tr remain almost unaffected by doping. With decreasing temperature, the effective transport level goes down and approaches the Fermi energy. Arkhipov et al. found that the concept of effective transport energy is universal and can be applied to the consideration of carrier hopping around the Fermi level. They claim that this concept is fully applicable to the problem of charge carrier transport in doped hopping systems at both low and high temperatures. Using strong donor or acceptor molecules that basically introduce shallow dopant states, a superlinear increase of conductivity with the doping ratio has been observed [96]. This increase can be explained by the saturation of the energetic states in the tail of the distribution, while states close to the center of the DOS are occupied. Here, the density of states is high, the mean hopping distance is accordingly low and the hopping rate is high. The whole material is electrically neutral with the concentration of electrons n and holes p corresponding to the density of negatively charged acceptors N_A^- or positively charged donors N_D^+, respectively.

Determination of the charge carrier mobility

To determine the charge carrier mobility of an organic material, different approaches can be applied. Each method has its advantages and disadvantages, in particular dependent on the condition under which the mobilities are measured. Due to the fact that the mobility depends on various parameters, the measuring conditions have a huge impact on the results. In some cases device stacks have to be made which differ compared to a typical solar cell stack. The morphology which might depend on the layer device stack influence the mobility as well. Therefore, a crucial question is how a method can be applied and compared to others. Common methods are now considered, with focus on the field effect transistor which is used in this work:

Space charge limited current (SCLC)

The theory of space charge limited current (SCLC) between plane parallel electrodes was first given by Mott and Gurney [97] (1940) and has been extended by several authors, e.g. Lampert [98] in 1956. Later in 1969 it was also shown for organics [99].

The current flow is limited either by barriers at the electrodes (injection and extraction) or through transport in the organic layer. To get space charge limited current (SCLC) Ohmic contacts are required. The current flow is then limited by the charge carrier mobility. A further essential requirement is that only one kind of charge carriers is injected and the other one is blocked. This can be realized by choosing a suitable stack design (e.g. electron- or hole only devices [100, 101]). Applying a voltage to the device charges are injected and disturb the neutrality of the material, which can not quickly be regulated. The time in which the sample relaxes into the state of equilibrium is denoted as relaxation time τ_D. If τ_D is larger than the transit time τ_t, the injected charge carriers accumulate at the injection electrode. Consequently, a space charge region is generated and hinders further charge carrier injection.

$$\tau_\mathrm{d} = \frac{\epsilon}{en\mu} > \tau_\mathrm{t} = \frac{d^2}{\mu V}, \tag{2.16}$$

where ϵ is the dielectric constant, d the thickness of the intrinsic layer, and V the applied voltage. In the case of SCLC, the current-voltage characteristic does not satisfy the Ohmic law any longer and shows a superlinear behavior of V^2 and is described in the absence of any trapping effects by the Mott-Gurney law [102]:

$$J = \frac{9}{8}\mu\epsilon\epsilon_0\frac{V^2}{L^3}. \tag{2.17}$$

Time of flight (TOF)

The time of flight (TOF) method is a rather simple and direct approach, shown by Warta and Karl [78] for naphthaline and Kitamura et al. [103] for the molecule CuPc. A layer with a well known thickness between a pair of plane electrodes is excited by a short intense light pulse. Free charge carriers are generated in the organic layer and accelerated by the applied voltage V towards the electrodes, where one electrode has to be transparent for the light pulse. The ratio of the layer thickness where the photons are absorbed δx and the overall layer thickness should be very small to achieve a rather narrow mobility scattering. This requires a strong photon absorbing material, an accurate layer thickness determination, and good charge extraction properties. For the mobility calculation the thickness d, the applied voltage V, and the transit time τ_d between the optical excitation and the arrival of the charges at the electrode have to be known:

$$\mu = \frac{d^2}{\tau_\mathrm{d} V}. \tag{2.18}$$

Impedance spectroscopy (IS)

Using impedance spectroscopy, dielectric properties of a sample under alternate current voltage conditions, can be investigated. Similar to the SCLC method, a specific device geometry is required which allows the transition of only one kind of charge and blocks the other one. Ohmic contacts to get an efficient charge carrier injection are also necessary. For charge carrier injection a direct current voltage is applied.

To get a transition time which is rather large, thicknesses of several hundred nanometers are required. The transition time τ_{dc} can be obtained from the frequency dependent susceptance B, shown by Martens [104], Tsang [105], and others. The imaginary part of the complex susceptance $\tilde{Y}$ is the susceptance B

$$\tilde{Y} = G + \mathrm{i}B \tag{2.19}$$

$$B = \mathrm{i}\omega C \tag{2.20}$$

and is given by the capacity C of the sample. G is the conductance, $\tilde{Y}$ is the inverse of the complex impedance $\tilde{Z} = \tilde{Y}^{-1}$. For high frequencies the sample behaves like a plate capacitor with a geometrical capacitance $C_{\mathrm{geo}} = \epsilon A/d$. If that high frequency range the charge carriers are not able to reach the counter electrode and the organic semiconductor behaves like a dielectric. If the frequency decreases below the inverse of τ_{dc}, the charge carriers are able to transit and the capacitance is decreased below the geometric capacity C_{geo}. It means for materials with rather high charge carrier mobilities, either higher frequencies have to be applied or very thick layers are required. Similar to the TOF method, ohmic contacts are essential.

The τ_{dc} can be evaluated graphically by plotting C versus frequency. Hence, the mobility can be obtained similar to TOF by:

$$\mu = \frac{d^2}{\tau_{\mathrm{dc}} V}. \tag{2.21}$$

Organic field effect transistor (OFET)

A common used method to determine the charge carrier mobility of organic materials is the organic field effect transistor (OFET) [106, 107]. The first OFET was investigated by Tsumara et al. [108] in 1986. An FET is a thin film transistor (TFT), where the commonly used amorphous silicon (Si) is replaced by an organic semiconductor. The transistor is based on a plate capacitor which is often assembled by a highly doped silicon wafer and the deposited organic layer. The silicon is highly n- or p-doped to achieve quasi-metallic conduction properties. Furthermore, the silicon wafer is used due to an easy and well controllable thermally deposition of the silicon oxide (SiO_2) layer with a small roughness. The SiO_2 is used as dielectric medium. The Si wafer represents the gate contact as sketched in Fig. 2.9. If a gate voltage V_G is applied, charges are induced in the

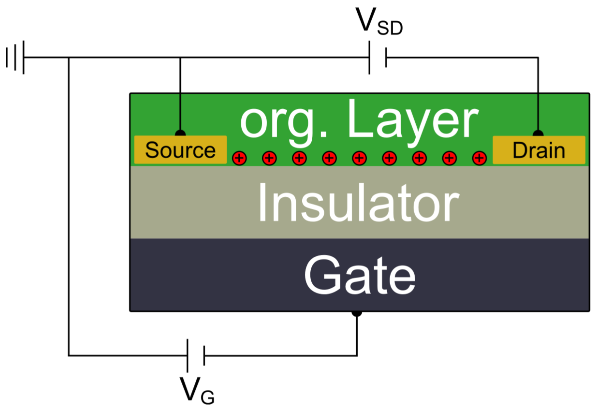

Figure 2.9: *Structure of a bottom-gate organic field effect transistor (OFET), the gate consist typically of Si and is followed by an insulating layer of SiO. The organic layer is deposited on it. The source and drain Au contact are pre-structured.*

organic semiconductor and a region (channel) with an increased charge carrier density is generated at the interface SiO/organics. The kind of the charge and the charge carrier density can be set by the applied voltage V_G. The gold contacts source and drain have a well defined distance L, the channel length. Due to the low conductivity of the semiconductor, a very small current flows at low voltage. By increasing V_G, charges accumulate and the conductivity increases by several order of magnitudes and the transistor is "open". In this work, transistors with source and drain contacts between the SiO_2 layer and the organic semiconductor on top of the gate, called bottom-gate structure, are used. To determine the charge carrier mobilities, the conductivity is measured between source and drain as a function of current and voltage.

Using the Shockley model, the characteristic of a metal oxide semiconductor field effect transistor (MOSFET) can be described very well and can also applied to OFETs [109] although no inversion, but only charge carrier accumulation occur. Figure 2.10 shows an OFET characteristic that can be separated in two parts, the linear and the saturation regime. In the linear regime, the voltage between source and drain V_{SD} is significantly lower than V_G. An accumulation channel is established with a rather high conductivity, it behaves like an Ohmic resistor. The current between source and drain I_{SD} depends on the mobility μ, channel length L and width W, capacitance of the oxid C_i, V_G, V_{SD}, and the threshold

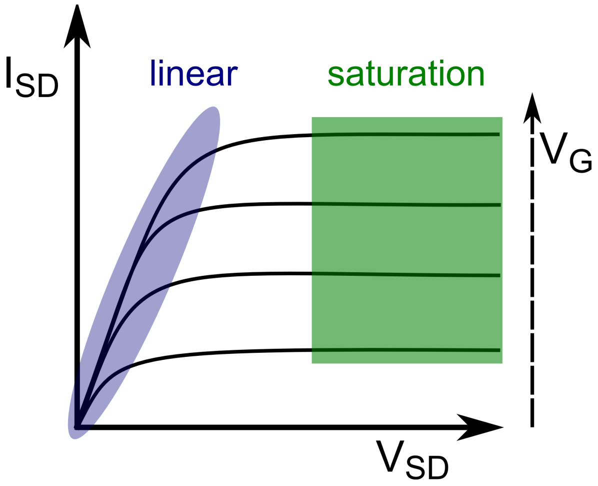

Figure 2.10: *The OFET characteristic can be divided in two regions, the linear regime (ellipse) and the saturation regime (rectancle). In both regions the mobilities can be determined.*

voltage V_{TH} which is necessary to create a channel:

$$I_{\mathrm{SD}} = \frac{C_{\mathrm{i}}W}{L}\mu\left(V_{\mathrm{G}} - V_{\mathrm{TH}} - \frac{V_{\mathrm{SD}}}{2}\right)V_{\mathrm{SD}}. \tag{2.22}$$

By differentiating equation 2.22 with respect to V_{G} and V_{SD}, μ can be obtained:

$$\frac{\partial^2 I_{\mathrm{SD}}}{\partial V_{\mathrm{G}}\partial V_{\mathrm{SD}}} = \frac{C_{\mathrm{iW}}}{2}\mu. \tag{2.23}$$

The saturation regime can be reached for higher V_{SD}. The induced charge carriers limit the current between source and drain. Close to the drain contact a depletion zone is created, which hinders a further increase of the current and saturates the current. The current flow depends only on V_{G} and the parameter of the transistor. A current between source and drain I_{SD} for this regime can be given as:

$$I_{\mathrm{SD}} = \frac{C_{\mathrm{i}}W}{2L}\mu\left(V_{\mathrm{G}} - V_{\mathrm{TH}}\right)^2. \tag{2.24}$$

The mobility can determined from equation 2.24 by plotting the square root of I_{SD} versus V_{G}. The slope in the saturation regime is proportional to $\sqrt{\mu}$

$$\sqrt{I_{\mathrm{SD}}} = \sqrt{\frac{C_{\mathrm{i}}W}{2L}}\mu V_{\mathrm{G}} - \sqrt{\frac{C_{\mathrm{i}}W}{2L}}\mu V_{\mathrm{TH}}. \tag{2.25}$$

2.2.1.6 Doping

The principle of controlled molecular doping of organic materials was invented by Pfeiffer et al. [26,110,111] in 1999. They demonstrated that organic semiconductors can be systematically doped n- or p-type by a controlled co-evaporation of organic acceptor- and donor molecules [112–114]. Using the principle of doping an increase of conductivities by 5 - 6 orders of magnitude can be achieved [115], which often results in a device improvement. Ohmic losses of up to 100 nm thick charge transport layers are marginal ($\Delta\,\mathrm{V} < 10\,\mathrm{mV}$). Doping enables a quasi-Ohmic injection of charge carriers through a very thin depletion layer around 5 nm [116], despite a relatively high injection barrier, visualized in Fig. 2.11. The principle of doping of organic semiconductors is similar to inorganic semiconductors. Through a systematic addition of acceptor or donor molecules, free charge carriers are generated. Thereby, either electrons are added to the LUMO (n-doping) or holes to the HOMO (p-doping). In case of p-doping this can be achieved by adding a acceptor molecule (dopant). Electrons are transferred from the HOMO of the matrix to the LUMO of the dopant and free holes are generated on the HOMO of the matrix, shown schematically in Fig. 2.12.

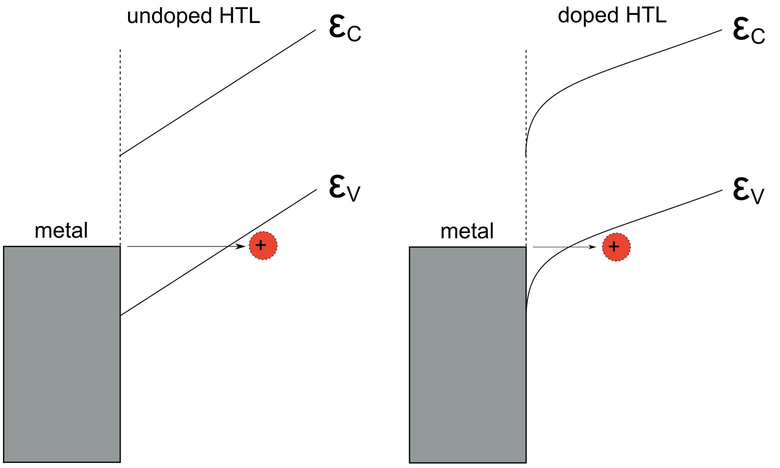

Figure 2.11: *Quasi-ohmic contact realized by doping; due to doping the depletion layer can be reduced and thus the charge carrier injection improved.* ϵ_C *is the electron transport and* ϵ_V *the hole transport level of the hole transport layer (HTL).*

To achieve an effective p-doping through an energetically preferential electron transition, the LUMO level of the dopant should ideally lie energetically deeper than the HOMO of the matrix. The p-doping process can be described by the following reaction [26]:

$$M + \tilde{M}A \rightleftharpoons M + [\tilde{M}^{+}A^{-}] \rightleftharpoons M^{+} + \tilde{M}A^{-}. \tag{2.26}$$

The doping process can be split in two steps. The host material is the matrix molecule (M) and acceptor molecule (A) is the dopant. Firstly, a charge transfer occurs between A and a neighboring matrix molecule ($\tilde{M}$). M and A form in the intermediary complex state ($\tilde{M}^{+}A^{-}$). In the second step an unbound charge carrier pair with a free positive charge is generated far away from A on M, so that Coulomb interaction has no effect anymore [26]. The negative charge itself remains on A. The charge transfer of the

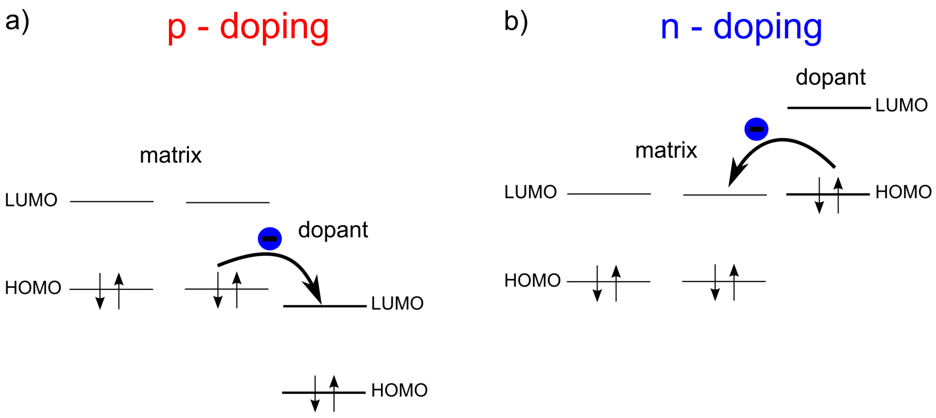

Figure 2.12: *Doping principle: a) p-doping, an electron is transferred from the HOMO of the matrix to the LUMO of the dopant; b) n-doping, an electron is transferred from the HOMO of the dopant to the LUMO of the matrix. The arrows symbolize the electron occupation.*

first step takes place completely. Therefore, only the second step and the doping concentration have an influence on the free charge carrier concentration. However, the exact doping process is yet not completely understood.

In case of n-doping a dopant molecule is required with a HOMO which lies energetically close to the LUMO of the matrix. Matrix molecules with relatively high LUMO levels in the range of -2 - -4 eV are required, but the material is then vulnerable concerning oxidation. Effective and stable dopants with such a high HOMO levels were developed and provided in recent years by Novaled AG (Dresden, Germany). The n-doping process is similar to the p-doping, free charge carriers go from the HOMO of the dopant to the LUMO of the acceptor and create free electrons, schematically shown in Fig. 2.12.

2.2.1.7 Thin film optics

Very thin layers on the order of several nanometers are deposited on top of another in many applications (e.g. organic solar cells, organic light emitting diodes, passivation layers, insulating layers between conductors, diffusion barriers, and hardness coatings for scratch and wear resistance). The understanding and modeling of device optics are extremely important to use their full potential. The solar cells with which we investigate have thicknesses $< 300\,\mathrm{nm}$ and are on the order of a fractions of the wavelength of the incident light. Due to the thin layer design, coherence effects caused by the reflective metal electrode lead to standing waves within the device. Therefore, thin film optics have to be considered as well as the interface properties (refraction, reflection, and transmission) between different layers.

n and k definition

The refractive index n is defined as the ratio of the speed of light in vacuum c_0 to the speed of light v in the material and comes from the refraction term and its appearance in Snellius´s refraction law,

$$n = \frac{c_0}{v}. \tag{2.27}$$

n is usually defined by the material relative permittivity ϵ_{r} and relative permeability μ_{r}:

$$n = \sqrt{\epsilon_{\mathrm{r}} \mu_{\mathrm{r}}}. \tag{2.28}$$

In the case of a non-magnetic material μ_{r} is approximately 1. The complex refractive index $\tilde{n}$ can then be defined by the complex permittivity $\tilde{\epsilon_{\mathrm{r}}}$ as:

$$\tilde{n} = \sqrt{\tilde{\epsilon_{\mathrm{r}}}} = \sqrt{\epsilon_1 + \mathrm{i}\epsilon_2}. \tag{2.29}$$

$\tilde{n}$ is frequency and wavelength dependent, which is called dispersion. To consider additional effects like absorption of the wave in the medium, the refractive index can be given as a complex number:

$$\tilde{n}(\omega) = n'(\omega) + \mathrm{i}n''(\omega) = n'(\omega) + \mathrm{i}k(\omega), \tag{2.30}$$

where ω is the angular frequency.
Using equation 2.29 and 2.30 the correlation between the permittivity and n and k can be shown:

$$\epsilon_1 = n^2 - k^2 \tag{2.31}$$

$$\epsilon_2 = 2nk \tag{2.32}$$

$$n = \sqrt{\frac{\sqrt{\epsilon_1^2 + \epsilon_2^2} + \epsilon_1}{2}} \tag{2.33}$$

$$k = \sqrt{\frac{\sqrt{\epsilon_1^2 - \epsilon_2^2} + \epsilon_1}{2}} \tag{2.34}$$

The extinction coefficient is a quantity for how much light is absorbed in the material. The optical constants n and k describe how light propagates through a film. In simple terms, the electromagnetic field $\vec{E}$ describes how light travels through a material (z-direction). E is given by:

$$\vec{E} = \vec{E}_0 e^{\mathrm{i}\left[\vec{k_{\mathrm{w}}} \cdot \vec{r} - \omega t\right]} = \vec{E}_0 e^{\mathrm{i}[k_{\mathrm{w}} \cdot z - \omega t]}, \tag{2.35}$$

where k_w is the wave vector and not the extinction coefficient $k = n''$. The wave vector is defined by

$$k_\mathrm{w} = \frac{\omega}{c_0}\left(n' + \mathrm{i}n''\right). \tag{2.36}$$

c_0 is the speed of light in vacuum. Implementing the wave vector in equation 2.35 an electromagnetic wave is obtained:

$$\vec{E} = \vec{E}_0 e^{\mathrm{i}\left[(n'+\mathrm{i}n'')\frac{\omega}{c_0}z-\omega t\right]} = \vec{E}_0 e^{n''\frac{\omega}{c_0}z} e^{\mathrm{i}\left[n'\frac{\omega}{c_0}z-\omega t\right]}. \tag{2.37}$$

The intensity $I \propto |E|^2$ decreases exponentially

$$I = I_0 e^{-2n''\frac{\omega}{c_0}z} = I_0 e^{-\alpha z} \tag{2.38}$$

expressed by the Beer-Lambert law, where α is the absorption coefficient

$$\alpha = 2n''\frac{\omega}{c_0} \quad \text{or} \quad \alpha = 4\pi\frac{k_\mathrm{w}}{\lambda} \tag{2.39}$$

Absorptance, transmittance and reflectance

The Beer-Lambert law defines the absorption intensity of a layer with the thickness $z = d$. I is the remaining light intensity after absorption of the incident light I_0 through the absorbing material. The absorbance A is defined as:

$$A = -ln\left(\frac{I}{I_0}\right). \tag{2.40}$$

Often absorbance and absorptance (Abs) are mistaken or misunderstood in literature. Abs is the quantity of absorption in the layer, because the reflectance R is taken into account.

Absorbance is the light intensity which travels through the layer without regarding the reflectance. The transmission is then defined as:

$$T = \frac{I}{I_0}. \tag{2.41}$$

However, the power balance has to be fulfilled as follows:

$$1 = R + Abs + T, \tag{2.42}$$

where R is the quantity for the reflectance and is defined as the fraction of reflected light intensity I_{R} and incident light intensity I_0,

$$R = \frac{I_{\mathrm{R}}}{I_0}. \tag{2.43}$$

The reflectance can also be expressed in n and k by [117–119]

$$R = \frac{(n-1)^2 + k^2}{(n+1)^2 + k^2}. \tag{2.44}$$

An accurate consideration of the dependency of T from n and k in thin films turns out to be very difficult. T can not be expressed easily by a formula, but can be determined by applying an algorithm. The basis are the Fresnel-formula 2.45 for the reflectance and transmittance at phase interfaces and the Beer-Lambert law for the transmittance through the layer:

$$R_{\|} = \frac{tan^2(\Theta_{\mathrm{i}} - \Theta_{\mathrm{e}})}{tan^2(\Theta_{\mathrm{i}} + \Theta_{\mathrm{e}})} \qquad R_{\perp} = \frac{sin^2(\Theta_{\mathrm{i}} - \Theta_{\mathrm{e}})}{sin^2(\Theta_{\mathrm{i}} + \Theta_{\mathrm{e}})}, \tag{2.45}$$

where $\mathrm{R}_{\|}$ and $\mathrm{R}_{\perp}$ are the reflection coefficients with parallel ($_{\|}$) and perpendicular ($_{\perp}$) polarization plane of incidence and Θ_{i} and Θ_{e} the angle of incidence (i) and emergent angle (e). For a single layer without absorption a formula can be given, see reference [120]. Mostly, a thin layer is placed on a substrate, which generates an additional interface and has also to be considered. Therefore, a matrix-algorithm shown by Pettersson et al. [120, 121] is mostly used for R and T determination (e.g. in the optic simulation program OSOLemio [122]).

As already mentioned above, in organic solar cells thin film optics like interference patterns and multiple reflections have to be optimized concerning the optical field distribution. Simulations are required to model this optical field pattern in advance to save time and reduce material costs. For the simulation and modeling software, n and k values for each layer and material are needed. Therefore, the optical constants have to be determined by measuring R and T. Fritz, Hahn, and Böttcher [123] established in 1989 a procedure and algorithm to determine the optical constants of evaporated dye layers based on simultaneous analysis of reflectance and transmittance at normal light incidence.

2.2.2 Photovoltaic principle and organic solar cells

2.2.2.1 Conversion of solar heat into chemical energy

We consider the principle of conversion of solar heat into chemical energy based upon Würfel's study in solar cells [9, 74]. The sun provides solar energy with a black body temperature of $T_\mathrm{S} = 5800\,\mathrm{K}$, which gets converted into electrical energy in a solar cell. Through absorption of the whole or just a part of this radiation, excitations are generated of high density and same energy spectrum. At this time the excitations (generation of excitons/electron-hole pairs) have the same high temperature/heat T_S before they interact with lattice or molecular phonons.

As in any other heat engine, the working medium, the excitation in this case, has to be cooled down. If this is performed reversibly, it means no additional entropy is generated, the same amount of entropy can be discharged into a heat sink at a lower temperature T_0 and creating free energy. Therefore, less energy is lost with entropy than is absorbed, approximately a fraction $\frac{T_0}{T_\mathrm{S}}$ of the absorbed energy. The remaining energy (1-$\frac{T_0}{T_\mathrm{S}}$) is then free of entropy [9]. The interaction of the excitations and the vibrations correspond to the working of the heat engine. The excitations are cooled down to T_0 by vibrations on a picosecond scale. In broad band absorbers, the cooling reduces their energy and makes the energy spectrum narrower. A loss of energy of the excitation during the cooling process is irreversible and directly transformed into low temperature heat of the vibrations. To avoid this loss, broad band absorbers must be replaced by narrow band absorbers. To absorb all or most of the photons from the broad solar spectrum, many different narrow band absorbers are required.

Since the cooling leaves the high concentration of electrons and holes unchanged, the Fermi level, which is unique in thermal equilibrium, splits up into so called quasi-Fermi levels for the upper (electrons) -$\mu_\mathrm{n} = \epsilon_\mathrm{F,e}$ and lower (holes) $\mu_\mathrm{h} = \epsilon_\mathrm{F,h}$ level, as depicted in Fig. 2.13.

The electrochemical potential μ_cp is denoted as Fermi energy ϵ_F in semiconductor physics. This potential can be defined as free energy for one particle as follows:

$$\mu_\mathrm{cp} := \left(\frac{\partial F}{\partial N}\right)_\mathrm{T,N}, \tag{2.46}$$

N is the number of particles and T is temperature. The free energy can be calculated from the energy E and the entropy S:

$$F(T,V) = E(S,V) - TS, \tag{2.47}$$

V the volume. The free energy corresponds to the maximum work, which a system can obtain in thermal contact from a heat reservoir of constant temperature. The difference of these quasi-Fermi levels is the free energy per electron-hole pair which can be obtained from solar energy. The free energy is changed through the difference of the quasi-Fermi levels, if one electron-hole pair is taken out:

$$dF = dF_\mathrm{e} + dF_\mathrm{h} = (\epsilon_\mathrm{F,e} - \epsilon_\mathrm{F,h})dN \tag{2.48}$$

The Fermi level splits up at the position where the excitation takes place and charge carriers are generated.

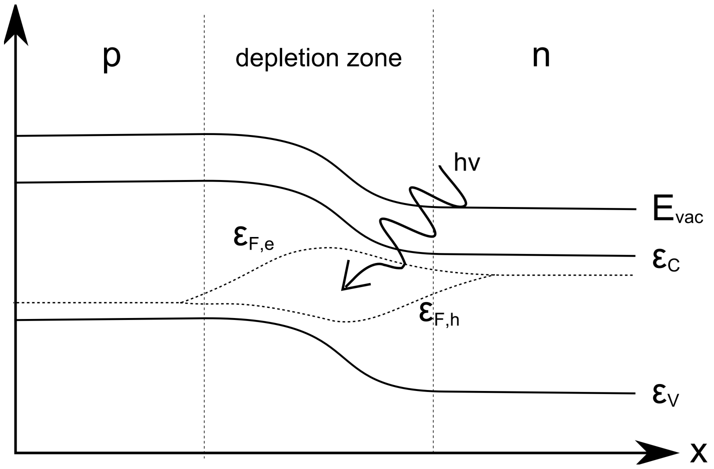

Figure 2.13: *Quasi-Fermi level splitting in an illuminated pn-junction [after [74]], depicted for a voltage between 0 V and the open circuit voltage.*

2.2.2.2 Generation and recombination processes

The amount of chemical energy which can be obtained depends on the concentration of the excitations in steady state and the probability of recombination. As already discussed, excitons have certain lifetimes before they recombine radiatively (photoluminescence) and/or non-radiatively. This recombination processes are loss mechanisms. In the non-radiative process, the energy is transferred to vibrations (v) (phonons). To transfer all the energy of the excitation, one phonon with a very large amplitude (or many phonons) must be generated. However, this process has a very small probability. If intermediate states (e.g. impurities) between the excited (S_1) and the ground state (S_0) exist, the energy transfer can occur in small amounts in several steps. However, if impurities can be eliminated it results in a more improbable non-radiative recombination. Therefore, radiative recombination is the major recombination process. In addition to fluorescence, phosphorescence emission may occur when an excitation recombines radiatively from an excited triplet state (T_1) in the ground state (S_0). To get an excited triplet state, an intersystem crossing from an excited singlet state to an excited triplet state has to take place, visualized in a Jablonski diagram [124, 125] in Fig. 2.14. The exciton generation rate $dG_{\mathrm{e,h}}$ results from photon absorption with energy $\hbar\omega$ of a black body at temperature T_{S} which is seen under solar angle Ω [9, 74]:

$$dG_{\mathrm{e,h}} = \alpha(\hbar\omega)\frac{\Omega}{4\pi^3\hbar^3c^2}\frac{(\hbar\omega)^2}{\exp\left(\frac{\hbar\omega}{kT_{\mathrm{S}}}\right)-1}d\hbar\omega, \tag{2.49}$$

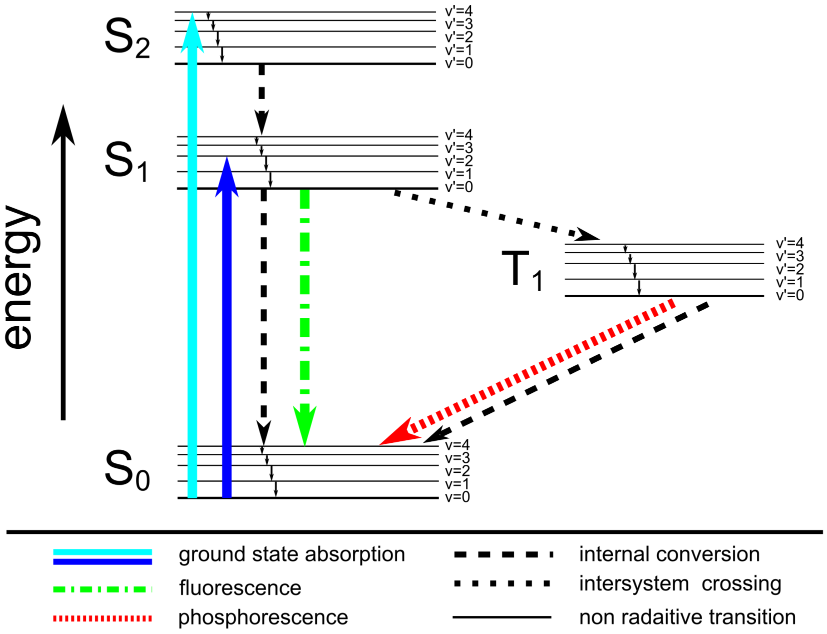

Figure 2.14: *Jablonski-diagram: energetic transitions of excited states with singlet (S_0, S_1, S_2, ...), triplett (T_1, T_2, ...), and vibronic (ν_0, ν_0, ...) states, [after [124, 125]].*

where $\alpha(\hbar\omega)$ is the absorption coefficient. The radiative recombination rate $dR_{\mathrm{e,h}}$ at the same energy $\hbar\omega$ is given as follows:

$$dR_{\mathrm{e,h}} = \alpha(\hbar\omega)\frac{\Omega}{4\pi^3\hbar^3c^2}\frac{(\hbar\omega)^2}{\exp\left(\frac{\hbar\omega-(\epsilon_{\mathrm{F,e}}-\epsilon_{\mathrm{F,h}})}{kT_0}\right)-1}d\hbar\omega. \tag{2.50}$$

If generation and non-radiative recombination occur for a monochromatic absorber in the same photon energy interval under open circuit conditions, both rates must be equal. From equation 2.49 and 2.50 the Carnot factor can be found:

$$\epsilon_{\mathrm{F,e}} - \epsilon_{\mathrm{F,h}} = \hbar\omega\left(1-\frac{T_0}{T_{\mathrm{S}}}\right). \tag{2.51}$$

The Carnot-factor proves that under monochromatic absorption and radiative recombination, the conversion of solar heat into chemical energy of excitons is reversible and occurs at the highest possible efficiency. This can not be further improved [9].

2.2.2.3 Flat and bulk heterojunctions

For small molecule organic solar cells, two approaches are used for the photoactive layer, the flat [126] and bulk [127,128] heterojunction. A flat heterojunction is a stack of two different organic layers deposited on top of one another (Fig 2.15 a)), while the bulk heterojunction is a mixture of organic materials as abstractly shown in Fig 2.15 b).

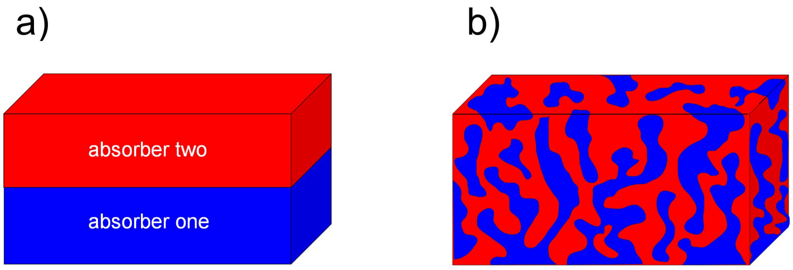

Figure 2.15: *Flat (a) and bulk (b) heterojunctions.*

For the flat heterojunction, the photocurrent generation is limited by the exciton diffusion length which is dependent on the material (e.g. for phthalocyanines on the order of 1-12 nm [59]). Only the excitons which are able to reach the separating interface contribute to the photocurrent, the others recombine and are lost. Therefore, the flat heterojunction is restricted in the absorber layer thickness.

To achieve an efficient charge carrier separation at the interface, the exciton energy which is released due to the charge transfer at the interface has to be larger than the energy sum of the free charge carriers. A rough criterion is: level offset $\mathrm{HOMO_{donor}}$-$\mathrm{HOMO_{acceptor}}$ or $\mathrm{LUMO_{donor}}$-$\mathrm{HOMO_{acceptor}}$ larger than the exciton binding energy around 0.3-0.5 eV [129, 130]. However, these neat layers also provide better percolation paths and charge carrier mobilities of the respective charges compared to a bulk heterojunction, where the different materials are blended. In case of the bulk heterojunction isolated islands, clusters, and dead ends can occur; even the mobility might be lower, which increases the charge carrier recombination probability. This system has a huge advantage concerning photocurrent generation. In contrast to the limitation of exciton diffusion length in flat heterojunctions, the generated excitons in the blend layer are directly separated into free charge carriers and contribute to the photocurrent.

However, in both approaches an energy offset between the LUMOs as well between the HOMOs of the acceptor and the donor materials is required to get the excitons separated into free charge carriers.

The conversion of photon energy into free charge carriers is explained by splitting the process into six simplified steps, shown schematically in Fig. 2.16.

Exciton generation and separation process:

1. light absorption of the molecule in one of the respective absorber layers (shown here for an acceptor layer)

2. a Frenkel exciton is created within the photoactive layer

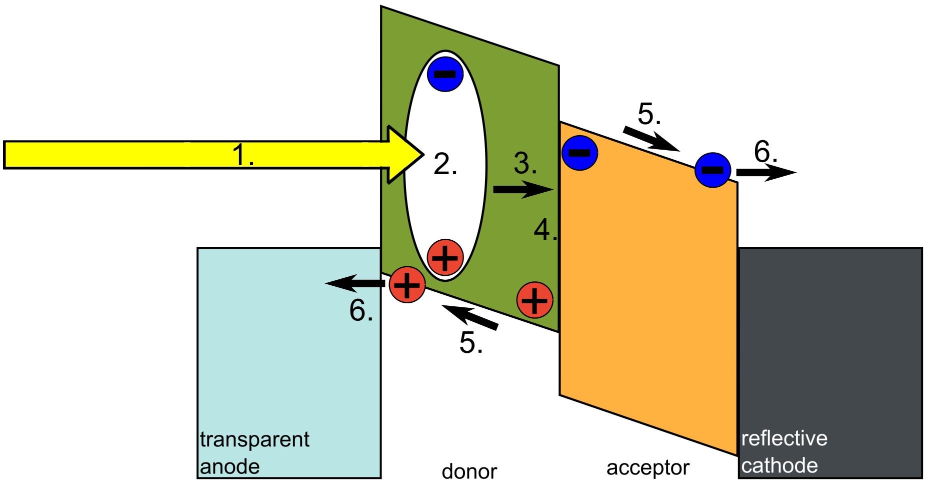

Figure 2.16: *Exciton generation and separation process shown here for a flat heterojunction at short circuit condition: 1) photon absorption, 2) exciton generation, 3) exciton diffusion, 4) exciton separation, 5) free charge carrier transport, and 6) charge carrier extraction.*

3. exciton diffuses to the interface of the two different absorber layers
4. a charge transfer state is created and the exciton gets separated due to a favorable energy offset overcoming the exciton binding energy
5. free charge carriers are generated and transported through the layer, respectively
6. finally, the charges are extracted at the electrodes, realized by Ohmic contacts

2.2.2.4 pin-concept

To transport electrical energy a current flow of charge carriers is required. The generated excitons must be separated into free charge carriers, the hole has to move to the anode and the electron to the cathode. Such a directional movement of the electrons and holes in the absorber layer takes place if the electrons are able to leave the absorber layer only on one side and the holes on the other side. This can be realized by using doped layers to create selective contacts, as proposed by Würfel [74]. The semipermeable contacts let one kind of charge carriers through and block the other one.

This ideal case can be realized by a pin solar cell [131, 132]. Such a solar cell consists of a photoactive intrinsic (i) layer, responsible for sun light absorption and photo current generation, and p- and n-doped regions, realized using doped wide gap materials E_g>3 eV, visualized in Fig. 2.17 a).
The doping shifts the Fermi level of the transport materials to their charge transport levels and induces an electrical field which provides an effective charge transport. The

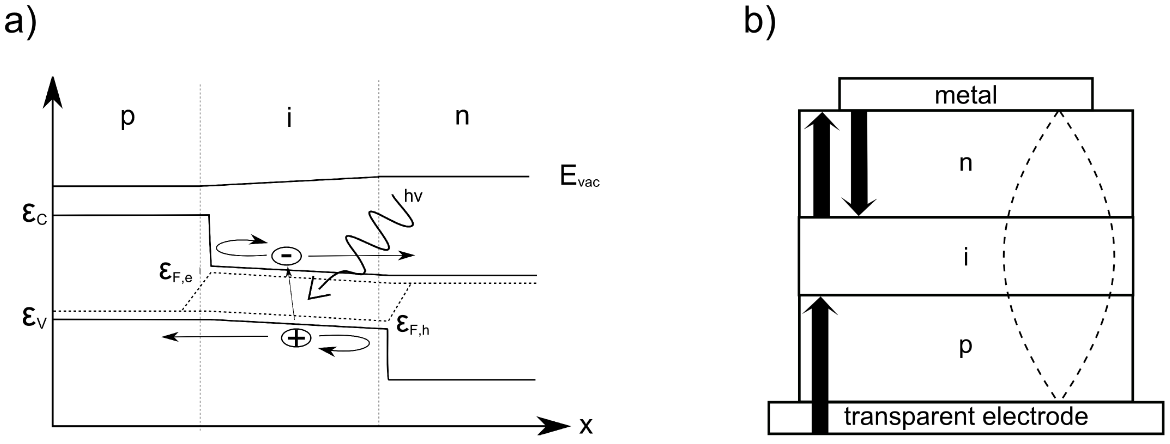

Figure 2.17: *Schematic energy diagram of an ideal pin-solar cell at open circuit condition: p- and n-layers are created using doped transport layers with large energy gaps. The transport layers behave like selective membranes due to the offset to the intrinsic material [74].*

built-in field is given by the difference of the Fermi levels of the transport layers and responsible for the drift of the charge carriers. In case of a completely intrinsic organic solar cell, a difference in work function of the electrodes is essential to realize an electrical field for the charge carrier extraction.
To ensure that charge carriers can move barrier and loss-free from the photoactive layer to the transport layer. The transport layers have to be chosen in a way that they are energetically well aligned. A further advantage of transport layers is the possibility of layer thickness variation, which allows a placement of the photoactive layer in the interference maximum of the optical field distribution, indicated by a dashed line in Fig. 2.17 b). This is even or more important for applications of organic tandem solar cells [133].

The used wide-gap transport materials are almost transparent in the visible range of light [115] and cause no parasitic absorption. Furthermore, the transport materials are excellent exciton and charge carrier blockers (p-layer blocks electrons and vice versa), due to their large E_g. They act as protective layers against damage by the thermally evaporated hot and highly reflective metal electrode.

Morphology

All organic molecule solar cells struggle with problems concerning charge carrier transport and percolation in bulk heterojunctions. Several differing layer architectures [134] in addition to the commonly known flat and bulk heterojunctions (2.15) are proposed to achieve an optimum between charge carrier generation and charge carrier percolation, as shown in Fig. 2.18.

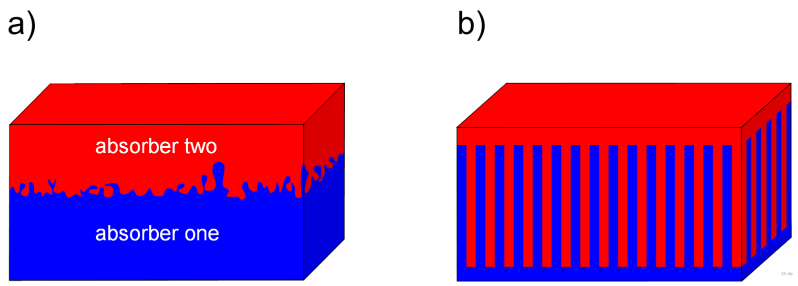

Figure 2.18: *a) flat heterojunction with increased interface area and b) desired rod like structure.*

1. ***Flat heterojunction with increased interface***
   The advantage of this design is the larger donor-acceptor interface surface compared to a usual flat heterojunction made of two amorphously grown materials, where only a flat interface is present. The larger interface allows an exciton dissociation at an extended interface and increases the photocurrent generation. Excitons can now be separated which were not able to reach the interface before. On the other hand, the percolation paths of each kind of charge carrier are not disturbed and they can move toward their electrodes. This layer morphology can be achieved by different measures:

   Organic vapor phase deposition (OVPD)
   Organic vapor phase deposition is a technique where the molecules are transported to the substrate via an inert carrier gas. Due to this technique the layers grow cavernous and form large hetero interfaces [135].

   Deposition of a crystalline growing sublayer
   When depositing a crystalline layer a larger surface is formed first. The additional layer has to grow amorphously to fill up the valleys and voids. The disadvantage is that in most cases the crystal size can not be controlled and leads to short cuts.

   Weak epitaxy growth (WEG)
   By using the technique WEG, developed by Wang et al. [136], highly oriented crystalline films can be fabricated [137]. Reducing the interaction between the organic semiconductor molecules and the substrates through introducing an ordered interlayer made of p-6P and controlling the substrate temperature, the oriented epitaxy growth of ZnPc has been realized with molecules standing upright on the substrates.

2. ***Rod structure***
   The rod structure [138] seems to be the most promising design, but making such

a structure on a nanoscale is still a challenge and not easy to process.

Plenty of hetero interfaces are available to get the excitons separated. The column diameters have to be chosen with a size that the generated excitons can reach the interface easily before recombination. If they get separated into free charge carriers, they can move towards the respective electrode. The highest probability for charge carrier recombination might be along the interfaces between both absorber materials. Self-assembly of copper phthalocyanine (CuPc) in small molecules [134] and PBTTT in polymer solar cells [139,140] lead to this rod like structure.

To improve the solar cell performance with respect to morphology (bulk and flat heterojunction), further processing steps [141] were introduced mainly for polymer based solar cells in the past:

Thermal post treatment
Due to an additional energy supply in terms of thermal post treatment, nanocrystalline morphology in polymer solar cells can be obtained [142–147].

Vapor annealing of blends
Vapor treatment (e.g. 1,2-dichlorobenzene) can induce self-organizing of the polymer P3HT into ordered structure, leading to enhanced absorption and high hole mobility [148].

Solvent choice
Using different solvents or a mixture of solvents, the morphology in polymer based solar cells can be controlled [149–152]. Furthermore, a higher boiling point of the solvent [153] plays an important role by influencing the evaporation speed during spin-coating of the P3HT:[C_{60}]PCBM.

Slow drying of spin-coated films
Controlling the active layer growth rate results in an increased hole mobility and balanced charge transport [154].

In case of small molecule solar cells other methods are applied:

Substrate heating/cooling
By using thermal energy to keep molecules mobile on the substrate surface, e.g. by heating [155], or trap them, e.g. by cooling [156, 157], the morphology can be influenced.

Current treatment
By applying a higher current to the solar cell, shunts can be burned and the shunt resistance can be increased [157].

Not only extrinsic, but also intrinsic properties (e.g. functional end groups of the molecules) can influence the morphology and molecule packing [158].

2.2.2.5 Solar cell characteristic and parameters

In this section, a typical *J(V)*-curve and the parameters of an illuminated solar cell are shown and discussed. The maximum power (MPP) of a solar cell can be measured in the fourth quadrant of the *J(V)*-curve which is schematically shown in Fig. 2.19. An important quality factor is the fill factor (FF) which is defined by the short circuit photocurrent density (J_{SC}) and the open circuit voltage (V_{OC}):

$$FF = \frac{J_{\mathrm{MPP}} V_{\mathrm{MPP}}}{J_{\mathrm{SC}} V_{\mathrm{OC}}}. \tag{2.52}$$

A quantity for the squareness is the FF, the larger the value the better the solar cell efficiency and performance. The FF depends on several parameters:

1. Bad saturation of the backward current, which is mainly caused by e.g. partial shortcuts, material impurities [159] and thus charge carrier recombinations.
2. High series resistance in forward direction, e.g. due to bad charge carrier transport and limitation in conductivity of each solar cell component.
3. Charge recombination process in the photoactive layers, e.g. due to low or unbalanced charge carrier mobilities [72, 160], material impurities, injection and extraction barriers [161].

The saturation factor $J(\text{-1V})/J_{\mathrm{SC}}$, defined as the quotient of photocurrent measured at -1 V and 0 V, is an indicator for bad charge carrier extraction caused by energetic barriers, recombination losses, impurities, shunts, and others.

The most important parameter of a solar cell is the power conversion efficiency (η), which defines the efficiency of energy conversion of incoming light power I_0 and produced electrical power:

$$\eta = FF \cdot \frac{J_{\mathrm{SC}} V_{\mathrm{OC}}}{I_0}. \tag{2.53}$$

Photocurrent density

An organic solar cell is a photo diode. Under dark conditions and an applied positive voltage with the anode at the hole transport layer and the cathode at the electron transport layer, charge carriers move through the layers and a recombination current flows. If the solar cell is operated in reverse bias, the diode blocks and only a small reverse-blocking current flows. In this case, the only processes in the diode that contribute

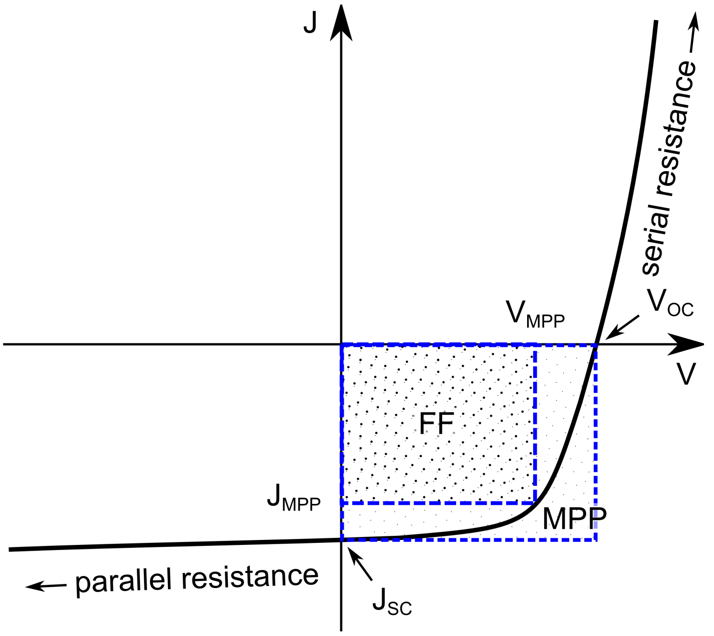

Figure 2.19: *J(V)-curve of a solar cell with the typical solar cell parameters open circuit voltage (V_{OC}), photocurrent density at short circuit (J_{SC}), fill factor FF, maximum power point MPP, photocurrent density at MPP J_{MPP}, and voltage at MPP V_{MPP}.*

to the current are drift (due to electrical field), diffusion, and thermal recombination-generation. The ideal Shockley diode equation is derived [74, 162]

$$J = J_{\mathrm{S}} \left[\exp\left(\frac{eV}{k_{\mathrm{B}}T} \right) - 1 \right], \tag{2.54}$$

where J is the current density, J_{S} reverse bias saturation current density, k_{B} the Boltzmann constant, and T the absolute temperature. When the solar cell is illuminated photons are absorbed and excitons are generated. After exciton separation a hole on the HOMO level and an electron on the LUMO level are found. Due to the internal electrical field, the charge carriers move to the respective electrodes. Assuming a generation rate of charge carriers which is independent of the applied voltage V, the current density in the solar cell is given as [74]:

$$J = J_{\mathrm{S}} \left[\exp\left(\frac{eV}{k_{\mathrm{B}}T} \right) - 1 \right] - J_{\mathrm{SC}}. \tag{2.55}$$

Under dark conditions and at very high negative voltage ($\exp(eV/k_{\mathrm{B}}T) \ll 1$) one can find a voltage independent reverse bias saturation current density

$$J = -eG^0_{\mathrm{e,h}}(L_{\mathrm{e}} + L_{\mathrm{h}}) = -J_{\mathrm{S}}, \tag{2.56}$$

where $G^0_{\mathrm{e,h}}$ is the generation rate in the dark and L_e and L_h are the charge carrier diffusion lengths for electrons and holes [74], respectively. With equation 2.56 J_S can be calculated for an ideal pn-junction, where electron-hole pairs are only generated by absorbing 300 K background radiation. In a real pn-junction the generation which is caused by non-radiative transitions also counts as an inversion of non-radiative recombination processes ($R^0_{\mathrm{e,h}}$). Therefore, no general recombination rate can be given. However, it can be expressed with the diffusion length, which includes the lifetime τ and reflects the real recombination processes. The generation rate is defined by τ and the concentration n of the minority carrier in the case of balanced generation and recombination

$$G^0_{\mathrm{e,h}} = R^0_{\mathrm{e,h}} = \frac{n^\mathrm{p}_\mathrm{e}}{\tau_\mathrm{e}} = \frac{n^\mathrm{n}_\mathrm{h}}{\tau_\mathrm{h}}. \tag{2.57}$$

With L=$\sqrt{D\tau}$ (D is the diffusion constant), $n^\mathrm{p}_\mathrm{e} = n^2_\mathrm{i}/n_\mathrm{A}$, and $n^\mathrm{n}_\mathrm{h} = n^2_\mathrm{i}/n_\mathrm{D}$, J_S can be written as [74]:

$$J_\mathrm{S} = en^2_\mathrm{i}\left(\frac{D_\mathrm{e}}{n_\mathrm{A}L_\mathrm{e}} + \frac{D_\mathrm{h}}{n_\mathrm{D}L_\mathrm{h}}\right). \tag{2.58}$$

Therefore, the Shockley-equation can be quoted as follows:

$$J = en^2_\mathrm{i}\left(\frac{D_\mathrm{e}}{n_\mathrm{A}L_\mathrm{e}} + \frac{D_\mathrm{h}}{n_\mathrm{D}L_\mathrm{h}}\right)\left[\exp\left(\frac{eV}{k_\mathrm{B}T}\right) - 1\right] - J_\mathrm{SC}, \tag{2.59}$$

The influence of the electrical field on every single charge carrier in a solar cell leads to a field current $j_{\mathrm{QF,i}}$ and density gradients resulting in a diffusion current $j_{\mathrm{QD,i}}$. The field current for electrons can be described by:

$$j_{\mathrm{QF,n}} = -en_\mathrm{n}\mu_\mathrm{n}E = -\sigma_\mathrm{n}E, \tag{2.60}$$

where n_i is the density of the kind of charge i, μ_i the mobility, σ_i the conductivity, and E the electrical field. With E=-gradφ (φ is the electrical potential) we get

$$j_{\mathrm{QF,n}} = \frac{\sigma_\mathrm{n}}{e}\mathrm{grad}(-e\varphi). \tag{2.61}$$

The diffusion current for electrons $j_{\mathrm{QD,n}}$ can be derived from Fick's law:

$$j_{\mathrm{QD,n}} = eD_\mathrm{n}\mathrm{grad}n_\mathrm{n}, \tag{2.62}$$

where D_n is the diffusion constant. With

$$\frac{\mathrm{grad}n_\mathrm{i}}{n_\mathrm{i}} = \mathrm{grad}\left(\frac{n_\mathrm{i}}{N_\mathrm{C}}\right) \tag{2.63}$$

and the chemical potential

$$\mu_{\mathrm{i}}^{chem} = \mu_{\mathrm{i},0}^{\mathrm{chem}} + k_{\mathrm{B}}T\ln\frac{n_{\mathrm{i}}}{N_{\mathrm{C}}} \tag{2.64}$$

we get

$$j_{\mathrm{QD,n}} = \frac{en_{\mathrm{n}}D_{\mathrm{n}}}{k_{\mathrm{B}}T}\mathrm{grad}\mu_{\mathrm{n}}^{\mathrm{chem}}. \tag{2.65}$$

Using the Einstein relation

$$\frac{D_{\mathrm{i}}}{\mu_{\mathrm{i}}} = \frac{k_{\mathrm{B}}T}{e} \tag{2.66}$$

one obtains:

$$j_{\mathrm{QD,n}} = n_{\mathrm{n}}\mu_{\mathrm{n}}\mathrm{grad}\mu_{\mathrm{n}}^{\mathrm{chem}} = \frac{\sigma_{\mathrm{n}}}{e}\mathrm{grad}\mu_{\mathrm{n}}^{\mathrm{chem}}. \tag{2.67}$$

The total charge current $j_{\mathrm{Q,i}}$ can be composed of the field current $j_{\mathrm{QF,i}}$ and the diffusion current $j_{\mathrm{QD,i}}$. For electrons it can be written as:

$$j_{\mathrm{Q,n}} = \frac{\sigma_{\mathrm{n}}}{e}\left[\mathrm{grad}\left(\mu_{\mathrm{n}}^{\mathrm{chem}}\right) + \mathrm{grad}(e\varphi)\right] = \frac{\sigma_{\mathrm{n}}}{e}\mathrm{grad}\eta_{\mathrm{n}}, \tag{2.68}$$

where $\eta_{\mathrm{i}} = \mu_{\mathrm{i}}^{\mathrm{chem}} + e\varphi$ is the electrochemical potential. The electrochemical potential η_{i} is commonly called Fermi energy ϵ_{F} in semiconductor physics. The total current for electrons and holes can be written with the quasi-Fermi levels as:

$$j_{\mathrm{Q}} = \frac{\sigma_{\mathrm{n}}}{e}\mathrm{grad}\epsilon_{\mathrm{F,n}} + \frac{\sigma_{\mathrm{h}}}{e}\mathrm{grad}\epsilon_{\mathrm{F,h}}. \tag{2.69}$$

Open circuit voltage

From equation 2.55 V_{OC} is given as:

$$V_{\mathrm{OC}} = \frac{k_{\mathrm{B}}T}{e}\cdot\ln\left[\frac{J_{\mathrm{SC}}}{J_{\mathrm{S}}} + 1\right]. \tag{2.70}$$

V_{OC} is defined by the quasi-Fermi levels $\epsilon_{\mathrm{F,e}}$ and $\epsilon_{\mathrm{F,h}}$ for electrons and holes, respectively:

$$V_{\mathrm{OC,max}} = \frac{1}{e}\left(\epsilon_{\mathrm{F,e}} - \epsilon_{\mathrm{F,h}}\right). \tag{2.71}$$

V_{OC} depends on the charge carrier concentration in the device, which is caused by e.g. the incident light intensity. The Fermi-Dirac distribution at thermal equilibrium is given as:

$$f_{\mathrm{e}}(\epsilon_{\mathrm{e}}) = \frac{1}{\exp\left(\frac{\epsilon_{\mathrm{e}}-\epsilon_{\mathrm{F}}}{k_{\mathrm{B}}T}\right) + 1}, \tag{2.72}$$

where ϵ_{e} is the electron energy and ϵ_{F} the Fermi energy. With the density of electrons

$$dn_{\mathrm{e}}(\epsilon_{\mathrm{e}}) = D_{\mathrm{e}}(\epsilon_{\mathrm{e}}) f_{\mathrm{e}}(\epsilon_{\mathrm{e}}) d\epsilon_{\mathrm{e}} \tag{2.73}$$

in the interval

$$[\epsilon_{\mathrm{e}}, \epsilon_{\mathrm{e}} + d\epsilon_{\mathrm{e}}]\,, \tag{2.74}$$

and with the electron density of states $D_{\mathrm{e}}(\epsilon_{\mathrm{e}})$ in the conduction band ϵ_{C},

$$D_{\mathrm{e}}(\epsilon_{\mathrm{e}}) = 4\pi \left(\frac{2m_{\mathrm{e}}^*}{h^2} \right)^{\frac{3}{2}} (\epsilon_{\mathrm{e}} - \epsilon_{\mathrm{C}})^{\frac{1}{2}}, \tag{2.75}$$

and m_{e}^* (effective electron mass), the density of free electrons in ϵ_{C} can be integrated. Assuming that the density of free electrons n_{e} in ϵ_{C} is much smaller than the effective density of states N_{C}, we can use

$$N_{\mathrm{C}} = 2 \left(\frac{2\pi m_{\mathrm{e}}^* k_{\mathrm{B}} T}{h^2} \right)^{\frac{3}{2}} \tag{2.76}$$

to calculate n_{e} from equation 2.73 by solving the integral:

$$n_{\mathrm{e}} = \int_{\epsilon_{\mathrm{e}}}^{\infty} D_{\mathrm{e}}(\epsilon_{\mathrm{e}}) f_{\mathrm{e}}(\epsilon_{\mathrm{e}}) d\epsilon_{\mathrm{e}} = \int_{\epsilon_{\mathrm{e}}}^{\infty} 4\pi \left(\frac{2m_{\mathrm{e}}^*}{h^2} \right)^{\frac{3}{2}} \cdot \frac{(\epsilon_{\mathrm{e}} - \epsilon_{\mathrm{C}})^{\frac{1}{2}}}{\exp\left(\frac{\epsilon_{\mathrm{e}} - \epsilon_{\mathrm{F}}}{k_{\mathrm{B}} T} \right)} d_{\mathrm{e}} = N_{\mathrm{C}} \exp\left(-\frac{\epsilon_{\mathrm{e}} - \epsilon_{\mathrm{C}}}{k_{\mathrm{B}} T} \right). \tag{2.77}$$

Similarly, it can also be calculated for the holes with the density of holes n_{h} in the valence band ϵ_{V} and the effective density of states.

$$n_{\mathrm{h}} = N_{\mathrm{V}} \exp\left(-\frac{\epsilon_{\mathrm{e}} - \epsilon_{\mathrm{C}}}{k_{\mathrm{B}} T} \right) \qquad N_{\mathrm{V}} = 2 \left(\frac{2\pi m_{\mathrm{h}}^* k_{\mathrm{B}} T}{h^2} \right)^{\frac{3}{2}}. \tag{2.78}$$

In section 2.2.2.1 we have introduced without giving any explanation that the equilibrium in the semiconductor under illumination is disturbed and the Fermi level splits up into quasi-Fermi levels for electrons $\epsilon_{\mathrm{F,e}}$ and holes $\epsilon_{\mathrm{F,h}}$, respectively. Since $\epsilon_{\mathrm{F}} \propto$ -$\ln\frac{n_{\mathrm{h}}}{N_{\mathrm{V}}}$ and at the same time $\epsilon_{\mathrm{F}} \propto \ln\frac{n_{\mathrm{e}}}{N_{\mathrm{C}}}$, the Fermi energy can be decreased for a higher hole density and increased for a higher electron density. In equilibrium the electron and hole density is the same. Thus, the Fermi energy must also be the same. To solve this contradiction, quasi-Fermi levels are introduced to describe the electron and hole population separately. The quasi-Fermi level for electrons $\epsilon_{\mathrm{F,e}}$ and holes $\epsilon_{\mathrm{F,h}}$ are defined as:

$$\epsilon_{\mathrm{F,e}} = \epsilon_{\mathrm{C}} - k_{\mathrm{B}} T \ln\frac{N_{\mathrm{C}}}{n_{\mathrm{e}}} \qquad \epsilon_{\mathrm{F,h}} = \epsilon_{\mathrm{V}} - k_{\mathrm{B}} T \ln\frac{N_{\mathrm{V}}}{n_{\mathrm{h}}} \tag{2.79}$$

Thus, V_{OC} can be written as

$$V_{\mathrm{OC,max}} = \frac{1}{e}\left(\epsilon_{\mathrm{C}} - \epsilon_{\mathrm{V}} - k_{\mathrm{B}}T\ln\frac{N_{\mathrm{C}}N_{\mathrm{V}}}{n_{\mathrm{e}}n_{\mathrm{h}}}\right). \tag{2.80}$$

External quantum efficiency

A further crucial characterization parameter for solar cell is the external quantum efficiency (EQE), which determines the conversion efficiency of an absorbed photon into a free charge carrier (extracted electron-hole pair). The EQE is dimensionless and is usually below one, because processes where more than one electron-hole pair is generated through a single absorbed photon are very unlikely. The EQE of photovoltaic devices is given as follows:

$$EQE = \eta_{\mathrm{A}} \cdot \eta_{\mathrm{ED}} \cdot \eta_{\mathrm{CT}} \cdot \eta_{\mathrm{CC}}, \tag{2.81}$$

where η_{A} is the absorption efficiency, η_{ED} exciton diffusion efficiency to the donor-acceptor interface, η_{CT} the charge transfer efficiency, and η_{CC} the carrier collection efficiency. The EQE is taken for the whole solar spectrum usually at zero bias, in particular where the utilized materials absorb. The photocurrent is recorded for different wavelengths and normalized to the irradiated light power. The spectral response $S(\lambda)$ represents the current per irradiated light power in A/W for a certain wavelength [163]. Using the spectral response, the EQE can be determined as

$$EQE(\lambda) = \frac{hc}{e\lambda} \cdot S(\lambda), \tag{2.82}$$

where e is the elementary charge, λ the wavelength, h the Planck's constant, and c the speed of light. From spectra of the EQE, the contribution of photocurrent of a definite wavelength region can be shown, in particular for organic solar cells with heterojunctions made of two different materials absorbing in different spectral regions. Hence, the contribution of each material to photocurrent can be obtained. If the absorption characteristics in thin films are known for the used materials, loss mechanism like recombination of electron-hole pairs can be determined.

Internal quantum efficiency

If the absorption η_{A} is known the internal quantum efficiency (IQE(λ)) can be calculated as follows [164, 165]:

$$IQE(\lambda) = \frac{EQE(\lambda)}{\eta_{\mathrm{A}}(\lambda)}. \tag{2.83}$$

The IQE represents the ratio of extracted electron-hole pairs to the absorbed photons, whereas losses like reflection at the substrate surface are not taken into account. The

IQE is defined differently in recent publications. On the one hand, the total device absorption (including parasitic absorption) ($\eta_{\mathrm{A}}^{\mathrm{total}}$) is used [166] and on the other hand, only the absorption of the photoactive layer ($\eta_{\mathrm{A}}^{\mathrm{active}}$) is taken into account [165] and determines the IQE of the photoactive layer. Thus, further considerations can be made with respect to η_{ED}, η_{CT}, and η_{CC} [165].

2.2.2.6 Accurate measurement and characterization of organic solar cells

Efforts have been made in the past to reach high efficiencies in organic solar cells. Now, they are at a level where they are already commercially available (e.g. polymer based solar cells by Konarka Technologies) or where they are ready to enter the market (e.g. small molecule organic solar cells by Heliatek). For a reliable and fair comparison between different research groups which are dealing with organic solar cells, an accurate determination of the efficiency of the solar cells is necessary. In the past efforts have been made to accurately determine the efficiency of inorganic solar cells, and a standard test method has been established [167]. In 1980 the Cell Performance Laboratory was established by the US Department of Energy at the National Renewable Energy Laboratory (NREL) to provide the US photovoltaics community with standardized efficiency measurement and reference-cell calibration. In the early 1980s similar laboratories were set up in Germany (Fraunhofer ISE (certified since 2001)) and Japan (Japan Aerospace Exploration Agency (1976)). In the 1980s US and international standards were developed and adopted by the national photovoltaic calibration laboratories around the world. For organic solar cells, these internationally accepted norms are rarely followed at the research level. Lack of awareness of these norms and limited resources result in reports of efficiency values under various testing conditions. A reliable comparison of data between different research groups is very difficult. In Germany standards are composed and governed by the Deutsche Institut für Normung (DIN). On European and international levels the "'Europäisches Komitee für Elektrotechnische Normung"' (CENELEC) and the Internationale Elektrotechnische Kommission (IEC) are responsible for most relevant standards. Due to a close cooperation, the DIN standards are mostly German versions of the European standards (EN) and conform with the IEC standards. For the US the American Society for Testing and Materials (ASTM) is responsible for the standards. However, in the field of solar cell characterization the standards in Europe and US match fundamentally.

General guidelines of measurements of current-voltage characteristics can be found in the standards ASTM E 948 *Test Method for Electrical Performance of PV Cells using Reference Cells under Simulated Sunlight* [168] and IEC 60904-1 *Messen der photovoltaischen Strom-Spannungskennlinien* [169]. The standard reporting conditions (SRC) are defined in ASTM E 948. The SRC contain the irradiation spectrum, irradiance as well as the temperature conditions. 1000 W/m^2 for the irradiation intensity and 25°C for the solar cell temperature are defined as standard measuring conditions. To characterize a solar cell used on the earth surface, a reference spectrum AM 1.5 G is used. AM signifies the *Air Mass* and 1.5 the sea level spectrum, which correspond to zenith angle of 48.19°. The G indicates the global spectrum consisting of direct and diffuse irradiation. The ASTM G 173-03 spectrum published in 2003 was generated using the software SMARTS 2.9.2 (Simple Model for Atmospheric Transmission of Sunshine [170, 171]) and does not correspond to the time- and position-dependent real sun spectrum.

Furthermore, different items for accurate efficiency measurement have to be considered. First of all a well defined shadow mask for the J(V) measurement under illumination has to be used to avoid an inaccurate determination of the active area (e.g. shadow effects) and to avoid additional photocurrent contribution from the edges of the substrates. Secondly, the reference solar cell must be calibrated and certified. Thirdly, the used sun simulator shows variations of intensity over the whole solar spectrum in comparison to the standardized solar AM 1.5 G irradiation.

Mismatch factor

The irradiance incident on the photovoltaic cell is typically measured with a reference solar cell. For IV measurements with respect to a reference spectrum, there is a spectral error in the measured photocurrent of the solar cell, because of the following two reasons: 1) the spectral irradiance of the defined light source does not match the reference spectrum and 2) the spectral responses of the reference detector and test cell are different. This error can be given based upon the assumption that the photocurrent is the integral of the product of the cell responsivity and incident spectral irradiance. This error can be expressed as spectral mismatch correction factor M [167, 172, 173].

$$M = \frac{\int_{\lambda_1}^{\lambda_2} E_{\mathrm{Ref}}(\lambda) S_{\mathrm{R}}(\lambda)\mathrm{d}\lambda}{\int_{\lambda_1}^{\lambda_2} E_{\mathrm{Ref}}(\lambda) S_{\mathrm{T}}(\lambda)\mathrm{d}\lambda} \cdot \frac{\int_{\lambda_1}^{\lambda_2} E_{\mathrm{S}}(\lambda) S_{\mathrm{T}}(\lambda)\mathrm{d}\lambda}{\int_{\lambda_1}^{\lambda_2} E_{\mathrm{S}}(\lambda) S_{\mathrm{R}}(\lambda)\mathrm{d}\lambda}, \tag{2.84}$$

where E_{Ref} is the reference spectral irradiance, E_{S} is the source spectral irradiance, S_{R} is the spectral responsivity of the reference cell, and S_{T} is the spectral responsivity of the test cell, each as a function of wavelength (λ). Different sun simulators are available on the market (e.g. Photo Emission Tech., Inc. (USA), Dr. Hoenle AG UV Technology (Germany), OptoPolymer (Germany), and K. H. Steuernagel Lichttechnik GmbH (Germany)) which match the standard AM 1.5 G quite well, but there are still some deviations to the simulated sun spectrum. In Fig. 2.20 the standardized and simulated AM 1.5 G (standard ASTM G 173-03) solar spectrum is compared with the solar spectra from Optopolymer and Hoenle. These solar simulators are used in this

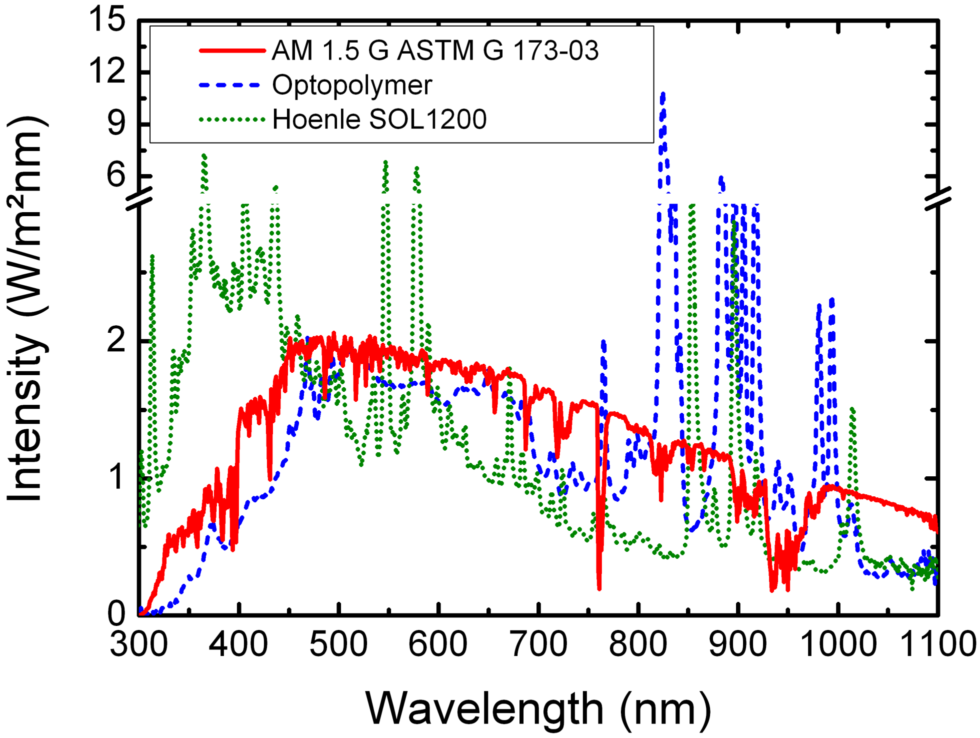

Figure 2.20: *Illustration of the simulated AM 1.5 G (standard ASTM G 173-03) solar spectrum (solid red line) and two solar spectra of sun simulators from Optopolymer (dashed blue line) and from Hoenle SOL 1200 (dotted green line)*

work for the solar cell characterization. The used sun simulators show deviations in the spectral region of interest between 300 - 1100 nm. The sun spectrum from OptoPolymer follows nicely the shape of AM 1.5 G up to 700 nm, then the illumination intensity is partially increased by a factor of 10. The simulator from Hoenle shows larger errors over the whole spectrum. Thus, for each material combination used in the solar cell the EQE and the mismatch have to be determined to get reliable solar cell results. The solar cell has to be measured with the correct mismatch and intensity. To set the correct intensities for the measurement, the sun simulator can be set by using a silicon reference cell (calibrated by ISE). Photocurrent correction after measurement is not representative, because FF and V_{OC} are also slightly affected by the incident light intensity: the FF tends to decrease at higher photocurrents, while V_{OC} increases due to higher quasi-Fermi level splitting. A first estimation of the influence of M on V_{OC} can be calculated using the one-diode-model:

$$\Delta V_{\mathrm{OC}} = \frac{k_{\mathrm{B}}T}{e}\left[\ln\left(\frac{J_{\mathrm{SC}}}{J_0}\right) - \ln\left(M\frac{J_{\mathrm{SC}}}{J_0}\right)\right] = \frac{k_{\mathrm{B}}T}{e}\ln(M). \qquad (2.85)$$

Due to experimental reasons it is not always possible to measure EQE and determine the mismatch factor. However, for some experiments it is not necessary to determine the correct mismatch, e.g. for comparison of transparent transport layers keeping the same absorber system. Here, relative data are sufficient for the evaluation.

2.3 Motivation

As we have seen, the power conversion efficiency depends on the parameters J_{SC}, V_{OC}, and *FF*. To further increase the efficiency of the solar cells the influences and impacts on the parameters have to be investigated, understood, and then improved. In case of J_{SC} this can be realized by employing new materials with higher absorption coefficients or materials having larger exciton diffusion lengths.

V_{OC} is also dependent on many factors, e.g. interface properties, exciton binding energies, recombination processes, and the effective gap $\mathrm{HOMO}_{\mathrm{donor}}$-$\mathrm{LUMO}_{\mathrm{acceptor}}$. The main improvement can be achieved by increasing the effective gap up to the limit where the excitons can barely be separated into free charge carriers.

The *FF* reflects mainly the transport properties in the blend, interface effects, and recombination processes. It means that having materials providing high J_{SC} and V_{OC}, it might be possible that such a solar cell will show low efficiency due to a lousy *FF*. At least each variable and single process in the solar cell has an influence on all other parameters and results in a complex treatment.

This work is a contribution to further improve and understand the effects and mechanisms in organic solar cells.

First, a new promising acceptor molecule C_{70} concerning increased photon harvesting is characterized and its applications in organic solar cells investigated in chapter 4.

Second, improvements of the blend layer morphology and charge carrier transport due to substrate heating during deposition of mixed C_{60}, C_{70}:ZnPc are studied and discussed in chapter 5.

Third, the V_{OC} dependency on the mixing ratio and the role of injection barriers of fullerene:ZnPc bulk heterojuction solar cells are shown and considered in chapter 6.

3 Materials & Methods

In this chapter, we provide detailed information on the molecules which we use as standard materials for our solar cells. We comment on the sample preparation and the different vacuum systems where the layers and devices are processed. The chosen layer sequences of the stacks are explained concerning choice of material and thickness. The characterization tools for solar cells as well as for single or multi layers are introduced and explained. Additionally, the powerful electrical and optical simulation programs used for stack optimization, result validation, and prediction are explained.

3.1 Organic Materials

3.1.1 Standard photoactive materials

C_{60} and ZnPc are organic semiconductors which are used in this work as standard photoactive absorber materials in organic solar cells. Both materials are well characterized in literature and also used for other applications (C_{60}: e.g. biologically as enzyme inhibition, antiviral activity, and DNA cleavage [174–176] and phthalocyanine: inks, paints, lacquers, etc. [177]).

C_{60}

In 1996, R.F. Curl, H.W. Kroto, and R.E. Smalley were awarded the Nobel prize for the 1985 discovery of C_{60}, also known as Buckminster fullerene [178]. This was the starting point of investigations on a new material class, the fullerenes. Fullerenes are highly symmetric and spheric molecules composed of carbon atoms, which are in addition to diamond, graphite, and graphene [179] the fourth known modification of carbon.

W. Krätschmer and coworkers [180] found a method to produce fullerenes on a gram scale in the beginning of 1990. Using this method, graphite is evaporated by an arc discharge in an inert gas atmosphere and produces soot of 5 % fullerenes, mainly C_{60} (80 %), C_{70} (15 %), and further higher carbon cluster like C_{76}, C_{80}, C_{82}, C_{84}, C_{86} etc. in minor quantities.

Despite C_{60} beeing listed here in the section of organic materials, please note that C_{60}

is no hydrocarbon and is thus not an organic compound. The molecular structure is shown in Fig. 3.1.

C_{60} is used as electron acceptor and electron transporting molecule. The energy levels of C_{60} are reported in literature for the IP to be between 6.2 - 6.4 eV [181–183] and for EA 3.6 - 4.1 eV [182,184]. The EA -IP gap is given to be 2.3 ± 0.1 eV [185]. C_{60} is so far the best known electron transporter material with an EA around 4.0 eV. Electron mobilities measured with an organic field effect transistor (OFET) are around $10^{-4}\,\mathrm{cm}^2/\mathrm{Vs}$ [186, 187]. Using atomically flat pentacene coated substrates and deposited at ambient condition (increased C_{60} crystallinity) for C_{60}, values of 2.0 - 4.9 $\mathrm{cm}^2/\mathrm{Vs}$ [188] were achieved. Highly crystalline C_{60} layers give 6.0 $\mathrm{cm}^2/\mathrm{Vs}$ [189], this is achieved by substrate heating during deposition at 250 °C. With the method of molecular beam deposition, the mobility was shown to be between 0.5 – 0.3 $\mathrm{cm}^2/\mathrm{Vs}$ [190]. AOB-doped (3,6-bis(dimethylamino)acridine) C_{60} OFET showed mobilities on the order of 0.2 $\mathrm{cm}^2/\mathrm{Vs}$ [187].

C_{60} has an optical gap around 1.6 eV [191] and an absorption maximum at 450 nm for a thin solid film, as depicted in Fig. 3.3. Exciton diffusion length of C_{60} is reported to be between 19 nm [192, 193] and 40 nm [164]. C_{60} deposited at room temperature on carbon coated Cu-grids show an amorphous and polycrystalline growth with crystallites ranging between 5 - 10 nm [194]. The density as determined by a profilometer is 1.54 $\mathrm{g/cm}^3$.

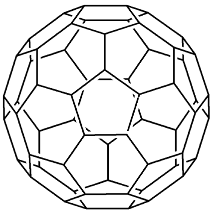

C_{60}

Figure 3.1: *Molecular structure of the acceptor molecule C_{60}, also known as Buckminster fullerene.*

ZnPc

Zinc-phtalocyanine, as sketched in Fig. 3.2, is used as electron donating and hole transporting molecule in organic solar cells.

The IP of ZnPc is measured as 5.07 eV[1] or given in literature between 4.9 - 5.3 eV [195–197]. The EA and EA -IP gap is measured to be 3.3 eV and 1.9 eV [196], respectively.

The hole mobility is 9.2×10^{-6} cm^2/Vs measured via space charge limited current (SCLC) [198]. Different groups [26, 199] have shown that ZnPc is dopable by the molecule F_4-TCNQ and forms a quasi-Ohmic contact to Au [200], which is necessary to achieve good charge extraction in a solar cell.

An important parameter in particular for flat heterojunction solar cells is the exciton diffusion length, which is 30 ± 10 nm [201] for ZnPc.

The absorption spectrum of a thin ZnPc film on quartz glass is shown in Fig. 3.3. The absorption maxima are at 630 and 704 nm with absorption coefficients on the order of 10^5 cm^{-1} [202].

While the starting product (ZnPc powder) for the thermally evaporated ZnPc films is present in the stable monoclinic β-phase, the deposited ZnPc films are crystalline in a triclinic (α-ZnPc, alpha-polymorph, space group P^{-1}) or monoclinic (γ-ZnPc, space group *C2/n*) phase, independent of the type of substrate and layer thickness, measured by X-ray diffraction [203].

When heating the substrate to a temperature of 200 °C during deposition of ZnPc, the phase changes from α-phase to β-phase as visualized in Fig. 3.2, also visible in distinct absorption spectra [204]. Furthermore, the absorption characteristics of ZnPc layers deposited at -150 °C (amorphous phase) and RT (α-phase) differ as well in peak position and peak ratio [113]. The density as determined by a profilometer is 1.34 g/cm^3.

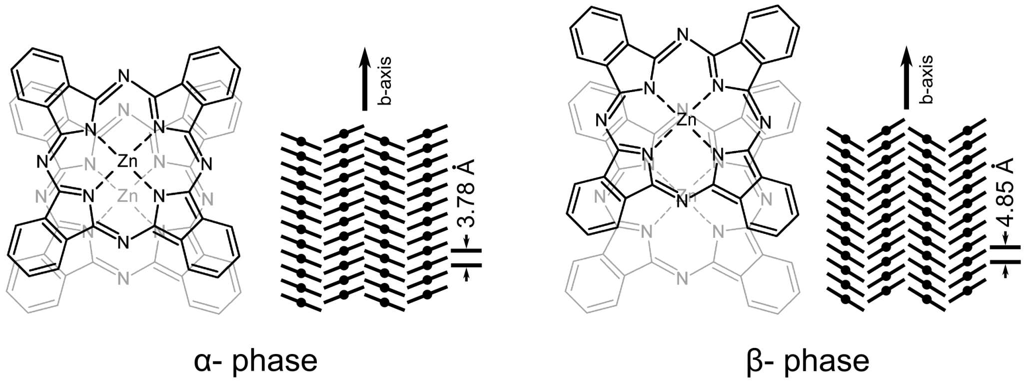

Figure 3.2: *Modifications of ZnPc: the α (left) and the β (right) phase, after [204].*

---

[1] measured via UPS by Selina Olthof, IAPP, TU-Dresden

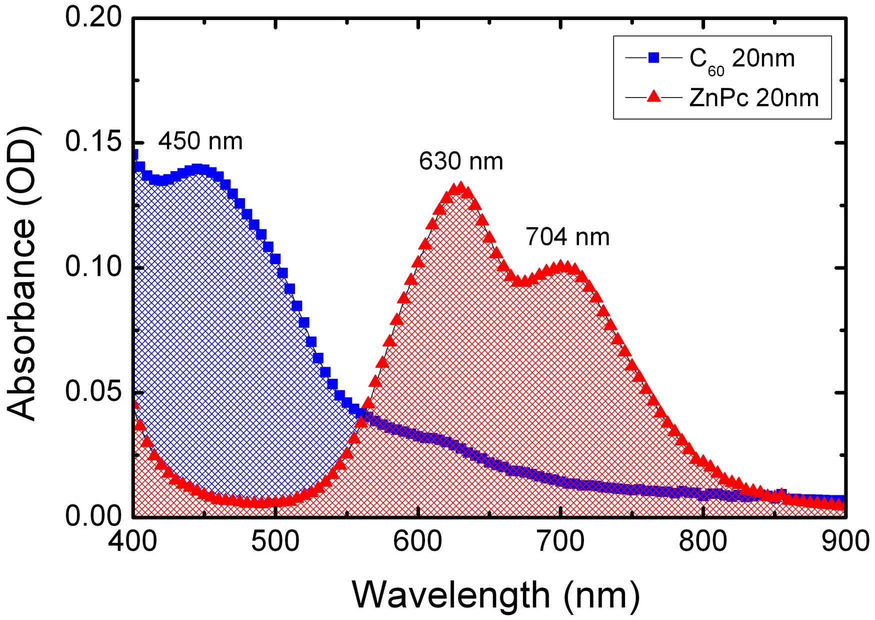

Figure 3.3: *Absorption spectra of 20 nm thick* C_{60} *(squares) and ZnPc (triangles) layers deposited on quartz glass.*

3.1.2 Transport materials and dopants

MeO-TPD

N,N,N,N-tetrakis(4-methoxyphenyl)-benzidine supplied by Sensient (Wolfen, Germany) is a wide-gap hole transport and electron blocker material [205] with an IP of 5.1 eV [2]. The molecular structure is shown in Fig. 3.4. The first absorption maximum is at 363 nm with an optical gap of 2.9 eV. The material grows amorphous with a density of 1.46 g/cm^3. The low glass transition temperature of $T_g = 70\,°C$ [115] results in a morphological instable solar cell under operating conditions. Thus, MeO-TPD is usually replaced by more stable materials like PV-TPD, Di-NPD, and BF-DPB.

PV-TPD

N,N'-di(4-(2,2-diphenyl-ethen-1-yl)-phenyl)-N,N'-di(4-methylphenylphenyl)benzidine supplied by Sensient (Wolfen, Germany) is a wide-gap hole transport and electron blocker material [115] with an IP of 5.2 eV [2]. The molecular structure is shown in Fig. 3.4. The first absorption maximum is at 395 nm with an optical gap of 2.8 eV [115]. The material grows amorphous with a density of 1.14 g/cm^3. The glass transition temperature of $T_g = 118\,°C$ [115] allows long term stable solar cells.

Di-NPD

N,N'-diphenyl-N,N'-bis(4'-[N,N-bis(naphth-1-yl)-amino]-biphenyl-4-yl)-benzidine [206] supplied by Sensient (Wolfen, Germany) is a wide-gap hole transport and electron blocker material [115] with an IP of 5.33 eV [2]. The molecular structure is shown in Fig. 3.4. The first absorption maximum is at 400 nm with an optical gap of 2.9 eV [115]. The material grows amorphous with a density of 1.15 g/cm^3. The glass transition temperature T_g is 158 °C [115].

BF-DPB

N4,N4'-bis(9,9-dimethyl-9H-fluoren-2-yl)-N4,N4'-diphenylbiphenyl-4,4'-diamine supplied by Sensient (Wolfen, Germany) is a wide-gap hole transport and electron blocker material with an IP of 5.23 eV [2]. The molecular structure is shown in Fig. 3.4. The first absorption maximum is at 376 nm. The material grows amorphous with a density of 1.21 g/cm^3. The glass transition temperature T_g is 160 °C.

BPhen

Bathophenanthroline or 4,7-diphenyl-1,10-phenanthroline [207] is a wide-gap electron transport and exciton blocking material [208] with an IP of 6.5 eV and an EA of 3.0 eV [209]. The molecular structure is shown in Fig. 3.4. The first absorption max-

---

[2] measured via UPS by Selina Olthof, IAPP, TU Dresden

imum is at 278 nm. BPhen grows mainly amorphous with a density of 1.24 g/cm^3. However, in combination with the electron transport material C_{60}, having a higher EA of 1.0 eV compared to BPhen, the layer might act as electron blocker. However, in various publications it is assumed that aluminum, which is deposited on top of the BPhen layer, penetrates into the BPhen layer or forms metal-BPhen adducts [210], which might enable the electrons to travel trough the BPhen layer. The material is purchased from ABCR (Karlsruhe, Germany) and purified by CreaPhys GmbH (Dresden, Germany).

NDP2

NDP2 is a strong acceptor molecule which is used to p-dope hole transport materials. The material is provided by Novaled AG (Dresden, Germany).

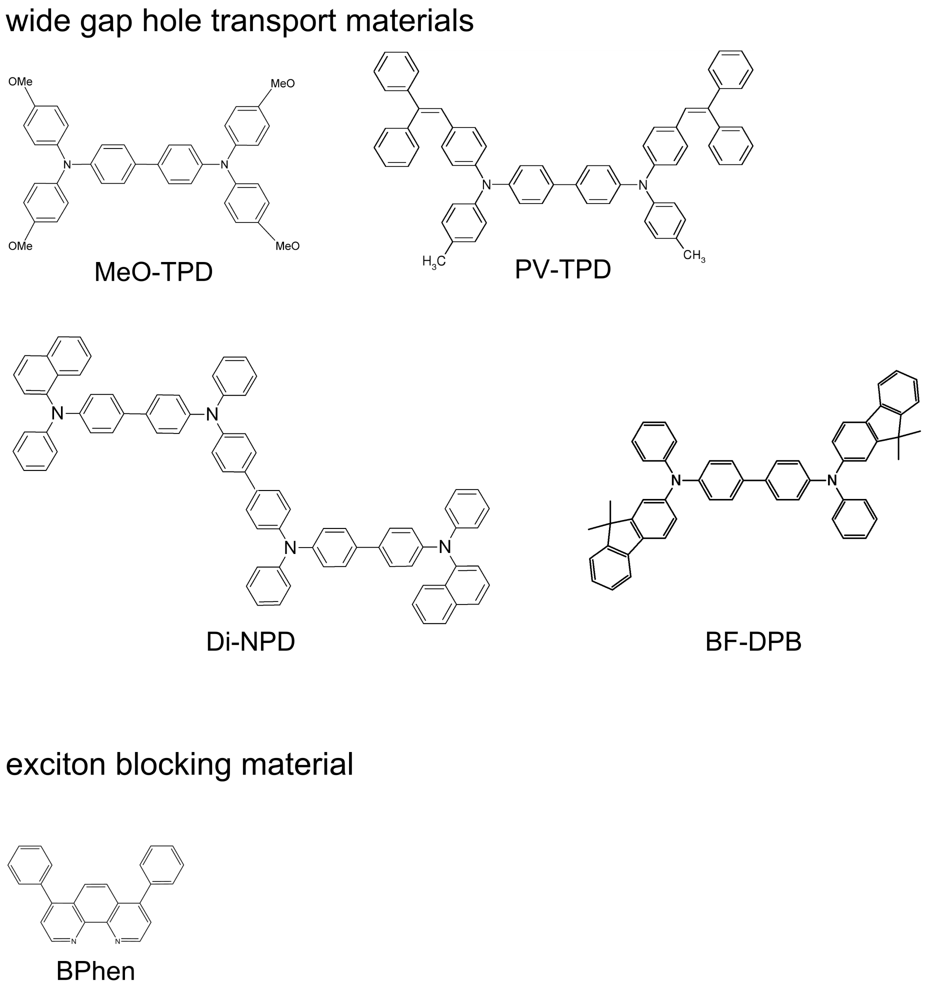

Figure 3.4: *Molecular structures of the wide-gap hole transport materials: MeO-TPD, PV-TPD, Di-NPD, and BF-DPB and wide-gap electron transport and exciton blocking material BPhen.*

3.1.3 Material purification

Due to the negative effects [159] of impure materials (e.g. byproducts from synthesis, residual solvents, etc.) on the solar performance the used materials in this work, except of dopants, are purified at least twice by vacuum gradient sublimation[3].

Vacuum gradient sublimation

A standard vacuum sublimation system is schematically shown in Fig. 3.5. It consists of a horizontal glass tube with a regulation of the temperature gradient along the tube by an external zone-oven. The sublimation is performed under vacuum and allows purification of organic materials which are sensitive and reactive with/to oxygen and/or water at elevated temperatures. The concept is to heat the material in a multiple zone furnace in vacuum. The temperature gradient has to be chosen in a way that the pure material can be harvested from the sliding tube in the middle zone. The impurities can sediment before and behind the middle zone. Therefore, the pure material can easily be separated from the impurities.

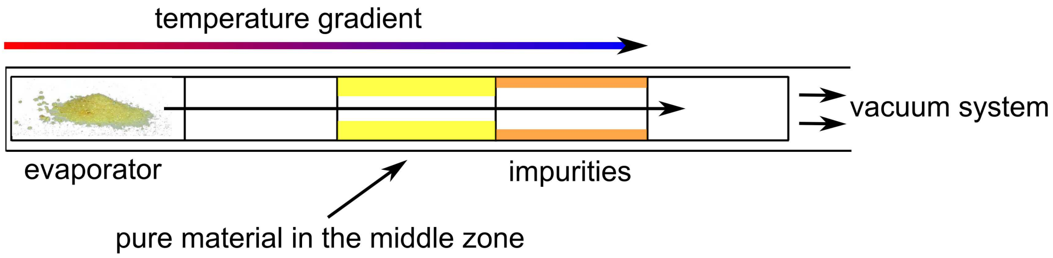

Figure 3.5: *Sketch of the vacuum gradient sublimation tool.*

The standard photoactive materials C_{60} and ZnPc are required in large quantities with identical qualities. Thus, the materials are purified in a vacuum sublimation unit with a charge capacity up to 200 g by CreaPhys GmbH (Dresden, Germany). This ensures comparability and stable performance of the devices. All other materials in smaller quantity are purified in smaller sublimation tool in-house.

---

[3] material sublimation by Annette Petrich, IAPP, TU Dresden

3.2 Sample preparation and vacuum tools

3.2.1 Sample preparation

For the different substrates (e.g. ITO coated glass, silicon (for XRD), silicon oxide (for OFET), and quartz glass (absorption)) used for the different applications, we applied distinct cleaning procedures.

For the silicon and ITO substrates the same cleaning procedure is applied.

The single pre-structured ITO substrates are cleaned in the following order: extran in ultransonic bath (UB), acetone (UB), ethanol (UB), isopropanol, dry blowing with nitrogen, and oxygen plasma treatment.

The Lesker samples with pre-structured ITO are pre-treated in the following order: NMP (N-Methyl-2-pyrrolidon) in UB, rinsing with deionized water, deionized water in UB, ethanol in UB, spin rinsing and dry blowing with nitrogen, and UVOCS (UV ozone cleaner).

The OFET substrates are cleaned as the single ITO samples without the extran cleaning step.

The quartz glass substrates are cleaned as the single ITO samples without oxygen plasma treatment.

In case of the single samples for the UFO tool, we use liquid silver to electrically contact the ITO with measuring pins mounted on the substrate holder. Thus, the sample is heated at 150 °C for 30 min in a drying oven to remove of residual solvents.

To ensure clean and organic free Au and Ag substrates for the UPS measurements, the samples are sputtered with Ar+ ions for at least 1h before usage.

3.2.2 Vacuum tools

For the device and layer production, we have several vacuum tools available. They have thermal evaporation sources, which are operated under high vacuum ($< 10^{-7}$ mbar). The organic materials are evaporated from ceramic crucibles. To heat the crucibles they are coiled by a heating wire made of tungsten. To ensure a homogeneous heating of the material, the tungsten wire is shielded by a copper casing. The deposition can be either controlled by a Eurotherm controller with a Ni/CrNi thermocouple attached to the crucible or by heating power. For metal evaporation a boron nitride crucible for aluminum and a molybdenum boat for gold is used. The coating area on the substrate is defined by using different shadow masks with respect to the application of the layer. Layer thickness is measured using oscillating quartz crystals, as shown in Fig. 3.6 for a co-deposition process. The deposited material on the oscillating crystal results in a shift of the eigenfrequency which is measured by a IC/4 Plus Thin Film Deposition Controller and Deposition Monitor XTM/2 (Leybold Inficon Inc.). Deposition rates can accurately be displayed with resolutions as small as 0.01 Å/s. Usually, deposition rates used in this work are between 0.1 - 0.6 Å/s.

The dopant concentration is given in weight percent (wt%), meaning that the dopant is set to the same density as the matrix material. Due to different source positions, distances, and deposition characteristics, each source has to be calibrated with respect to the substrate holder. Thus, an aditional oscillating quartz crystal can be put at the position where the sample is processed and the corresponding tooling factors can be determined. For the Lesker tool, the tooling factors are determined by measuring the real deposited layer thickness by a profilometer.

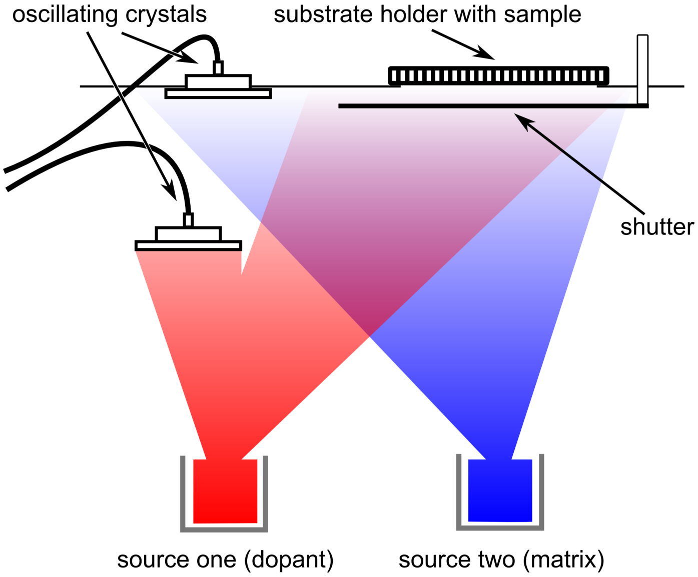

Figure 3.6: *Sketch of a co-deposition process of two different materials (e.g. dopant and matrix) with layer thickness control by oscillating quartz crystals.*

Evaporation System Königbau (ESK)

This tool consists of two vacuum chambers assembled by CreaPhys GmbH (Dresden, Germany) which are individually connected to a nitrogen filled glovebox from MBraun (Garching, Germany). One chamber is used for intrinsic absorber materials and the other for n-doping and metal evaporation. The ESK and the UFO have the same sample holder design, which allows an easy sample transfer and processing.

UFO

The UFO is a custom-made multichamber cluster tool from Bestec GmbH (Berlin, Germany) with five independent evaporation chambers. With this tool it is possible to transfer and process samples without breaking the vacuum between different evaporation chambers. The multichamber tool is connected to a load lock, a glovebox with nitrogen atmosphere, and a flow-box for sample preparation. A sun simulator is installed below the glovebox for measuring the non-encapsulated solar cells in an inert atmosphere. Furthermore, a measurement set up for photoelectron spectroscopy (UPS) is directly connected to the cluster tool.

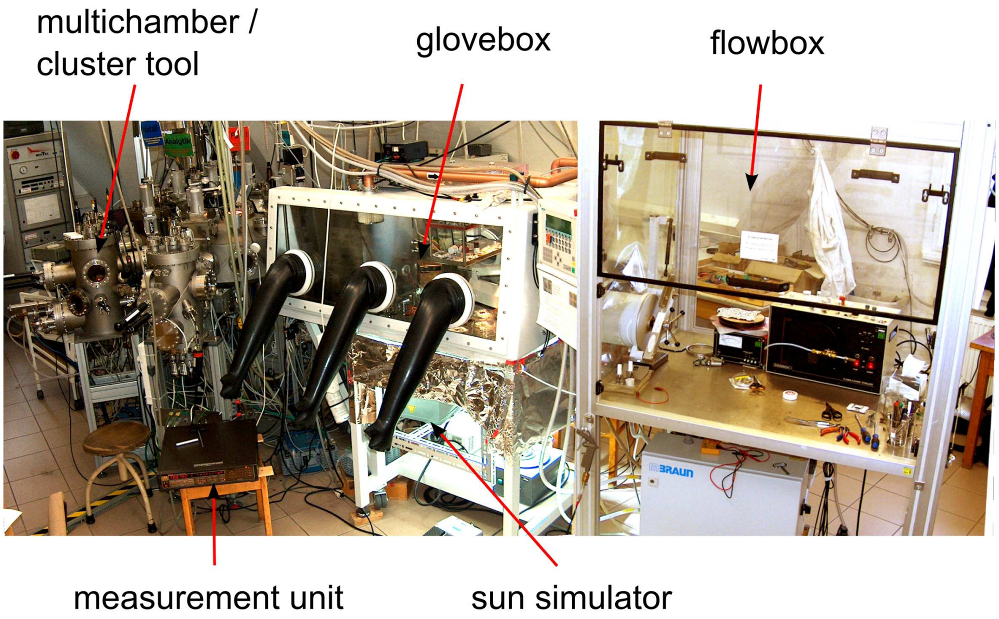

Figure 3.7: *UFO: multichamber cluster tool, glovebox with sun simulator, and flowbox.*

Lesker tool

With the tool from Kurt J. Lesker Company LTD. (East Sussex, England) we have the capability to process on one wafer 36 samples (6 rows x 6 columns) at the same time, resulting in devices which are processed under the same conditions. We further have the option to vary each column and row, e.g. mixing ratio and thickness gradient, which gives us the advantage of easy layer stack optimization and systematic investigations. Substrate heating is realized by four 50 W quartz halogen lamps which illuminate the backside of the sample.

After processing, the samples are encapsulated in the glovebox (nitrogen atmosphere) attached to the Lesker tool by glueing an encapsulation glass with epoxy UV resin glue. To avoid early device degradation by oxygen or water, a moisture sheet is placed between the solar cell and the encapsulation glass.

3.2.3 Substrates and layer stacks

3.2.3.1 Substrates

The glass substrates with the pre-structured semitransparent ITO (tin-doped indium oxide) electrode from Thin Film Devices Inc. (Anaheim, USA) have a sheet resistance of $30\,\Omega/\square$), with a sample size of $2.5 \times 2.5\,\mathrm{cm}^2$. The pre-structured four ITO stripes, the deposited organic layers layer, and the deposited metal electrode compose the solar cells by using special designed shadow masks. The photoactive area is defined by the overlap of ITO and metal contact with a size of 6.4-6.7 mm^2, as schematically shown in Fig. 3.8.

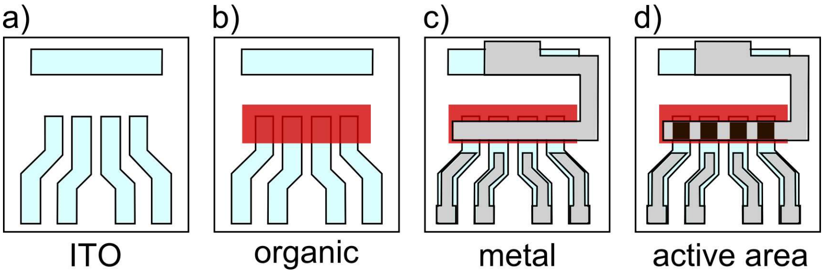

Figure 3.8: *Sketch of a substrate at various stages during deposition: a) glass substrate with pre-structured ITO, b) organic layers on top of the ITO, c) top metal contact, and d) overlap between ITO and metal defines the minimal active area of the solar cell (brown squares).*

For substrate heating we use two different methods: copper block heating for the OFETs, and ITO substrate heating for all other samples. The copper block with heating cartridges is thermally connected to the sample and controlled by a thermocouple. The method of ITO substrate heating is shown schematically in Fig. 3.9, where an additional ITO substrate below the sample is used as resistive heater. A thermocouple is glued on the deposition face to control the temperature. For later measurements we have to take the absorption of the additional ITO heater substrate into account. The average transmission is 85 % [211] in the spectral range of 350–900 nm, as shown in the absorption spectrum in Fig. 3.10.

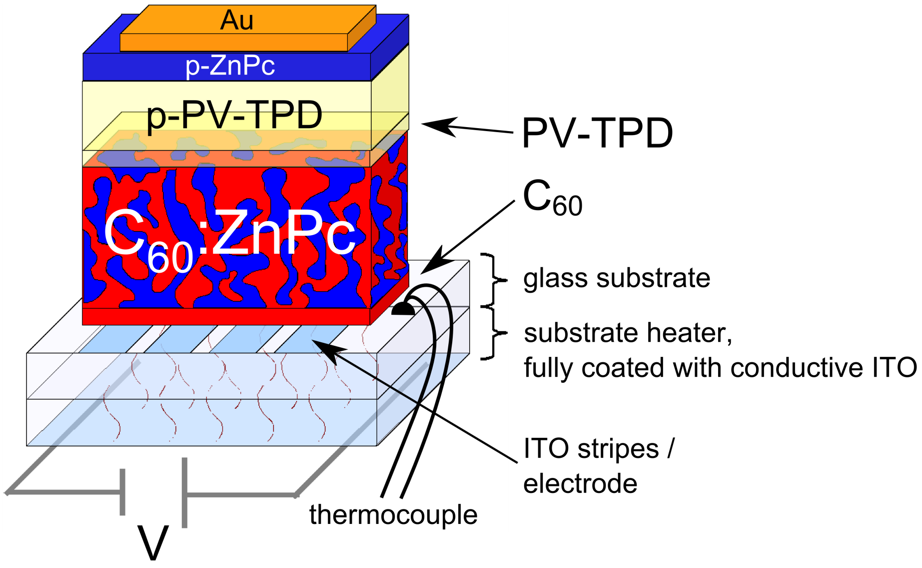

Figure 3.9: *Sketch of a m-i-p solar cell on a additional fully coated ITO substrate used as resistive substrate heater; temperature control is done by a thermocouple glued with silver paste on the deposition face of the sample.*

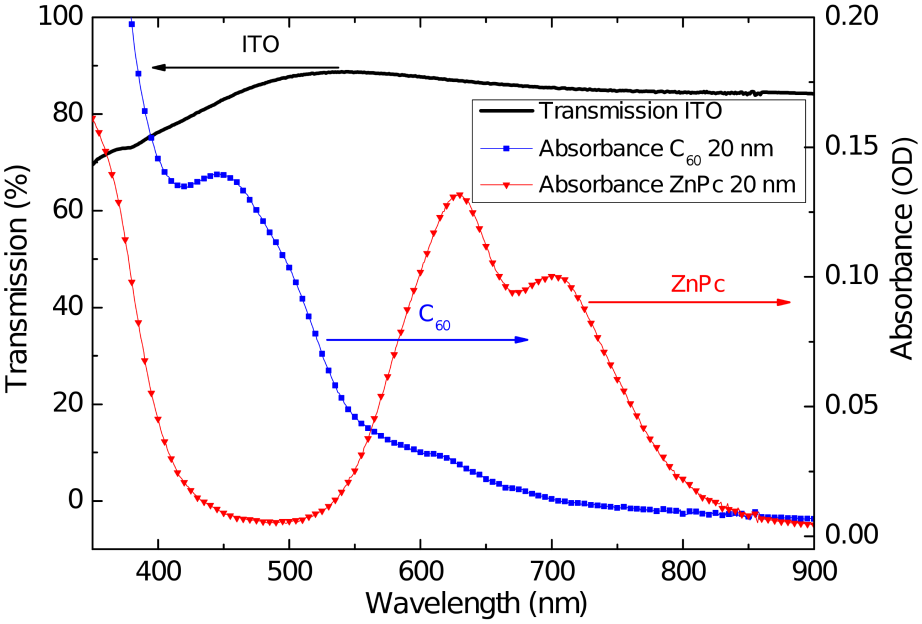

Figure 3.10: *Transmission of the ITO coated substrate heater (continuous line) and absorbance of 20 nm thick C_{60} (filled squares) and ZnPc (filled upside-down triangles) layers in the spectral range from 350 - 900 nm. An average transmission for ITO substrate of 85% is determined.*

3.2.3.2 Layer stacks

In this work we use standard m-i-p and p-i-i layer solar cell stacks with the concepts of flat and bulk heterojunctions. The choice of layer sequence and thicknesses for both architectures is explained in the following.

m-i-p stack

The abbreviation m-i-p stands for metal - intrinsic - p-doped, and roughly describes the layer sequence. The layer stack is sketched in Fig. 3.11. The initially deposited organic layer C_{60}(5 nm) forms an interface dipole [212] and allows a good charge extraction at the interface to ITO (work function 4.7 eV). Additionally, the thin C_{60}(5 nm) layer prevents a direct contact of the blend layer (fullerene:ZnPc) to the electrode and thus avoids charge carrier and exciton quenching.

Above the mixed layer we used a 5 nm intrinsic layer of PV-TPD to prevent exciton quenching and charge carrier recombination at the dopant molecules of the p-PV-TPD layer. Furthermore, the energy level of PV-TPD allows a good charge carrier extraction from the bulk C_{60}:ZnPc.

Taking the optical field distribution into account, the optical maximum is roughly placed within the 60 and 150 nm thick blend layer for a p-PV-TPD layer thickness of 20 nm. The doped layers ensure high conductivities, narrow depletion zones to adjacent layers, and thus good charge extraction. The extra 10 nm p-ZnPc layer is used to ensure sufficient charge carrier extraction [200] between the p-HTL and Au cathode. The additional absorption of ZnPc is marginally due to the low intensities of the optical field at the electrode.

p-i-i stack

The p-i-i stack can be considered as an inverted m-i-p structure. P-i-i stands for a p-doped - intrinsic - intrinsic layer sequence. Both concepts of flat and bulk heterojunctions used in this work are sketched in Fig. 3.11. Following, we elucidate the bulk heterojunction layer design.

The first 1 nm NDP2 ensures a sufficient charge extraction to the ITO electrode, the next layer of p-doped Di-NPD (60 nm) allows high conductivities and narrow depletion zones to adjacent intrinsic layers. In this case no intrinsic Di-NPD layer of 5 nm is used between p-HTL and blend, because i-Di-NPD leads in this layer design to an extraction barrier and thus bad *FF*. Therefore, we accept a loss of quenched charge carriers instead of having a loss in *FF*.

Due to the interference pattern of the optical field distribution in the solar cell, we chose the intrinsic C_{60} layer as electron transport layer on top of the blend to be 40 nm. C_{60} is so far the best known electron transport material. No transparent and electron transport acceptor material has currently the potential to replace the absorber material C_{60}. Due to the fact that C_{60} has an exciton diffusion length between 19 - 40 nm [164,192,193], we assume also a contribution from the intrinsic C_{60} layer to J_{SC}. BPhen of 6 nm [213] is used as exciton blocker layer and as a protection layer against the hot Al atoms during deposition.

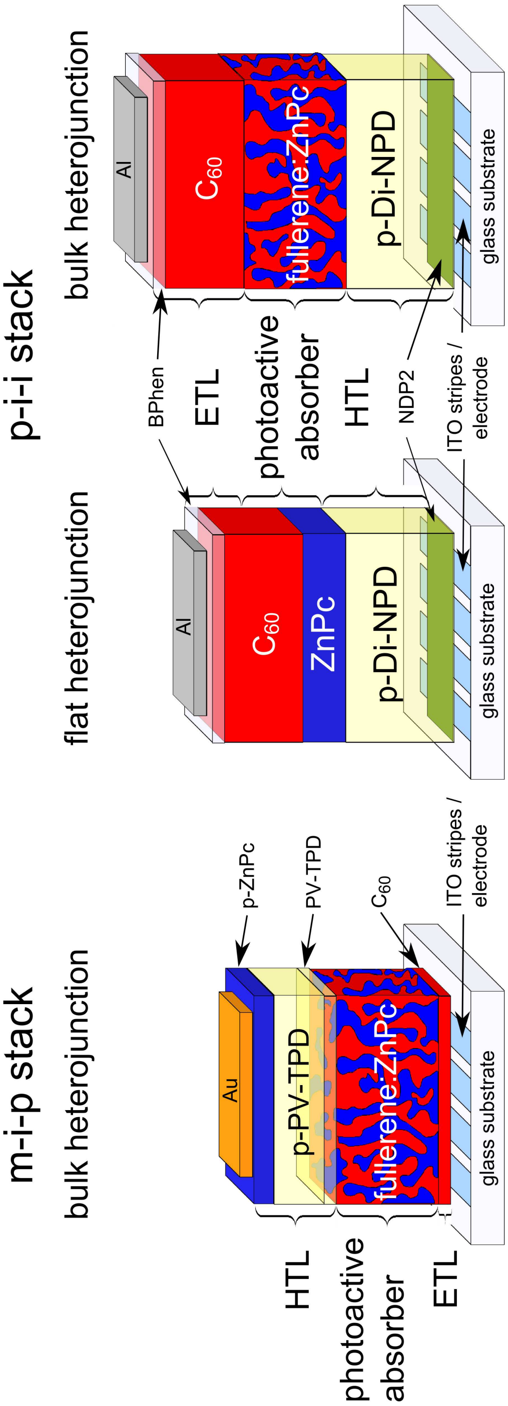

Figure 3.11: *Sketch of the m-i-p (bulk heterojunction) and p-i-i solar cell stacks (flat and bulk heterojunction).*

3.3 Solar cell characterization tools

3.3.1 *J(V)*-measurements

UFO
A AM 1.5G sun simulator SOL 1200 from Hoenle AG (Gräfelfing, Germany) is installed and later replaced by a SoCo 1200 MGH from K. H. Steuernagel Lichttechnik GmbH (Mörfelden-Walldorf, Germany). They are used to directly measure the samples after processing in an inert nitrogen atmosphere. The solar radiation enters the glovebox via a quartz glass embedded in the bottom of the glovebox. The sun intensity can be varied and set with respect to the measured photocurrent by a calibrated silicon diode (Fraunhofer Institute for Solar Energy Systems (ISE)) before *J(V)*-measurement. Above the solar cell, a fan is mounted to cool the solar cell to around 35 °C under illumination. *J(V)*-characteristics are measured using a source measurement unit 236 SMU (Keithley).

LIV-robot
In case of solar cells processed in the Lesker tool, we have a the possibility to characterize a complete wafer in one measurement cycle by a series of single measurements under ambient conditions. To ensure constant temperature conditions, the sun simulator 16S-003-300 from the Solarlight Company Inc. (Glenside, USA) and the source measurement unit 2400 Sourcemeter (Keithley) are placed outside the *J(V)*-measurement box. The illumination from the sun simulator is guided close to the wafer surface via a glass fiber into the measurement box.
For the device characterization we can set the desired sun intensity with respect to the measured photocurrent of a calibrated reference diode S1337-33BQ (Hamamatsu).

3.3.2 EQE

The external quantum efficiency (EQE) is the quantity of conversion of incoming photons into electrical power per wavelength. The design of the EQE measurement setup is schematically shown in Fig. 3.12.
A grating monochromator (Cornerstone 260) is used to achieve narrowband and quasi-monochromatic illumination from the xenon lamp in the Oriel Apex Illuminator. To avoid interference effects two different edge filters are implemented: Newport FSR-OG550 ($T > 550$ nm) and Newport FSR-RG1000 ($T > 1000$ nm). As connector between the monochromator and the illuminator a tube is used with an implemented reflection lattice to spectrally split up the light. The spectral range is selected using an slit mounted at the outside. Two reflection lattice are available. For wavelengths

between 280 and 1000 nm, the reflection grating Newport 74163 and above 1000 nm the Newport 74167 is utilized. A part (10 %) of the light is guided to a photodiode to monitor the stability of the xenon lamp. The beam is chopped and focused by a lens. The sample is positioned out of focus to achieve a homogeneous illumination of the active area of the sample. The sample is then adjusted such that the photocurrent is maximized. The reference diode, which has to be measured as well, needs to be placed at the same position. The current signal of the solar cell is amplified using a current-voltage amplifier (Signal Recovery Model 5182) and converted into a voltage signal, detected by a Lock-In amplifier (Signal Recovery Modell 4262) to improve the signal-to-noise ratio. Further details can be found in reference [214]).

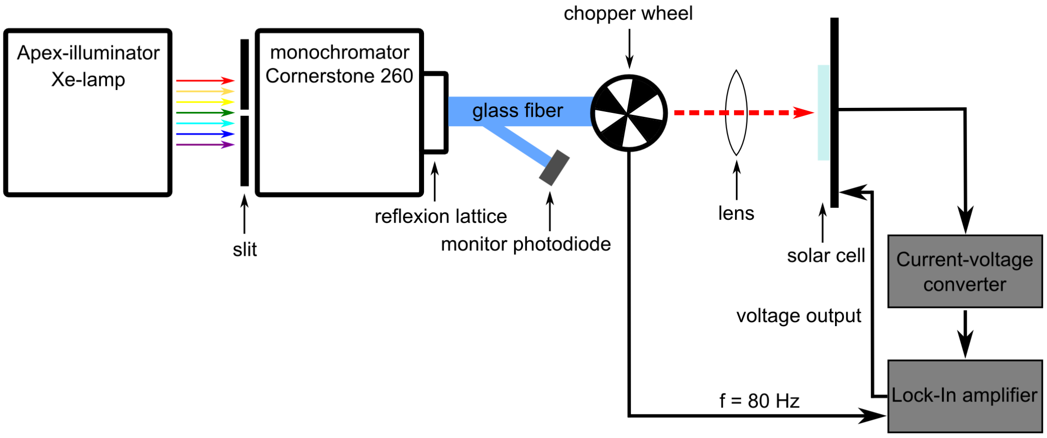

Figure 3.12: *Schematics construction of the EQE measurement setup, after [214].*

3.4 Further characterization tools

3.4.1 UPS and XPS

In ultraviolet photoelectron spectroscopy[4] (UPS) photons from an ideally monochromatic light source are directed onto a sample. This leads to emission of photoelectrons, which can be measured by an electrostatic analyzer.

The basic principle is the external photo effect, described by Einstein in 1905, which relates the maximum kinetic energy $E_{\mathrm{kin}}^{\mathrm{max}}$ of an electron escaping from a sample with work function ϕ to the frequency ν of the exciting photon:

$$E_{\mathrm{kin}}^{\mathrm{max}} = h\nu - \phi. \tag{3.1}$$

With different photon energies, either the density of states (DOS) of the delocalized valence band of the molecule or the localized core level peaks of the individual atoms can be measured. Thus, we can differentiate between UV photoelectron spectroscopy (UPS) for energies of 21.22 eV (He I excitation line) and X-ray photoelectron spectroscopy (XPS) at 1486 eV. Commonly gas discharge lamps are used for the generation of UV photons and Al Kα soft X-ray sources for XPS. The photons penetrate several μm into the sample, but the probing depth is limited to a few Å depending on the electron kinetic energy. Therefore, the emitted electrons can only be measured from the topmost molecular layers. However, this leads to a lower polarization screening of the topmost layer in organic semiconductors compared to the bulk molecules as it is exposed to the vacuum. This usually leads to an increased IP of 100 meV determined by recent experiments using synchrotron high resolution UPS [215].

The photoelectron spectroscopy (PES) measurement setup is directly connected to the multichamber tool (UFO) and allows layer preparation without braking the vacuum and keep the surface contamination very low. The PES setup used for this work is a Phoibos 100 built by the company Specs in Germany. The instrument is incorporated in a UHV chamber at a base pressure of $< 10^{-10}$ mbar. The photogenerated electrons have to pass the hemispherical analyzer that consists of two half spheres. Only electrons which have a centrifugal force equal to the electrostatic force of the analyzer can pass. To image the complete DOS the retardation voltage V_0 is swept. The UV photoelectron spectroscopy measurements are performed using a helium discharge lamp (UVS10/35, Specs) with photo currents of 20 nA. In Fig. 3.13 it is illustrated how photons with an energy hν excite electrons from the valence band above the vacuum level for a gold sample. The kinetic energy distribution directly resembles the DOS of the bound electrons. The IP, for e.g. organics, is given by the difference of the excitation energy

---

[4] carried out by Selina Olthof and Max Tietze, IAPP, TU Dresden

and the width of the measured spectrum:

$$\mathrm{IP} = h\nu - (E_{\mathrm{HBEC}} - E_{\mathrm{HOMO}}), \tag{3.2}$$

where E_{HBEC} is the high binding energy cutoff (point at low kinetic energies where this background ends abruptly) and E_{HOMO} is the HOMO cutoff position. For further information about UPS/XPS we refer to reference [216].

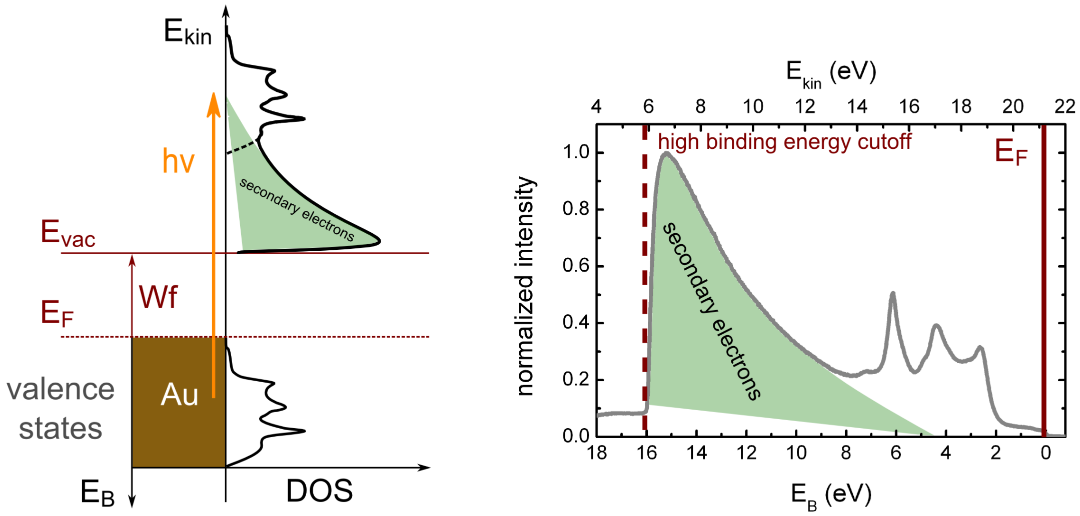

Figure 3.13: *The left graph shows the schematic process of UV excitation in a sample of gold by a photon with the energy $h\nu$. The measurement accesses the values of work function (ϕ), ionization potential (IP), hole injection barrier (HIB), and interface dipole. The right graph shows typical UPS measurements of Au as a function of kinetic energy and binding energy. After [216].*

3.4.2 OFET

Organic field effect transistors (OFET) are used in this work to determine charge carrier mobilities. This method allows a fast and material-conserving processing and quick characterization.

Due to substrate dependent modifications of the layer morphology which influence the charge carrier mobility, we here have the advantage to utilize the same sublayer (substrate) for electron and hole mobility measurements in comparison to, e.g., hole or electron only devices. In case of hole or electron only devices, the layer which is intended to be characterized is sandwiched either by doped hole or a doped electron transport layers. This might have a different impact on the layer morphology and is therefore not suitable for temperature and morphology dependent investigations. A drawback of the OFET is that the mobility is measured perpendicular to the substrate and charge transport in a solar cell. A possible structural anisotropy of the material is not considered. Furthermore, the charge carrier density is in an OFET much higher, which might change μ.

The electron mobility μ_e and hole mobility μ_h can be determined from both linear and saturation regime of the *J(V)*-characteristics. The OFET substrate consist of a silicon gate and silicon dioxide. The OFET substrates with pre-structured source and drain Au contacts and a channel width of 10 mm and length in the range of $2.5-20\,\mu$m are purchased from the Fraunhofer IPMS (Dresden, Germany). In Fig. 3.14 a SEM picture of an OFET with a 30 nm C_{60}:ZnPc blend layer is shown.

OFETs are prepared in the ESK tool and are electrically characterized[5] in the connected glovebox. The OFETs are electrically contacted using a micro positioner from Signatone (S-750 with pivot head) and measured with two source measurement units

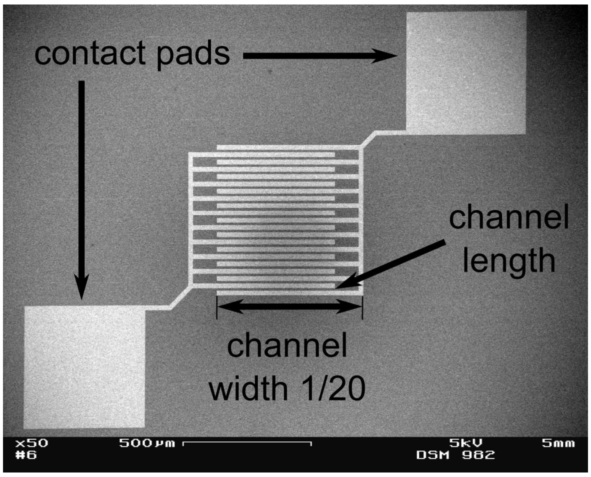

Figure 3.14: *SEM picture of an OFET with 30 nm C_{60}:ZnPc blend layer.*

---

[5] measured by Jens Jankowski and Moritz Hein, IAPP, TU Dresden

SMU 2400 (Keithley). More information about this set up and the measurement technique can be found in reference [217].

3.4.3 AFM, SEM, TEM, and WAXRD

The following methods are used to analyze the morphology of thin organic films with respect to topography and crystallinity.

AFM

The topography is analyzed using an atomic force microscopy (AFM) Nanoscope IIIa (Digital Instruments) in tapping mode at room temperature with tips made of silicon (NSC15, MicroMasch (USA)). Further information about AFM can be found in reference [218].

SEM

For scanning electron microscopy (SEM) (Zeiss DSM 982 Gemini) the samples (with ITO) are electrically contacted to ground with either liquid silver or copper stripes to avoid electrical charging. The secondary electrons are detected with an in-lens detector. All SEM measurements are carried out at room temperature under high vacuum and with an acceleration voltage of 5 kV[6].

TEM

The transmission electron microscopy (TEM, Tecnai) measurements are carried out at the Leibniz-Institut für Festkörper- und Werkstoffforschung Dresden (Dresden, Germany)[7]. For the TEM measurements 10 – 15 nm carbon coated nickel grids (300 mesh, Athene-grids) and an accelerating voltage of 200 kV are used.

WAXRD

Structure analysis is carried out using wide-angle X-ray diffraction URD-6 X-ray powder diffractometer (Seifert FPM GmbH) designed in Bragg–Brentano geometry with monochromatized Cu-Kα radiation[8].

The XRD patterns are recorded in the symmetrical coupled $\omega - 2\,\theta$-scan mode (where $\omega = 2\,\theta\,/2$ and θ are, respectively, the angles of incidence and reflection of X-rays). The XRD measurements are carried out for $2\,\theta$ with steps of 0.01 - 0.05°. The sampling time is chosen between 60 - 180 s according to the intensity and width of the reflexions.

With this method only Bragg reflections from lattice planes parallel to the substrate surface can be detected. The XRD data are analyzed to determine peak position ($2\,\theta$),

---

[6] measured by Ellen Kern, physical chemistry, TU Dresden

[7] measurement support by Christine Mickel

[8] measured by Christoph Schünemann and Alexandr A. Levin, IAPP, TU Dresden

interplane distance (d), peak width at half maximum intensity (FWHM), and crystallite size (D).
The interplane distance is given by Bragg´s law:

$$n\lambda = 2sin(\theta) \cdot d, \tag{3.3}$$

and the crystal size by the Scherrer equation:

$$D = \frac{K\lambda}{\beta cos(\theta)}, \tag{3.4}$$

where K is the shape factor ($K = 0.94$ is used here) and β the line broadening at half the maximum intensity in radians. The line broadening component of the FWHM is determined by subtracting the corresponding components of instrumental broadening and microstrain.
To identify lattice planes by WAXRD reflection positions the Cambridge Structural Database (CSD) [219] is used. All measurements are performed under ambient conditions on Si substrates.

3.4.4 Optical Spectroscopy

For the optical characterization (absorption, reflexion, and transmission) of the organic layers we performed measurements at the two-beam spectrometer Lamda 900 UV/VIS/NIR (Perkin-Elmer) and the MPC-3100 (Shimadzu Corporation).

3.5 Simulation and modeling software

3.5.1 Optical simulation

To investigate and optimize the thin film optics of organic solar cells [220], the devices are optically modeled using the program OSOLemio[9]. This program is based on a transfer-matrix-formalism [221]. The program OSOLemio displays the absorbance and absorbed photon flux of each organic layer as well as the photon flux profile of the layer sequence. Values of the optical constants n & k used in this work are derived by fitting transmission and reflection spectra of thin film layers with a thickness layer variations between 10 - 60 nm.

3.5.2 Electrical simulation

To understand the *J(V)*-curves and characteristics of solar cells, electrical simulations are performed[10] [160,161,222]. A one-dimensional continuity model is used to describe the solar cells. The Poisson, continuity, and transport equations are discretized and the solution is found with an algorithm based numerical model [223]. The charge transport in organic materials can be described by a hopping mechanism [90] rather than by band transport. This approach is taken into account and leads to good results, when temperature-, field-, and charge carrier density dependent mobilities are used for the present molecular disorder [224].

In the last decade such models have been successfully used to describe organic solar cells [225]. To obtain qualitative good accordance to experimental data for, e.g. V_{OC}, a bimolecular recombination model with a modified Langevin expression [226] is used, where the recombination constant

$$\beta = \frac{e}{\epsilon_0 \epsilon_r} min(\mu_{\mathrm{e}}, \mu_{\mathrm{h}}) \tag{3.5}$$

is proportional to the mobility μ of the slower charge carrier [226]. Due to the fact that the recombination constant in blend layers is often observed to be lower as predicted by conventional Langevin theory, this modification is proposed. However, the overall applicability to organic solar cells is still under discussion [227]. Further details concerning equations and simulation can be found in reference [222].

---

[9] programmed by Mauro Furno, IAPP, TU Dresden

[10] simulation performed by Wolfgang Tress, IAPP, TU Dresden

4 Results: C_{70} as acceptor molecule for organic solar cells

Fullerene C_{60} is used as standard acceptor molecule by many groups in organic photovoltaics, due to its good electron transport properties, suitable energy levels (e.g. air stability), and processability. Despite its good electrical properties, absorption in the visible range of light is too low to achieve highly efficient devices. C_{70} as an alternative compound is found in the same molecule class. It has also been of interest for polymer based solar cells, e.g., [70]PCBM [228] and has shown excellent properties.
In this chapter, C_{70} is investigated and characterized as alternative for the acceptor molecule C_{60} in small molecule organic solar cells. Therefore, measurements of the optical properties, charge carrier mobility, and energy levels are carried out. Using simple solar cell stacks, further properties of C_{70} are determined, e.g. LUMO and exciton diffusion length. C_{70} is employed in bulk heterojunction fullerene:ZnPc solar cells to determine its potential for applications in organic solar cells and replacement of C_{60}. Optimizations concerning fullerene:ZnPc blend ratios are experimentally performed.

4.1 Optical characterization

20 nm of pure C_{60}, see Fig. 4.1a, and C_{70}, see Fig. 4.1b, are deposited separately on quartz glass and investigated spectroscopically. As shown in the absorption measurements in Fig. 4.2, C_{70} exhibits a stronger absorption in the visible range of light between 380-800 nm [229]. The different absorption behavior observed for C_{60} and C_{70} is caused by transitions which are forbidden in C_{60} due to the high molecular symmetry and allowed for the ellipsoid-shaped C_{70}: For C_{70}, the molecular symmetry is lowered and the degeneracy of electronic states decreases. This fact leads to an increase in the density of electronic states and in the relative number of states with spectroscopically allowed transitions [230]. In general, the allowed transitions for C_{60} are assigned to the 190 - 410 nm region, whereas the forbidden singlet-singlet transitions are observed between 410 and 620 nm [231]. Orlandi et al. [230] determined a series of very weak bands associated with the low energy states for symmetry forbidden transitions to or

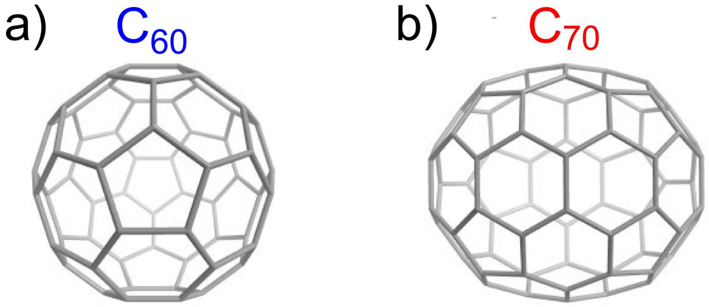

Figure 4.1: *Molecular structures of a) fullerene C_{60} and b) ellipsoid shaped fullerene C_{70}. Both are about 10 Å in diameter.*

from S_0 between 430 - 640 nm. The latter optical activity has been assigned to Jahn-Teller and/or Herzberg-Teller vibronic interactions by Leach et al. [232]. However, the

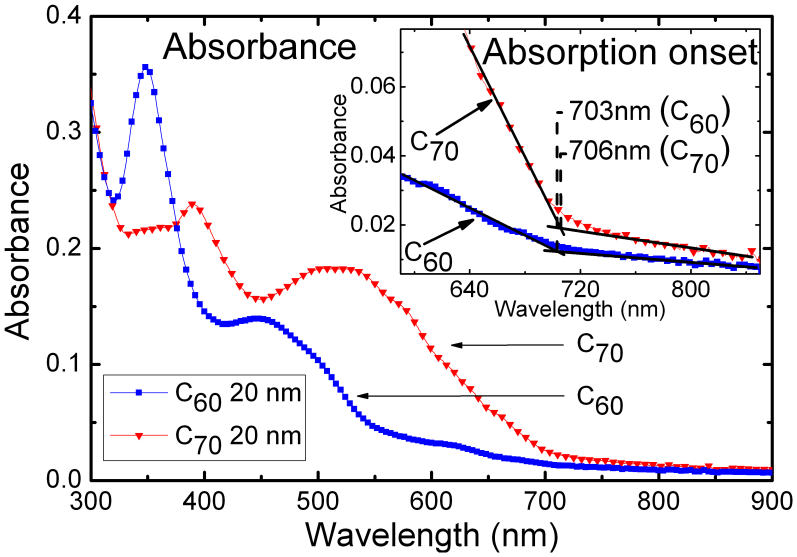

Figure 4.2: *Absorption measurements of 20 nm C_{60} (filled squares) and C_{70} (filled up side down triangles), C_{70} shows a broadened and stronger absorption in the visible range of light compared to C_{60}. Inset: Fit of the absorption onset of C_{60} and C_{70}, determined for both to be approx. 705 nm.*

absorption onset is around 705 nm for both materials, shown in the inset of the graph in Figure 4.2. The optical bandgap is calculated using the following equation:

$$E_G^{opt} = \frac{hc}{\lambda_{onset}}. \tag{4.1}$$

The optical bandgap around 1.76 eV is similar for both C_{60} and C_{70}. The absorption coefficient α can be calculated using equation 4.2 with absorbance A and layer thickness d.

$$A = \lg(e)\alpha d \tag{4.2}$$

Broad absorption is observed around the absorption maximum at 515 nm for C_{70}, with a calculated α of $2.1\times10^{5}\,\mathrm{cm}^{-1}$. In comparison, C_{60} has a smaller α of $1.6\times10^{5}\,\mathrm{cm}^{-1}$ calculated for the absorption maximum at 447 nm. To check if the enhanced photon absorption of C_{70} can efficiently be used by photon conversion into free charge carriers, BHJ solar cells are processed and discussed in sections 4.4 and 4.5.

4.2 Mobility measurements

To ensure high V_{OC}, efficient charge carrier extraction out of the bulk layer and reduced charge carrier recombination is required. For this reason, mobilities of both electrons and holes in single and mixed layers should be in the range of $10^{-4}\,\mathrm{cm^2/Vs}$ to $10^{-2}\,\mathrm{cm^2/Vs}$ [233]. Mobility measurements[1] for the acceptor-like fullerenes are carried out. Usually, in organic solar cells, charge carriers move perpendicular to the substrate, while in OFET the mobility of the charge carriers parallel to the substrate is measured. Due to the fact that C_{60} and C_{70} are symmetric and shaped like a ball or an ellipsoid, no preferential molecular arrangement should exist. Therefore, using the OFET method, no large deviations in mobilities are expected. A 50 nm thick C_{60} or C_{70} layer is deposited on the substrate and characterized electronically. The electron mobility μ_e can be determined from either the linear or saturation regime. For these measurements, OFETs with a channel width of 10 mm and a channel length of 20 μm for C_{60} and 2.5 μm for C_{70} are used. The μ_e calculated from the linear regime as well from saturation regime are shown in Table 4.2. The obtained mobilities for the linear and saturation regime differ slightly, but show μ_e in the order of $10^{-3}\,\mathrm{cm^2/Vs}$. Higher mobilities for the saturation regime are caused by a higher charge carrier density which is created in the source drain channel at the SiO_2/fullerene interface. Comparing C_{60} and C_{70}, a slightly better mobility is determined for C_{60}, but both are on the same order and thus hints at comparable charge carrier transport properties.

Table 4.1: *Electron mobilities of C_{60} and C_{70} determined in the linear and saturation regime by OFET mobility measurements.*

	C_{60}	C_{70}
μ_e linear regime ($\mathrm{cm^2/Vs}$)	3.4×10^{-3}	2.0×10^{-3}
μ_e saturation regime ($\mathrm{cm^2/Vs}$)	9.2×10^{-3}	6.9×10^{-3}

---

[1] measured by Moritz Philipp Hein

4.3 Ultraviolet photoelectron spectroscopy

To determine the IP of fullerenes in solid state, 10 nm of C_{60} and 15 nm of C_{70} are deposited on a 0.5 mm thick silver foil. The IP can be calculated from the measured values[2] of hole injection barrier (HIB), high binding energy cutoff (HBEC), and the given energy of the helium discharge lamp (21.22 eV) in the UPS by:

$$\mathrm{IP} = 21.22\,\mathrm{eV} - \mathrm{HBEC} + \mathrm{HIB}. \tag{4.3}$$

The HBEC and HIB indicated in Fig. 4.3 are determined to be 16.55 eV and 1.74 eV for C_{60} and 16.72 eV and 1.91 eV for C_{70}. This leads to a similar IP of 6.41 eV for both C_{60} and C_{70}. Taking the electron affinity (EA) at around -4.0 eV for C_{60} [184] and C_{70} (see section 4.4) an electrical bandgap $E_G^{\mathrm{el}} = E_{\mathrm{HOMO}}$- E_{LUMO} of around 2.4 eV [185] is determined. The difference between E_G^{el} and E_G^{opt} can be attributed to the exciton binding energy. This amount of energy is essential to dissociate the exciton into free charge carriers. This required energy can be provided by a favorable energy offset to the adjacent energy level.

The obtained IP of C_{70} at 6.41 eV provides an energy offset of at least 1.13 eV to the IP of ZnPc (5.0 eV to 5.28 eV [199, 234]). For both fullerenes the exciton binding energy can be estimated to be 0.65 eV (in solution, it is about 0.4 eV [235]) and is lower than the IP offset between fullerene and ZnPc of 1.13 eV. Therefore, an efficient exciton dissociation is expected [130, 236].

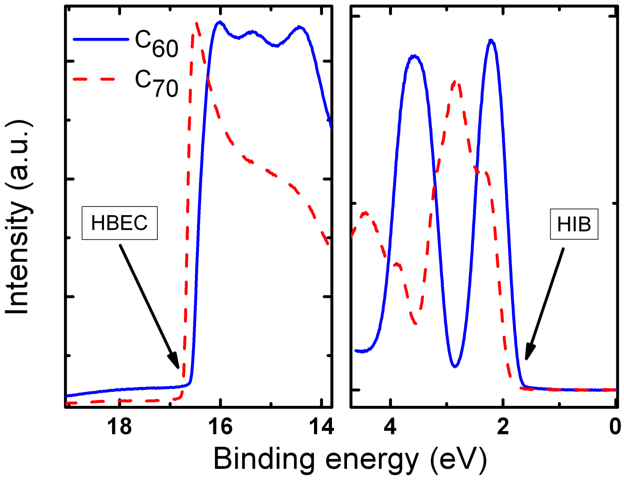

Figure 4.3: *UPS measurement of 10 nm C_{60} (solid line) and 15 nm C_{70} (dashed line) on silver foil, respectively. The left graph shows the high binding energy cutoff (HBEC) and the right graph the hole injection barrier for both fullerenes.*

---

[2] measured by Selina Olthof

4.4 p-i-i flat heterojunction solar cells

4.4.1 Di-NPD/fullerene flat heterojunction solar cells

For a reliable LUMO estimation of C_{70} relative to C_{60}, the concept of flat heterojunction solar cell is applied. Using this approach [115], a junction to a wide gap (no contribution to photocurrent) donor layer is required, so that the quasi-Fermi level splitting caused by free charge carriers is mainly dominated by the acceptor layer. If both solar cells are adjusted to the same J_{SC}, a similar Fermi level splitting in the fullerene layers is expected and the logarithmic term in equation 4.4 is supposed to be similar for both C_{60} and C_{70}.

$$V_{\mathrm{OC,max}} = \frac{1}{e}\left(\epsilon_{\mathrm{C}} - \epsilon_{\mathrm{V}} - k_{\mathrm{B}}T\ln\frac{N_{\mathrm{C}}N_{\mathrm{V}}}{n_{\mathrm{e}}n_{\mathrm{h}}}\right) \tag{4.4}$$

The V_{OC} depends on the remaining terms, the HOMO level (ϵ_{V}) of the donor and the LUMO level (ϵ_{C}) of the acceptor. Utilizing the same donor material in the solar cells with both C_{60} and C_{70}, the change in V_{OC} is directly correlated to the change in the LUMO level of the acceptor. This estimation is only valid assuming similar interface properties for both solar cells. The LUMO level of C_{70} can be calculated by adding the absolute difference in V_{OC} to the reference LUMO value for C_{60}, measured via inverse photoemission spectroscopy (IPES) to -4.0 eV [184]. This method provides at least a better accuracy compared to IPES which is on the order of 450 meV [237, 238].

Here, we used an non-optimized solar cell stack concerning optical field distribution:
ITO/NDP2(1 nm)/p-Di-NPD(60 nm;5wt %)/Di-NPD(10 nm)/
fullerene(15 nm)/BPhen(6 nm)/Al(100 nm).

The C_{70}-containing cell is measured at one sun with a mismatch of 0.73 and displays a J_{SC} of 1.30 mA/cm^2. In order to reach the same J_{SC}, the C_{60}-containing cell is set to 1.42 suns with a mismatch of 0.67.

At these intensities, the V_{OC} for Di-NPD/C_{60} interface is measured to 0.784 V and for Di-NPD/C_{70} to 0.705 V, which suggests a lower LUMO level of C_{70} compared to C_{60} of approximately 0.08 eV. In Fig. 4.4 the *J(V)* characteristics of the flat heterojunctions are shown. These results are also checked for double sun intensity. V_{OC} of 0.798 V for Di-NPD/C_{60} and 0.721 V for Di-NPD/C_{70} are obtained. The same difference in V_{OC} of around 0.08 V is determined and is confirmed.

Measuring both solar cells under one sun illumination (mismatch is taken into account), the C_{70}-containing cell provides a 56 % higher J_{SC} of 1.30 mA/cm^2 compared to 0.83 mA/cm^2 for C_{60} as shown in Fig. 4.5. This means that the larger amount of generated excitons compared to C_{60} efficiently diffuse to the separating interface and contribute to J_{SC}. The larger J_{SC} reflects the better thin film absorption of C_{70} shown

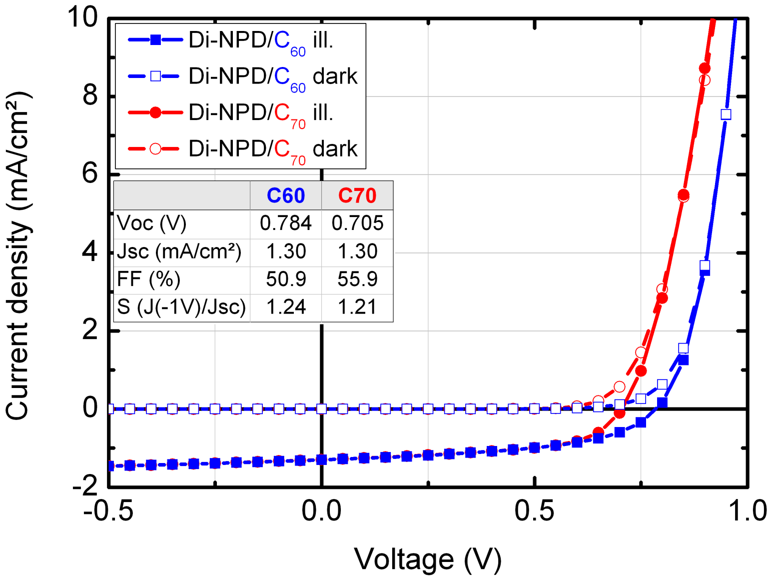

Figure 4.4: *Flat heterojunction OSC using the interface Di-NPD/fullerene for a LUMO level estimation of C_{70} relatively to C_{60}. The same J_{SC} of 1.30 mA/cm^2 for both cells ensures roughly similar quasi-Fermi level splitting in the fullerene layers. Difference in V_{OC} between Di-NPD/C_{60} (filled squares) and Di-NPD/C_{70} (filled circles) of the FHJ is directly related to difference in LUMO of C_{60} and C_{70}.*

in Fig. 4.2.

The difference in *FF* between 51 % for Di-NPD/C_{60} and 56 % for Di-NPD/C_{70} might be caused by a higher non-geminate recombination probability for Di-NPD/C_{60}. Graja et al. [231] have shown by transient absorption measurements that a rapid intersystem crossing between S_1 and T_1 states takes place. While the singlet state lifetime for C_{60} is 1.3 ± 0.2 ns and for C_{70} 0.7 ± 0.05 ns, the triplet states in C_{70} have a longer lifetime of 130 μs compared to 40 μs for C_{60}. Therefore, the generated C_{70} excitons which diffuse to the separating interface have a higher chance to get dissociated before they recombine and this affects the *FF* positively.

4.4.2 ZnPc/fullerene flat heterojunction solar cells

All obtained material parameters for C_{70}, e.g. high photon absorption, μ_e, HOMO, and LUMO, suggest that efficient flat and bulk heterojunction solar cells are possible. As a first implementation of C_{70} in combination with the donor molecule ZnPc, p-i-i flat heterojunctions solar cells are made using the following stack:

ITO/NDP2(1 nm)/p-Di-NPD(60 nm;5wt %)/ZnPc(25 nm)/
fullerene(40 nm)/BPhen(6 nm)/Al(100 nm).

As discussed previously, the *J(V)* characteristics shown in Fig. 4.6a) show a similar

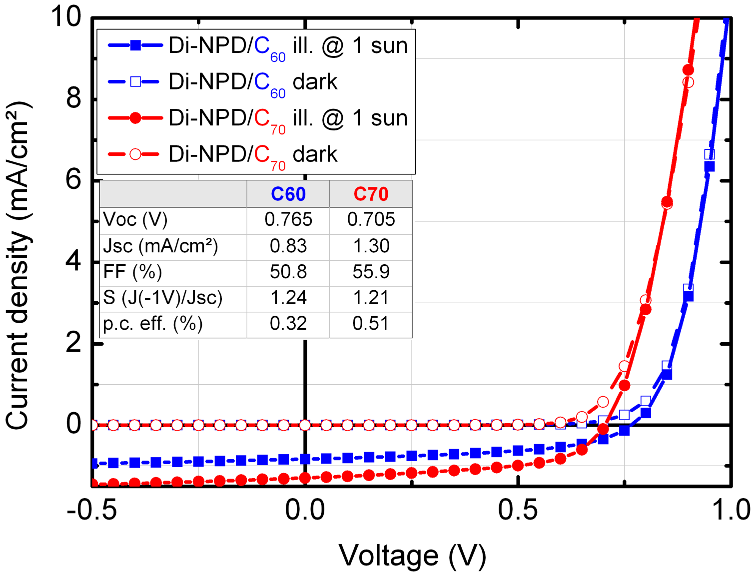

	C60	C70
Voc (V)	0.765	0.705
Jsc (mA/cm²)	0.83	1.30
FF (%)	50.8	55.9
S (J(-1V)/Jsc)	1.24	1.21
p.c. eff. (%)	0.32	0.51

Figure 4.5: *Flat heterojunction OSC measured at 1 sun light intensity, mismatch is taken into account. Di-NPD/C_{70} (filled circles) FHJ shows a 56 % higher contribution to J_{SC} of 1.30 mA/cm^2 compared to 0.83 mA/cm^2 for Di-NPD/C_{60} FHJ (filled squares), which reflects the high photon absorption of C_{70} in thin film.*

difference in V_{OC} caused by the lower LUMO of C_{70}. Contrary to the Di-NPD/C_{70} flat heterojunction, the ZnPc/C_{70} solar cell shows no improvement concerning J_{SC}. The measured J_{SC} of 3.9 mA/cm^2 for C_{60} and 3.2 mA/cm^2 for C_{70} are in good accordance to the J_{SC} determined by the EQE of 3.9 mA/cm^2 and 3.3 mA/cm^2. Due to the comparable mobilities of C_{60} and C_{70}, no limitations of charge carrier transport are expected. Furthermore, the simulation of both stacks as depicted in Fig. 4.7 exhibits that the photoacative layers are in the optical field maximum. The simulated J_{SC} generation of ZnPc in the C_{70} cell is slightly lower and might be caused by a reduced backscattered light intensity from the reflective metal back contact due to parasitic C_{70} absorption. The C_{70} contribution to J_{SC} is given by the simulation to be about 9.2 mA/cm^2 compared to C_{60} of 4.8 mA/cm^2. From the EQE shown in Fig. 4.6b) it can be seen, that C_{70} shows only 50 % of the photon conversion of C_{60} and leads to the conclusion that the exciton diffusion length of C_{70} is much smaller compared to C_{60}. Therefore, the lower J_{SC} can be attributed to a lower exciton diffusion length of C_{70} and not to a reduced ZnPc contribution to J_{SC}. From experience and literature [47] the exciton diffusion length of C_{60} is on the order of 20 nm. In section 4.4.1 we have discussed a Di-NPD/C_{70} solar cell with 15 nm thick layer of C_{70}, which shows a high C_{70} contribution to J_{SC}. However, with a thicker C_{70} layer of 40 nm the contribution from C_{70} is very small. From the organic solar cells and their corresponding EQEs we estimate the exciton diffusion length of C_{70} to be between 10-15 nm. As mentioned before, the fact that the

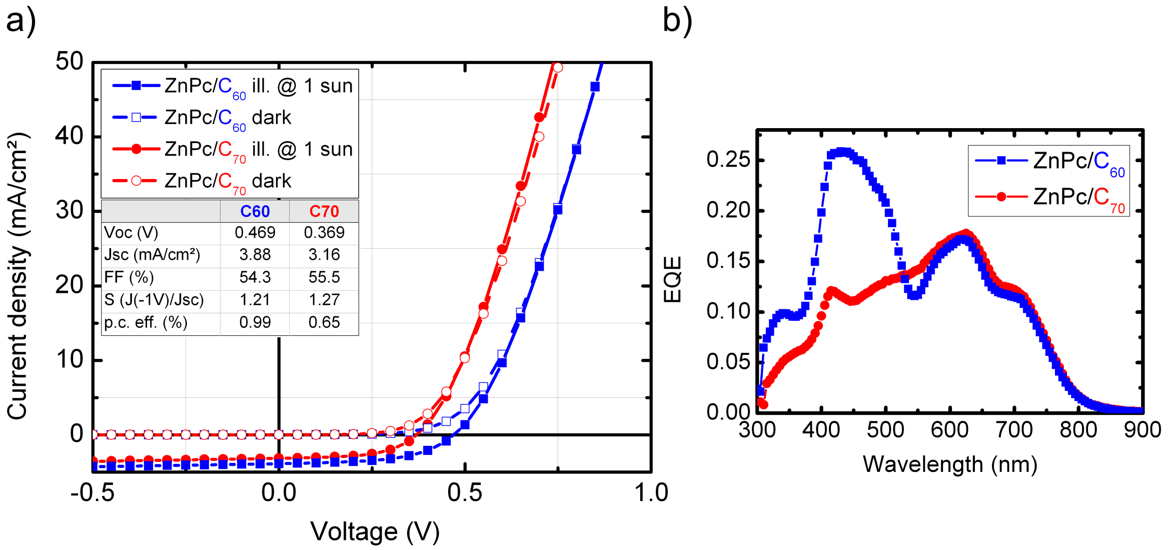

Figure 4.6: *ZnPc/fullerene FHJ a) J(V) characteristics with 40 nm of* C_{60} *(filled squares) and* C_{70} *(filled circles), respectively. b) EQE measurements of ZnPc/*C_{60} *(filled squares) and ZnPc/*C_{70} *(filled circles) shows similar EQE in ZnPc absorption region, while at 450 nm* C_{60} *has doubled EQE compared to* C_{70}*. This is attributed to the lower exciton diffusion length of* C_{70} *and is reflected in the lower* J_{SC} *compared to ZnPc/*C_{60}*.*

generated C_{70} triplet excitons have a longer lifetime than those of C_{60} and is not in contradiction to a smaller exciton diffusion length of C_{70}. The exciton diffusion length L_D is defined by [239, 240]:

$$L_D = \sqrt{D \cdot \tau}, \tag{4.5}$$

where D is the exciton diffusion coefficient and τ the lifetime of the exciton. It means that the C_{70} exciton diffusion length is not limited by the lifetime, but rather by the small exciton diffusion coefficient of the excitons.

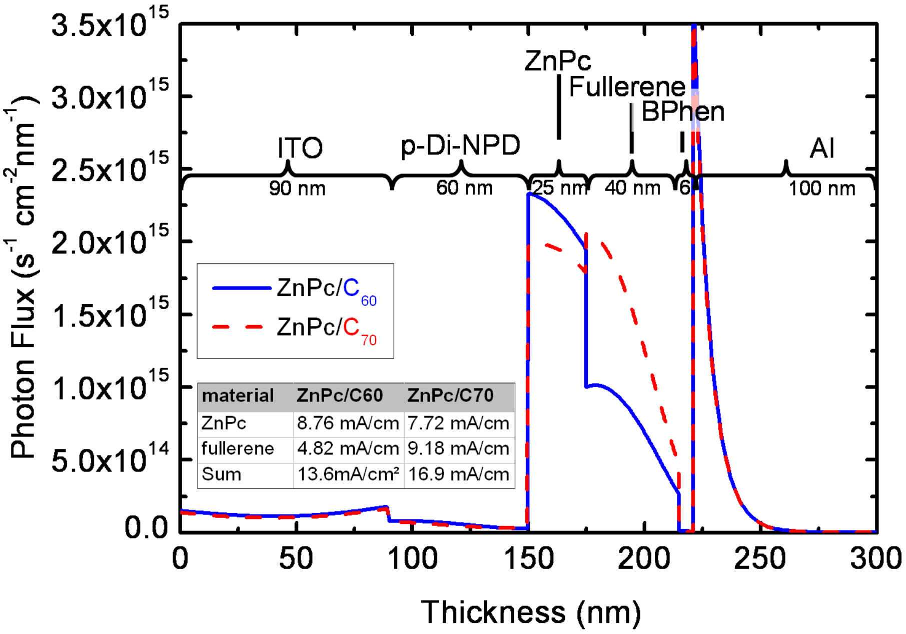

material	ZnPc/C60	ZnPc/C70
ZnPc	8.76 mA/cm	7.72 mA/cm
fullerene	4.82 mA/cm	9.18 mA/cm
Sum	13.6mA/cm²	16.9 mA/cm

Figure 4.7: *Photon flux simulation of each layer in ZnPc/*C_{60} *(solid line) and ZnPc/*C_{70} *(dashed line) FHJ OSCs.*

4.5 p-i-i bulk heterojunction solar cells

BHJ are more efficient concerning J_{SC} generation compared to FHJ, due to no limitations by exciton diffusion length. Since in BHJ OSC the transport properties of the charge carriers depends additionally on the mixing ratio, the ratio is varied by the fullerene:ZnPc blend to find the optimum performance of these devices. Here, we show the implementation of C_{70} in comparison to C_{60} in ZnPc-containing p-i-i BHJs. To ensure a good comparability of such a parameter variation, the processing potential of the Lesker tool is used. Due to better processability, we changed the m-i-p solar cell structure to p-i-i. Using the simulation program OSOLemio and by varying the intrinsic C_{60} layer between 30-45 nm, the optical field can be shifted within the blend layer and is found to be the maximum in the blend for 40 nm C_{60} for both cells as depicted in Fig. 4.8. The intrinsic C_{60} layer thickness variation is validated experimentally, but is not shown here. To obtain comparable results for C_{60} and C_{70}, the following optically optimized device structure with 40 nm C_{60} is used:
ITO/NDP2(1 nm)/p-Di-NPD(60 nm;5wt %)/fullerene:ZnPc(30 nm,X:Y)/ C_{60}(40 nm)/BPhen(6 nm)/Al(100 nm).

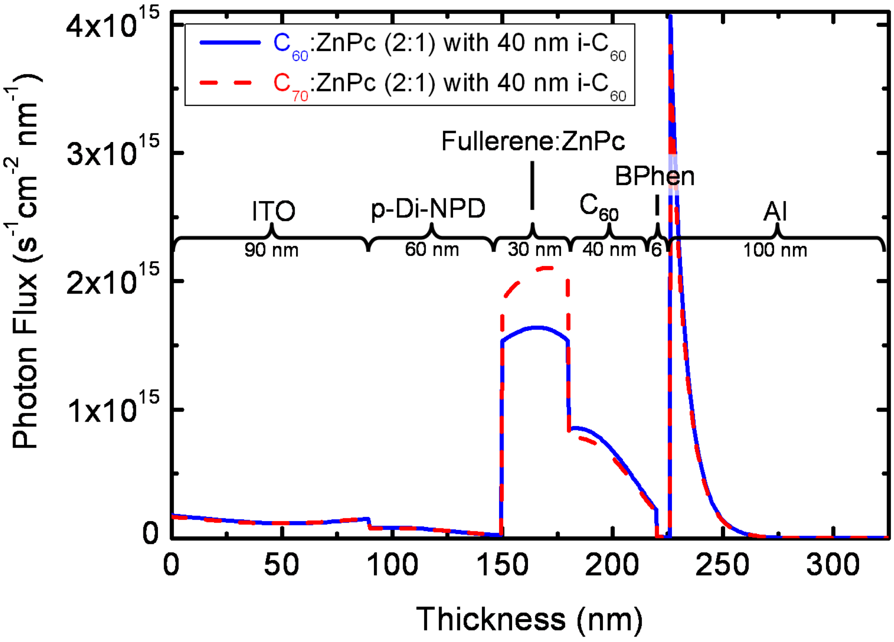

Figure 4.8: *Photon flux simulations of fullerene:ZnPc BHJ OSCs with blend ratio 2:1 and 40 nm intrinsic C_{60}. The maximum absorbed photon flux can be shifted within the blend layer by varying the intrinsic C_{60} layer caused by thin film optics. For both blends C_{60}:ZnPc (solid line) and C_{70}:ZnPc (dashed line) the optimum is found for 40 nm intrinsic C_{60}.*

Investigations for fullerene:ZnPc blend ratios of 1:1, 2:1, 3:1, and 4:1 are carried out. The *J(V)* parameters are shown in Table 4.2 and Table 4.3 for C_{60}:ZnPc and C_{70}:ZnPc, respectively. Taking a closer look at the C_{60}:ZnPc results, we see that V_{OC} increases from 0.55 V to 0.62 V with larger amounts of C_{60} in the blend. This effect is considered and discussed separately in chapter 6.

Table 4.2: *J(V) parameters of C_{60}:ZnPc BHJ OSC for different blend ratios 1:1, 2:1, 3:1, and 4:1. Best p.c. efficiency is determined for blend ratio 1:1.*

C_{60}:ZnPc ratio	**1:1**	**2:1**	**3:1**	**4:1**
V_{OC} (V)	0.55	0.59	0.61	0.62
J_{SC} (mA/cm^2)	8.1	7.4	6.3	5.4
FF (%)	56.6	55.9	50.2	47.4
S J(-1V/J_{SC})	1.12	1.11	1.14	1.18
p.c. eff. (%)	**2.5**	2.5	1.9	1.6

J_{SC} decreases for less ZnPc in the blend. This is attributed to a smaller contribution of ZnPc to J_{SC} ZnPc, which can clearly be seen in the ZnPc absorption region between 550-800 nm in the EQE measurement of Fig. 4.9. ZnPc peaks are decreased for lower ZnPc amount. The EQE below 550 nm attributed to C_{60} absorption remains constant

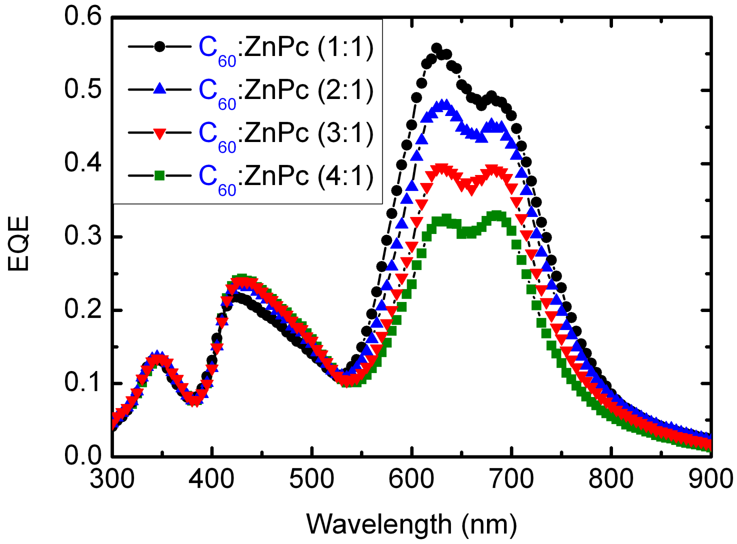

Figure 4.9: *EQE measurements of C_{60}:ZnPc BHJ OSC for different blend ratios 1:1 (circles), 2:1 (triangles), 3:1 (up side down triangles), and 4:1 (squares). EQE vary above 550 nm due to different ZnPc amounts in the BHJ and its contribution to J_{SC}, while below 550 nm the EQE for C_{60} remain constant.*

for all ratios and does not increase with the amount of C_{60}. This might be caused by an increased charge carrier recombination. Thus, the loss of ZnPc absorption can not be compensated for by an increased C_{60} absorption.

The *FF* decreases from ≈56 % to 47 % and hints at higher charge carrier recombination due to inefficient charge carrier separation and transport (e.g. unbalanced charge carrier mobilities [72, 160]) for an increasing amount of C_{60} in the blends. Furthermore, the increased saturation factor is an additional indication for bad charge transport.

The optimum blend ratio for C_{60}:ZnPc is determined with respect to p.c. efficiency of 2.5 % to 1:1 (marked green in Table 4.2). The favourable blend ratio leads to high J_{SC} of 8.1 mA/cm^2 and high *FF* of 56 %. However, for a ratio 2:1 a similar p.c. efficiency of 2.5 % is obtained. As seen in Table 4.2 the V_{OC} is slighly increased, while the J_{SC} is slightly decreased compared to the ratio 1:1. For all ratios of the C_{60}:ZnPc BHJs a determined mismatch of 0.81 is taken into account.

The same devices are made for C_{70}:ZnPc, and the corresponding *J(V)* characteristics are shown in Table 4.3. As already observed for the C_{60}:ZnPc solar cell, a similar increase in V_{OC} from 0.51 V to 0.60 V for higher C_{70} amount is determined. The best J_{SC} of 10.1 mA/cm^2 and *FF* of 56 % is found for the blend ratio 2:1. For all blend ratios of the C_{70}:ZnPc BHJs a mismatch of 0.83 is determined. For the other ratios J_{SC} and *FF* are decreased. The high EQE of ≈35 % at λ<550 nm is attributed to C_{70} absorption and observed for all ratios in Fig. 4.10. The EQE decreases significantly above 550 nm for lower amount of ZnPc, as already observed for C_{60}:ZnPc. Similar to the argumentation for C_{60}:ZnPc, the lowered J_{SC} and *FF* might be caused by a higher charge carrier recombination due to inefficient charge carrier separation and transport (e.g. unbalanced charge carrier mobilities [72, 160]). The best p.c. efficiency is determined to 3.1 % for the blend ratio 2:1, but 3:1 ratio shows also good performance with a p.c. efficiency of 3.0 %. Compared to C_{60}:ZnPc the optimum ratio for C_{70}:ZnPc is shifted from 1:1-2:1 to 2:1-3:1. This might be explained by a compensation of the lower μ_e of C_{70} compared to C_{60} by a larger amount of C_{70} in the blend.

Table 4.3: *J(V) parameters of C_{70}:ZnPc BHJ OSC for different blend ratios 1:1, 2:1, 3:1, and 4:1. Best p.c. efficiency is determined for blend ratio 2:1.*

C_{70}:ZnPc ratio	**1:1**	**2:1**	**3:1**	**4:1**
V_{OC} (V)	0.51	0.55	0.58	0.60
J_{SC} (mA/cm^2)	9.6	10.1	9.6	8.8
FF (%)	54.2	56.1	53.3	52.4
S J(-1V)/J_{SC}	1.18	1.13	1.13	1.14
p.c. eff. (%)	2.7	**3.1**	3.0	2.8

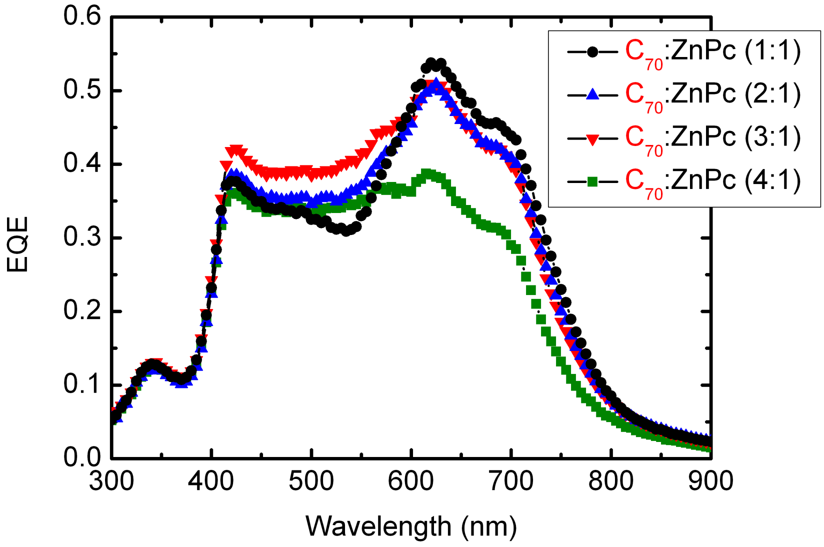

Figure 4.10: *EQE measurements of C_{70}:ZnPc BHJ OSC for different blend ratios 1:1 (circles), 2:1 (triangles), 3:1 (up side down triangles), and 4:1 (squares). EQE vary due to different C_{70} and ZnPc amounts in the BHJ and its contribution to J_{SC}.*

For a reliable comparability of the fullerenes in BHJs concerning fullerene amount, we use the blend ratio 2:1. From the *J(V)* characteristics shown in Fig. 4.11 b) and Table 4.4, we see that the V_{OC} is slightly reduced for the C_{70}:ZnPc BHJ caused by the lower LUMO of C_{70}. This loss is overcompensated for by a 35 % higher contribution of C_{70} to J_{SC} and leads to a 27 % improved p.c. efficiency of 3.1 %. The higher J_{SC} can be explained by the closed absorption gap between 450-600 nm, which is present for C_{60}:ZnPc, visualized in the EQE in Fig. 4.11 b). An EQE of nearly 40 % is achieved below 550 nm, where C_{70} mainly absorbs, while the EQE contribution of ZnPc above 550 nm is the same for both cells. No strong distinctions are assumed for charge recombination, transport and interface properties due to the same *FF* of 56 % and same *J(V)* slope in forward bias.

Table 4.4: *J(V) parameters of C_{60}:ZnPc and C_{70}:ZnPc BHJ OSC for same blend ratio of 2:1 due to better comparability. The best p.c. efficiency is obtained for C_{70}-containing OSC because of the 35 % higher J_{SC} contribution compared to C_{60}:ZnPc.*

ratio (2:1)	V_{OC} (V)	J_{SC} (mA/cm^2)	*FF* (%)	J(-1V)/J_{SC}	p.c. eff. (%)
C_{60}:ZnPc	0.59	7.4	55.9	1.11	2.5
C_{70}:ZnPc	0.55	10.1	56.1	1.13	3.1

C_{70} as an alternative photoactive absorber in organic solar cells delivers with high J_{SC}

and EQE in the spectral region between 400 nm and 550 nm in different organic solar cell stacks. Almost similar values in comparison to C_{60} are obtained for the optical gap, μ_e, HOMO, and LUMO. Therefore, C_{70} is a highly suitable acceptor molecule to replace C_{60} in organic solar cells.

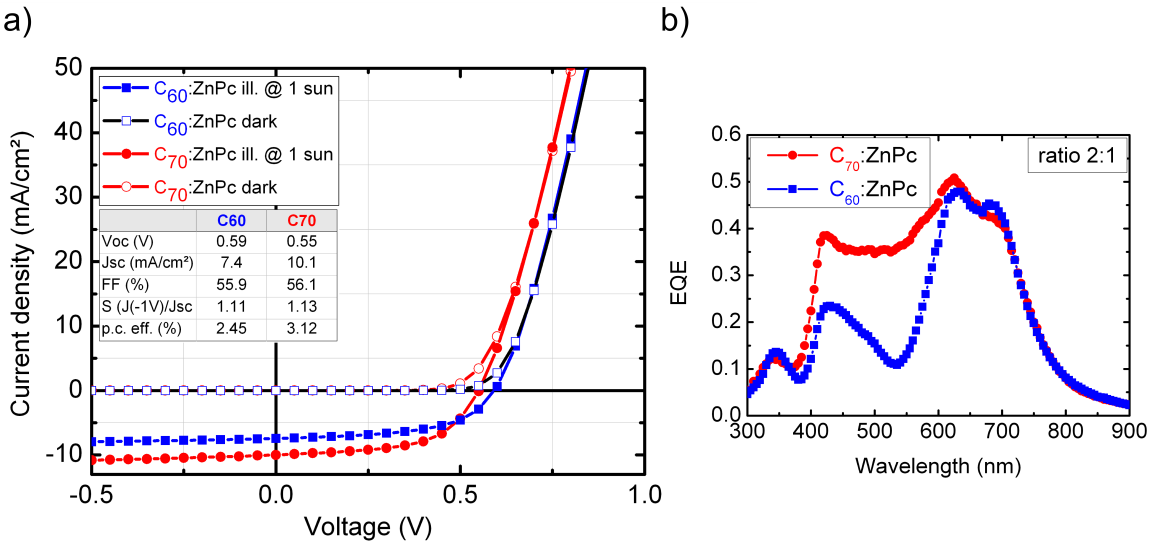

	C60	C70
Voc (V)	0.59	0.55
Jsc (mA/cm²)	7.4	10.1
FF (%)	55.9	56.1
S (J(-1V)/Jsc	1.11	1.13
p.c. eff. (%)	2.45	3.12

Figure 4.11: *BHJ OSC with fullerene:ZnPc blend ratio 2:1: a) J(V) characteristics of C_{60}:ZnPc (filled squares) and C_{70}:ZnPc (filled circles). b) EQE measurements of C_{60}:ZnPc (filled squares) and C_{70}:ZnPc (filled circles) BHJs. The best p.c. efficiency is obtained for C_{70}-containing OSC because of the 35 % higher J_{SC} contribution compared to C_{60}:ZnPc.*

4.5.1 p-i-i mixed C_{60}:C_{70}:ZnPc bulk heterojunction solar cell

C_{70} is commercially available in purities between 95 % and 99.9 %, whith a price difference between both purities up to a factor of five [241]. C_{60} costs around 250 \$/10 g and C_{70} around 5000 \$/10 g. The main impurity of the 95 % pure C_{70} is C_{60} [241]. Usually, the amount of fullerene which is obtained by the standard arc burning production process is on the order of 5 %, where C_{60} occurs with 80 % and C_{70} between 15 % to 20 %. To check if such a high purity of C_{70} is needed and how a larger amount of C_{60} in C_{70} or vice versa influences the device performance, a mixed bulk heterojunction composed of C_{60}:C_{70}:ZnPc in a ratio of 1:1:1 is made. The following solar cell stack is used:
ITO/NDP2(1 nm)/p-Di-NPD(60 nm;5wt %)/
C_{60}:C_{70}:ZnPc(30 nm,1:1:1)/C_{60}(40 nm)/BPhen(6 nm)/Al(100 nm).
The corresponding *J(V)* curve and EQE are plotted in Fig. 4.12a and b in comparison to bulk heterojunctions of C_{60}:ZnPc and C_{70}:ZnPc, all with same fullerene amount of ratio 2:1. From the *J(V)* we see that blending C_{60}, C_{70} and ZnPc results in a p.c. efficiency of approximately 2.7 %, between 2.5 % for the C_{60}-containing BHJ and 3.1 % for

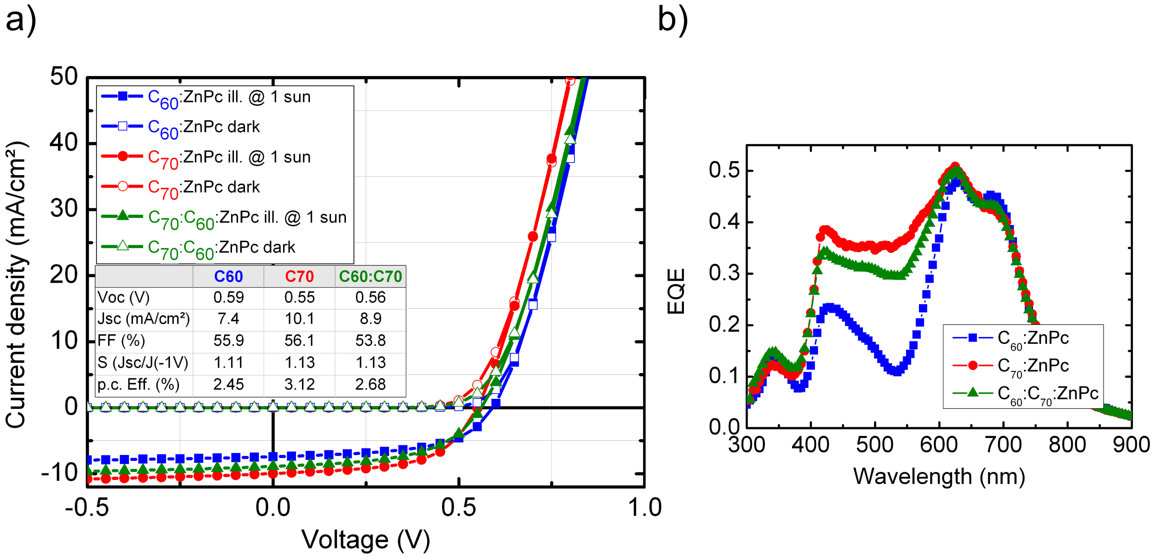

	C60	C70	C60:C70
Voc (V)	0.59	0.55	0.56
Jsc (mA/cm²)	7.4	10.1	8.9
FF (%)	55.9	56.1	53.8
S (Jsc/J(-1V)	1.11	1.13	1.13
p.c. Eff. (%)	2.45	3.12	2.68

Figure 4.12: *BHJ OSC with fullerene:ZnPc blend ratio 2:1: a) J(V) characteristics of C_{60}:ZnPc (filled squares), C_{70}:ZnPc (filled circles), and C_{60}:C_{70}:ZnPc (filled circles). b) EQE measurements of C_{60}:ZnPc (squares), C_{70}:ZnPc (circles), and C_{60}:C_{70}:ZnPc (circles) BHJs.*

the C_{70}-containing BHJ solar cell. The triple blend cell shows a high photon conversion efficiency in the region between 400 nm and 600 nm and reflects the J_{SC} of 8.9 mA/cm^2. The slightly decreased *FF* may be caused by C_{70} which acts as a shallow trap state in a C_{60} layer, caused by the lower LUMO of C_{70}. The charges have to move through an energetically extened distribution of localized hopping sites (C_{60} and C_{70}) which leads to a different transport performance. We conclude that mixing C_{60} with C_{70} is possible and leads to good solar cell performance. Depending on the fullerene ratio the performance shifts either to properties of C_{60}:ZnPc or C_{70}:ZnPc BHJ. Therefore, an expensive isolation procedure of different fullerenes is not required and low cost production is possible.

4.6 Outlook: fullerene C_{84}

Another interesting fullerene for applications in organic small molecule solar cells is C_{84}. In contrast to C_{60} and C_{70} which have no isomers due to the Isolated Pentagon Rule (IPR), 24 isomers are available for C_{84}. The reason for the preferential formation of the IPR-isomers is the maximization of the resonance energy and the minimization of the steric strain. Not all IPR isomers can be found in the soot of the fullerene production. Especially for C_{84} two isomers of symmetry D_2 and D_{2d} mainly appear with an abundance ratio of 2:1. Li et al. [242] studied the electronic structure of a C_{84} film by photoemission measurement and first preliminary calculation. HOMO levels are found to be approximately between -5.6 eV and -5.3 eV and the LUMO levels between -4.0 eV and -4.6 eV. The energy gaps between HOMO and LUMO are 1.35 eV, 0.99 eV, 0.53 eV, 1.03 eV and 1.09 eV for the $D_2(1)$-C_{84}, $D_2(5)$-C_{84}, $D_2(21)$-C_{84}, $D_2(22)$-C_{84}, and $D_{2d}(23)$- C_{84}, respectively. The energy gaps hint to photon absorption in the near infrared (NIR) and infrared (IR) of the solar spectrum and makes the C_{84} highly interesting for transparent solar cell applications. However, some of these isomers may act as trap states due to their different LUMO levels and therefore decrease the device performance. There are methods available to separate the isomeric mixture D_2 and D_{2d} (e.g. using an $Ir(CO)Cl(PPh_3)_2$ complex [243], high performance liquid chromatography (HPLC) [244], and Bingel-retro-Bingel method [245]).

Even broader and extended absorption into the NIR of C_{84} in toluene compared to C_{60} and C_{70} are shown by Cho et al. [246] and for [84]PCBM by Kooistra et al. [247]. Recently, Kooistra et al. [247] implemented a C_{84} derivative [84]PCBM in a solution processed polymer based BHJ organic solar cell. They reached a power conversion efficiency of 0.25 % for the MDMO-PPV:[84]PCBM-containing device. The V_{OC} is around 0.3 V smaller compared to a device composed of [60]PCBM, which gives V_{OC} around 0.8 V. This is attributed to the lower LUMO level of [84]PCBM compared to [60]PCBM. The J_{SC} is around 30 % of the current obtained with the [60]PCBM solar cell.

Based on these results, an investigation of C_{84} in small molecule solar cells concerning transparent solar cells or tandem solar cells applications is highly interesting. Due to financial reasons, it was not possible to do that in this work.

Currently, 10 mg of C_{84} in a purity of 95 % cost 180 $ and are approximately a factor of 8000 more expensive than C_{60} available in a purity of 99 % [241]. At least 200 mg after vacuum gradient sublimation for a suitable and reliable test procedures (e.g. absorption, UPS, BHJ, and FHJ solar cells) are required.

5 Results: Bulk heterojunction solar cells deposited on heated substrates

In this chapter the influence of substrate heating during deposition of fullerene:ZnPc blend layers in BHJ OSC is investigated. We prepared OSC with different substrate temperatures T_{sub}, blend ratios, blend layer thicknesses, and sublayers of the blend. Initial investigations are made using m-i-p structures with 150 nm thick C_{60}:ZnPc blend layers (volume ratio 1:1) to determine the optimum substrate temperature. By reducing BHJ thickness to 60 nm, a better performance is achieved concerning FF and p.c. efficiency. To clarify the origin of these improvements, AFM, SEM, X-ray, TEM, and mobility measurements are performed. Similar investigations are made for the p-i-i solar cells which are interesting for tandem solar cell applications [28]. Furthermore, when exchanging C_{60} with C_{70} in the heated blend layer of the organic solar cells, a different morphological behavior is observed.

5.1 150 nm thick C_{60}:ZnPc blend layers in m-i-p bulk heterojunctions

In 2004 Suemori et al. [248] showed the influence of substrate heating during co-deposition of C_{60} and phthalocyanine on the performance of organic solar cells.
In 2008 Sakai et al. [249] performed substrate heated organic solar cells with blend layers up to 1200 nm with photocurrents of 18.3 mA/cm^2 and a p.c. efficiency of 5.3 %. To find a correlation between substrate temperature T_{sub} and OSC performance of thick blend layers of 150 nm, T_{sub} is varied during evaporation of the C_{60}:ZnPc blend from 80 °C to 130 °C in steps of 10 K and compared to a solar cell without substrate heating. The following m-i-p OSC stack is used:
ITO/C_{60}(5 nm)/C_{60}:ZnPc(150 nm,1:1)/PV-TPD(5 nm)/p-PV-TPD(20 nm;3.2 wt%) /p-ZnPc(10 nm;4.4 wt%)/Au(40 nm).

The reduction of illumination due to the additional ITO glass substrate, used here as resistive substrate heater, with an average transmission of 85 % [211] in the spectral range of 350–900 nm is taken into account for photocurrent correction as shown in section 3.2.3.1. Detailed dependencies of the main OSC characteristics J_{SC}, *FF*, J(-1V)/J_{SC}, and p.c. efficiency on T_{sub} are shown in Fig. 5.1. Corresponding *J(V)* parameters of the devices are summarized in table 5.1. Generally, the low *FF* hints at exciton recombination within the solar cell, especially for bad charge percolation in a blend layer. It is observed that heating leads to improved lower saturation J(-1V)/J_{SC}, which changes from 1.6 at RT to < 1.3 for $T_{sub} > 90\,°C$. This indicates a better charge carrier separation and a better transport to the electrodes. At the same time, the dark currents in the forward bias indicate lower series resistances for higher T_{sub}. While *FF* and saturation are positively influenced by heating, the most decisive improvement that ultimately leads to the increased efficiency is in J_{SC}. Starting with 8.1 mA/cm^2 at RT, the J_{SC} reaches a maximum at $T_{sub} = 110°C$ of $J_{SC} = 12.3$ mA/cm^2 before dropping to values around 11 mA/cm^2 for higher substrate temperatures. Combined with the higher *FF*, this increase in J_{SC} of about 50 % leads to an increase in p.c. efficiency of > 60 %. To examine if the absorption is improved upon heating, e.g. by changing ZnPc phase [250] or molecule arrangement, absorption measurements on quartz glass of C_{60}(5 nm)/C_{60}:ZnPc(20 nm,1:1) processed at T_{sub} = RT and 110 °C are carried out. However, a significant increase in absorption of the heated layer compared to

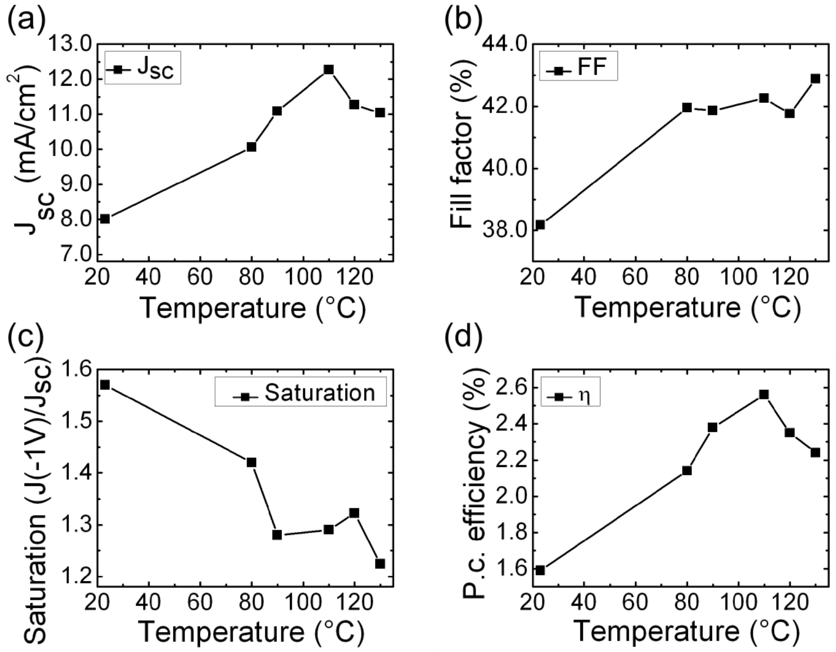

Figure 5.1: *(a) J_{SC}; (b) FF; (c) saturation J(-1V)/J_{SC}, and (d) p.c. efficiency (η) vs. temperature. J_{SC} is normalized to 100 mW/cm^2 with respect to the Si reference diode. Lines are guide to the eye.*

Table 5.1: *J(V) characteristics of the 150 nm thick blend layer BHJ deposited on heated substrates at different substrate temperatures (T_{sub}) 80-130° C and room temperature (RT). All J_{SC} are normalized to 100 mW/cm^2 with respect to the Si reference diode, mismatch is not taken into account.*

T_{sub}	V_{OC} (V)	J_{SC} (mA/cm^2)	*FF* (%)	J(-1V)/J_{SC}	p.c. eff. (%)
RT	0.51	8.1	38	1.57	1.6
80°C	0.51	10.1	42	1.42	2.1
90°C	0.51	11.1	42	1.29	2.4
110°C	**0.49**	**12.3**	**42**	**1.29**	**2.6**
120°C	0.50	11.3	42	1.32	2.4
130°C	0.47	11.0	43	1.22	2.2

the unheated is not observed in Fig. 5.2, which might explain the enhancement of J_{SC} in the OSC. The slight change in absorption in particular for the ZnPc peak around 625 nm is negligible concerning the large enhancement of J_{SC}, but discussed in more detail concerning blend layer morphology in section 5.2.2. Therefore, the improved J_{SC} and *FF* can clearly be attributed to a change in the BHJ layer morphology and not to an improved thin layer absorption. Substrate heating increases the thermal energy of molecules evaporated onto the substrate, which can then diffuse over a larger

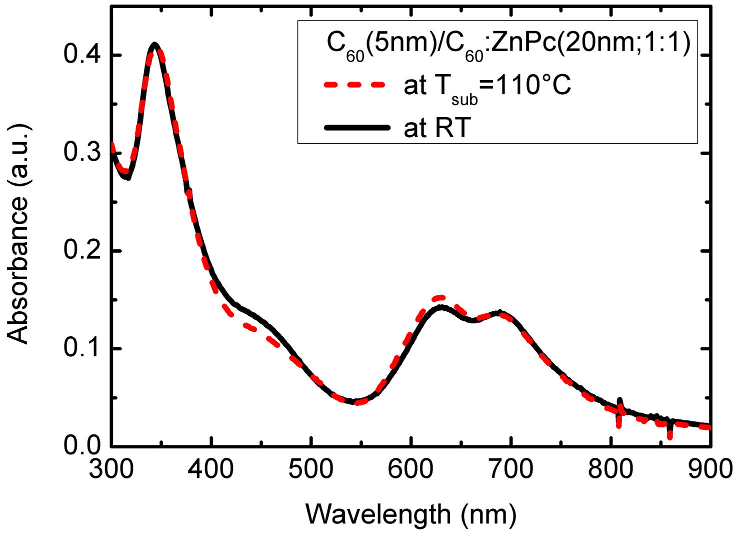

Figure 5.2: *Absorption measurement of C_{60} (5 nm)/C_{60}:ZnPc(20 nm, 1:1) on quartz glass processed at room temperature (RT) (solid line) and $T_{sub} = 110°$ C (dashed line). No significant enhancement in absorption of the heated layer compared to the unheated is observed, which might explain the enhanced J_{SC} of the heated OSC.*

area before adsorption. It is estimated that the interaction energies between nearest neighbors are 0.87 eV (CuPc–CuPc) [251], 1.5 eV (C_{60}–C_{60}) [185, 252], and 0.44 eV (CuPc–C_{60}) [253], respectively. Due to the similarity of CuPc and ZnPc in terms of molecular structure, optical properties, and energy levels, comparable properties are assumed for ZnPc. These high energies suggest a preferential aggregation of like molecules. Given sufficient thermal energy for diffusion, the formation of interconnected ZnPc and C_{60} networks can occur. This network would allow for easier extraction of charge carriers generated from dissociated excitons and leads to less charge recombination in the BHJ, increasing J_{SC}, FF, and R_{p}. There exists an optimum temperature, in the current case of 110 °C, for maximum solar cell efficiency. For higher substrate temperatures, J_{SC} decreases. This might be explained by formation of too large clusters and therefore reduced charge carrier-separating interfaces. At the same time, the transport properties are yet further improved due to better developed percolation paths, which is indicated by lower saturation and higher FF. Thus, for the substrate temperature of 110 °C an optimum between charge carrier separation and charge transport is found for the blend layer C_{60}:ZnPc with ratio 1:1.

5.2 60 nm thick C_{60}:ZnPc blend layers in m-i-p bulk heterojunctions

Here, we use a 60 nm instead of 150 nm C_{60}:ZnPc blend layer due to a more distinct heating effect and better processability (e.g. shorter evaporation time). This difference can be attributed to fewer recombination losses due to shorter transport paths in the bulk to the adjacent charge transport layers. The probability to form percolation paths without dead ends is higher for thinner blend layers. Furthermore, series resistance and charge carrier mobilities have to be considered as limiting parameters. This means that for thicker blend layers, the probability for charge carrier recombination is increased even if perfect percolation paths are formed. Therefore, the solar cell performance is further improved with respect to FF and saturation $S=(J(\text{-1V})/J_{\mathrm{SC}})$. The following OSC stack is used:
ITO/C_{60}(5 nm)/C_{60}:ZnPc(60 nm,1:1)/PV-TPD(5 nm)/p-PV-TPD(20 nm;3.2 wt%) /p-ZnPc(10 nm;4.4 wt%)/Au(40 nm).
$J(V)$ curves under simulated sunlight are shown in Fig. 5.3 and in the dark (inset of Fig. 5.3) for samples processed at $T_{\mathrm{sub}} = \mathrm{RT}$, 110 °C, and 150 °C. The characteristics of the complete devices are summarized in table 5.2. J_{SC} is corrected due to the transmission loss by the additionally used ITO substrate as resistive heater [211]. Generally, a low FF hints at charge carrier recombination in the photoactive blend layer within the solar cell or at interfaces with extraction barriers [222], unbalanced charge carrier mobilities [160], disturbed transport paths, and trap states in the blend layer [254]. It is observed that heating leads to an improved saturation S and series resistance. The saturation changes from 1.3 at room temperature to 1.1 for 110 °C substrate temperature. The better saturation suggests a better charge carrier separation and transport in the blend layer to the respective electrode. For the heated blend layer, the charge carriers can be more easily extracted out of the blend layer before they recombine. In case of the unheated blend layer, a higher electric field in backward direction is required to extract the photo generated charge carriers due to poor transport paths

Table 5.2: *Solar cell parameters (J_{SC}, V_{OC}, FF, $(J(\text{-1V})/J_{\mathrm{SC}})$, and η) for substrate temperatures $T_{\mathrm{sub}} = RT$, 110 °C, and 150 °C. J_{SC} is normalized to 100 mW/cm^2 with respect to a calibrated Si reference diode.*

T_{sub}	V_{OC} (V)	J_{SC} (mA/cm^2)	FF (%)	$J(\text{-1V})/J_{\mathrm{SC}}$	η (%)
RT	0.53	7.2	36	1.29	1.4
110 °C	0.52	10.3	57	1.09	3.0
150 °C	0.11	4.6	18	18.9	0.1

or to dissociate the excitons. While at 0 V the difference of J_{SC} between heated and unheated solar cells is 41 %, at -1.5 V. The photocurrent differs only by 15 %. Since only the blend layer is deposited during substrate heating, no influence of heating on other layers, or changes in energy level alignment are expected.

Thus, the improved series resistance of $7.8\,\Omega\,\mathrm{cm}^2$ compared to $28.9\,\Omega\,\mathrm{cm}^2$ is an additional indication for a better charge transport through the blend layer in forward bias. The series resistance is obtained using the one diode equation [255] and fitting of the *J(V)* characteristics of the illuminated solar cell for $V > V_{\mathrm{OC}}$. V_{OC} is comparable for both devices. Saturation factors are positively influenced by substrate heating during deposition, while the most decisive improvements which ultimately lead to the increased η are in the *FF* and J_{SC}.

Values of $FF = 36\,\%$ and $J_{\mathrm{SC}} = 7.2\,\mathrm{mA/cm^2}$ for the device processed at RT are achieved, whereas *FF* of 57 % and J_{SC} of $10.3\,\mathrm{mA/cm^2}$ are measured for $T_{\mathrm{sub}} = 110\,°\mathrm{C}$. Both improvements in *FF* of over 55 % and J_{SC} of over 43 % lead to an increase of η by a factor of two. For the sample processed at $T_{\mathrm{sub}} = 150\,°\mathrm{C}$, no further improvement is obtained.

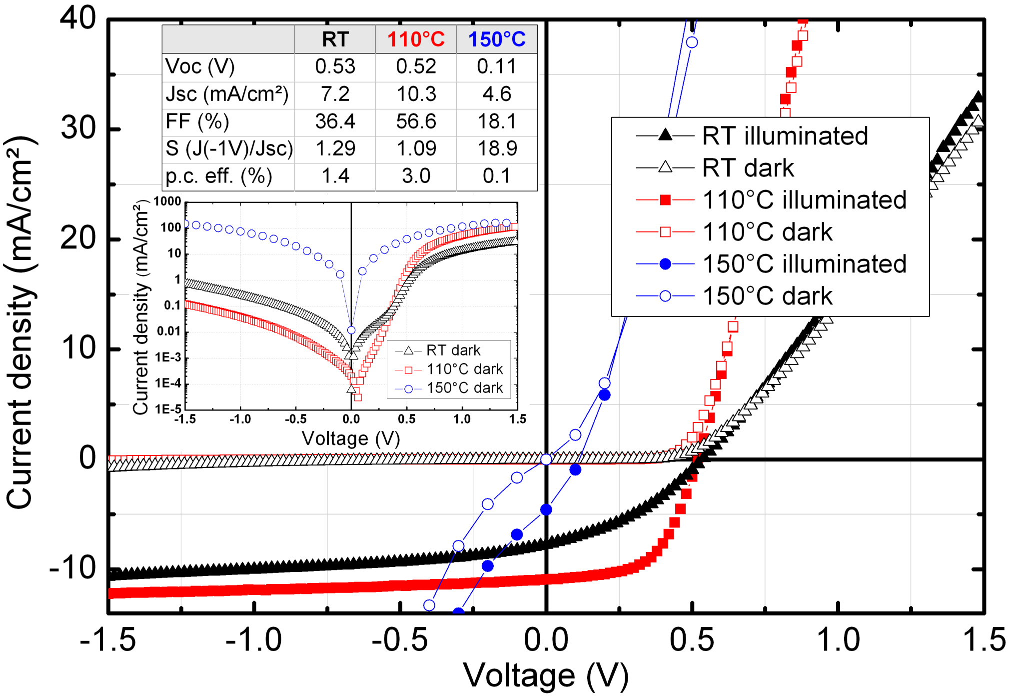

	RT	110°C	150°C
Voc (V)	0.53	0.52	0.11
Jsc (mA/cm²)	7.2	10.3	4.6
FF (%)	36.4	56.6	18.1
S (J(-1V)/Jsc)	1.29	1.09	18.9
p.c. eff. (%)	1.4	3.0	0.1

Figure 5.3: *J(V) characteristics of 60 nm thick* C_{60}*:ZnPc blend layer BHJ solar cells. Blend layers are deposited at RT (filled triangles),* $T_{sub} = 110°C$ *(filled squares), and 150°C (filled circles). Inset: semi-log plot of the dark J(V) curves.* J_{SC} *is normalized to 100 mW/cm² with respect to a Si reference diode.*

Quite the opposite, the *J(V)* characteristic is very bad with low V_{OC}, J_{SC}, *FF*, and high saturation. These values indicate partial shortcuts from the blend to the Au electrode, probably caused by a too rough blend layer (C_{60} directly in contact with the Au electrode). This could be solved by using a thicker hole transport layer to cover the spikes from the blend layer. However, a thicker hole transport layer would change the optical field distribution and requires a further optimization concerning HTL thickness and T_{sub}.

5.2.1 AFM and SEM measurements

To check for preferential aggregation, the morphology of the bulk layers is investigated by AFM and SEM. For AFM and SEM[1] investigations, the following stack is used: C_{60}(5 nm)/C_{60}:ZnPc(30 nm; volume ratio 1:1) which is similar to the first layers of the solar cell. The C_{60} layer is deposited at RT, followed by the second layer deposited at RT, $T_{\mathrm{sub}} = 110\,°\mathrm{C}$, or 150 °C on ITO, respectively. Results are shown in Fig. 5.4 a), b), and c). While the unheated device forms a smooth amorphous surface with peak heights of 4 nm and a root mean square (RMS) roughness of 0.5 nm, the heated devices for $T_{\mathrm{sub}} = 110\,°\mathrm{C}$ and 150 °C show rough surfaces with peak heights of 37 nm and 48 nm and RMS roughness of 6.4 nm and 6.7 nm, respectively. Here, the measured peak height of the 150 °C sample confirms the predication of partial shortcuts of the solar cell processed at $T_{\mathrm{sub}} = 150\,°\mathrm{C}$.

Island and cluster-like growth can also clearly be seen in the SEM pictures in Fig. 5.4 e) and f) for the heated layer, while for the unheated layer in Fig. 5.4 d) no such features are observed. Clusters on the heated samples have diameters in the range of 20 nm. Bright spots correspond to high peaks on the surface.

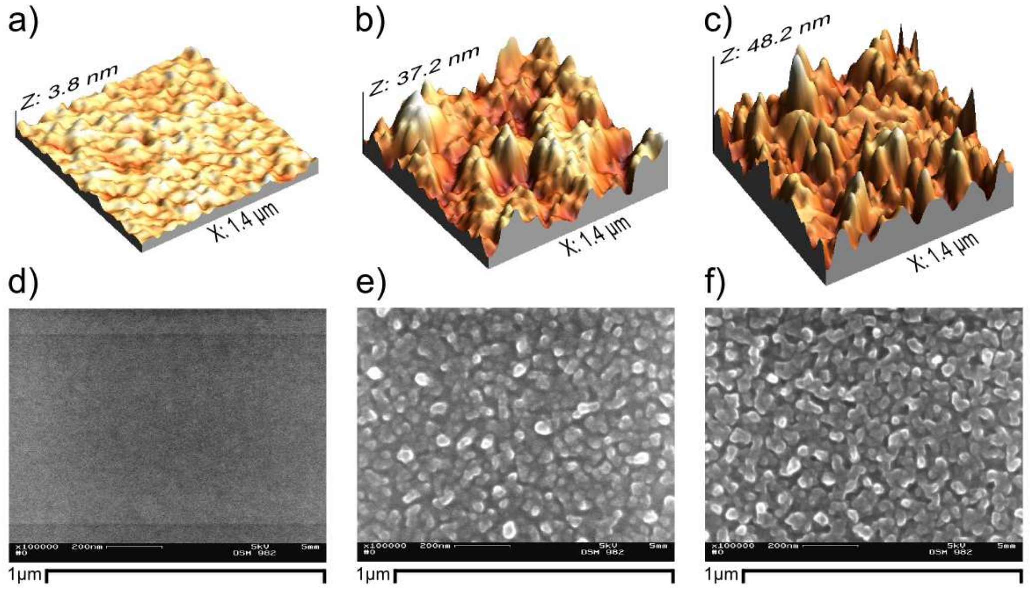

Figure 5.4: *AFM (a, b, c) and SEM (d, e, f) measurements of the first layer of the solar cell stack ITO/C_{60}(5 nm)/C_{60}:ZnPc(30 nm, 1:1): a) unheated blend layer with RMS roughness of 0.5 nm; b) blend layer deposited at $T_{sub} = 110°C$ with RMS roughness of 6.4 nm; c) blend layer deposited at $T_{sub} = 150°C$ with RMS roughness of 6.7 nm; d) unheated blend layer, smooth surface is formed; e) blend layer deposited at $T_{sub} = 110°C$; f) blend layer deposited at $T_{sub} = 150°C$, aggregation and cluster-like growth is observed.*

---

[1] measured by Ellen Kern, physical chemistry of TU Dresden

5.2.2 Absorption measurements

Maennig and co-workers [113] showed absorption measurements (Fig. 5.5 a)) of ZnPc prepared at different substrate temperatures: the RT sample was prepared while the substrate was held at 25 °C. The low temperature (LT) sample was prepared while the substrate was cooled to -150 °C. They obtained for the RT sample discrete diffraction spots using transmission electron microscopy due to the polycrystalline morphology of the phthalocyanine. For the LT sample no such features were observed, which hints at a stable amorphous phase.

From the absorption measurements shown in Fig. 5.5 a), it was concluded that in the solid state, the electronic excitation of ZnPc splits up into two parts because of the molecular interactions [256]. The peak positions of ZnPc were at 625 nm and 710 nm for the RT sample and at 635 nm and 688 nm for the LT sample. The peak separation was smaller for the amorphous than for the polycrystalline sample. This is a strong hint towards a lower interaction of the molecules of the LT sample, which fits well with the lower degree of order.

To check whether polycrystalline domains of ZnPc in the heated blend layers are present in our devices, absorption measurements are carried out for samples consisting of C_{60}(5 nm)/C_{60}:ZnPc(20 nm) made at RT, $T_{\mathrm{sub}} = 110$ °C, and 150 °C on quartz glass and depicted in Fig. 5.5 b). The peak positions of the RT sample are at 631 and 688 nm and indicate amorphous growth, as reported by Maennig et al. [113]. We conclude that the polycrystalline growth of ZnPc is suppressed in the unheated C_{60}:ZnPc blend layer. A peak shift, which might have indicated polycrystalline domains in the heated blend

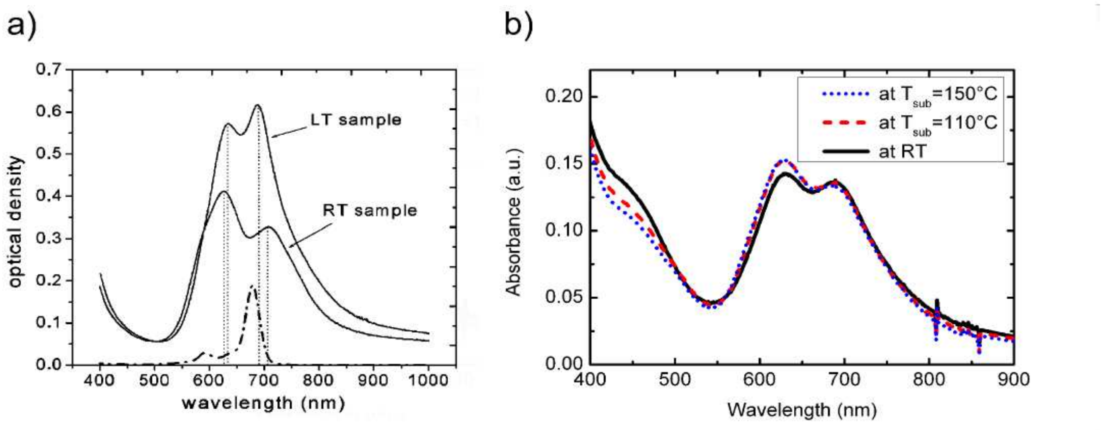

Figure 5.5: *Absorption spectra of a) ZnPc layers (50 nm thick) with permission taken from [113]: The RT sample was prepared at 25° C substrate temperature and the low temperature (LT) sample at -150° C substrate temperature. The dotted line shows schematically the absorption of ZnPc dissolved in 1-chloronaphthaline; b)* C_{60}*(5 nm)/*C_{60}*:ZnPc(20 nm; volume ratio 1:1) made at RT (solid line),* $T_{\mathrm{sub}} = 110°C$ *(dashed line), and* $T_{sub} = 150°C$ *(dotted line).*

layers, is not observed.

Another feature is the peak ratio dependency of ZnPc for amorphous and polycrystalline layer. In Fig. 5.5 a) it can be seen that for the amorphous layer (LT sample) the first peak is smaller than the second one and vice versa for the polycrystalline layer (RT sample) [113].

Such a peak ratio shift is also observed in Fig. 5.5 b) for the blend layer. For the sample at RT, both peaks have almost the same height, while for the heated samples, the first peaks are increased compared to the second peaks. This suggests at least a certain amount of polycrystalline domains of ZnPc in the heated blend layers.

5.2.3 X-Ray (WAXRD)

To find out if the clusters observed by AFM and SEM and the small change in absorption that can be attributed to nanocrystalline and polycrystalline structures, wide angle X-ray diffraction (WAXRD) measurements are performed[2]. A layer sequence of C_{60}(5 nm)/C_{60}:ZnPc(50 nm, 1:1) is deposited on silicon at ambient conditions, $T_{\mathrm{sub}} = 100\,^{\circ}\mathrm{C}$, or $T_{\mathrm{sub}} = 150\,^{\circ}\mathrm{C}$. Silicon substrates are used to avoid amorphous features in the XRD measurements caused by standard glass substrate which would prevent an accurate peak determination. To check whether similar cluster formations occur when using a silicon substrates instead of ITO, additional SEM measurements of these samples are carried out[3] and show similar aggregation and cluster assembly as shown in Fig. 5.6. Differences in surface morphology might be caused by the thicker blend layer of the silicon substrate sample.

Measuring over diffraction angle diapazon of 2θ (2-28 °), no characteristic WAXRD reflections indicating nanocrystalline growth of ZnPc and C_{60} in the blend layers are observed in Fig. 5.7. Additionally, pristine 25 nm thick C_{60} and ZnPc layers deposited on heated silicon substrate ($T_{\mathrm{sub}} = 90\,^{\circ}\mathrm{C}$) are investigated by WAXRD. In contrast to the heated C_{60}:ZnPc blend layers, nanocrystalline growth is observed, in heated pristine ZnPc indicated by a set of WAXRD reflections. For C_{60} only a very weak reflection is seen and shown in Fig. 5.7. However, for the $T_{\mathrm{sub}} = 150\,^{\circ}\mathrm{C}$ sample a broader peak at the Bragg-angle of (2 0 0) ZnPc occurs, which might hint on crystalline growth. Due to the appearance of the instrumental peak at the same position it is not possible to draw a clear conclusion. Probably, the nanocrystalline growth of ZnPc in the blend is reduced resulting in a material that is at least X-ray amorphous. According to the

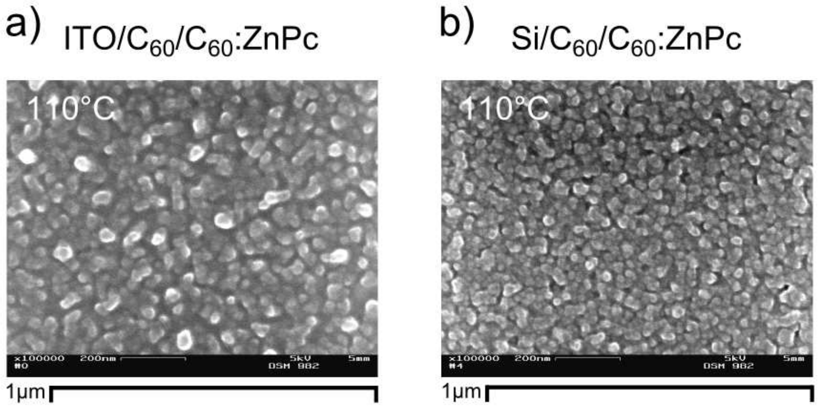

Figure 5.6: *Comparison of SEM measurements of a) ITO/C_{60}(5 nm)/C_{60}:ZnPc(30 nm, 1:1) stack deposited at $T_{sub} = 110°C$ and b) silicon/C_{60}(5 nm)/C_{60}:ZnPc(50 nm, 1:1) stack deposited at $T_{sub} = 100°C$.*

---

[2] measured by Christoph Schünemann and Alexandr A. Levin, IAPP, TU Dresden

[3] measured by Ellen Kern, physical chemistry of TU Dresden

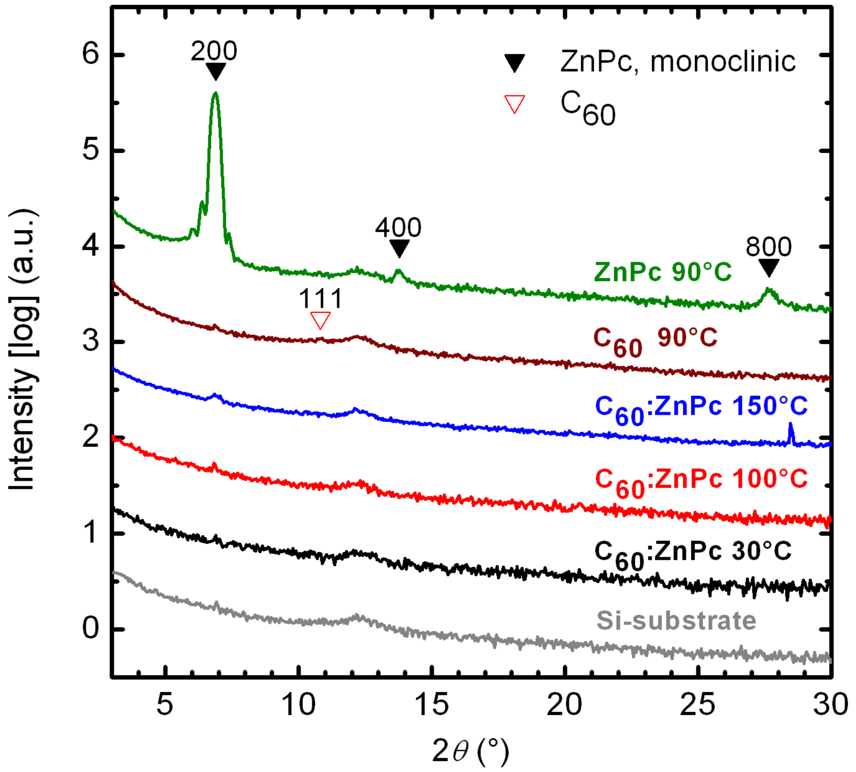

Figure 5.7: *WAXRD patterns of silicon/*C_{60}*(5 nm)/*C_{60}*:ZnPc(50 nm, 1:1) samples of unheated* $T_{sub} = 30\,°C$ *(black), heated* $T_{sub} = 100\,°C$ *(red) and* $T_{sub} = 150\,°C$ *(blue) blend layer, heated* $T_{sub} = 90\,°C$ *25 nm thick pristine* C_{60} *(brown), and ZnPc (green) layers deposited at silicon substrate (gray). For comparison WAXRD pattern of Si substrate is shown at bottom. The thickness fringes for ZnPc (2 0 0) reflection at Bragg angles* $2\theta = 6.02°$, $6.38°$, $6.89°$, *and* $7.42°$ *appear due to diffraction at thin layer, and are resolved in the reflection profile. The Miller indices of the observed ZnPc reflections are indicated accordingly to possible monoclinic* α*-polymorphs. The Miller indices of the* C_{60} *phase are indicated for cubic (space group* $Fm\bar{3}m$*) structure modelß, [257]. For better visualization the WAXRD patterns are shifted vertically.*

Crystal Structure Database (CSD) [219], the reflections detected for the thin ZnPc film can be attributed to modifications, which are isomorphous with triclinic (space group $P\bar{1}$) [258] and monoclinic α-polymorphs (space group $C2/n$) of CuPc [259]. CuPc and ZnPc are characterized by similar molecular structures, molecular weight, and atomic radii of metal elements, Zn and Cu. The observed reflection positions of heated ZnPc, $2\theta = 6.89\,°$, $13.76\,°$ and $27.66\,°$ correspond, to the reflections 100 (theoretical $2\theta = 6.86\,°$), 200 ($13.73\,°$), and 400 ($27.67\,°$) of the triclinic modification, or to the reflections 200 ($6.73\,°$), 400 ($13.45\,°$), and 800 ($27.15\,°$) of the monoclinic phase.

Note that in both cases, the ZnPc film exhibits a preferred orientation along the [100] crystallographic direction of the corresponding crystalline lattice.

5.2.4 TEM

The methods used before show indications for molecular phase separation and nanocrystalline growth of ZnPc in the blend. To further investigate the blend layer morphology, TEM measurements are performed[4]. The following layer sequence is deposited on a carbon coated nickel grid, C_{60}(5 nm)/C_{60}:ZnPc(30 nm, 1:1). The mixed layer is deposited at different substrate temperatures of RT, $T_{\mathrm{sub}} = 110\,^{\circ}\mathrm{C}$, or 150 °C. The TEM results are shown in Fig. 5.8 with magnifications of 15,000, 43,000, and 195,000. For the sample made at RT, depicted in Fig. 5.8 a), d), and g) only a homogeneous gray area is observed. It indicates amorphous layer growth, which is confirmed by the Fourier transformation as shown in Fig. 5.8 h), where a pattern with a halo ring typical for amorphous growth can be seen.

In the TEM images of the $T_{\mathrm{sub}} = 110\,^{\circ}\mathrm{C}$ sample shown in Fig. 5.8 b), e), and i) and the $T_{\mathrm{sub}} = 150\,^{\circ}\mathrm{C}$ sample, shown in Fig. 5.8 c), f), and j) bright and dark regions are observed. The dark regions can be related to thicker layers or molecules with a higher scattering factor, caused by e.g. Zn with a higher atomic number of $Z = 30$ compared to $Z = 6$ for C. It means that molecular phase separation occurs due to heating, and a rougher surface is formed, which was already observed in the AFM measurements.

The dark regions are framed by a circle and the bright regions by a rectangle in Fig. 5.8. Polycrystalline structures within the circle in Fig. 5.8 i) are observed for the 110 °C sample, which is not the case for the bright region (rectangle). The region of the circle in Fig. 5.8 i) is enlarged and shown in Fig. 5.8 k). Large polycrystalline domains with lateral diameters of 50 nm are obtained, in which the lateral nanocrystal sizes are in the range of 10 nm. A Fourier transform of this region is shown in Fig. 5.8 m) and exhibits a mixture of polycrystalline (diffraction spots) and amorphous (halo ring) domains. In case of the 150 °C sample even larger crystalline domains of lateral dimensions of > 60 nm are detected in the dark regions of Fig. 5.8 j). The Fourier transformation of the nanocrystalline region depicted in Fig. 5.8 l) is shown in picture n) and shows clear diffraction spots. This means that due to higher supplied thermal energy, the molecular phase separation is more pronounced, and larger nanocrystals are formed. In the bright regions no lattice planes are observed, which would hint at crystalline growth.

15 images are taken with a magnification of 195,000 at different sample positions of the 110 °C and 150 °C sample, respectively, and evaluated using Fourier transformation to investigate the polycrystalline structure with respect to its composition, either to ZnPc or C_{60} and exhibits similar appearance of lattice planes.

The same data from the CSD [219] is used for structure determination, which had already been utilized for the WAXRD measurements.

---

[4] supported by Christine Mickel, Leibniz Institute for Solid State and Materials Research Dresden (IFW)

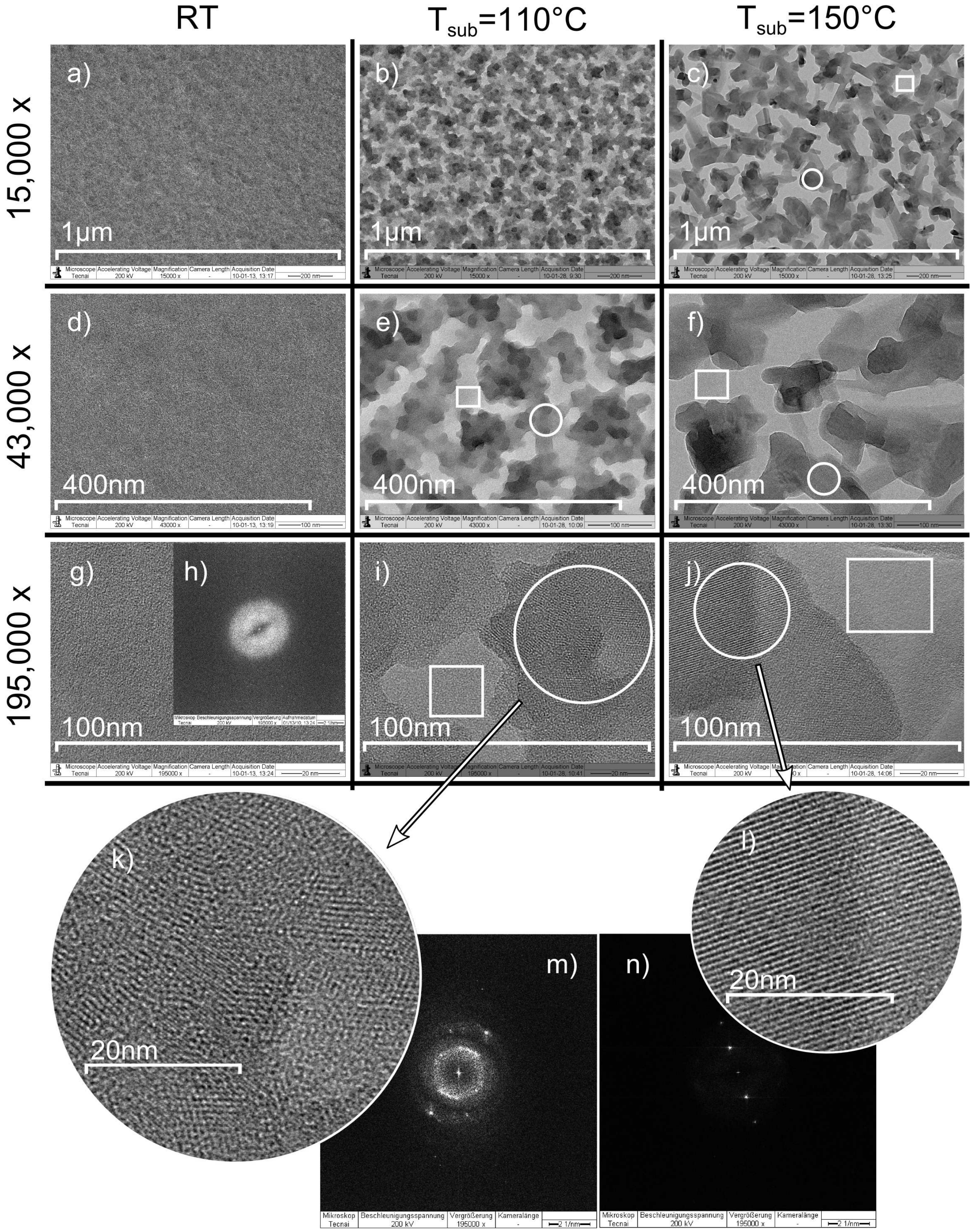

Figure 5.8: *TEM measurements of C_{60}(5 nm)/C_{60}:ZnPc(30 nm,1:1) samples deposited on a carbon coated nickel grid at RT, T_{sub} = 110° C, and 150° C. Measurements with magnifications of 15,000, 43,000, and 195,000, are shown, respectively.*

The correlation between theoretical lattice plane spacing d_{hkl} from CSD and the theoretical lattice planes of ZnPc and C_{60} are summarized in table 5.3. For both heated samples, only very few crystals can be attributed to C_{60} (1 1 1) atomic planes. Some of the observed lattice plane spacings d_{hkl} are around 8.0 Å and can not clearly be attributed to C_{60} ($d_{\mathrm{hkl}} = 8.175$ Å) or ZnPc (7.882 Å). However, the majority of the reflections is attributed to monoclinic ZnPc [259] and consist of 003, 403, and 005 reflections. Usually they are forbidden for space group $C2/n$ due to extinction laws. Evidently, the appearance of the forbidden reflections is related to strong dynamic interaction between the electron beam and crystalline lattice [260] and faulting in the stacking [261] of the monoclinic ZnPc in the thin blend layers. Aside from weak intensities of the forbidden reflections, the small scattering volume of the crystalline ZnPc prevents the observation of ZnPc reflections in the WAXRD measurements.

Table 5.3: *Correlation between the theoretical lattice spacing (d_{hkl}) from CSD and lattice planes (h k l) for monoclinic ZnPc [259] and C_{60} [257]. Measured d_{hkl} are sorted and related to the theoretical lattice planes.*

	lattice plane spacing (d_{hkl}) (Å)	lattice plane (h k l)
ZnPc monoclinic, space group $C2/n$	7.88	(0 0 3)[5]
	4.87	(4 0 3)[5]
	4.73	(0 0 5)[5]
C_{60}, space group $Fm\bar{3}m$	8.19	(1 1 1)

---

[5] forbidden reflections (lattice planes) according to extinction law

5.2.5 OFET

To check whether the mobilities of C_{60} and ZnPc are positively influenced by the formation of polycrystals due to substrate heating, OFET measurements in the saturation regime of unheated and heated blend layers are carried out[6]. Using the OFET method, where the sublayer of silicon oxide is the same for all devices, a reliable comparison of the mobilities of different samples is possible. A similar aggregation of heated C_{60}:ZnPc on silicon oxide compared to C_{60} is observed by SEM as shown in Fig. 5.9.

All measured mobilities by OFET are summarized in table 5.4. The hole mobility

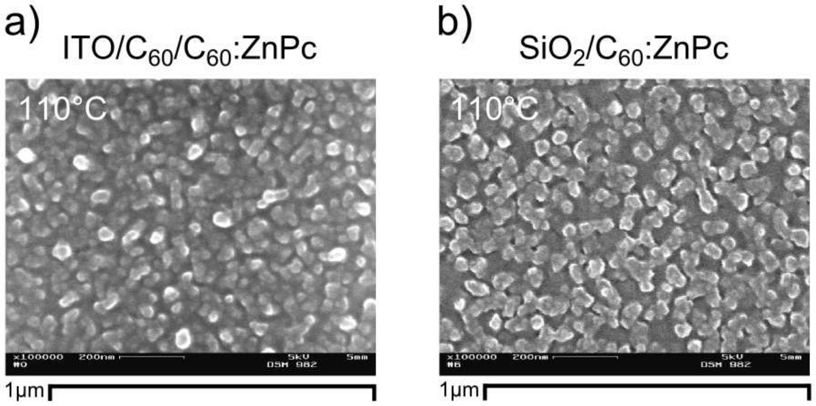

Figure 5.9: *Comparison of SEM measurements of a) ITO/C_{60}(5 nm)/C_{60}:ZnPc(30 nm,1:1) stack deposited at $T_{sub} = 110°C$ and b) SiO_2/C_{60}:ZnPc(30 nm, 1:1) stack deposited at $T_{sub} = 110°C$ as used for OFETs. Both show similar molecule aggregation and cluster formation.*

μ_h of neat ZnPc of $6.5\times10^{-4}\,cm^2/Vs$ is decreased in a blend layer with C_{60} (volume ratio 1:1) to $5.1\times10^{-5}\,cm^2/Vs$. This might be attributed to a smaller overlap of the π-orbitals of ZnPc due to a higher disorder in the blend [72] and to the reduction of the effective channel width by a factor around two upon mixing. Similar observations are made for the electron mobility μ_e of C_{60}. For the neat layer, $\mu_e = 9.2\times10^{-3}\,cm^2/Vs$ and for the blend layer, $\mu_e = 5.2\times10^{-3}\,cm^2/Vs$ is measured.

The neat layer of ZnPc deposited during substrate heating shows a μ_h which is one order of magnitude higher compared to the layer deposited at RT. The better charge transport is attributed to a better molecule arrangement and formation of crystalline ZnPc. The heated blend layers show a clear tendency to higher μ_h of ZnPc. Values of $2.2\times10^{-4}\,cm^2/Vs$ and $1.8\times10^{-4}\,cm^2/Vs$ are achieved due to the polycrystalline growth of ZnPc. In case of C_{60}, no improvement of μ_e is determined for the heated samples compared to the unheated, values are on the order of $5.0\times10^{-3}\,cm^2/Vs$.

This fits to the observations in TEM that no or only very few C_{60} crystals are formed, which would lead to an improvement of the mobility. Furthermore, the decreased

---

[6] Jens Jankowski and Moritz P. Hein, IAPP, TU Dresden

difference between μ_h for ZnPc and μ_e for C_{60} might positively influence the charge carrier balance [160] within the blend layer and leads to less charge carrier recombination and therefore to a higher *FF*. Not only the formation of percolation paths caused by molecular phase separation, but also the increased mobility lead to the improved performance of heated solar cells.

Table 5.4: *Summarized μ_h and μ_e mobilities of neat and blend layers composed of C_{60} and ZnPc deposited at RT, 110° C, and 150° C.*

	neat layer		**blend layer volume 1:1**		
T_sub	**RT**	**110 °C**	**RT**	**110 °C**	**150 °C**
μ_h (cm^2/Vs) of ZnPc	6.5×10^{-4}	5.5×10^{-3}	5.1×10^{-5}	2.2×10^{-4}	1.8×10^{-4}
μ_e (cm^2/Vs) of C_{60}	9.2×10^{-3}	—	5.2×10^{-3}	5.0×10^{-3}	5.1×10^{-3}

5.2.6 C_{70}:ZnPc m-i-p bulk-heterojunctions

In chapter 4 we have shown that C_{70} used as acceptor molecule in solar cells leads to improved J_{SC} compared to C_{60}. In this chapter we have shown that substrate heating during evaporation of the photoactive blend layer of C_{60}:ZnPc has a decisive effect on the device performance. Thus, we investigate if substrate heating can be used to further improve the performance of solar cells with C_{70} as acceptor. The same solar cell stack and $T_{sub} = 110\,°C$ as for the C_{60} m-i-p is used:
ITO/C_{60}(5 nm)/C_{70}:ZnPc(60 nm, 1:1)/PV-TPD(5 nm)/p-PV-TPD(20 nm;3.2 wt%) /p-ZnPc(10 nm;4.4 wt%)/Au(40 nm).
In Fig. 5.10 the $J(V)$ curves under simulated sunlight and in dark (inset Fig. 5.10) are shown for samples processed at RT and $T_{sub} = 110\,°C$. The characteristics of the complete devices are summarized in table 5.5. J_{SC} is again corrected for the transmission loss by the additionally used ITO substrate as resistive heater [211]. From the *J(V)* characteristics, only a marginal improvement for the heated sample can be determined. The increased J_{SC} from 9.4 to 10.1 mA/cm^2, the increased *FF* from 40 to 43 %, and decreased saturation from 1.43 to 1.24 hint on one hand to improved transport properties. On the other hand, it looks like the heating effect is not as distinct

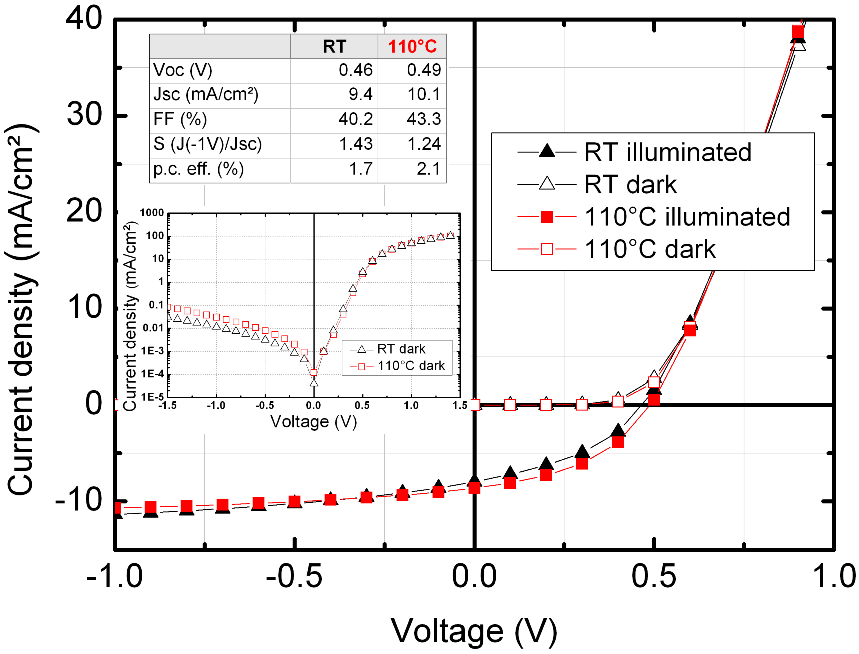

	RT	110°C
Voc (V)	0.46	0.49
Jsc (mA/cm²)	9.4	10.1
FF (%)	40.2	43.3
S (J(-1V)/Jsc)	1.43	1.24
p.c. eff. (%)	1.7	2.1

Figure 5.10: *J(V) characteristics of 60 nm thick C_{70}:ZnPc blend layer BHJ solar cells. Blend layers are deposited at RT (filled triangle) and $T_{sub} = 110°C$ (filled squares). Inset: semi-log plot of the dark J(V) curves. J_{SC} is normalized to 100 mW/cm^2 with respect to a Si reference diode.*

Table 5.5: *Solar cell parameters (J_{SC}, V_{OC}, FF, $(J(\text{-}1V)/J_{SC})$, and η) for substrate temperatures T_{sub} = RT and 110° C. J_{SC} is normalized to 100 mW/cm^2 with respect to calibrated Si reference diode.*

T_{sub}	V_{OC} (V)	J_{SC} (mA/cm^2)	*FF* (%)	J(-1V)/J_{SC}	η (%)
RT	0.46	9.4	40	1.43	1.7
110°C	0.49	10.1	43	1.24	2.1

as for the C_{60} m-i-p. To check how the morphology of the C_{70}:ZnPc layer is influenced by substrate heating SEM and TEM measurements are carried out. A layer sequence of ITO/C_{60}(5 nm)/C_{70}:ZnPc(30 nm,1:1,110°C) is used for the SEM measurement[7] and shown in Fig. 5.11c). Compared to the C_{60}:ZnPc blend shown in Fig. 5.11b) no dark and bright features are visible which would indicate a morphological modification and molecular aggregation. Only a smooth surface indicated by the homogeneous gray area is formed.

The TEM measurement shown in Fig. 5.11d) exhibits single cluster formation for blend C_{70}:ZnPc deposited during substrate heating on C_{60}. The phase analysis of C_{70} is performed using the Powder Diffraction File (PDF) [262] and Inorganic Crystal Structure Database (ICSD) [263]. The interplane distances are calculated by program PowderCell 2.3 [264].

While in Fig. 5.11b) of the C_{60}:ZnPc sample, a clear molecular phase separation occurs, only single clusters are formed for C_{70}:ZnPc. The clusters have lateral diameters between 50-100 nm as visible in Fig. 5.11e). About 50 % of the clusters observed for e.g Fig. 5.11f) are polycrystalline domains and can not decisively be attributed to monoclinic ZnPc [259] or C_{70} [265]. Many more lattice formations of C_{70} are possible than for C_{60}. For this reason C_{70} and ZnPc have lattice spacings which are similar and thus it is not possible to distinguish between both and draw a clear conclusion. In the bright regions no crystal formations are detected. However, the poor cluster formation might be due to the different shape of C_{70} compared to C_{60}. The C_{70} molecule seems not to be as mobile on the surface as C_{60}. Applying a higher thermal energy to the substrate one might be able to increase the molecular aggregation and phase separation [266]. Furthermore, probable different interaction energies between C_{70} and C_{60} and C_{70} and ZnPc might also be considered. The Coulomb interaction energy for C_{70}-C_{70} [267] is 1.2 eV and lower compared to 1.5-1.6 eV for C_{60}-C_{60}, [185, 252, 267].

---

[7] measured by Ellen Kern, physical chemistry of TU Dresden

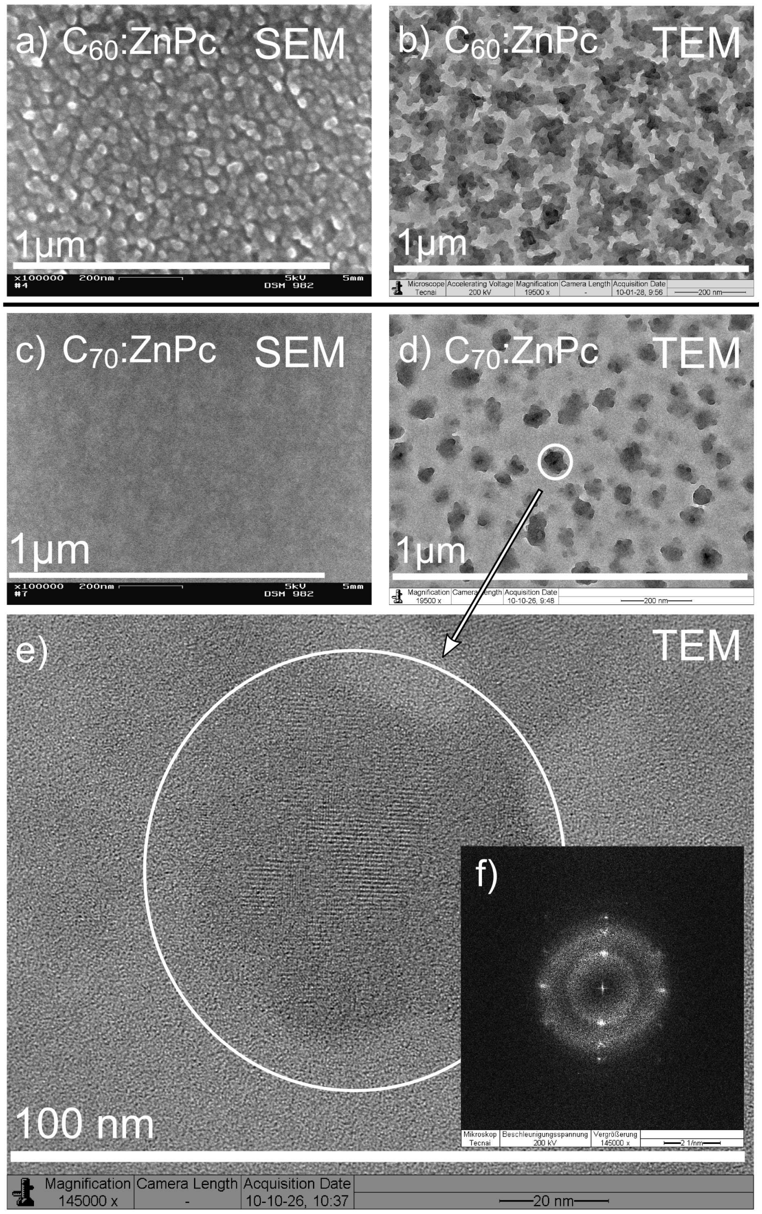

Figure 5.11: *Comparison of SEM measurements of ITO/C$_{60}$(5 nm)/fullerene:ZnPc(30 nm,1:1) stacks with a) C$_{60}$ and c) C$_{70}$ deposited at $T_{sub} = 110°C$ and TEM measurements of C$_{60}$(5 nm)/fullerene:ZnPc(30 nm,1:1) stacks on a carbon coated nickel grid with a) C$_{60}$ and c) C$_{70}$ deposited at $T_{sub} = 110°C$. Enlarged cluster of C$_{70}$:ZnPc sample in e) with its Fourier transformed pattern in f).*

5.3 p-i-i bulk heterojunction solar cells deposited at 110°C

For further investigations concerning mixing ratio and blend layer thickness, the Lesker tool is used to ensure a good comparability of such a parameter variation. Therefore, we changed the m-i-p solar cell structure to p-i-i, due to a better processability at this tool.

Here, we use the same cell structure as in section 4.5:
ITO/NDP2(1 nm)/p-Di-NPD(60 nm;5 wt%)/fullerene:ZnPc(30 nm, volume ratio X:Y) /C_{60}*(40 nm)/BPhen(6 nm)/Al(100 nm).*

We investigate in this section the influence of substrate heating on p-i-i solar cells with different mixing ratios of C_{60}:ZnPc and C_{70}:ZnPc, respectively. In case of the p-i-i stack, the layers below the blend layer are subjected to the thermal energy during co-

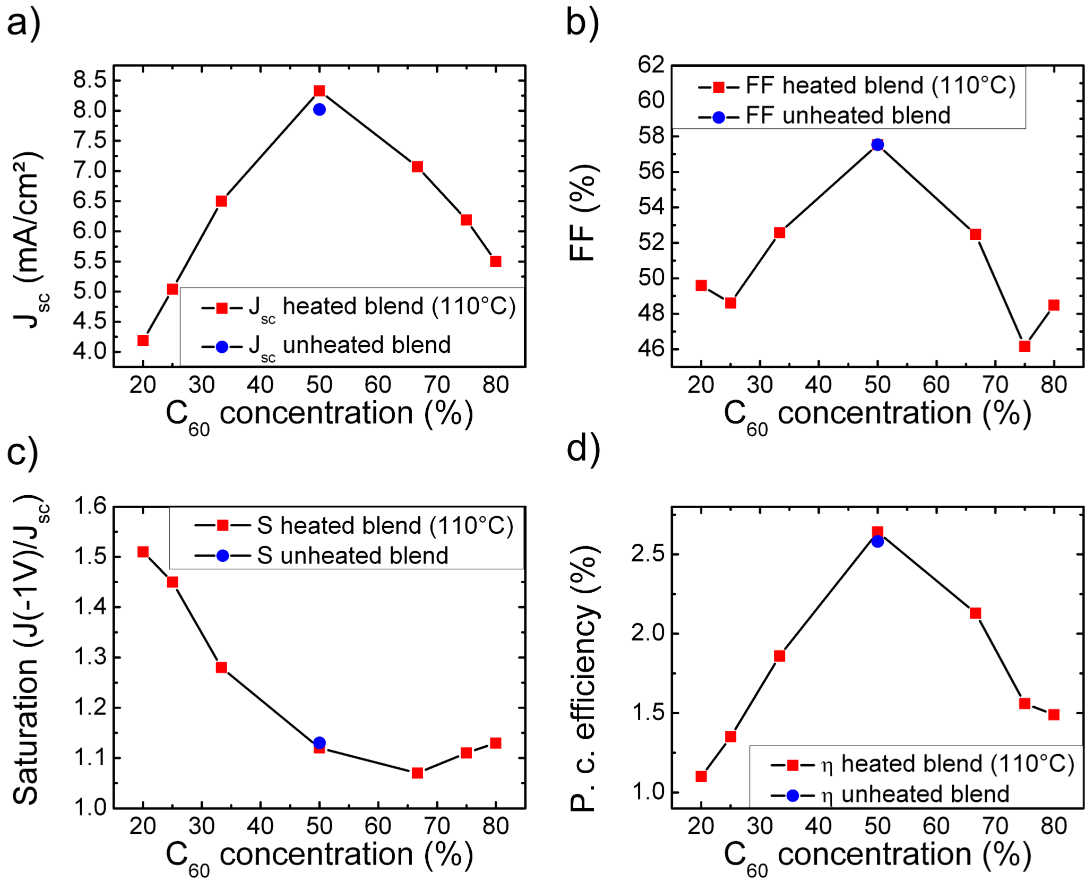

Figure 5.12: *a)* J_{SC}*; b) FF; c) Saturation J(-1V)/*J_{SC}*, and d) p.c. efficiency vs. mixing ratio of heated* C_{60}*:ZnPc p-i-i BHJ solar cells. The values indicated by squares correspond to the heated blend layer and the circles to the device where only the sublayers of the blend are subjected to heat.* J_{SC} *is measured setting the sun simulator intensity to a mismatch of 0.80 (the measured intensity with a Si reference diode is 125 mW/cm*^{2}*).*

deposition of the blend layer while heating the substrate . To investigate if the p-layers are somehow influenced by the additional thermal energy (e.g. dopant diffusion), solar cells are processed on the same Lesker run as reference, where the p-layers are subjected to the heat, but the blend layers are deposited at RT. As substrate temperature we use $T_{\mathrm{sub}} = 110\,°\mathrm{C}$ which was found to be the optimum for the m-i-p C_{60}:ZnPc devices. The C_{60}:ZnPc blend layer mixing ratio is varied from 4:1 (80% C_{60}) to 1:4 (20% C_{60}) by volume. The dependency of the solar cell characteristics in particular J_{SC}, FF, $S = J(\text{-1V})/J_{\mathrm{SC}}$, and p.c. efficiency on the mixing ratio are shown in Fig. 5.12. The V_{OC} does not change that strong as shown previously for the unheated solar cell and is stable around 0.55±0.02 V. Thus, we do not discuss the V_{OC} here. The values indicated by squares correspond to the heated blend layer and the circles to the unheated blend, but heated sublayer.

The shift of the optimal mixing ratio to 1:1 of the heated sample from the optimal mixing ratio between 1:1-2:1 determined for the sample processed at RT in section 4.5), can be attributed to a more favorable molecule arrangement. All other ratios show a strong decrease in J_{SC} and FF. In case of a blend ratio 1:1 the $J(V)$ parameters of the heated BHJ solar cell are similar to the device processed at RT and the device where only the sublayers are heated (indicated as unheated). The values are summarized in table 5.6. Just J_{SC} is slightly increased for $T_{\mathrm{sub}} = 110\,°\mathrm{C}$, which is confirmed by a slightly better EQE in the ZnPc region as shown in Fig 5.13 a) and indicating improved percolation.

Table 5.6: *$J(V)$ parameters of C_{60}:ZnPc and C_{70}:ZnPc p-i-i BHJ solar cells (volume ratio 1:1) for the RT, unheated blend and heated sublayer, and heated blend layer devices at $T_{sub} = 110°C$.*

ratio (1:1)	V_{OC} (V)	J_{SC} (mA/cm^2)	FF (%)	$J(\text{-1V})/J_{\mathrm{SC}}$	η (%)
C_{60}:ZnPc (RT)	0.55	8.1	57	1.12	2.5
C_{60}:ZnPc unheated	0.56	8.0	58	1.13	2.6
C_{60}:ZnPc heated	0.55	8.3	58	1.12	2.7
C_{70}:ZnPc (RT)	0.51	9.6	54	1.18	2.7
C_{70}:ZnPc unheated	0.53	9.3	55	1.17	2.7
C_{70}:ZnPc heated	0.52	9.6	55	1.15	2.8

Firstly, we can conclude that substrate heating does not negatively affect the p-doped sublayer and secondly, we surprisingly do not obtain a distinct and pronounced heating effect of the blend layer, as seen in the m-i-p like solar cells (section 5.2).

The main difference between the m-i-p and the p-i-i stack are the different sublayers of the blend layer, which seem to play a role concerning morphology modification upon substrate heating.

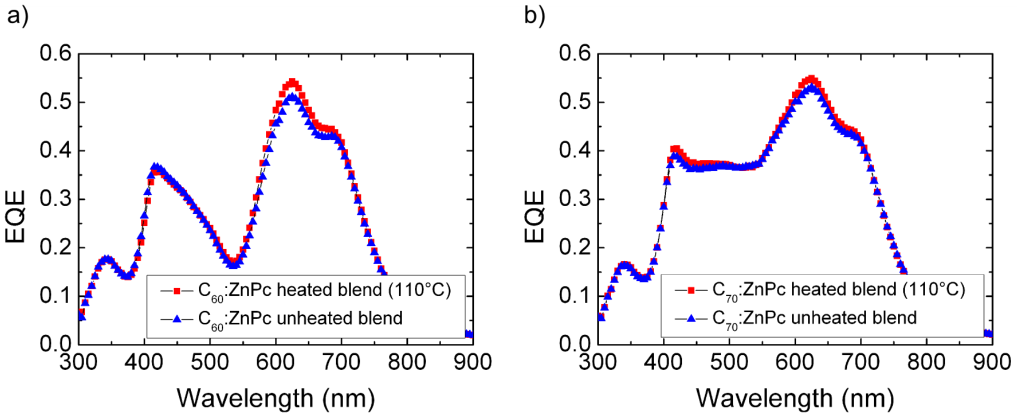

Figure 5.13: *EQE of the heated blend (squares) and unheated blend with heated sublayers (circles) of a)* C_{60}*:ZnPc and b)* C_{70}*:ZnPc BHJ solar cells (mixing ratio 1:1).*

The same investigation is performed for C_{70}:ZnPc with a mixing ratio variation between 1:1 (50 % C_{70}) and 4:1 (80 %) by volume. The *J(V)* characteristics are shown in Fig. 5.14.

Contrary to the observation made for the heated C_{60}:ZnPc solar cells, the V_{OC} increases with higher C_{70} concentration from 0.52 V(50% C_{70}) to 0.60 V (80%C_{70}). This is in good accordance to the increase of V_{OC} observed for the unheated C_{70}:ZnPc solar cells shown in section 4.5 table 4.3.

Here, we also observe a shift of the optimum ratio from 2:1-3:1 for the sample made at RT (see section 4.5) to 1:1-2:1 for the heated sample, which might be due to a more favorable molecule arrangement upon heating. All *J(V)* parameters of the heated BHJ solar cell are similar to the device made at RT and the device where the sublayers are heated. Only the J_{SC} is slightly increased and S decreased which is attributed to an improved blend morphology. The increased J_{SC} is confirmed by the EQE measurement in Fig. 5.13 b), which show increased values in the C_{70} and ZnPc spectral absorption region. In the absorption regions of both ZnPc and C_{70} a marginal increase is observed. It seems that the molecular arrangement of C_{70} is positively influenced by heating. Despite a better *FF* and similar J_{SC} the p.c. efficiency is only marginally better for blend ratio 2:1 compared to 1:1. Only the 40 mV higher V_{OC} for ratio 2:1 overcompensates the lower *FF* and leads to the better p.c. efficiency. Nevertheless, the better charge carrier separation and transport indicated by a higher *FF* is determined for ratio 1:1.

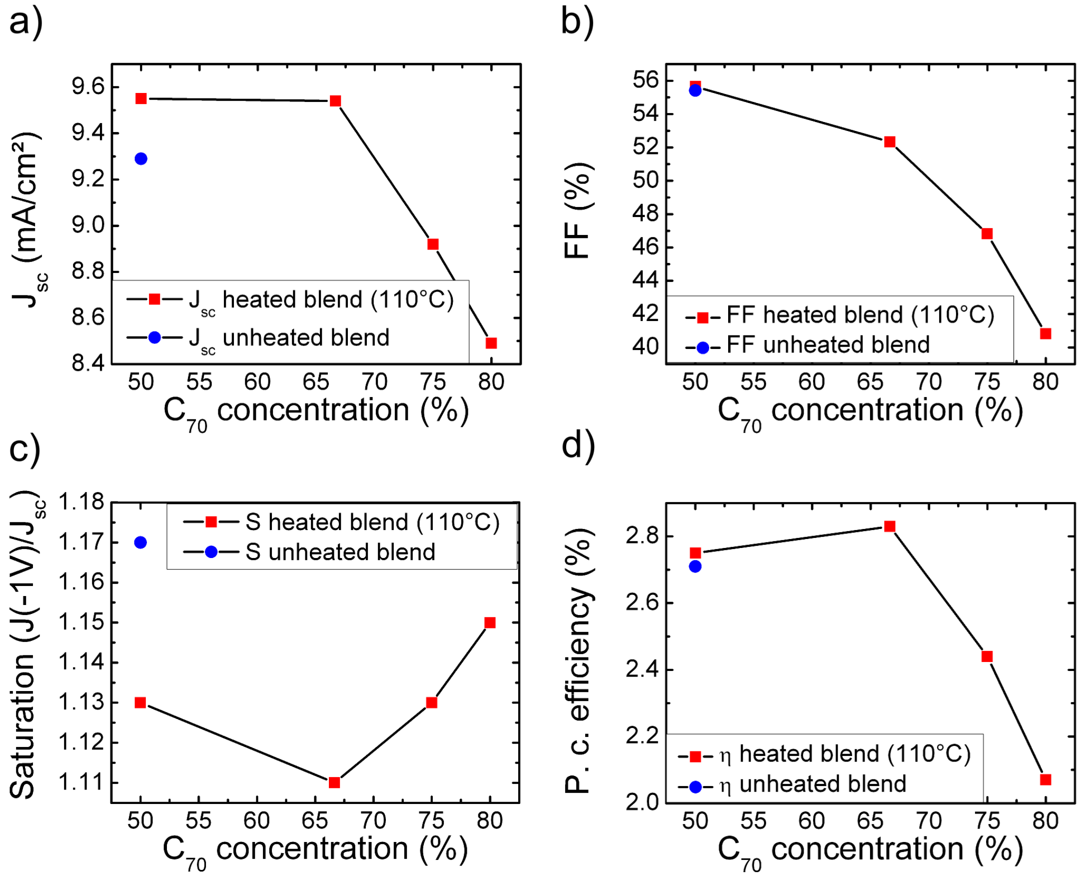

Figure 5.14: *a) J_{SC}; b) FF; c) Saturation J(-1V)/J_{SC}, and d) p.c. efficiency vs. mixing ratio of a heated C_{70}:ZnPc p-i-i BHJ solar cells. The values indicated by squares correspond to the heated blend layer and the circles to the device where only the sublayers of the blend are subjected to heat. J_{SC} is measured setting the intensity of the sun simulator to a mismatch of 0.81 (the measured intensity with a Si reference diode is 123 mW/cm^2).*

5.3.1 Influence of sublayer on blend layer morphology

5.3.1.1 SEM and TEM

The main difference between the p-i-i and the m-i-p stack is the sublayer of the blend. In the m-i-p stack 5 nm C_{60} is used, compared to the p-i-i stack with 60 nm p-doped Di-NPD. To check if the choice of sublayer influences the morphology of the heated C_{60}:ZnPc and C_{70}:ZnPc blend layers, SEM[8] and TEM[9] measurements are performed. For the SEM measurements, the heated blend layer at $T_{\mathrm{sub}} = 110\,^{\circ}\mathrm{C}$ is deposited on different sublayers, respectively. In Fig. 5.15 the results are shown for C_{60}:ZnPc and 5 nm sublayer on ITO: a) C_{60}, b) Di-NPD, c) ZnPc, and d) p-ZnPc(5 wt%), respectively. With 5 nm C_{60} the same aggregation of C_{60}:ZnPc is observed, as already shown in section 5.2.1. In case of Di-NPD only very few clusters are present. It seems that a molecular phase separation does not appear and the aggregation is suppressed. This would explain the unchanged performance of the heated p-i-i solar cell, due to unimproved transport properties in the blend. With 5 nm ZnPc the aggregation is increased

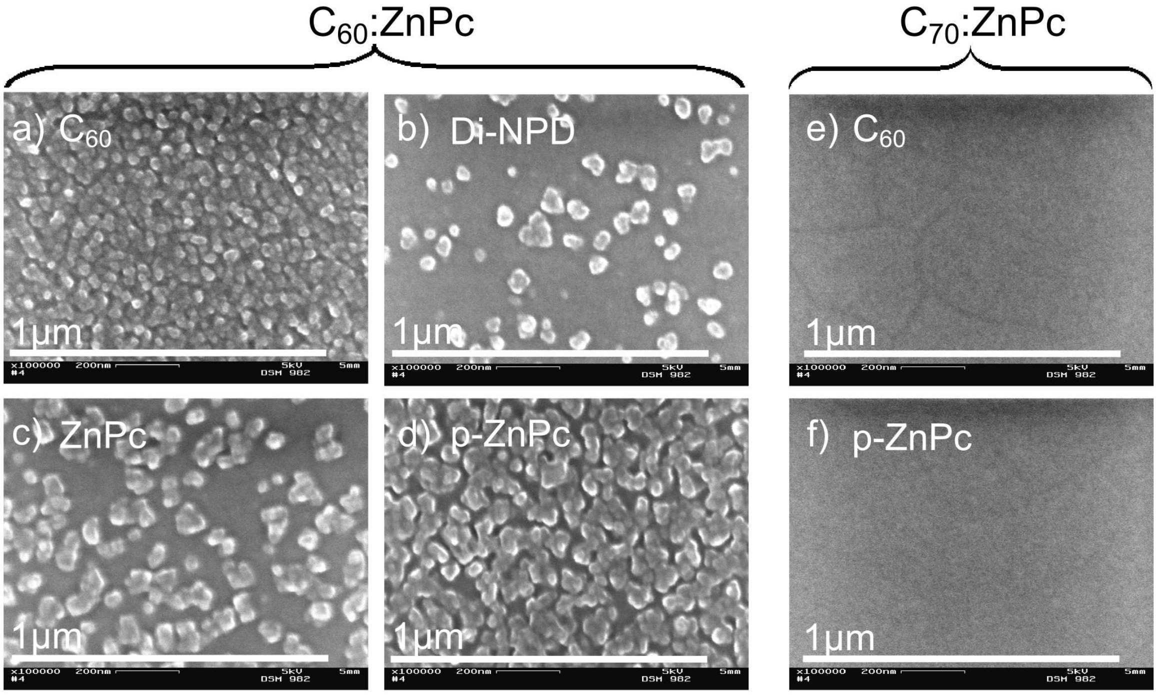

Figure 5.15: *SEM measurements of fullerene:ZnPc blend layers deposited during substrate heating at $T_{\mathrm{sub}} = 110\,^{\circ}C$ on different sublayers. C_{60}:ZnPc is deposited on 5 nm a) C_{60}, b) Di-NPD, c) ZnPc, and d) p-ZnPc, respectively. C_{70}:ZnPc is deposited on 5 nm a) C_{60} and f) p-ZnPc, respectively. ITO coated glass is used as substrate.*

---

[8] measured by Ellen Kern, physical chemistry of TU Dresden

[9] supported by Christine Mickel, Leibniz Institute for Solid State and Materials Research Dresden (IFW)

compared to Di-NPD, but not as good as with C_{60}. If we dope the ZnPc sublayer, a much stronger aggregation compared to intrinsic ZnPc is observed.
Due to the same composition of the blend layers, we attribute these observations to a strong impact of the sublayer on the blend layer morphology. The influence can be energetically or morphologically. The energetic impact might be caused by the molecular interaction between the molecules in the sublayer and the molecules in the blend, which is assumed to be different for the various sublayers. Furthermore, the molecules of the sublayers mostly arrange in an amorphous structure, but differ in molecular size and steric order. We assume that C_{60} as sublayer supports the molecular mobility and arrangement for the blend materials due to its highly symmetric and ball shaped structure. On the contrary, the larger and disordered molecule Di-NPD seems to hinder a molecular surface diffusion. In the case of doped ZnPc also both effects probably influence the blend layer morphology. The dopant might interact more strongly with the blend materials or positively changes the molecular arrangement of the ZnPc in the sublayer.
Concerning C_{70}:ZnPc blend layers, no morphological changes are observed for the different sublayers. Thus, we show here only the measurements for 5 nm C_{60} and p-ZnPc in Fig. 5.15 e) and f). The only difference between the C_{60}:ZnPc Fig. 5.15a) and C_{70}:ZnPc Fig. 5.15e) is the kind of fullerene in the blend. Therefore, no restrictions by the sublayer of C_{60} are expected. One reason for the completely suppressed cluster formation and aggregation might be due to the ellipsoid shaped C_{70}, with less degree of freedom concerning surface mobility compared to the ball shaped C_{60}. In addition, ZnPc also does not seem to be as mobile as C_{60}. If only one kind of the molecules in the mixed layer is mobile enough to diffuse over the surface or in the bulk, e.g. by providing thermal energy, the molecular mobility of the other kind of molecule is simultaneously increased. Therefore, it is concluded that C_{70} and ZnPc are not as mobile as C_{60} and remain more or less at the position where they are deposited. Supplying more thermal energy to the C_{70}:ZnPc layer might increase the molecule mobility and lead to aggregation. Another reason might be a different molecular interaction in the blend between C_{70} and ZnPc or C_{70} and C_{60} in the sublayer, as already mentioned previously for C_{60}-CuPc in section 5.1 and C_{70}-C_{70} in section 5.2.6.

Obtaining information about the morphological change in the blend layer by the variation of the sublayer TEM measurements are carried out. The phase analysis of C_{70} is performed using Powder Diffraction File (PDF) [262] and Inorganic Crystal Structure Database (ICSD) [263]. The interplane distances are calculated by the program PowderCell 2.3 [264].
To reduce the influence of the carbon layer on the nickel grid, 10 nm p-Di-NPD is used below the sublayer and is deposited as follows for the C_{60}:ZnPc and C_{70}:ZnPc blend

layer, respectively: 5 nm C_{60} (Fig. 5.16a),e)), p-Di-NPD(10 nm,5 wt%) (Fig. 5.16b),f)), p-Di-NPD(10 nm,5 wt%)/ZnPc(5 nm) (Fig. 5.16 c),g)), and p-Di-NPD(10 nm,5 wt%)/p-ZnPc(5 nm,5 wt%) (Fig. 5.16d),h)).

First of all, the SEM and TEM measurements show similar levels of aggregation for

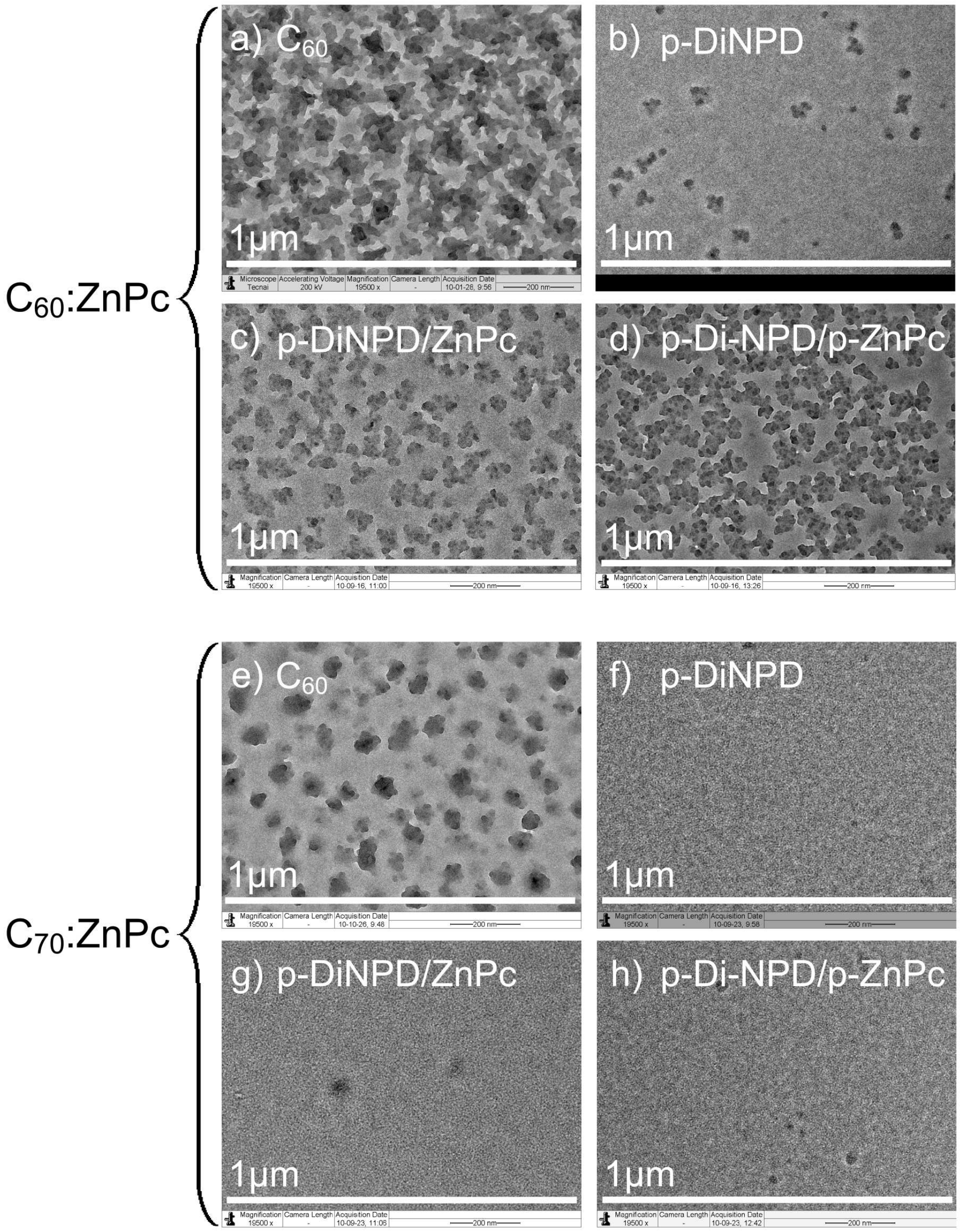

Figure 5.16: *TEM measurements of fullerene:ZnPc blend layers deposited during substrate heating at* $T_{\mathrm{sub}} = 110^{\circ}C$ *on different sublayers.* C_{60}*:ZnPc is deposited on a)* C_{60}*(5 nm), b) p-Di-NPD(10 nm,5 wt%)/Di-NPD(5 nm), c) p-Di-NPD(10 nm,5 wt%)/ZnPc, and d) p-Di-NPD(10 nm,5 wt%)/p-ZnPc, respectively.* C_{70}*:ZnPc is deposited on e)* C_{60}*(5 nm), f) p-Di-NPD(10 nm,5 wt%)/Di-NPD(5 nm), g) p-Di-NPD(10 nm,5 wt%)/ZnPc, and h) p-Di-NPD(10 nm,5 wt%)/p-ZnPc, respectively. A carbon coated nickel grid is used as substrate.*

the heated C_{60}:ZnPc layers with the same sublayer. The bright spots and clusters in the SEM pictures can be attributed to the dark clusters in the TEM pictures. The dark regions in the TEM measurements are rich in ZnPc clusters or polycrystalline domains. TEM investigations on the heated C_{60}:ZnPc on 5 nm C_{60} were already shown and evaluated in detail in section 5.2.4.

We observe few isolated clusters for the p-Di-NPD sample which shows polycrystalline growth. Compared to p-DiNPD the sample with ZnPc exhibit increased aggregation and clusters with polycrystalline domains which are partially interconnected. With doped ZnPc even more clusters with polycrystals are formed and show increased interconnection.

All dark spots and regions, which exhibit polycrystalline domains, are mainly attributed to monoclinic ZnPc [259] and show the 003, 403, and 005 reflections (see section 5.2.4). Due to a better molecular phase separation for the C_{60} sample, the regions between the polycrystalline domains are brighter compared to the blends of the other sublayer samples, assuming to be a mixture of amorphous C_{60} and ZnPc.

The same measurements are carried out for the heated C_{70}:ZnPc blend layer. We observe single cluster formations for blend C_{70}:ZnPc deposited on C_{60} which differ in shape and size from the single clusters observed for the C_{60}:ZnPc devices on HTL sublayer. The clusters appear circular shaped and larger with lateral diameters between 50-100 nm. In 50 % of the clusters, polycrystalline domains are found and can not precisely be attributed to monoclinic ZnPc [259] or C_{70} [265]. Many more lattice planes of C_{70} are possible compared to C_{60}. For this reason C_{70} and ZnPc exhibit lattice spacings which are similar. Thus it is not possible to distinguish between both and draw a clear conclusion. In the bright regions no crystal formations are detected. However, partially crystalline C_{70} would be in good aggreement with the observed marginally improved EQE in the C_{70} region for the heated p-i-i solar cell, shown in Fig. 5.13, due to improved transport properties. For the ZnPc and p-ZnPc sublayer samples, small dark spots arise which hints on initial molecule aggregation, but are not polycrystalline. To further enhance the aggregation, parameters like T_{sub}, sublayer, and mixing ratio need to be optimized. Here, only the effect of 5 nm sublayer on the blend layer has been investigated. A thicker sublayer might shield the energetic influence of p-DiNPD on the blend layer morphology. Therefore, the influence of sublayer thickness on the blend layer morphology might also be considered and investigated.

In the following, we show the impact of mixing ratio on morphology for a 60 nm thick C_{70}:ZnPc blend layer deposited during substrate heating at $T_{\text{sub}} = 120\,^{\circ}\mathrm{C}$ on 5 nm C_{70} (on ITO). The dependency and change of cluster formation is shown in the SEM pictures in Fig. 5.17 for mixing ratios a) 1:1, b) 2:1, c) 3:1, and d) 4:1 by volume. The cluster size increases with a larger amount of C_{70}, which is attributed to an easier

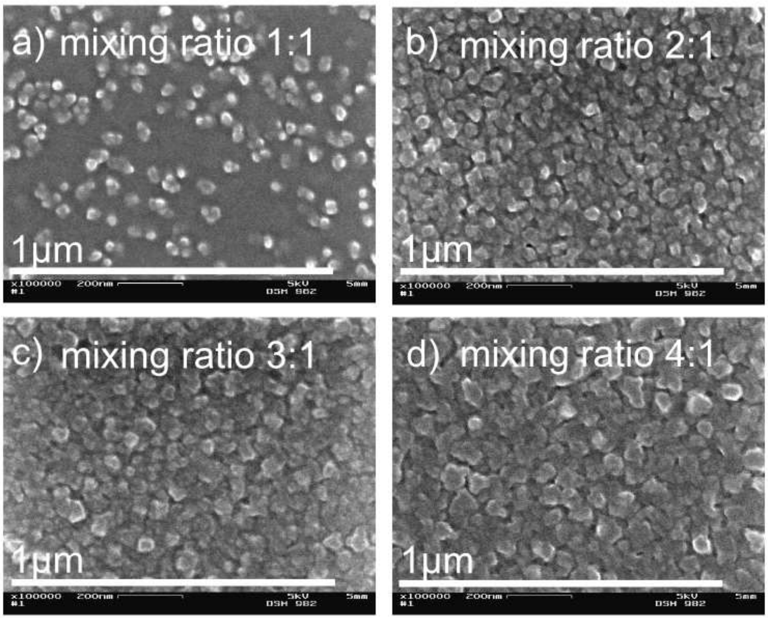

Figure 5.17: *SEM measurements of a variation of mixing ratio of C_{70}:ZnPc blend layer deposited during substrate heating at $T_{\mathrm{sub}} = 120°C$ on 5 nm C_{70}. Mixing ratios are a) 1:1, b) 2:1, c) 3:1, and d) 4:1 by volume. ITO coated glass is used as substrate.*

molecule arrangement and molecular diffusion mobility on the surface of C_{70}. In the case of ratio 4:1 (80 % C_{70}), ZnPc is surrounded mainly by C_{70} molecules and can be considered to be in a C_{70} matrix. The hindrance of molecular phase separation by the sterical planar ZnPc molecule is therefore increased. However, the large cluster formation obtained for ratio 4:1 does not imply that this ratio results in best solar cell performance. Further criteria depending on mixing ratio like spectral photon absorption and contribution to J_{SC}, efficient exciton separation, and good charge carrier extraction have to be taken into account, as shown in section 5.3. We see that for each blend combination, T_{sub}, mixing ratio, and choice of sublayer have to be considered to achieve the best p.c. efficiency in organic solar cells.

5.3.1.2 60 nm p-i-i bulk-heterojunction solar cells deposited at 110°C with thin ZnPc interlayer

In the previous section, we have shown that polycrystalline growth of ZnPc in particular for heated C_{60}:ZnPc blend layer can be induced by a 5 nm thick sublayer of ZnPc or p-ZnPc with respect to the p-i-i solar cell stack. Now we investigate if 5 nm are suitable as interlayer between p-Di-NPD and blend layer and lead to improved p-i-i solar cells. Furthermore, the blend layer thickness is increased from 30 nm to 60 nm, to see if the morphology changes for thicker blend layers. Investigations are carried out for 60 nm C_{60}:ZnPc blend layer (ratio 1:1) deposited during evaporation at $T_{\mathrm{sub}} = 110\,^{\circ}\mathrm{C}$. 5 nm ZnPc and p-ZnPc are used as interlayer. Here, we use the following solar cell stack:
ITO/NDP2(1 nm)/p-Di-NPD(60 nm;5 wt%)/interlayer(0 nm,ZnPc(5 nm), p-ZnPc(5 nm))/C_{60}*:ZnPc(60 nm, 1:1)/*C_{60}*(40 nm)/BPhen(6 nm)/Al(100 nm).*

The *J(V)* characteristics are shown in Fig. 5.18 with the dependency of the sublayers. Solar cells where the sublayers are subjected to heat and the blend layer deposited at RT are taken as reference. Corresponding values are indicated by squares in Fig. 5.18. Due to the usage of the same ZnPc material batch in the blend and for the interlayer, no energetic barrier between both ZnPc HOMOs is expected. Thus, the decrease of V_{OC} from 0.55 V for p-Di-NPD to around 0.52 V for ZnPc and p-ZnPc is yet unclear. The reduction of V_{OC} and the absence of s-kinks in the *J(V)* curves indicate an injection barrier from interlayer to the blend. This effect is investigated and discussed in more detail in chapter 6.

The interesting parameters which are correlated with improved morphology are *FF* and J_{SC}. The *FF* is increased from 44.0 % to 47.5 % for ZnPc and from 46.5 % to 49.5 % for p-ZnPc and hints at an improved blend layer morphology as already indicated previously by the SEM and TEM measurements.

As seen in Fig. 5.18 b) J_{SC} is increased for the ZnPc sublayer by 0.7 mA/cm^2, while J_{SC} is unchanged for p-Di-NPD and even decreased for p-ZnPc comparing heated and unheated blend layer. The 5 nm intrinsic ZnPc should additionally contribute to J_{SC} in contrast to the doped ZnPc layer, where all generated excitons are assumed to be quenched at the dopant molecules. However, we do not observe any enhancement of J_{SC} of the unheated blend layer compared to p-Di-NPD sublayer, but a slight decrease. A reason for that can be a different energy level alignment inducing charge carrier recombination, visible in a low *FF* of 44 %. No clear explanation can be given here. The improved J_{SC} is also attributed to improved blend layer morphology and consistent with the higher *FF*. The heated sample with ZnPc shows indeed increased J_{SC} and *FF*, but this increase is compensated by a lower V_{OC} compared to the p-Di-NPD sample as shown in Fig. 5.19.

Due to the fact that J_{SC} remains similar for p-Di-NPD for both heated and unheated blend layers, the cluster formation in the blend layer on p-ZnPc seems to support the exciton quenching at the interface blend/p-ZnPc, visible in a decreased J_{SC} of the heated blend layer compared to the unheated blend layer sample. The solar cell performance does not benefit from the stronger aggregation and polycrystalline formation of the blend layer on p-ZnPc compared to ZnPc.

Furthermore, despite a rather thick blend layer, the morphology of the 60 nm thick C_{60}:ZnPc is not in case of p-Di-NPD sublayer or in case of ZnPc sublayer only marginally improved compared to the 30 nm blend layer. One might assume that after several molecule layers or a certain blend layer thickness, the molecule arrangement is independent from the sublayer and phase separation appears. For the device with p-Di-NPD sublayer it is clearly not the case, FF and J_{SC} remain similar for both heated and unheated blend layers. This shows additionally how strong the impact on layer morphology can be by the choice of sublayer.

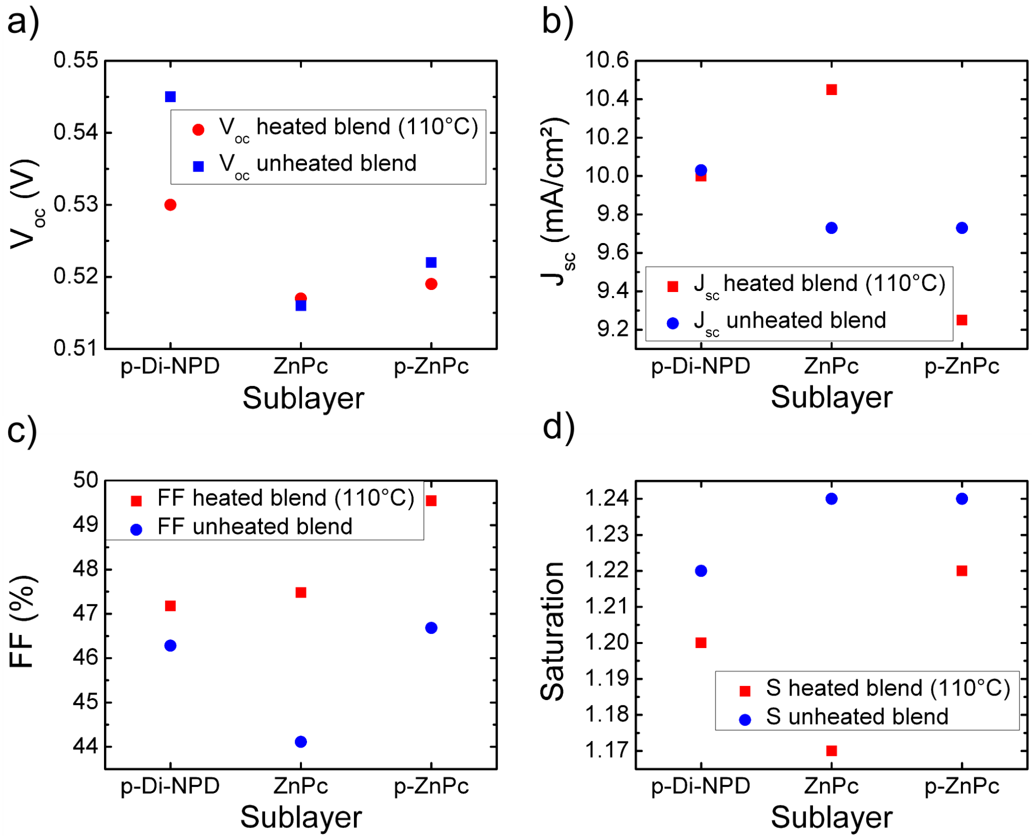

Figure 5.18: *a)* V_{OC}*; b)* J_{SC}*; c) FF; and d) Saturation* J*(-1V)/*J_{SC} *characteristics depending on different sublayers: p-Di-NPD, ZnPc, and p-ZnPc of heated (circles) and unheated (squares)* C_{60}*:ZnPc blend layers in p-i-i BHJ solar cells.* J_{SC}*s are measured setting the intensity of the sun simulator to a mismatch of 0.80 (the measured intensity with a Si reference diode is 125 mW/cm²).*

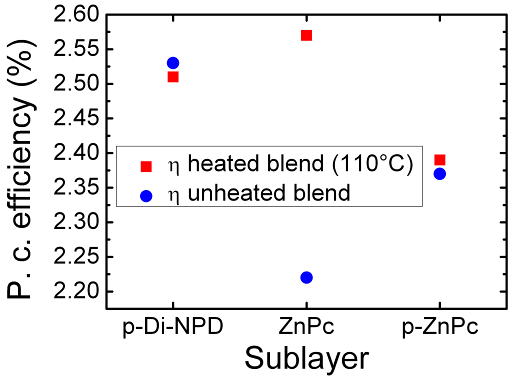

Figure 5.19: *P.c. efficiency depending on different sublayers: p-Di-NPD, ZnPc, and p-ZnPc of heated (circles) and unheated (squares)* C_{60}*:ZnPc blend layers in p-i-i BHJ solar cells.*

6 Results: On the influence of V_{OC} in p-i-i bulk heterojunction solar cells

In this chapter, we investigate the previously observed effect of the change of V_{OC} *as a function of mixing ratio in* C_{60}*:ZnPc p-i-i bulk heterojunction solar cells. To clarify the origin of this behavior and whether it can be attributed to an intrinsic bulk property or to an interface effect of the adjacent hole transport layer, different experiments are carried out. Varying the adjacent hole transport layer with different IPs we check its influence on* V_{OC}*. Spectral blue and red illumination measurements are performed, where either* C_{60} *or ZnPc molecules are excited. From these measurements we conclude that the change of* V_{OC} *is an intrinsic bulk effect. UPS is applied to determine the IPs in blend layers for various mixing ratios. Furthermore, the voltage drop that is observed for additional ZnPc and* C_{70} *interlayers in bulk heterojunction solar cells is investigated using the same measurement method. The assumed injection barrier between the interlayer and the blend is investigated preparing samples with a variation of the interlayer thickness of ZnPc. The results are compared with simulation data.*

6.1 Dependency of V_{OC} on C_{60}:ZnPc mixing ratio

In section 4.5, we observed an increase of V_{OC} from 0.55 V to 0.62 V for C_{60}:ZnPc p-i-i bulk heterojunction solar cells when blend ratios changed from 1:1 to 4:1. The solar cells composed of C_{70}:ZnPc exhibit a similar tendency, but with slightly overall reduced V_{OC} due to the higher EA of C_{70}. We assume the same effect for both fullerene solar cells and thus focus only on the C_{60}:ZnPc blend layer system.

To obtain more information about the correlation between V_{OC} and mixing ratio, we first make p-i-i bulk heterojunction solar cells with an extended C_{60}:ZnPc mixing ratio variation from 1:6 (14 vol% C_{60}) to 6:1 (86 vol% C_{60}). To exclude material dependent deviations due to impurities, the same material batches are used for C_{60}, ZnPc, and Di-NPD.

The following solar cell stack is used:
ITO/NDP2(1 nm)/p-Di-NPD(60 nm;5 wt%)/C_{60}*:ZnPc(30 nm,X:Y)/*C_{60}*(40 nm)/ BPhen(6 nm)/Al(100 nm).*
The characteristic parameters like J_{SC}, FF, and $J(\text{-1V})/J_{\mathrm{SC}}$ differ for the various mixing ratios. The highest J_{SC} is observed for a volume ratio of 1:1; it is strongly reduced for ratios of 1:6 and 6:1. Its impact on V_{OC} is assumed not to be dominant and is thus not further considered. The V_{OC} - mixing ratio dependency is shown in Fig. 6.1. We recognize an almost linear increase above a mixing ratio of around 1:3 (30 vol% C_{60}) of V_{OC} from 0.53 V up to 0.63 V. Interestingly, below ratio 1:3 (30 vol% C_{60}) the V_{OC} increases again up to 0.55 V.

Two different hypotheses which might explain the V_{OC} dependency are:

1. The increase in V_{OC} above ratio 1:3 might be explained by the additional C_{60}/p-HTL interface.
   C_{60} excitons generated close to the interface dissociate when the hole is transferred to the hole transport level of Di-NPD. Due to a larger effective gap ($\mathrm{IP}_{\mathrm{donor}}$ - $\mathrm{EA}_{\mathrm{acceptor}}$) between C_{60} and Di-NPD (IP of 5.33 eV[1]) compared to ZnPc (IP of 5.07 - 5.12 eV[2]) a higher V_{OC} can be obtained. This is schematically shown in Fig. 6.2. Usually, the V_{OC} for a C_{60}/Di-NPD flat heterojunction is around 0.76 V [115], compared to 0.47 V for a C_{60}/ZnPc flat heterojunction as shown in section 4.4.2. With an increasing amount of C_{60} in the blend, more C_{60} molecules are present at the interface. The separated C_{60} excitons at this interface contribute to a higher V_{OC}. On the electron transporting side, the intrinsic C_{60} layer does not provide any interface property to the blend layer concerning increasing effective gap.

2. The increase of V_{OC} is an intrinsic blend layer effect. Upon blending C_{60} and ZnPc in various mixing ratios, the strength of molecular interaction (e.g. polarization energies [268] and molecular arrangement [269]) between both molecules is changed and different energy level alignments are reasonable. This means that for a larger C_{60} amount in the blend, the effective gap $\mathrm{IP}_{\mathrm{donor}}$ - $\mathrm{EA}_{\mathrm{acceptor}}$ is increased.

With appropriate experiments we check the validity of the two hypotheses.

---

[1] measured via UPS by Selina Olthof, IAPP, TU Dresden
[2] measured via UPS by Max Tietze, IAPP, TU Dresden

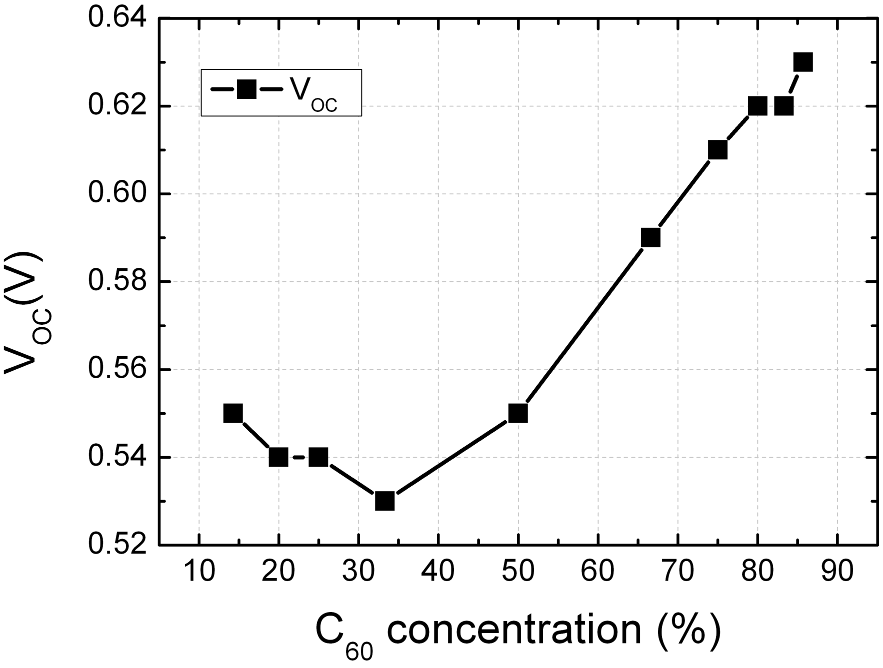

Figure 6.1: *V_{OC} dependency of p-i-i bulk heterojunction solar cells with a C_{60}:ZnPc mixing ratio variation from 1:6 (14 vol% C_{60} concentration) to 6:1 (86 vol% C_{60} concentration). The solid line is a guide to the eye.*

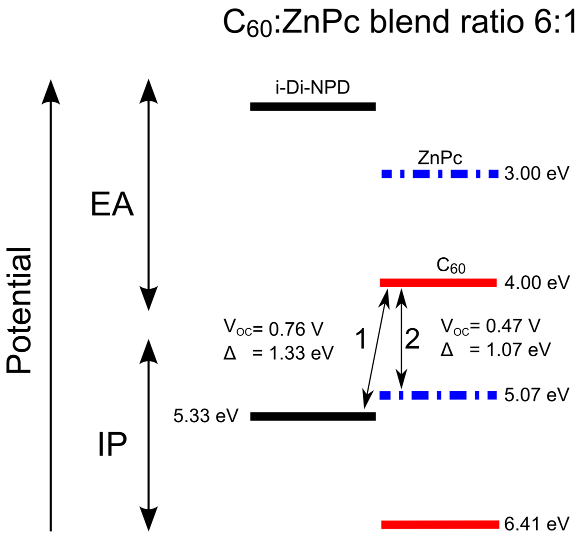

Figure 6.2: *Proposed interfaces for charge carrier and V_{OC} generation: 1) Di-NPD/C_{60} and 2) ZnPc/C_{60}. Given values are obtained from flat heterojunction solar cells and related to E_{vac}.*

6.2 Influence of different hole transport layers on C_{60}:ZnPc

To check how V_{OC} depends on hole transport layers (HTL) with different IPs, we prepared C_{60}:ZnPc p-i-i bulk heterojunction solar cells with three different HTLs: MeO-TPD (IP = 5.1 eV [3]), BF-DPB (IP = 5.23 eV [3]), and Di-NPD (5.33 eV [3]) for three different mixing ratios: 1:6, 1:1, and 6:1, respectively.

The following solar cell stack is used:

ITO/NDP2(1 nm)/p-HTL(60 nm;5 wt%)/HTL(5 nm)/C_{60}:ZnPc(30 nm,X:Y)/ C_{60}(40 nm)/BPhen(6 nm)/Al(100 nm).

In Fig. 6.3, the *J(V)* curves and characteristics are shown for blend ratio 1:1. Ratios 1:6 and 6.1 show different shaped *J(V)* curves (e.g. differently pronounced s-kink and *FF*). These are attributed to unbalanced charge carrier transport in the blend [72,161] and additionally to the already observed s-kinks for ratio 1:1.

To prevent a decrease of V_{OC} induced by an increased exciton and charge carrier recombination caused by dopant molecules at the blend/p-HTL interface, a 5 nm thick undoped HTL is inserted between blend and p-HTL. Consequently, extraction barriers are formed due to the larger IPs of the HTLs BF-DPB and Di-NPD. The extraction barriers are visible as s-kinks in Fig. 6.3 and expressed in low *FF* in the *J(V)* characteristics, strongly pronounced for BF-DPB and slightly for Di-NPD. Usually one expects a stronger s-kink [222] for the solar cell with Di-NPD due to the larger IP compared to BF-DPB, but this can not be confirmed here. One reason might be a different energy level alignment as expected from the IPs, due to a shift in the vacuum level [116,270]. Concluding from the larger s-kink for the BF-DPB solar cell, we assume therefore a larger extraction barrier compared to Di-NPD [222].

In case of MeO-TPD, having a lower IP, showing no s-kink, and a high *FF* of 52.7 % no extraction barrier is expected. However, an extraction barrier does not affect the V_{OC} [222] of a bulk heterojunction and allows a reliable consideration of the V_{OC} dependence on the HTL.

In Fig. 6.4 we see that V_{OC} increases for all HTLs with increasing C_{60} content in the BHJ. The contact area between C_{60}/HTL is largest for ratio 6:1 and would provide the largest V_{OC}, if V_{OC} is dominated by the C_{60}/HTL interface. With MeO-TPD, having a similar IP of 5.1 eV as ZnPc in the blend, a similar V_{OC} should be measured for both C_{60}:ZnPc ratios 1:1 and 6:1, but a much higher V_{OC} is measured for ratio 6:1. This observation supports hypothesis two. The lower V_{OC} obtained with MeO-TPD for ratio 6:1 compared to BF-DPB and Di-NPD, might be reasonably explained by an injection barrier, assuming an IP downshift of ZnPc in the blend which will be discussed in more

---

[3] measured via UPS by Selina Olthof, IAPP, TU Dresden

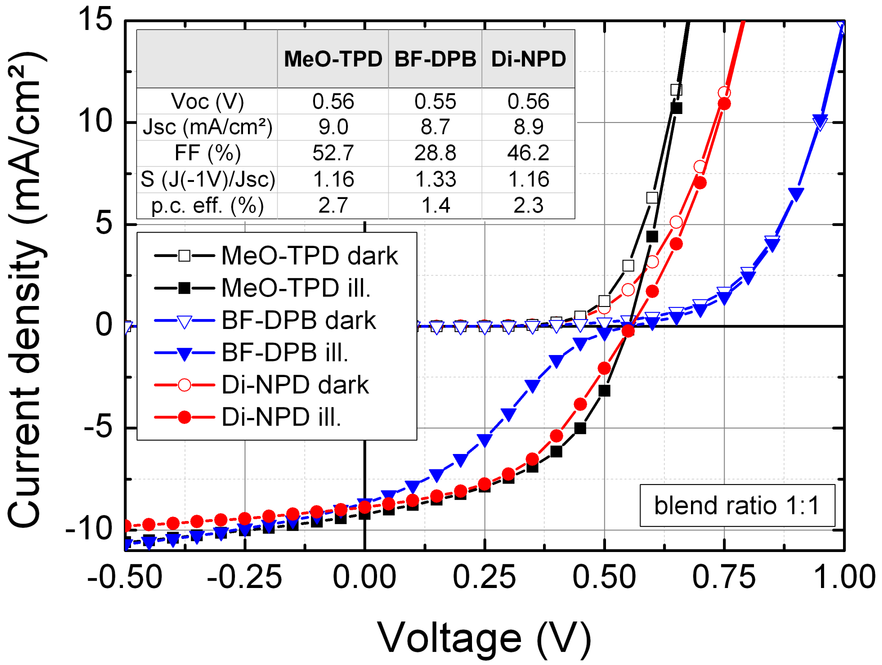

	MeO-TPD	BF-DPB	Di-NPD
Voc (V)	0.56	0.55	0.56
Jsc (mA/cm²)	9.0	8.7	8.9
FF (%)	52.7	28.8	46.2
S (J(-1V)/Jsc)	1.16	1.33	1.16
p.c. eff. (%)	2.7	1.4	2.3

Figure 6.3: *V_{OC} dependency of adjacent 5 nm intrinsic hole transport layer having diverse IPs between 5.1 and 5.33 eV. J(V)-characteristics shown for HTLs MeO-TPD (squares), BF-DPB (triangles), and Di-NPD (circles).*

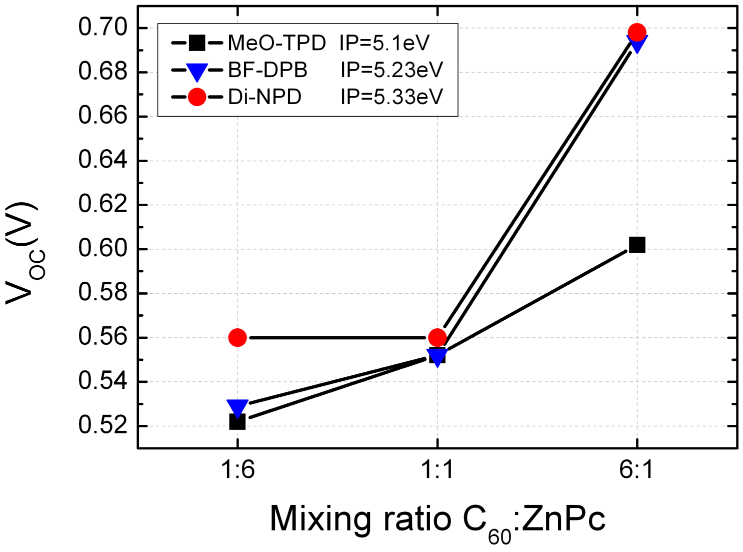

Figure 6.4: *V_{OC} dependency of C_{60}:ZnPc p-i-i bulk heterojunction solar cells with mixing ratio of 1:6, 1:1, and 6:1 on different i-HTLs: MeO-TPD (squares), BF-DPB (triangles), and Di-NPD (circles).*

detail in section 6.2.3.

This V_{OC} - HTL dependency can be explained presuming an energy level shift of C_{60} and/or ZnPc for larger amounts of C_{60}, resulting in a larger effective gap either to the HTL or ZnPc. Yet, we can not conclude whether the increase of V_{OC} is caused by the C_{60}/HTL interface or if this is an intrinsic blend layer effect.

From the EQE (Fig. 6.5) of the BF-DPB sample with a blend mixing ratio of 6:1 (14 vol% ZnPc), still a large J_{SC} contribution of ZnPc is measured. It is surprising that charges can still be extracted out of the bulk for such a small ZnPc amount of 14 vol. %. It seems that percolation in the blend is still sufficient for holes. Furthermore, the large EQE of 30 % in the ZnPc region and contribution of 3.66 mA/cm^2 to J_{SC} above 540 nm leads to the assumtion that J_{SC} is mainly generated in the bulk and not at the C_{60}/HTL interface. Thus, V_{OC} is mainly dominated by the quasi-Fermi level splitting between C_{60} and ZnPc in the blend. These results again hint at an intrinsic blend layer effect of the V_{OC}-mixing ratio dependency as stated in hypothesis two.

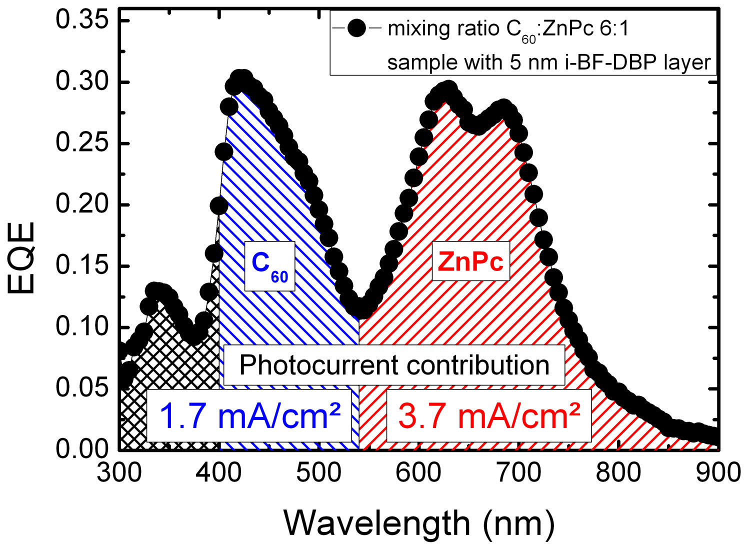

Figure 6.5: *EQE of p-i-i bulk heterojunction solar cells with a C_{60}:ZnPc mixing ratio of 6:1 and BF-DPB 5 nm hole transport interlayer. The photocurrent contribution below 540 nm is mainly attributed to C_{60} absorption (left striped pattern) and above 540 nm mainly to ZnPc absorption (right striped pattern).*

6.2.1 Red and blue illumination measurements

An advantage of the absorber materials utilized is that their absorption spectra only marginally overlap in the spectral region between 440 - 800 nm, as shown in Fig. 6.6. Thus, it is possible to illuminate the absorber molecules rather independently by using a red LED for ZnPc illumination and a blue LED for C_{60} illumination as depicted in Fig. 6.6. In detail, we use blue light at 470 nm (Philipps Lumileds, LUXEON LXK2-PB14-P00, spectral half-width 25 nm) and red light at 627 nm (Philipps Lumileds, LUXEON K2 LXK2-PH12-S00, spectral half-width 20 nm) [271]. This allows to check whether the V_{OC} is dominated by the C_{60}/HTL interface or the blend layer.

When exciting C_{60} molecules in the blend, the generated excitons have the possibility to get separated at the C_{60}/HTL or C_{60}/ZnPc interface. However, if we excite the ZnPc molecules, the excitons can only be separated at the C_{60} molecules. It means if we obtain a larger V_{OC} for the blue illumination, the exciton separation takes place at the C_{60}/HTL interface. However, when both red and blue illuminations exhibit the same V_{OC}, we can be sure that V_{OC} is mainly generated in the blend layer and the change in V_{OC} for different mixing ratios is an intrinsic blend layer effect. We measured the samples with C_{60}:ZnPc mixing ratio of 1:6 and 6:1 with the HTLs MeO-TPD, BF-DPB, and Di-NPD under red and blue light illumination. The values are summarized in table 6.1. The determined V_{OC} for red and blue illumination only marginally differs from the V_{OC} measured under one sun illumination for the mixing ratio 1:6 and 6:1. The deviations in V_{OC} are caused by different light intensities used for the red and

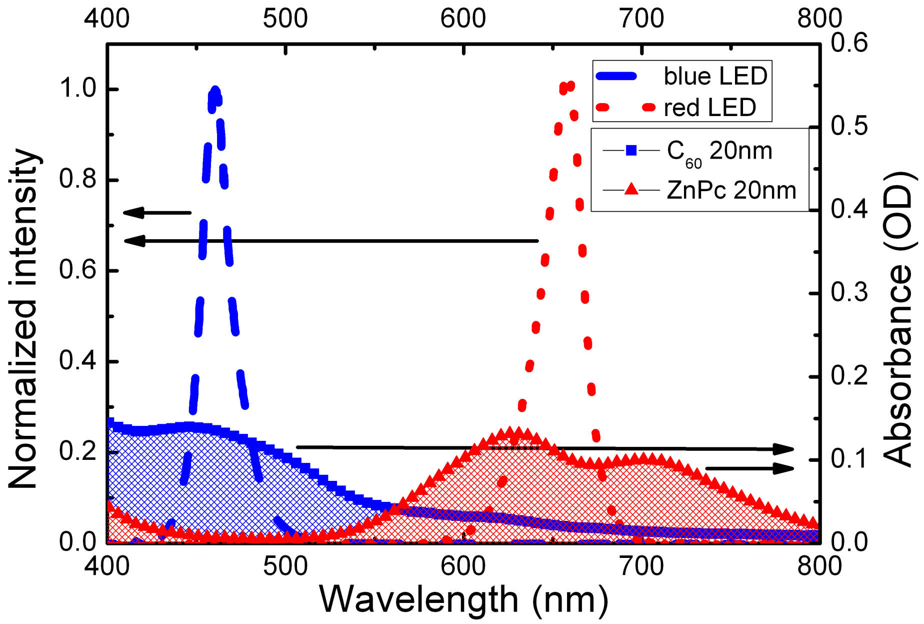

Figure 6.6: *Light emission spectrum of the red (dotted line) and blue (dashed line) LED and spectrum of the 20 nm thin film absorption of ZnPc (triangles) and C_{60} (squares).*

Table 6.1: *V_{OC} of p-i-i bulk heterojunction solar cells for C_{60}:ZnPc mixing ratio of 1:6 (upper table) and 6:1 (lower table), respectively, for different intrinsic HTLs (MeO-TPD, BF-DPB, and Di-NPD) and different illumination spectra (one sun, blue, and red).*

ratio (1:6)	**MeO-TPD**	**BF-DPB**	**Di-NPD**
V_{OC} (V) at 1 sun	0.52	0.53	0.56
V_{OC} (V) at blue ill.	0.49	0.50	0.59
V_{OC} (V) at red ill.	0.46	0.47	0.58

ratio (6:1)	**MeO-TPD**	**BF-DPB**	**Di-NPD**
V_{OC} (V) at 1 sun	0.60	0.69	0.70
V_{OC} (V) at blue ill.	0.54	0.65	0.73
V_{OC} (V) at red ill.	0.57	0.66	0.72

blue illumination, resulting in different quasi-Fermi level splitting. While for the HTL sample with MeO-TPD and BF-DPB, the intensity for the blue illumination is set to an operating current of 40 mA and for the red to 30 mA, the intensity for the Di-NPD sample is set to more than the double value, 95 mA for blue illumination and 70 mA for the red. The red and blue illumination intensities for MeO-TPD and BF-DPB are below the corresponding one sun intensity, resulting in a slightly lower V_{OC}, while for Di-NPD the red and blue illumination is well above the corresponding one sun intensity, resulting in a slightly higher V_{OC}. We determined that the V_{OC} for both illumination spectra obtained for the different mixing ratios is unchanged, shown for the sample with Di-NPD in Fig. 6.7. From these measurements, we conclude that the effect of changed V_{OC} upon mixing ratio variation is caused by the blend layer itself and not by the C_{60}/HTL interface.

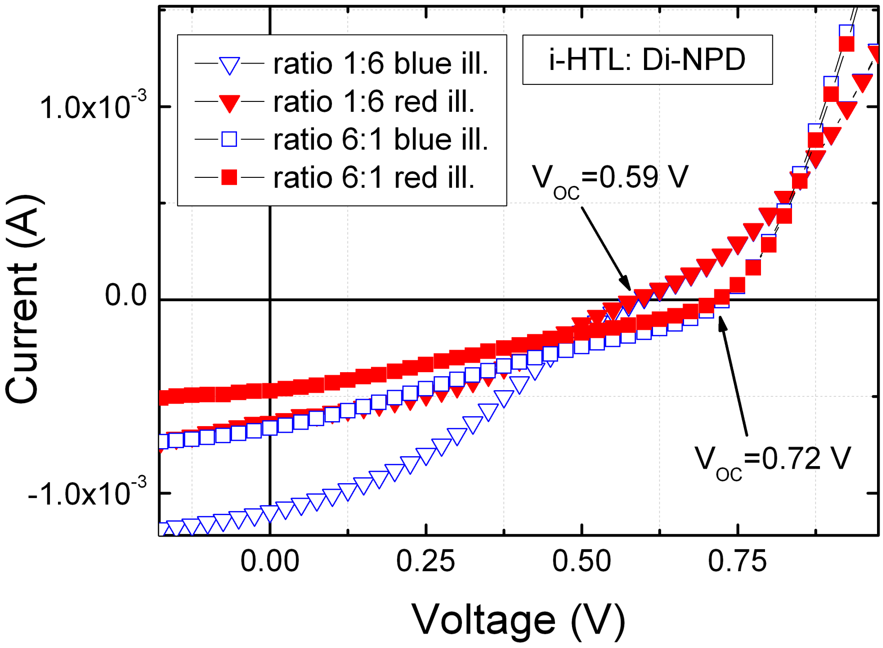

Figure 6.7: *J(V)-characteristics of p-i-i bulk heterojunction solar cells for* C_{60}*:ZnPc mixing ratio of 1:6 (upside down triangle) and 6:1 (square) with a Di-NPD hole transport interlayer measured under red (filled symbols) and blue (empty symbols) illumination.*

6.2.2 Optical characterization

In this section, we check the absorption properties for the different C_{60}:ZnPc mixing ratios of 1:6, 1:1, and 6:1. For that, we deposited 30 nm of the blend layer on quartz glass. In Fig. 6.8 we show that the absorption of C_{60} with a maximum around 450 nm is only weakly present for C_{60}:ZnPc mixing ratio 6:1, but visible for the ZnPc absorption with the two corresponding absorption peaks around 630 and 690 nm. Therefore, for the optical consideration we only focus on the ZnPc absorption. Both ZnPc peaks are red shifted by 7 nm from ratio 1:6 to 6:1. Furthermore, the peak ratios (peak heights) change for the different mixing ratios. From previous investigations, we can attribute this peak ratio shifts to a change of morphology in the blend layer, in particular to the presence of crystalline ZnPc in the 1:6 mixed layer. Due to the tendency of crystalline growth for neat ZnPc layers deposited at room temperature [113], it is not surprising that for the high ZnPc concentration of 86 vol% in the blend such features are observable. Indicated by the small peak ratio of the ZnPc, peaks of the mixing ratio 6:1, the crystalline growth of ZnPc is assumed to be supressed due to the large amount of C_{60} in the blend. However, the change of amorphous ZnPc to crystalline ZnPc in the blend might also be the reason for the slight red shift of the absorption peaks. Due to the small shift of only 7 nm, we do not expect a significant influence on the optical

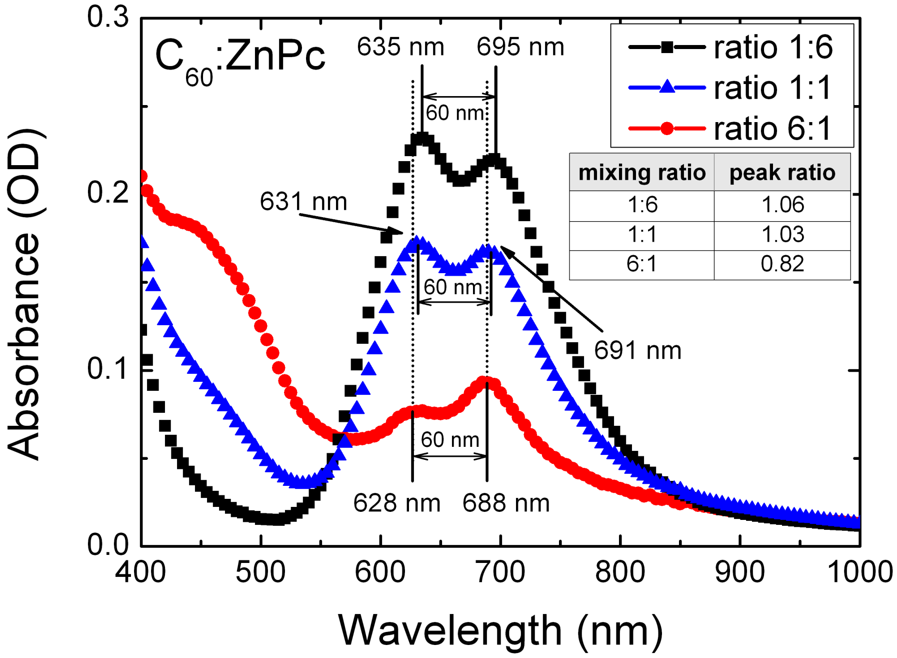

mixing ratio	peak ratio
1:6	1.06
1:1	1.03
6:1	0.82

Figure 6.8: *Absorption spectra of 30 nm C_{60}:ZnPc blend layers on quartz glass for different C_{60}:ZnPc mixing ratio mixing ratios: 1:6 (squares), 1:1 (triangles), and 6:1 (turned squares). Dotted and solid lines are guides to the eye.*

gap and the molecular energetic potentials. Thus, we also assume a constant EA - IP gap over the mixing ratio variation for at least ZnPc. Obtaining the optical gap from photoluminescence measurements is not possible due to a too low quantum yield of C_{60} and photoluminescence quenching in the blend layer. Inverse photoemission spectroscopy with an accuracy of 450 meV [237, 238] is not precise enough to get reliable information about a probable shift of the EA of C_{60} and ZnPc.

6.2.3 UPS measurements for different C_{60}:ZnPc mixing ratios

We have shown that the V_{OC} dependency on mixing ratio is an intrinsic blend layer effect, but so far we do not know what really causes this behavior. Therefore, we perform several UPS and XPS measurements on 15 nm thick C_{60}:ZnPc blend layers of different volume mixing ratios 1:6, 1:3, 1:1, 3:1, and 6:1 on Au, respectively[4]. The determined IPs of C_{60} and ZnPc are shown in Fig. 6.9. To verify this data a similar series of measurements is carried out. For clarity, they are not shown here, but confirm the observation. To accurately plot the measured IPs, the molar ratios are determined by XPS and recalculated to C_{60} volume concentration. Therefore, a shift to lower C_{60} concentration occurs, e.g. for volume ratio 1:1 (50 vol% C_{60}) to 40 vol% C_{60}. Reasons for that might be inaccurate tooling or density.

In Fig. 6.9 we illustrate the linear dependency of decreasing IP of ZnPc (filled squares) from volume ratio 6:1 to 1:3, while for high ZnPc concentrations the IP is increasing, with a linear trend to the intrinsic IP value of ZnPc (left of the dotted line). In the case of C_{60} (filled triangles) a similar behavior is observed. The IP decreases linearly up to a ratio of 1:3 and increases for lower C_{60} concentrations. For high C_{60} concentrations, the IP appears to reach the intrinsic IP value of C_{60} (right of the dotted line). ZnPc shows a much stronger decrease as C_{60}, visualized by plotting the calculated difference of the IPs in Fig. 6.10 a). The difference in the IPs is increasing linearly for lower C_{60} concentration and fits well to the observed linear V_{OC} dependency. The two values at low C_{60} concentration for C_{60} and ZnPc, which seem not to fit the linear behavior, are verified by additional measurements. However, the slope of decrease of the IPs is different for C_{60} and ZnPc.

Assuming an unchanged IP - EA gap for C_{60}, the EA of C_{60} is shifted similar to the IP. This means that the effective gap $\mathrm{IP}_{\mathrm{acceptor}}$ - $\mathrm{EA}_{\mathrm{donor}}$, which roughly determines the V_{OC}, is increasing for a higher C_{60} concentration in the blend. The difference of the IPs is increased by 0.14 eV from ratio 1:1 to 6:1 and fits well to the increase of V_{OC} from mixing ratio 1:1 to 6:1 for the BF-DPB and Di-NPD sample by 0.14 V, schematically shown for Di-NPD in Fig. 6.11. Recent UPS data of Park et al. [272] confirm this interpretation, showing that the IP of ZnPc is increased when blending with C_{60}.

However, this correlation differs for lower C_{60} concentrations due to unconsidered possible interface effects between blend and C_{60}.

In the case of MeO-TPD a lower V_{OC} of 0.60 V for mixing ratio 6:1 is observed compared to BF-DPB and Di-NPD. This loss might be explained by an injection barrier of approx. 0.2 eV between ZnPc in the mixed layer having an IP of 5.31 eV and MeO-TPD with an IP of 5.1 eV. The effect of injection barriers is discussed in more detail in section 6.3.2.

---

[4] measured by Max Tietze, IAPP, TU Dresden

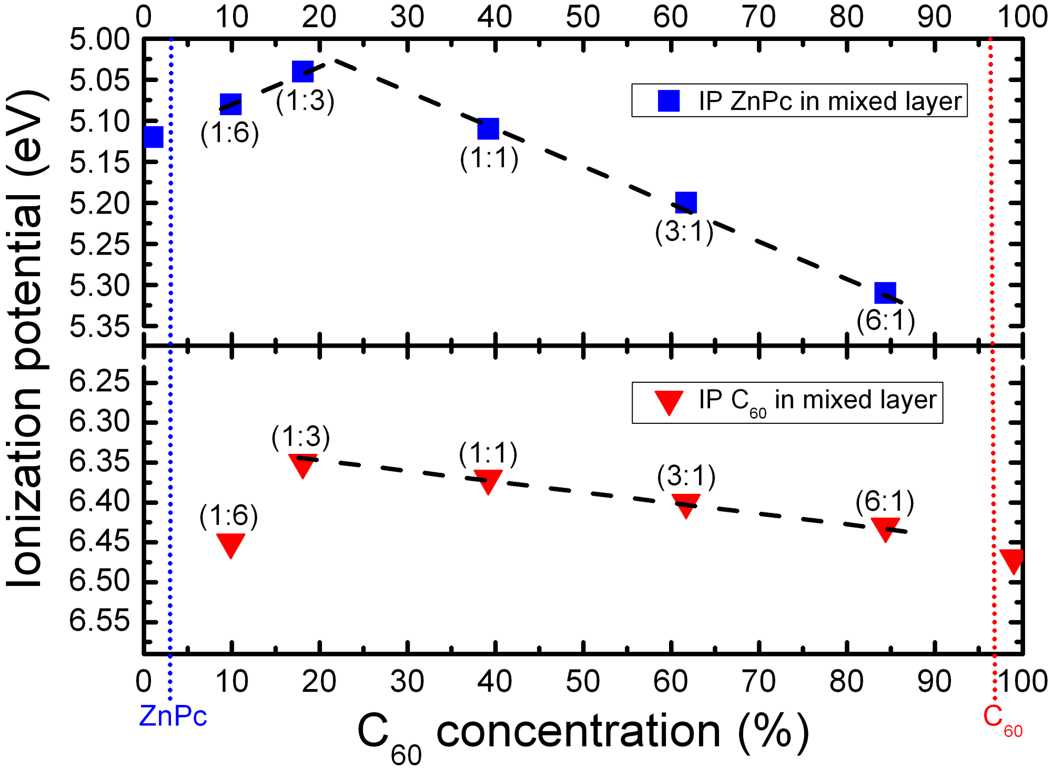

Figure 6.9: *Measured IPs of* C_{60} *(upside down triangle) and ZnPc (squares) in blend layers of different* C_{60}*:ZnPc mixing ratios (expected mixing ratio in brackets) plotted versus the mixing ratio recalculated from the molar ratio determined by XPS. Value to the left of the dotted ZnPc line corresponds to the IP of intrinsic ZnPc, similarly the value to the right of the dotted* C_{60} *line corresponds to the IP of intrinsic* C_{60}*. Dotted and dashed lines are guides to the eye.*

Of course, other factors like molecular arrangement, appearance of extraction barriers for low C_{60} concentrations in bulk heterojunction solar cells, and different interface properties between blend and i-HTL may play a role as well.

Another interesting feature is the dependency of the work function on the mixing ratio. In Fig. 6.10 b) we observe a linear correlation between work function and mixing ratio. For high C_{60} concentrations, the blend work function reaches the work function of pure C_{60}. However, in the reverse direction for low C_{60} concentrations, the blend work function does not reach the work function of pure ZnPc. A gap of approx. 0.3 eV is present. This leads to the assumption that the blend work function is dominated by the work function of C_{60}. In other words, the energetic influence of C_{60} on ZnPc seems to be stronger than the other way around. The IP of C_{60} is less affected compared to the IP of ZnPc by the variation of the mixing ratio. It seems that the attraction force with larger C_{60} amount is increased and leads to a larger IP of ZnPc. A different molecular interaction is reasonable. To verify this assumption, theoretical calculations

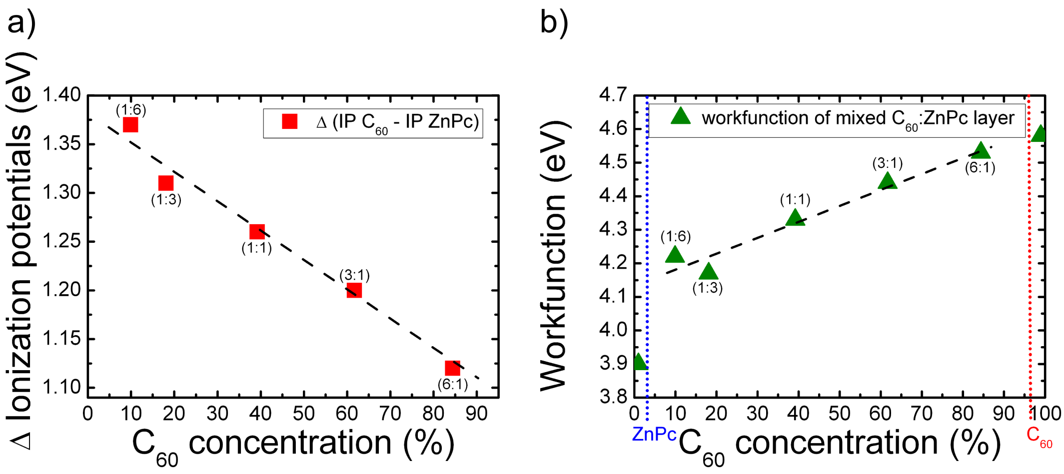

Figure 6.10: *a) Calculated difference of IP between C_{60} and ZnPc for the different mixing ratios recalculated from the molar ratio determined by XPS (expected ratios in brackets); b) measured work function versus the mixing ratio recalculated from XPS (expected ratios in brackets). Value to the left of the dotted ZnPc line corresponds to the work function of intrinsic ZnPc, the value to the right of the dotted C_{60} line corresponds to the work function of intrinsic C_{60}. Dotted and dashed lines are guides to the eye.*

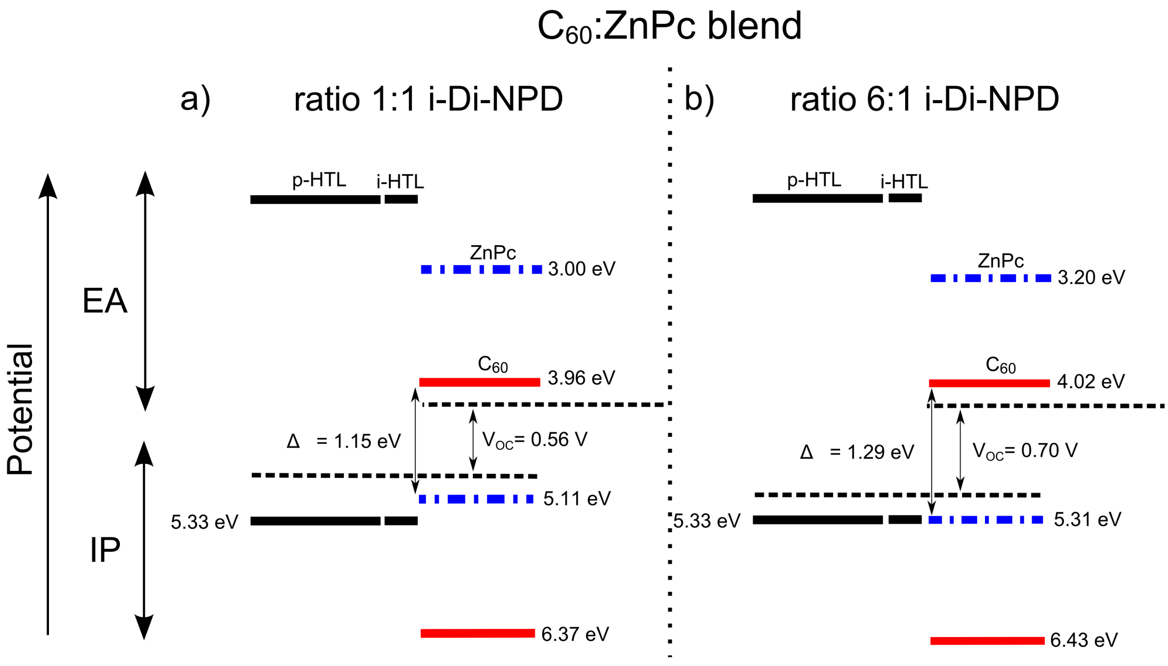

Figure 6.11: *Energy level alignment in the blend layer with C_{60}:ZnPc mixing ratio of a) 1:1 and b) 6:1, with 5 nm i-Di-NPD layer.*

are required. Independent of the exact microscopic mechanism, this interaction results in a larger effective gap IP_{donor} - $EA_{acceptor}$ and a work function dominated by C_{60}. These observations for the blend layer system of C_{60}:ZnPc differ from the observations obtained by Opitz et al. [273] for the C_{60}:CuPc system. They determined a linear energy level behavior over the whole range of mixing concentrations, for both C_{60} and CuPc. Even the difference between the energy levels remains constant, contrary to our observations. This is somehow surprising, since we expect similar molecular properties of CuPc and ZnPc [274].

In conclusion, we have shown by several experiments that the V_{OC}-mixing ratio dependency is an intrinsic blend layer effect and the change of V_{OC} is correlated to the shift of energy levels of C_{60} and ZnPc in the blend.

6.3 Influence of thin ZnPc and C_{70} interlayers on V_{OC}

In section 5.3.1.2 we showed a voltage drop by inserting a 5 nm ZnPc interlayer, in particular for blend layers with large C_{60} amounts as shown in Fig. 6.12. While V_{OC} is increased for a higher C_{60} concentration without the ZnPc interlayer (filled squares), the V_{OC} decreases for C_{60}:ZnPc mixing ratio of 1:3 with 5 nm ZnPc interlayer (filled triangles (dotted ellipse)) from 0.55 V to 0.45 V for ratio 6:1. The same phenomenon is observed inserting a 5 nm C_{70} layer between blend and C_{60} layer (filled upside down triangles (solid line ellipse)). The behavior of V_{OC} might be explained by injection barriers, which are formed at the interfaces blend/ZnPc or blend/C_{70} upon shifted IPs and EAs in the blend. Extraction and injection barriers are schematically shown in Fig. 6.13. C_{70} has a slightly higher EA (approx. 0.1 eV) as C_{60} (shown in section 4.4) which would mean an already present energy level offset of 0.1 eV from C_{60} in the blend to C_{70}. If we now take the slight change of the IP of C_{60} to smaller IPs for lower C_{60} concentrations into account, we would get an already reasonable injection barrier and thus a reduced V_{OC}.

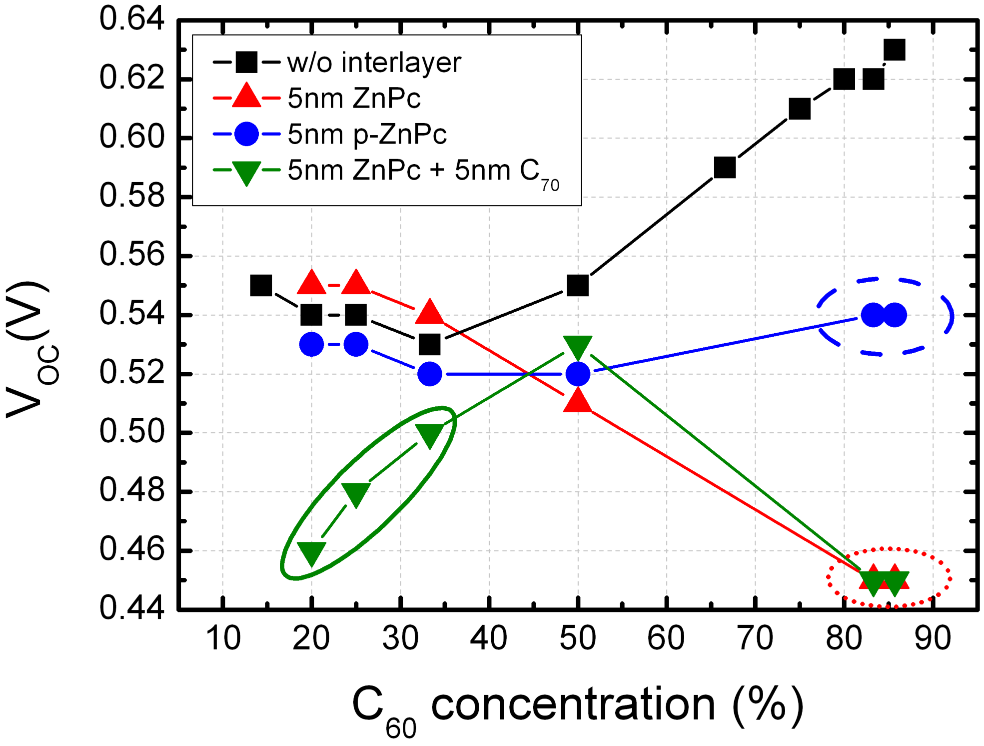

Figure 6.12: *Measured V_{OC} of p-i-i bulk heterojunction solar cells with different C_{60}:ZnPc mixing ratios and varying interlayers between p-HTL and blend: without (squares), 5 nm ZnPc (triangles), 5 nm p-ZnPc (circles), and 5 nm ZnPc + 5 nm C_{70} (between blend and i-C_{60}) (upside down triangles). Solid lines are guides to the eye.*

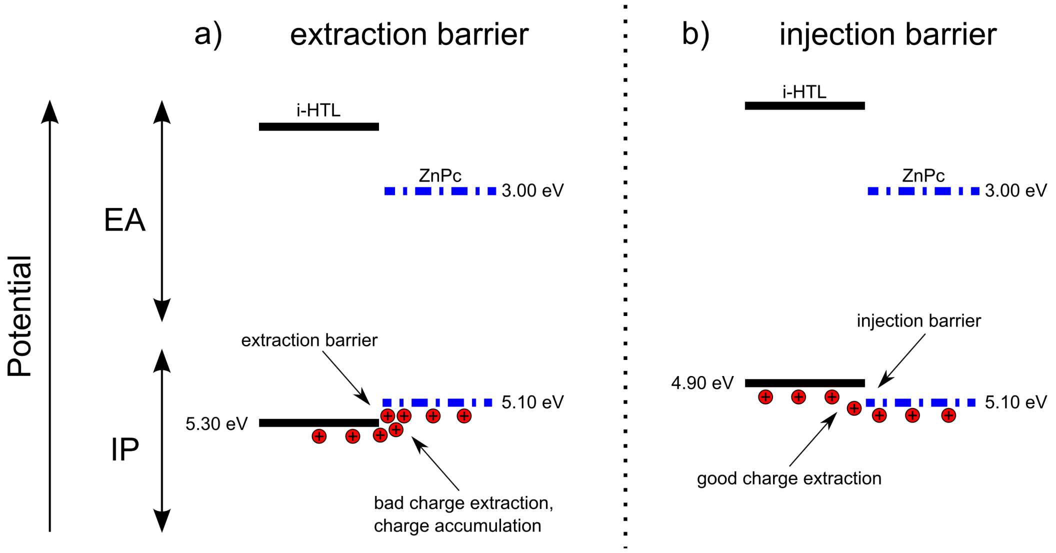

Figure 6.13: *Sketch of an a) extraction and b) non semipermeable injection barrier between an intrinsic ZnPc and hole transport layer.*

The samples with 5 nm 5 % NDP9 doped ZnPc interlayer (filled circles) exhibit no drop in V_{OC}, but a slightly higher V_{OC} with increasing C_{60} concentrations.
For a better visualization of the voltage loss, we show in Fig. 6.14 the difference of V_{OC} for the solar cells with and without 5 nm ZnPc interlayer. Up to a C_{60}:ZnPc mixing ratio of 1:2 (33 vol% C_{60}) the difference is negligible, but from ratio 1:3 up to 6:1 the difference (loss in V_{OC}) increases linearly. This observation fits well to the shift of IPs of ZnPc in the blends as shown in Fig. 6.9. We have shown that the IP of ZnPc increases with higher C_{60} concentrations. This means an increasing injection barrier to the intrinsic ZnPc layer, if we assume an unchanged IP of the adjacent intrinsic ZnPc layer.

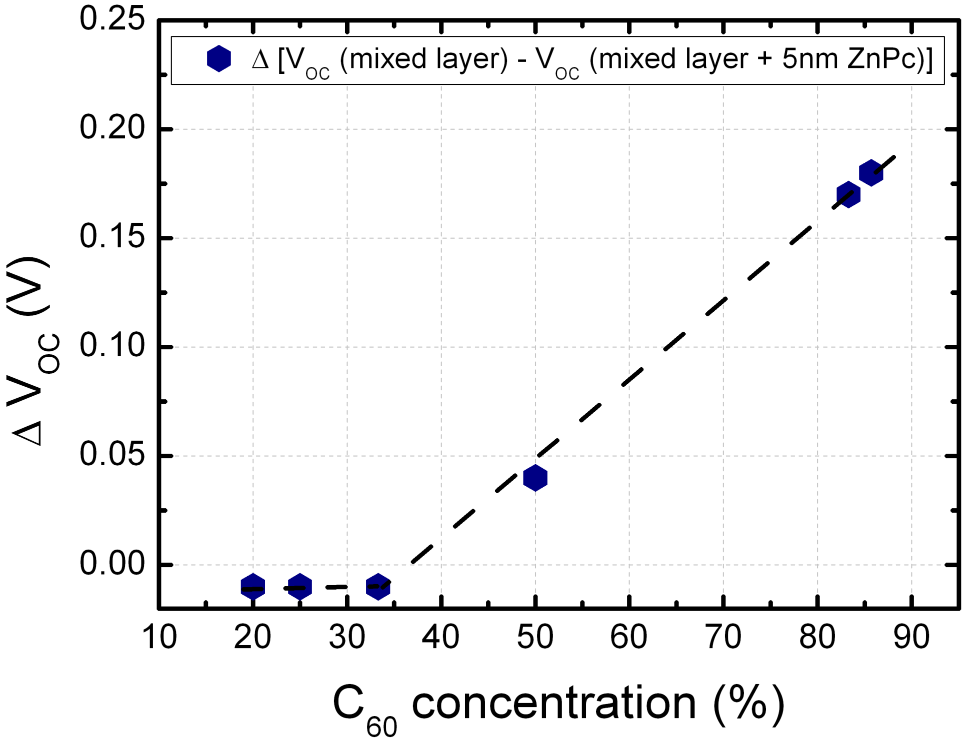

Figure 6.14: *Calculated difference of V_{OC} measured for the p-i-i bulk heterojunction solar cells with and without 5 nm ZnPc interlayer for different C_{60} mixing concentrations determined by XPS. The dashed line is a guide for the eye.*

6.3.1 UPS measurements of blend/ZnPc interfaces

To check how the additional 5 nm ZnPc layer is energetically aligned to the blend layer with different mixing ratios, UPS measurements are carried out[5]. Here, we use the already measured blend samples and measure again after depositing the intrinsic 5 nm ZnPc on top of the blend. In Fig. 6.15 the measured IPs of the additional ZnPc layer for the different mixing ratios are shown (filled circles). We obtain values of the IP of around 5.0 eV within the error range of 50 meV. The values are slightly below the IP of a thick intrinsic ZnPc layer (IP of 5.07 - 5.12 eV [5]).

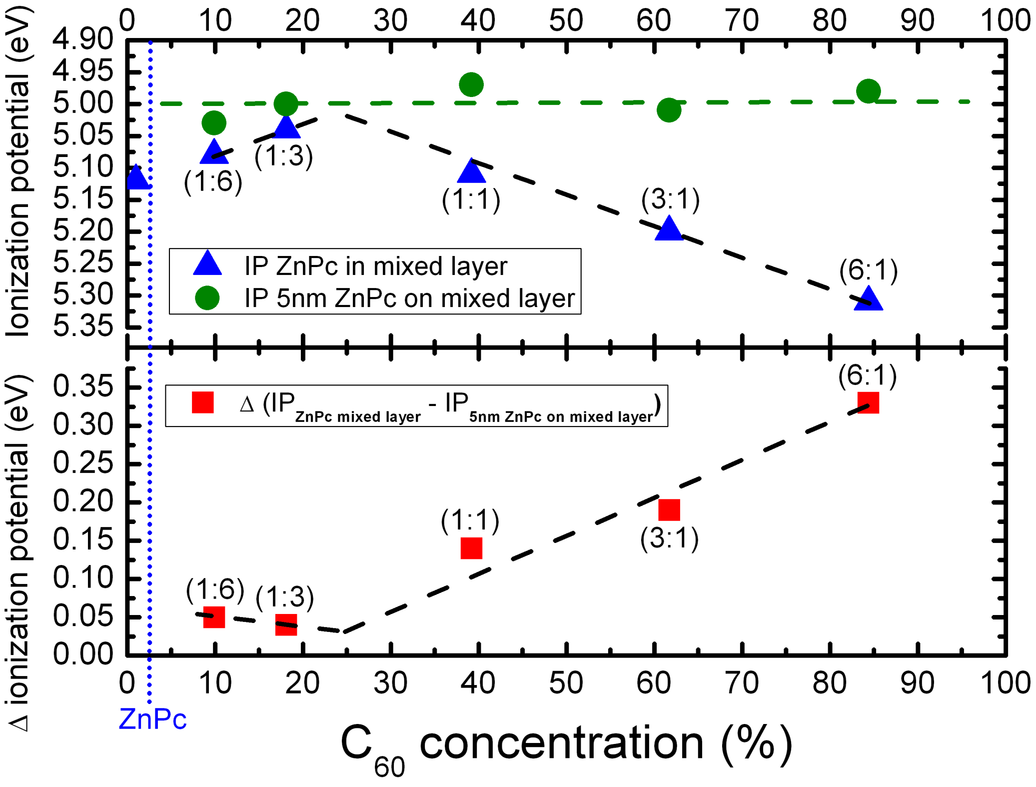

Figure 6.15: *Upper graph: measured IP of ZnPc (triangles) in the C_{60}:ZnPc blend and 5 nm ZnPc (circles) on the blend versus C_{60} mixing concentration determined by XPS (expected ratios in brackets). Value to the left of the dotted ZnPc line corresponds to the IP of intrinsic ZnPc; lower graph: calculated difference of the IP (squares) of ZnPc in the blend and ZnPc on the blend versus C_{60} mixing concentration. Dotted and dashed lines are guides to the eye.*

Comparing the determined IPs of the ZnPc layer with the IPs of ZnPc in the mixed layer (filled triangles) and calculating the difference of the IPs (filled squares), we observe an increasing gap between both IPs from 0.05 to around 0.30 eV with increasing C_{60} concentration. These energy barriers can be attributed to charge carrier injection

---

[5] measured via UPS by Max Tietze, IAPP, TU Dresden

barriers and are in good agreement with the observed V_{OC} drop as shown in Fig. 6.14. The observed Δ IP in Fig. 6.15 correlates with the ΔV_{OC} in Fig. 6.14 for the solar cell devices with and without the intrinsic ZnPc layer. The difference between the IP of around 0.30 eV leads to a drop of 0.18 V in V_{OC}.

However, for this layer sequence an interface dipole is measured for the samples with larger C_{60} concentrations. This induces a vacuum level shift between the ZnPc in the blend layer and intrinsic adjacent ZnPc layer. The vacuum level shift is on the order of 0.28 eV and might compensate the injection barrier.

Due to the fact that the solar cell is inversely stacked, we also performed UPS measurements for a mixing ratio of 6:1 with respect to the layer sequence. Starting with a doped MeO-TPD layer, the following layers are deposited successively after conducting the corresponding UPS measurement. The layer sequence and the measurement data are shown schematically in Fig. 6.16.

It can be seen that the ZnPc layer deposited on top of the p-MeO-TPD layer as well

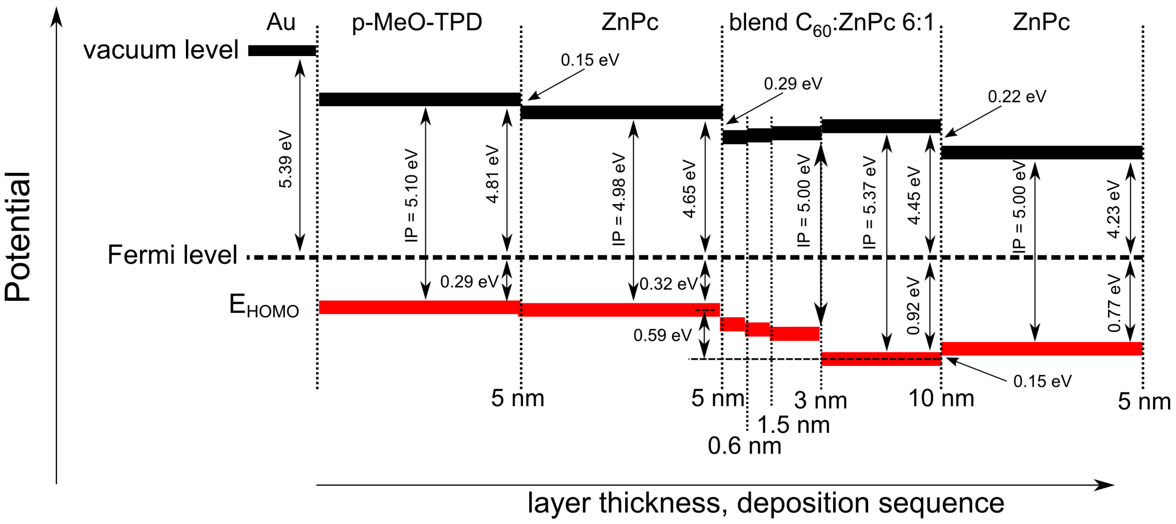

Figure 6.16: *UPS measurement of the layer sequence with respect to the solar cell. The vacuum levels (black solid lines) with the dipoles at the interfaces are shown above the Fermi level (dashed line). Below, the HOMO levels (red solid line) are shown which already imply the vacuum level shift caused by the interface dipoles.*

as the ZnPc layer deposited on top of the mixed C_{60}:ZnPc layer exhibit an IP of around 5.0 eV. The IP of the ZnPc in the blend layer is measured to be 5.37 eV and is in good accordance to the value determined previously from the inverted structure. This leads to a difference of the IPs between the blend and the adjacent ZnPc layer of around 0.37 eV. The low IP of ZnPc in the mixed layer of the first few nanometers is probably caused by the ZnPc signal of the layer below and the weak amount of ZnPc in the mixed layer leading to a rather small signal. Furthermore, we show that an interface dipole is also created between the intrinsic ZnPc layer and the ZnPc in the blend on the order of 0.2 eV. However, in this particular case, the vacuum level shift might even increase the effect of the injection barrier. In the following, we only focus on the IPs and their correlation to barrier heights and loss in V_{OC}.

6.3.2 Blend/ZnPc injection barrier: experiment and simulation

To clarify whether an injection barrier is really responsible for the drop in V_{OC} for the devices with the thin ZnPc interlayer, electrical simulations are carried out by Wolfgang Tress (IAPP).

In a first approximation, we use in the simulations the following layer sequence and parameters with a ZnPc layer thickness variations (d) of 5, 10, 15, 25 nm:

C_{60}(5 nm)/C_{60}:ZnPc(30 nm)/ZnPc(Δ d)/ZnPc(30 nm). The used energy levels and mobilities are listed in table 6.2 and the simulated *J(V)*-curves are shown in Fig. 6.17. To simulate a barrier free injection and extraction from the blend, we set the IP of the 10 nm i-ZnPc (squares) to the same IP in the blend of 5.2 eV. Realizing an injection barrier, we set the IP of i-ZnPc to 5.1 eV which is 0.1 eV lower compared the ZnPc in the blend. The simulation with an assumed injection barrier of 0.1 eV confirms a drop of V_{OC} with an adjacent 5 nm ZnPc layer. Additionally, the simulation shows a further decrease of V_{OC} with increasing ZnPc layer thickness.

Table 6.2: *Values and parameters used for the first approximation simulation of the J(V)-curve shown in Fig. 6.17.*

	IP (eV)	**E_g (eV)**	**μ_h (cm^2/Vs)**	**μ_e (cm^2/Vs)**
i-C_{60}	6.4	2.4	1.2×10^{-4}	1.0×10^{-3}
blend C_{60}	6.4	1.2	1.2×10^{-4}	1.0×10^{-3}
blend ZnPc	5.2	1.2	1.2×10^{-4}	1.0×10^{-3}
i-ZnPc (d)	5.1	3.0	1.2×10^{-4}	3.5×10^{-4}
i-ZnPc	5.1	3.0	1.2×10^{-4}	3.5×10^{-4}

To verify the simulations with experimental data, we perform a Lesker run with a C_{60}:ZnPc mixing ratio variation from 1:6 to 6:1 and intrinsic ZnPc layer thickness variation from 0 - 20 nm. The V_{OC} dependency of the samples is shown in Fig. 6.18.

We do not observe any drop in V_{OC} for the ZnPc layer thickness variation (left and right turned triangles), as expected from the IP measurements that no significant injection barriers are formed between the C_{60}:ZnPc mixing layers for ratios 1:6 and 1:3 to the intrinsic ZnPc layer. With increasing Δ IP, we see already a weak ZnPc layer thickness dependency for ratio 1:1 (tilted squares), which is much more pronounced for the ratios 2:1, 4:1, and 6:1. Especially for ratio 2:1, 4:1, and 6:1, the V_{OC} reaches a saturation value for thick ZnPc interlayers. Calculating the V_{OC} difference for the 6:1 ratio sample for 0 nm (0.65 V) and 20 nm (0.35 V) ZnPc layer, we get a difference of around 0.30 V. This fits very well to the Δ IP of 0.3 eV obtained in Fig. 6.15 for ratio 6:1 between the IP of ZnPc in the blend and the adjacent intrinsic ZnPc layer.

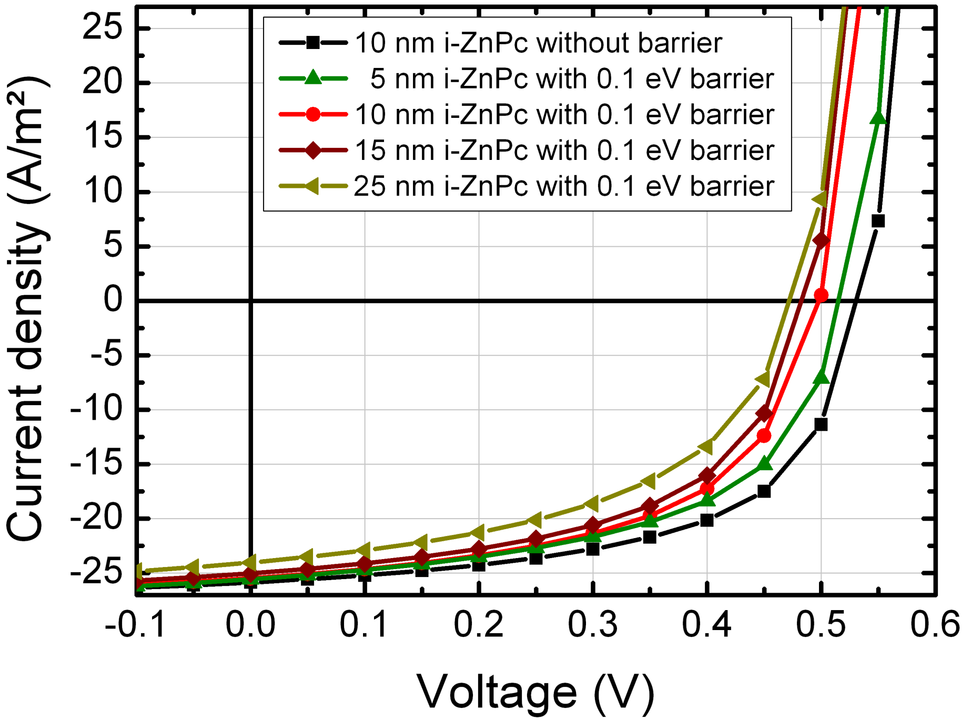

Figure 6.17: *Simulation of J(V)-curves with and without an injection barrier of 0.1 eV as a first approximation with a layer sequence of* C_{60}*(5 nm)/*C_{60}*:ZnPc(30 nm)/ZnPc(d)/ZnPc(30 nm), mixing ratio of 1:1 and intrinsic ZnPc layer thickness variation d from 5 - 25 nm.*

Also the $\Delta V_{OC} \approx \Delta$ IP dependency is observed for ratios 4:1 (0.26 V ≈ 0.27 eV) and 2:1 (0.17 V ≈ 0.17 eV). Only the ratio 1:1 shows a slight discrepancy which leads to the assumption that the V_{OC} has not reached the final drop for the 20 nm ZnPc layer and is expected to further decrease close to 0.40 V for a thicker ZnPc layer.

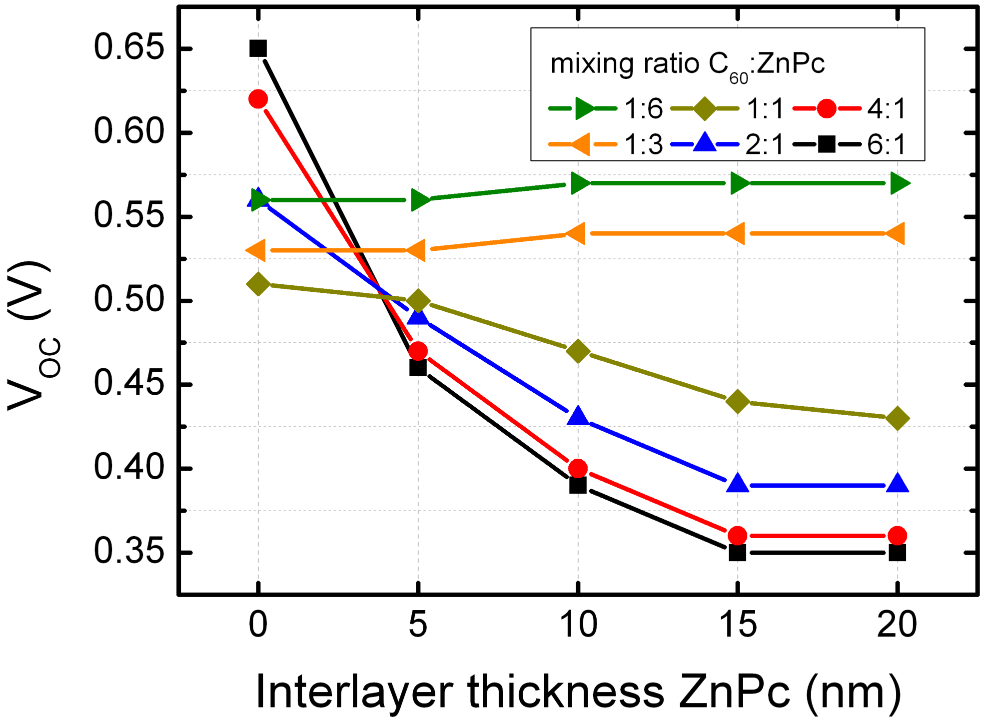

Figure 6.18: *Measured* V_{OC} *of p-i-i bulk heterojunction solar cells for different* C_{60}*:ZnPc mixing ratios: 1:6 (right turned triangles), 1:3 (left turned triangles), 1:1 (turned squares), 2:1 (triangles), 4:1 (circles), and 6:1 (squares) dependent on the ZnPc interlayer thickness between p-HTL and blend. Solid lines are guide for the eyes.*

With additional more to the solar cells stack related electrical simulations by taking the calculated E_g and measured IPs for ZnPc and C_{60} into account, we compare V_{OC} with the values obtained from the experiment.

For the simulation we used the following layer sequence as in the solar cells: p-HTL(5 nm)/ZnPc(Δ d)/C_{60}:ZnPc(30 nm;X:Y). The used energy levels and mobilities are listed in table 6.3. Because of simplification and the focus on the energetics of the device we used the same mobilites for ratio 1:1 and 6:1. The change of mobility would have a major impact on the *FF*, but a minor on V_{OC}. To achieve a similar V_{OC} as measured in the experiments for the sample without ZnPc interlayer, the β factor of the Langevin equation, which stands for the bi-molecular recombination process, is set to $0.5\,\mathrm{m}^3/s$ for ratio 1:1 and 6:1. In the case of the barrier free samples, we set the IP of the adjacent ZnPc layer to the same value of ZnPc in the blend, which means an IP of 5.11 eV for ratio 1:1 and 5.31 eV for ratio 6:1.

Table 6.3: *Values and parameters used for the simulation of the J(V)-curves shown in Fig. 6.19 a) and b). The layer sequence is: p-HTL(5 nm)/ZnPc(Δ d)/C_{60}:ZnPc(30 nm;X:Y) with mixing ratio of 1:1 and 6:1 and ZnPc layer thickness of 0, 5, and 15 nm. Energy levels and calculated E_g are taken determined by UPS measurements.*

ratio 1:1	**IP (eV)**	**E_g (eV)**	**μ_h (cm²/Vs)**	**μ_e (cm²/Vs)**
HTL	5.35	3.0	1.0×10^{-3}	1.0×10^{-5}
ZnPc (Δ d)	4.97	2.30	5.0×10^{-4}	1.0×10^{-3}
blend ZnPc	5.11	1.12	1.0×10^{-5}	1.0×10^{-3}
blend C_{60}	6.43	2.38	1.0×10^{-5}	1.0×10^{-3}

ratio 6:1	**IP (eV)**	**E_g (eV)**	**μ_h (cm²/Vs)**	**μ_e (cm²/Vs)**
HTL	5.35	3.0	1.0×10^{-3}	1.0×10^{-5}
ZnPc (Δ d)	4.97	2.3	5.0×10^{-4}	1.0×10^{-3}
blend ZnPc	5.31	1.26	1.0×10^{-5}	1.0×10^{-3}
blend C_{60}	6.43	2.38	1.0×10^{-5}	1.0×10^{-3}

From the simulations depicted in Fig. 6.19 a and b) for ratio 1:1 and ratio 6:1, respectively, we obtain similar values of V_{OC} compared to the values determined experimentally for the samples without a ZnPc interlayer. Furthermore, we observe a strong reduction of V_{OC} with a thin ZnPc interlayer of 5 nm. For the 15 nm ZnPc interlayer, the V_{OC} is then slightly further lowered. First of all, the decrease of V_{OC} for the 5 nm interlayer contradicts the first approach simulation. Reasons for that might be the inverted layer sequence and estimated parameters applied in the first simulation.

However, for ratio 6:1 with 15 nm ZnPc interlayer, we note that the V_{OC} reaches the

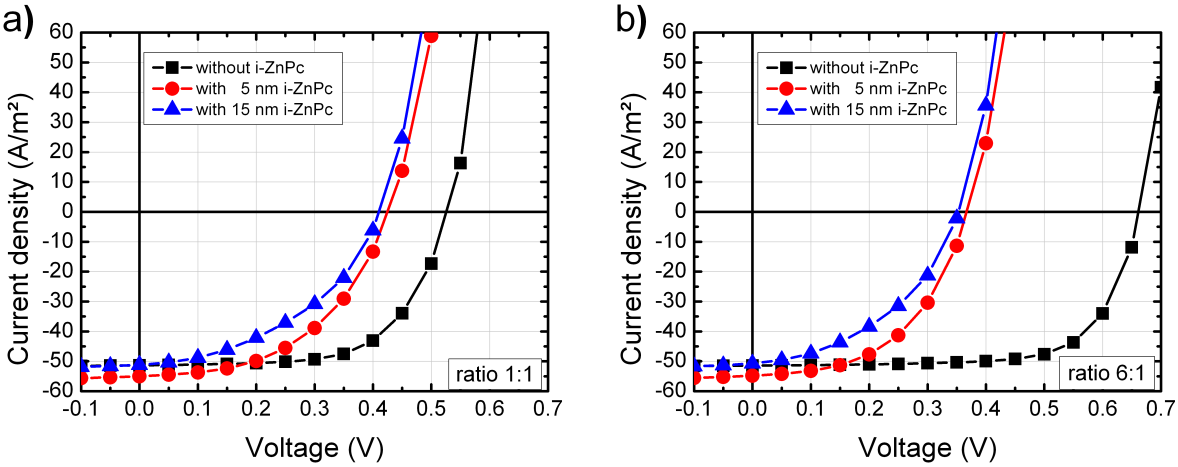

Figure 6.19: *Simulation of J(V)-curves of the layer sequence p-HTL(5 nm)/ZnPc(Δ d)/C_{60}:ZnPc(30 nm;X:Y) with mixing ratios a) 1:1 and b) 6:1. Dependency of the intrinsic adjacent ZnPc layer thickness is shown: 0 nm (squares), 5 nm (circles), and 15 nm (triangles), respectively.*

value of 0.35 V which is in agreement with the V_{OC} of 0.35 V obtained from experiment. Similar behavior is observed for ratio 1:1. The simulation gives a V_{OC} of 0.41 V and fits well to the experimentally measured V_{OC} of 0.43 V. It means that the height of the injection barrier strongly correlates with the loss of V_{OC} [222].

Accordingly, we formulate a hypothesis which might explain the increasing loss of V_{OC} for solar cells with mixing ratios of 1:1, 2:1, 4:1, and 6:1 with increasing intrinsic ZnPc layer thickness and increasing injection barriers.

By increasing the ZnPc layer thickness, the quasi-Fermi level which is created upon illumination for the holes in the blend is bent to lower potential energy to the IP of the adjacent intrinsic ZnPc layer and thus reduces the V_{OC}. The V_{OC} decreases until the ZnPc layer reaches a thickness of around 15 nm. The Fermi level of the doped HTL, which is close to the IP of the HTL, has a strong influence on the Fermi level alignment in the intrinsic ZnPc layer. It means that for a thin ZnPc layer, the quasi-Fermi level of the blend is pinned to the doped HTL through the thin intrinsic ZnPc layer up to a ZnPc layer thickness where the influence disappears.

For a better understanding, we visualize the hypothesis in Fig. 6.20 for C_{60}:ZnPc mixing ratio 1:1 and 6:1 for ZnPc interlayer thicknesses of 0 nm, 5 nm, and 15 nm. In case of C_{60}:ZnPc mixing ratio 1:1 and no ZnPc interlayer a) we have no injection barrier, but an extraction barrier which has no influence on V_{OC}. We assume a slight reduction of the quasi-Fermi level at the p-HTL/blend interface due to a direct recombination path, which means dopant induced charge carrier and exciton quenching. With the 5 nm ZnPc layer b) and an assumed injection barrier of 0.1 eV between blend and i-ZnPc, the quasi-Fermi level is slightly shifted upwards in comparison to a). We presume that the quasi-Fermi level of the blend is pinned through the thin ZnPc layer. Therefore, the injection barrier has only a small influence on V_{OC}. However, with increasing ZnPc layer thickness c) the pinning effect weakens and the quasi-Fermi level is further shifted upwards, meaning a further deceased V_{OC}. It seems that a stable value of V_{OC} is not reached yet. A further influence of the barrier is expected until a layer thickness where the V_{OC} becomes stable and the drop in V_{OC} is close to the barrier of approx. 0.1 eV.

The same conclusion can be drawn for C_{60}:ZnPc mixing ratio 6:1. Without a ZnPc layer d) we assume a similar dopant induced charge carrier and exciton quenching at the p-HTL/blend interface, leading to a reduction in V_{OC}. However, for this mixing ratio no extraction barrier is formed between blend and p-HTL due to similar IPs. When inserting a 5 nm ZnPc layer e) with an IP of approximately 5.0 eV, an assumed injection barrier on the order of 0.3 eV is created from the blend to the intrinsic ZnPc layer. With this 5 nm ZnPc interlayer, we observed a loss in V_{OC} of 0.19 V, which is lower than the injection barrier. Taking the assumed pinning effect into account would mean that the quasi-Fermi level is strongly shifted to the IP of the intrinsic ZnPc layer. With increasing ZnPc layer f) the pinning effect disappears and the quasi-Fermi level is shifted to lower potential energy on the order of the injection barrier of 0.3 eV and is in accordance with the loss in V_{OC} of 0.3 V.

In case of 5 nm 5 % NDP9 doped ZnPc interlayer we observe in Fig. 6.12 a different V_{OC} behavior. V_{OC} does not decrease, but slightly increases with larger C_{60} amount in the blend and shows the opposite behavior in comparison to intrinsic ZnPc. However, this behavior is also in accordance with our hypothesis: Due to the Fermi level shift in the doped ZnPc layer upon doping close to the IP, the quasi-Fermi level from the blend can easier pin through the thin p-doped ZnPc layer to the p-HTL. Upon doping the interface might also be energetically modified (e.g. band bending or vacuum level shift).

Additional electrical simulations shown in Fig. 6.21 are carried out to display the distribution of the IPs, EAs, and quasi-Fermi levels at V_{OC} condition of the layer sequence: p-HTL(5 nm)/ZnPc(Δ d)/C_{60}:ZnPc(30) nm for ratio 1:1 and 6:1 with and without 15 nm ZnPc interlayer, respectively. Note that band bending is taken into account which lead to shifted energy levels in the figures. The simulation confirms the bending of the quasi-Fermi level for holes to lower potential energy to the IP of the adjacent ZnPc layer, if an injection barrier is present. Without an injection barrier, the quasi-Fermi level is well aligned to the Fermi level of the p-doped layer. However, the correlation between ZnPc layer thickness and V_{OC} loss, attributed to a quasi-Fermi level pinning effect can not be reproduced by simulation. To clarify if the pinning effect is real, one might consider experiments where the quasi-Fermi level can be measured under illumination for the layer stack ZnPc/blend. These results can then be implemented into the model and might then further improve the simulation data.

The results shown on the injection barrier are in good accordance with the recent publication by Tress et al. [222].

In conclusion, we have shown that injection barriers reduce V_{OC} in the order of the barrier height. Furthermore, we showed that the decrease of V_{OC} depends on the thickness of adjacent intrinsic ZnPc layer. Upon these observations we proposed a hypothesis which explains the correlation between injection barrier, V_{OC}, and intrinsic layer thickness.

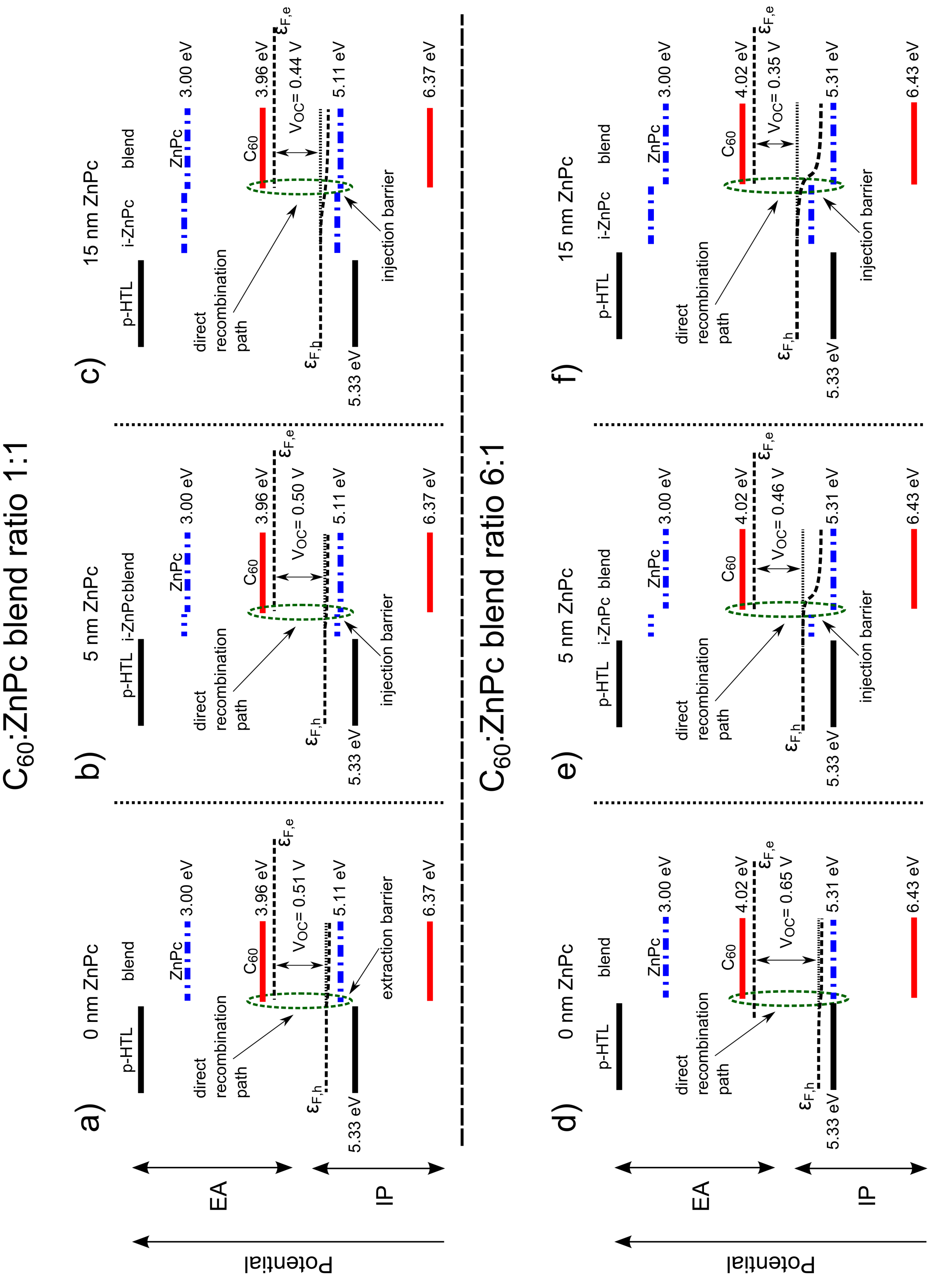

Figure 6.20: *Visualization of energy level alignment and quasi-Fermi level (ϵ_F) pinning depending on the adjacent ZnPc layer thickness (0, 5, and 15 nm) for C_{60}:ZnPc mixing ratio 1:1 and 6:1, respectively. Here, we focus only on the interface blend and adjacent layer and do not consider band bending or a shift of the vacuum level.*

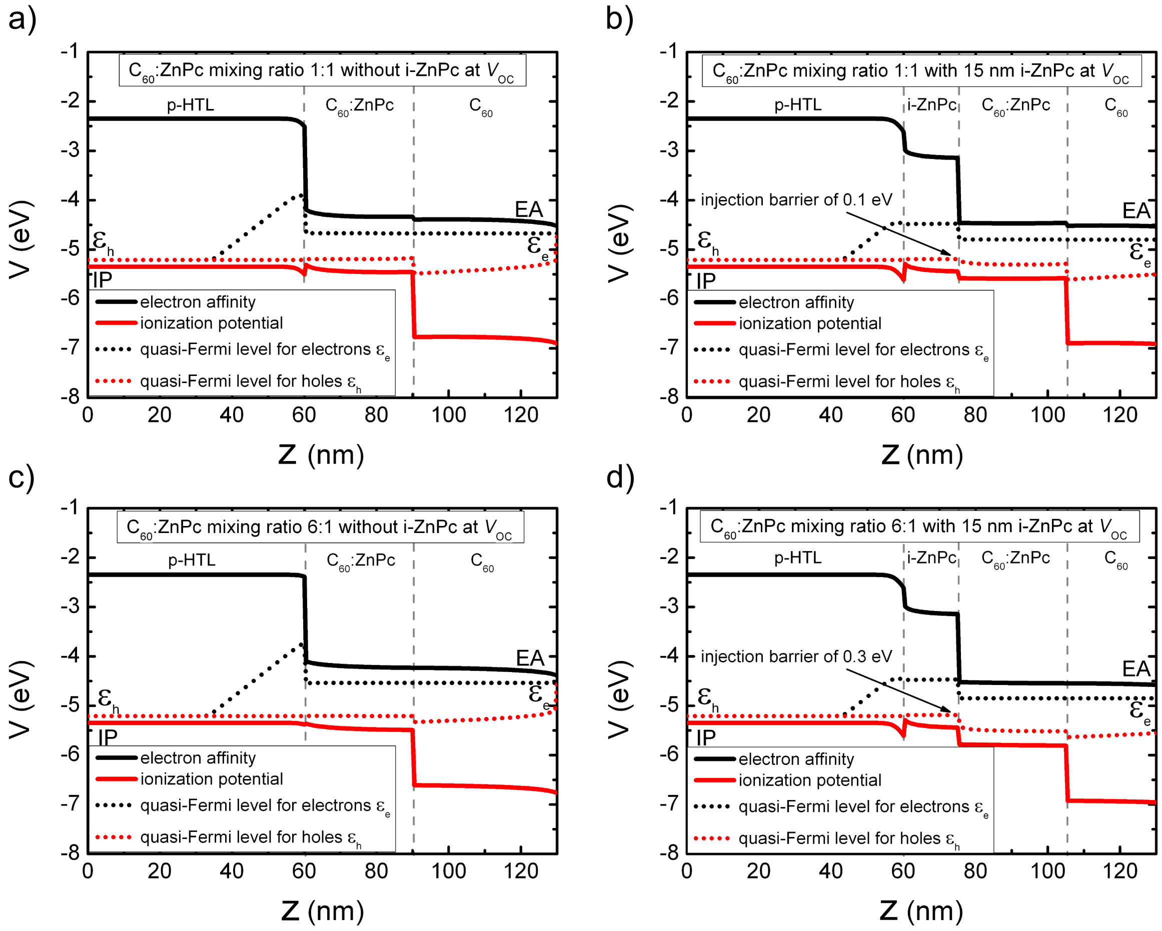

Figure 6.21: *Simulation of the potentials V (solid lines) and quasi-Fermi levels (dotted lines) in the stack: p-HTL(5 nm)/ZnPc(Δ d)/*C_{60}*:ZnPc(30 nm;X:Y) with mixing ratios 1:1 [a),b)] and 6:1 [c),d)]. Dependency of the intrinsic adjacent ZnPc layer thickness is shown for 0 nm [a),c)] and 15 nm [b),d)], respectively. Band banding leads to shifted energy levels in the plot. The gaps of the quasi-Fermi levels at the p-HTL and* C_{60} *interface, respectively, are caused by too low intrinsic charge carrier densities of electrons in the p-HTL and holes in the* C_{60} *layer and are simulation errors with no influence on the results of the J(V)-characteristics.*

7 Conclusion and Outlook

We briefly summarized the three main topics of this thesis: the new fullerene C_{70} as replacement for C_{60} in organic solar cells, the impact of substrate heating during blend layer deposition of BHJ with its sublayer dependency, and the correlation V_{OC}, C_{60}:ZnPc mixing ratio, and ZnPc interlayer. Furthermore, we give a short outlook and suggestions for future work.

In the part of this thesis we introduced C_{70} from the class of fullerenes. The motivation was to characterize the fullerene and to check a possible replacement of the standard acceptor molecule C_{60}, as used in vacuum processed organic solar cells.

From optical spectroscopic investigations we showed that a thin C_{70} layer has a stronger and spectrally broader absorption in the visible range of light compared to C_{60}. We determined an absorption coefficient of $2.1\times10^{5}\,\mathrm{cm}^{-1}$ for C_{70} at the maximum absorption peak at 515 nm. Mobility measurements in the saturation regime were carried out using organic field effect transistors. A smaller electron mobility of 6.9×10^{-3} for C_{70} in comparison to 9.2×10^{-3} for C_{60} was obtained. With ultraviolet photoelectron spectroscopy, the ionization potentials were measured for both C_{60} and C_{70} to 6.41 eV. Taking the obtained optical gap of around 1.8 eV and electrical gap of around 2.4 eV into account, we estimated an exciton binding energy of approximately 0.6 eV. We concluded from the IP that there exist an efficient exciton separation at the C_{70}/ZnPc heterojunction interface. First implementations of C_{70} in organic devices was done for flat heterojunction solar cells with a variation of the donor using the wide gap material Di-NPD and the absorber material ZnPc. From the variation of the fullerene layer thickness and external quantum efficiency measurements, we estimated the C_{70} exciton diffusion length to be between 10 - 15 nm, compared to 20 nm for C_{60}. Therefore C_{70} lead to a less efficient flat heterojunction solar cell. However, we showed with the concept of bulk heterojunctions, where the exciton diffusion length plays only a negligible role, the whole potential of C_{70}. For a C_{70}:ZnPc mixing ratio of 2:1, we obtained a p.c. efficiency of 3.1 % compared to 2.5 % for the C_{60} composed solar cell. We showed that this can mainly be attributed to the stronger absorption of C_{70} and efficient conversion into photocurrent.

Concerning future experiments, we dedicated an outlook section to the fullerene C_{84}

in the end of chapter 4 (page 101) with more details about its potential and the usage in vacuum processed organic solar cells. This fullerene was already investigated as [84]PCBM in solution processed organic solar cells, showing low performance with a power conversion efficiency of 0.25 %. However, C_{84} seem to have an exentended absorption in the near infrared and give the option to harvest photons from this so far rarely used part of the sun spectrum.

In the second part investigations on the influence of substrate heating during the deposition of the blend layer C_{60}:ZnPc with sublayer C_{60} were carried out. For 60 nm thick blends in a m-i-p stacked solar cells the maximum of J_{SC} and an increased FF at an optimum substrate temperature of 110°C was found. The p.c. efficiency was improved by a factor of two from 1.4 % to 3.0 %. With topography analyses by AFM and SEM and the observation of ZnPc nano and polycrystalline domains in a lateral dimension on the order of 50 nm measured by TEM, we were able to show molecular phase separation of C_{60} and ZnPc in the blend. The enhanced ZnPc hole mobility in the blend of $2.2\times10^{-4}\,\mathrm{cm}^2/\mathrm{Vs}$ measured using OFETs is one order of magnitude higher compared to the blend layer prepared at ambient condition. We concluded improved charge carrier percolation and charge transport in and through the blend layer with reduced charge carrier recombination.

Additionally, solar cells with a blend layer of C_{70}:ZnPc were processed during substrate heating, but only obtained small improvements with respect to J_{SC} and FF. From SEM and TEM measurements it turned out that the molecular phase separation, as observed for C_{60}:ZnPc, did not appear at higher substrate temperature.

We determined a similar suppressed aggregation and phase separation in the blend of p-i-i stacked solar cells, where the sublayer of the blend was a p-doped Di-NPD layer and not a C_{60} layer as in the m-i-p stack. We concluded that an influence, either energetically or morphologically, of the sublayer on the phase separation in the blend layer. With the usage of a 5 nm thin interlayer of ZnPc between p-HTL and blend, an initialized weak phase separation was observed with SEM and TEM, which lead to a small increase of J_{SC} and FF, but also to a drop in V_{OC}.

For future work, systematic investigations of the morphology and molecular phase separation of C_{70}:ZnPc blend layers depending on the substrate temperature during deposition and underlayer are of interest. The questions are, can a phase separation, as seen for the C_{60}:ZnPc blend, be achieved by supplying a higher thermal energy and how is it related to the molecular structure of the fullerenes? In addition, knowledge of the dependency on the molecular phase separation of the choice of sublayer is of importance. Can this be attributed to an energetic or morphological impact and does it follow a specific rule?

In the third part we focused on the V_{OC} dependency on the mixing ratio of C_{60}:ZnPc BHJ and the drop of V_{OC} when using an additional ZnPc layer between p-HTL and blend layer. With the variations of the HTL material and separated illumination measurements in the red and blue spectrum, we showed that the increase of V_{OC} on the order of 0.1 V, with larger C_{60} amounts, is attributed to an intrinsic blend layer effect. This hypotheses was proven by UPS measurements, where we determined and showed a different intense change of the IPs of 0.1 and 0.3 eV for C_{60} and ZnPc upon C_{60}:ZnPc mixing ratio from 1:3 - 6:1. The reason for the increase of V_{OC} depending on mixing ratios with larger C_{60} amount is the increased effective band gap, assuming an unchanged optical gap. In addition, we have shown the influence of a thin ZnPc interlayer between p-HTL and blend on V_{OC}. For blend layers with C_{60} concentrations larger than 30 %, we found that the ZnPc in the blend shows an increasing IP compared to the adjacent ZnPc layer having a constant IP of around 5.0 eV. Using electrical simulations, we confirmed our hypothesis of injection barriers and also showed the correlation between barrier height and voltage drop. Furthermore, we drew up a hypothesis on the observed correlation between V_{OC} reduction and ZnPc layer thickness.

For the future work, the different behavior of the molecules CuPc and ZnPc with respect to the change of IPs in the blend for different mixing ratios might be considered. Theoretical calculations might be useful to understand in detail the shift and dependency of the IP on the various blend ratios. Concerning the V_{OC} dependency on the ZnPc interlayer in p-i-i stacked solar cells, it is of interest to check this also for the inverted m-i-p or n-i-p stacked solar cells and imply the interface effects (e.g. interface dipoles) in the consideration. In the last part, we drew up the hypotheses of the ZnPc thickness dependency on V_{OC}, which have to be checked with appropriate experiments. The understanding of this issue helps to avoid an undesired loss in efficiency and to further improve device performance.

Bibliography

[1] W. E. Council, 2010 Survey of Energy Resources, (2010).

[2] IEA (International Energy Agency) World Energy Outlook 2006, (2006).

[3] IPC (International Post Corporation), Join IPC Live at Copenhagen Climate Conference, International Post Corporation **6** (2009).

[4] EPIA (European Photovoltaic Industry Association), 7th European PV Industry Summit: "Towards PV Competitiveness" 6 September 2010 - Valencia, Spain, (2010).

[5] W. B. der Bundesregierung Globale Umweltveränderungen (WBGU), Welt im Wandel-Energiewende zur Nachhaltigkeit, (2003).

[6] Solarbuzz, http://www.solarbuzz.com/industry-news/solarbuzz-reports-world-solar-photovoltaic-market-grew-182-gigawatts-2010-139-yy (accessed 6 June 2011).

[7] roll-to-roll production, http://www.osa-direct.com/osad-news/243.html (accessed 23 February 2011).

[8] D. Wallace, D. Hayes, T. Chen, V. Shah, D. Radulescu, P. Cooley, K. Wachtler, and A. Nallani, THINK ADDITIVE: Ink-Jet Deposition of Materials for MEMS Packaging, 6th Topical Workshop on Packaging of MEMS and Related Micro-Nano-Bio Integrated Systems, California (2004).

[9] P. Würfel, Photovoltaic Principles and Organic Solar Cells, CHIMIA International Journal for Chemistry **61**, 770 (2007).

[10] N. Sun, G. Fang, P. Qin, Q. Zheng, M. Wang, X. Fan, F. Cheng, J. Wan, X. Zhao, J. Liu, D. L. Carrol, and J. Ye, Efficient flexible organic solar cells with room temperature sputtered and highly conductive NiO as hole-transporting layer, Journal of Physics D: Applied Physics **43**, 445101 (2010).

[11] G. Dennler, C. Lungenschmied, H. Neugebauer, N. S. Sariciftci, M. Latreche, G. Czeremuszkin, and M. R. Wertheimer, A new encapsulation solution for flexible organic solar cells, Thin Soild Films **511**, 349 (2006).

[12] C. Lungenschmied, G. Dennler, H. Neugebauer, S. N. Sariciftci, M. Glatthaar, T. Meyer, and A. Meyer, Flexible, long-lived, large-area, organic solar cells, Solar Energy Materials And Solar Cells **91**, 379 (2007).

[13] B. Winther-Jensen and F. C. Krebs, High-conductivity large-area semi-transparent electrodes for polymer photovoltaics by silk screen printing and vapour-phase deposition, Solar Energy Materials and Solar Cells **90**, 123 (2006).

[14] J. Meiss, K. Leo, M. K. Riede, C. Uhrich, W.-M. Gnehr, S. Sonntag, and M. Pfeiffer, Efficient semitransparent small-molecule organic solar cells, Appl. Phys. Lett. **95**, 213306 (2009).

[15] M. A. Green, K. Emery, Y. Hishikawa, and W. Warta, Solar cell efficiency tables (version 37), Prog. Photovolt: Res. Appl. **19**, 84 (2011).

[16] B. Minnaert and M. Burgelman, Efficiency potential of organic bulk heterojunction solar cells, Prog. Photovolt: Res. Appl. **15**, 741 (2007).

[17] G. Dennler, M. C. Scharber, T. Ameri, P. Denk, K. Forberich, C. Waldauf, and C. J. Brabec, Design Rules for Donors in Bulk-Heterojunction Tandem Solar Cells-Towards 15% Energy-Conversion Efficiency, Adv. Mater. **20**, 579 (2008).

[18] W. Brütting, *Physics of Organic Semiconductors*, WILEY-VCH Verlag GmbH & Co. KGaA, Weinheim, 2005.

[19] H. J. Round, A note on carborundum, Electrical World **49**, 309 (1907).

[20] I. A. Vlasenko, N. A.; Popkov, Study of the Electroluminescence of a Sublimed ZnS-Mn Phosphor, Optics and Spectroscopy **8**, 39 (1960).

[21] N. Karl, M. Schulz, and H. W. (Eds.), *Semiconductors*, volume Group III, Springer, Berlin, 1985.

[22] E. A. Silinsh, *Organic Molecular Crystals*, Springer, Berlin, 1980.

[23] M. Pope and C. E. Swenberg, *Electronic Processes in Organic Crystals and Polymers*, Oxford University Press, Oxford University Press, New York City, 1999.

[24] C. K. Chiang, C. R. Fincher, Y. W. Park, A. J. Heeger, H. Shirakawa, E. J. Louis, S. C. Gau, and A. G. MacDiarmid, Electrical Conductivity in Doped Polyacetylene, Phys. Rev. Lett. **39**, 1098 (1977).

[25] M. Hiramoto, H. Fujiwara, and M. Yokoyama, p-i-n like behaviour in three-layerd organic solar cells having a co-deposited interlayer of pigments, J. Appl. Phys. **72**, 3781 (1992).

[26] M. Pfeiffer, T. Fritz, J. Blochwitz, A. Nollau, B. Plönnigs, A. Beyer, and K. Leo, Controlled Doping of Molecular Organic Layers: Physics and Device Prospects, Advances in Solid State Physics **39**, 77 (1999).

[27] B. Maennig, J. Drechsel, D. Gebeyehu, P. Simon, F. Kozlowski, A. Werner, F. Li, S. Grundmann, S. Sonntag, M. Koch, K. Leo, M. Pfeiffer, H. Hoppe, D. Meissner, N. Sariciftci, I. Riedel, V. Dyakonov, and J. Parisi, Organic p-i-n solar cells, Applied Physics A: Materials Science & Processing **79**, 1 (2004).

[28] R. Schueppel, R. Timmreck, N. Allinger, T. Mueller, M. Furno, C. Uhrich, K. Leo, and M. Riede, Controlled current matching in small molecule organic tandem solar cells using doped spacer layers, Journal of Applied Physics **107**, 044503 (2010).

[29] B. O'Regan and M. Grätzel, A low-cost, high-efficiency solar cell based on dye-sensitized colloidal TiO2 films, Nature **353**, 737 (1991).

[30] Q. Yu, Y. Wang, Z. Yi, N. Zu, J. Zhang, M. Zhang, and P. Wang, High-Efficiency Dye-Sensitized Solar Cells: The Influence of Lithium Ions on Exciton Dissociation, Charge Recombination, and Surface States, ACS Nano **4**, 6032 (2010).

[31] T. Daeneke, T.-H. Kwon, A. B. Holmes, N. W. Duffy, U. Bach, and L. Spiccia, High-efficiency dye-sensitized solar cells with ferrocene-based electrolytes, Nat Chem **3**, 211 (2011).

[32] S. Günes, H. Neugebauer, and N. S. Sariciftci, Conjugated polymer-based organic solar cells, Chemical Reviews **107**, 1324 (2007).

[33] K. Walzer, B. Maennig, M. Pfeiffer, and K. Leo, Highly efficient organic devices based on electrically doped transport layers, Chemical Reviews **107**, 1233 (2007).

[34] B. P. Rand, J. Genoe, P. Heremans, and J. Poortmans, Solar cells utilizing small molecular weight organic semiconductors, Prog. Photovolt: Res. Appl. **15**, 659 (2007).

[35] Heliatek GmbH http://www.heliatek.com (accessed 18 February 2011).

[36] Konarka Technologies Inc. http://www.konarka.com (accessed 18 February 2011).

[37] M. Schwoerer and H. C. Wolf, *Organische Molekulare Festkörper*, WILEY-VCH Verlag, 2005.

[38] S. Hunklinger, *Festkörperphysik*, Oldenburg Wissenschaftsverlag GmbH, 2009.

[39] H. Hoppe and N. Saricifci, Organic solar cells: An overview, Journal of Materials Research **19**, 1924 (2004).

[40] H. Hart, *Organische Chemie-Ein kurzes Lehrbuch*, VCH Verlagsgesellschaft mbH Weinheim, 1989.

[41] E. Neil, K. Schore, and P. C. Vollhardt, *Organische Chemie*, VCH Verlagsgesellschaft mbH Weinheim, 1995.

[42] N. Karl, Festkörperprobleme 14, Advances in Solid State Physics **14**, 261 (1974).

[43] M. Schwoerer and H. C. Wolf, *Organic Molecular Solids*, Wiley-VCH Verlag GmbH & Co. KGaA, 2006.

[44] C. A. Coulson, Excited Electronic Levels in Conjugated Molecules: I. Long Wavelength Ultra-Violet Absorption of Naphthalene, Anthracene and Homologs, Proceedings of the Physical Society **60**, 257 (1948).

[45] M. Whalley, 182. Conjugated macrocycles. Part XXXII. Absorption spectra of tetrazaporphins and phthalocyanines. Formation of pyridine salts, J. Chem. Soc. , 866 (1961).

[46] J. Meiss, M. Hummert, A. Petrich, S. Pfuetzner, K. Leo, and M. Riede, Tetrabutyl-tetraphenyl-diindenoperylene derivatives as alternative green donor in bulk heterojunction organic solar cells, Solar Energy Materials and Solar Cells **95**, 630 (2011).

[47] J. Meiss, M. Hermenau, W. Tress, C. Schuenemann, F. Selzer, M. Hummert, J. Alex, G. Lackner, K. Leo, and M. Riede, Tetrapropyl-tetraphenyl-diindenoperylene derivative as a green absorber for high-voltage stable organic solar cells, Phys. Rev. B **83**, 165305 (2011).

[48] M. Robin, I. Ishii, R. McLaren, and A. Hitchcock, Fluorination effects on the inner-shell spectra of unsaturated molecules, Journal of Electron Spectroscopy and Related Phenomena **47**, 53 (1988).

[49] J. Frenkel, On the Transformation of light into Heat in Solids. I, Phys. Rev. **37**, 17 (1931).

[50] W. Y. Liang, Excitons, Physics Education **5**, 226 (1970).

[51] G. H. Wannier, The Structure of Electronic Excitation Levels in Insulating Crystals, Phys. Rev. **52**, 191 (1937).

[52] C. Kittel, *Einführung in die Festkörperphysik*, Oldenbourg Verlag München Wien, 2002.

[53] J. Frenkel, On pre-breakdown phenomena in insulators and electronic semiconductors, Phys. Rev. **54**, 647 (1938).

[54] A. S. Brown, P. M. Levin, and E. W. Abrahamson, Dielectric Constant of Benzene at 25 °C by the Wyman Method, J. Chem. Phys. **19**, 1226 (1951).

[55] J. J. M. Halls and R. H. Friend, The photovoltaic effect in a poly(p-phenylenevinylene)/perylene heterojunction, Synthetic Metals **85**, 1307 (1997).

[56] S. Yoo, B. Domercq, and B. Kippelen, Efficient thin-film organic solar cells based on pentacene/C_{60} heterojunctions, Applied Physics Letters **85**, 5427 (2004).

[57] D. E. Markov, E. Amsterdam, P. W. M. Blom, A. B. Sieval, and J. C. Hummelen, Accurate Measurement of the Exciton Diffusion Length in a Conjugated Polymer Using a Heterostructure with a Side-Chain Cross-Linked Fullerene Layer, The Journal of Physical Chemistry A **109**, 5266 (2005).

[58] P. Blom, V. Mihailetchi, L. Koster, and D. Markov, Device Physics of Polymer:Fullerene Bulk Heterojunction Solar Cells, Adv. Mater. **19**, 1551 (2007).

[59] Y. Terao, H. Sasabe, and C. Adachi, Correlation of hole mobility, exciton diffusion length, and solar cell characteristics in phthalocyanine/fullerene organic solar cells, Appl. Phys. Lett. **90**, 103515 (2007).

[60] L. B. Schein, Temperature independent drift mobility along the molecular direction of As_2S_3, Phys. Rev. B **15**, 1024 (1977).

[61] R. C. Powell and Z. G. Soos, Singlet exciton energy transfer in organic solids, J. Lum. **11**, 1 (1975).

[62] J. B. Birks, *Organic molecular photophysics*, J. Wiley, London, New York, 1973.

[63] H. Bässler, Localized states and electronic transport in single component organic solids with diagonal disorder, Phys. Stat. Sol. (b) **107**, 9 (1981).

[64] T. Förster, Energiewanderung und Fluoreszenz, Naturwissenschaften **33**, 166 (1946).

[65] T. Förster, Zwischenmolekulare Energiewanderung und Fluoreszenz, Ann. Phys. **437**, 55 (1948).

[66] D. L. Dexter, A Theory of Sensitized Luminescence in Solids, J. Chem. Phys. **21**, 836 (1953).

[67] M. Klessinger and J. Michl, *Excited States and Photo-Chemistry of Organic Molecules*, Wiley-VCH, 1995.

[68] M. Knupfer and H. Berger, Dispersion of electron-hole excitations in pentacene along (1 0 0), Chemical Physics **325**, 92 (2006).

[69] M. Grobosch, R. Schuster, T. Pichler, M. Knupfer, and H. Berger, Analysis of the anisotropy of excitons in pentacene single crystals using reflectivity measurements and electron energy-loss spectroscopy, Phys. Rev. B **74**, 155202 (2006).

[70] R. Schuster, M. Knupfer, and H. Berger, Exciton Band Structure of Pentacene Molecular Solids: Breakdown of the Frenkel Exciton Model, Phys. Rev. Lett. **98**, 037402 (2007).

[71] P. W. M. Blom, M. J. M. de Jong, and J. J. M. Vleggaar, Electron and hole transport in poly(p-phenylene vinylene) devices, Appl. Phys. Lett. **68**, 3308 (1996).

[72] A. Opitz, M. Bronner, and W. Brutting, Ambipolar charge carrier transport in mixed organic layers of phthalocyanine and fullerene, J. Appl. Phys. **101**, 063709 (2007).

[73] J. Takeya, M. Yamagishi, Y. Tominari, R. Hirahara, Y. Nakazawa, T. Nishikawa, T. Kawase, T. Shimoda, and S. Ogawa, Very high-mobility organic single-crystal transistors with in-crystal conduction channels, Appl. Phys. Lett. **90**, 102120 (2007).

[74] P. Würfel, *Physik der Solarzellen*, Spektrum Akademischer Verlag, Heidelberg-Berlin, 2000.

[75] O. Ostroverkhova, D. G. Cooke, S. Shcherbyna, R. F. Egerton, F. A. Hegmann, R. R. Tykwinski, and J. E. Anthony, Bandlike transport in pentacene and functionalized pentacene thin films revealed by subpicosecond transient photoconductivity measurements, Physical Review B **71**, 035204 (2005).

[76] J. Schön, C. Kloc, and B. Batlogg, Band-Like Charge Transport in C_{60} Single Crystals, phys. stat. sol. (b) **225**, 209 (2001).

[77] W. Warta, R. Stehle, and N. Karl, Ultrapure, High mobility organic Photoconductors, Appl. Phys. A **36**, 163 (1985).

[78] W. Warta and N. Karl, Hot holes in naphthalene: High, electric-field-dependent mobilities, Phys. Rev. B **32**, 1172 (1985).

[79] Y. Shirota, S. Nomura, and H. Kageyama, Charge transport in amorphous molecular materials, Proc. SPIE **3476**, 132 (1998).

[80] Y. Shirota, Organic materials for electronic and optoelectronic devices, J. Mater. Chem. **10**, 1 (2000).

[81] Y. Shirota and H. Kageyama, Charge carrier transporting molecular materials and their applications in devices, Chemical Reviews **107**, 953 (2007).

[82] N. Sato, K. Seki, and H. Inokuchi, Polarization energies of organic solids determined by ultraviolet photoelectron spectroscopy, J. Chem. Soc., Faraday Trans. 2 **77**, 1621 (1981).

[83] A. N. Das and S. Sil, A study of the polaronic band width and the small-to-large-polaron transition in a many-polaron system, Journal of Physics: Condensed Matter **5**, 8265 (1993).

[84] M. Silver, G. Schoenherr, and H. Baessler, Dispersive hopping transport from an exponential energy distribution of sites, Phys. Rev. Lett. **48**, 352 (1982).

[85] B. Cleve, B. Hartenstein, S. Baranovskii, M. Scheidler, P. Thomas, and H. Baessler, High-field hopping transport in band tails of disordered semiconductors, Phys. Rev. B **51**, 16705 (1995).

[86] E. V. Emelianova and G. J. Adriaenssens, Stochastic approach to hopping transport in disordered organic materials, Journal of Optoelectronics and Advanced Materials **6**, 1105 (2004).

[87] E. A. Silinsh, *Organic Molecular Crystals - Their Electronic States*, Springer Verlag, 1980.

[88] L. Bergmann and C. Schaefer, *Festkörper-Lehrbuch der Experimentalphysik*, Walter de Gryter, Berlin - New York, 1992.

[89] J. Simon and J.-J. André, *Molecular Semiconductors - Photoelectrical Properties and Solar Cells*, Springer Verlag Berlin, 1985.

[90] H. Bässler, Charge Transport in Disordered Organic Photoconductors a Monte Carlo Simulation Study, Phys. Stat. Sol. (b) **175**, 15 (1993).

[91] P. M. Borsenberger, Charge Transport in Disordered Molecular Solids, Molecular Crystals and Liquid Crystals Science and Technology. Section A. Molecular Crystals and Liquid Crystals **228**, 167 (1993).

[92] A. Miller and E. Abrahams, Impurity Conduction at Low Concentrations, Phys. Rev. **120**, 745 (1960).

[93] A. Jonscher, P. Lecomber, and J. Mort, *Electronic and structural properties of amorphous semiconductors*, Academic Press, London, 1973.

[94] L. Pautmeier, R. Richert, and H. Bässler, Poole-Frenkel behavior of charge transport in organic solids with off-diagonal disorder studied by Monte Carlo simulation, Synthetic Metals **37**, 271 (1990).

[95] V. I. Arkhipov, P. Heremans, E. V. Emelianova, G. J. Adriaenssens, and H. Bässler, Charge carrier mobility in doped disordered organic semiconductors, Journal of Non-Crystalline Solids **338**, 603 (2004).

[96] M. Pfeiffer, T. Fritz, J. Blochwitz, A. Nollau, B. Plönnigs, A. Beyer, and K. Leo, Controlled Doping of Molecular Organic Layers: Physics and Device Prospects, Advances in Solid State Physics **39**, 77 (1999).

[97] N. F. Mott and R. W. Gurney, *Electronic Processes in Ionic Crystals*, Oxford University Press, New York City, 1940.

[98] M. A. Lampert, Simplified Theory of Space-Charge-Limited Currents in an Insulator with Traps, Phys. Rev. **103**, 1648 (1956).

[99] G. Caserta, B. Rispoli, and A. Serra, Space-Charge-Limited Current and Band Structure in Amorphous Organic Films, phys. stat. sol. (b) **35**, 237 (1969).

[100] H. Antoniadis, J. N. Miller, D. B. Roitman, and I. H. Cambell, Effects of hole carrier injection and transport in organic light-emitting diodes, IEEE Transactions On Electron Devices **44**, 1289 (1997).

[101] P. M. Blom, M. J. M. d. Jong, and C. T. Liedenbaum, Device physics of polymer light-emitting diodes, Polym. Adv. Technol. **9**, 390 (1998).

[102] P. N. Murgatroyd, Theory of Space-charge-limited Current Enhanced By Frenkel Effect, Journal of Physics D-applied Physics **3**, 151 (1970).

[103] M. Kitamura, T. Imada, S. Kako, and Y. Arakawa, Time-of-Flight Measurement of Lateral Carrier Mobility in Organic Thin Films, Jpn. J. Appl. Phys. **43**, 2326 (2004).

[104] H. C. F. Martens, H. B. Brom, and P. W. M. Blom, Frequency-dependent electrical response of holes in poly(p-phenylene vinylene), Phys. Rev. B **60**, R8489 (1999).

[105] S. W. Tsang, K. L. Tong, S. C. Tse, and S. K. So, Direct determination of carrier mobilities of OLED materials by admittance spectroscopy, Proc. SPIE **6333**, 633313 (2006).

[106] H. Katz, Organic molecular solids as thin film transistor semiconductors, J. Mater. Chem. **7**, 369 (1997).

[107] C. D. Dimitrakopoulos and D. J. Mascaro, Organic thin-film transistors: a review of recent advances, IBM J. Res. Dev. **45**(1), 11 (2001).

[108] A. Tsumura, H. Koezuka, and T. Ando, Macromolecular electronic device: Field-effect transistor with a polythiophene thin film, Appl. Phys. Lett. **49**, 1210 (1986).

[109] G. Horowitz, R. Hajlaoui, and F. Kouki, An analytical model for the organic field-effect transistor in the depletion mode. Application to sexithiophene films and single crystals, Eur. Phys. J. AP **1**, 361 (1998).

[110] M. Pfeiffer, T. Krieg, A. Beyer, T. Fritz, and K. Leo, Controlled doping of phthalocyanine thin films by cosublimation with acceptor molecules, Proc. 4th European Conference on Molecular Electronics, Cambridge , 63 (1997).

[111] M. Pfeiffer, A. Beyer, T. Fritz, and K. Leo, Controlled doping of phthalocyanine layers by cosublimation with acceptor molecules: A systematic Seebeck and conductivity study, Appl. Phys. Lett. **73**, 3202 (1998).

[112] A. Nollau, M. Pfeiffer, T. Fritz, and K. Leo, Controlled n-type doping of a molecular organic semiconductor: naphthalenetetracarboxylic dianhydride (NTCDA) doped with bis(ethylenedithio)-tetrathiafulvalene (BEDT-TTF), J. Appl. Phys. **87**, 4340 (2000).

[113] B. Maennig, M. Pfeiffer, A. Nollau, X. Zhou, P. Simon, and K. Leo, Controlled p-doping of polycrystalline and amorphous organic layers: Self-consistent description of conductivity and field-effect mobility by a microscopic percolation model, Phys. Rev. B **64**, 195208 (2001).

[114] A. Werner, F. Li, K. Harada, M. Pfeiffer, T. Fritz, K. Leo, and S. Machill, n-Type Doping of Organic Thin Films Using Cationic Dyes, Adv. Funct. Mater. **14**, 255 (2004).

[115] S. Pfuetzner, A. Petrich, C. Malbrich, J. Meiss, M. Koch, M. K. Riede, M. Pfeiffer, and K. Leo, Characterisation of different hole transport materials as used in organic p-i-n solar cells, Proc. SPIE **6999**, 69991M (2008).

[116] S. Olthof, R. Meerheim, M. Schober, and K. Leo, Energy level alignment at the interfaces in a multilayer organic light-emitting diode structure, Phys. Rev. B **79**, 245308 (2009).

[117] K. R. Rajesh and C. S. Menon, Estimation of the refractive index and dielectric constants of magnesium phthalocyanine thin films from its optical studies, Materials Letters **53**, 329 (2002).

[118] F. Yakuphanoglu, M. Arslan, and S. YIldIz, Determination and analysis of the dispersive optical constants of the 2,9,16,23-tetraneopentoxyphthalocyaninatozinc(II) charge transfer complex with 2,3-dichloro-5,6-dicyano-p-benzoquinone thin film, Optical Materials **27**, 1153 (2005).

[119] M. Wojdyla, W. Bala, B. Derkowska, M. Rebarz, and A. Korcala, The temperature dependence of photoluminescence and absorption spectra of vacuum-sublimed magnesium phthalocyanine thin films, Optical Materials **30**, 734 (2008).

[120] O. S. Heavens, Optical properties of thin films, Rep. Prog. Phys. **23**, 1 (1960).

[121] L. A. A. Pettersson, L. S. Roman, and O. Inganas, Modeling photocurrent action spectra of photovoltaic devices based on organic thin films, J. Appl. Phys. **86**, 487 (1999).

[122] M. Furno, R. Meerheim, M. Thomschke, S. Hofmann, B. Lussem, and K. Leo, Outcoupling efficiency in small-molecule OLEDs: from theory to experiment, Proc. SPIE **7617**, 761716 (2010).

[123] T. Fritz, J. Hahn, and H. Böttcher, Determination of the optical constants of evaporated dye layers, Thin Solid Films **170**, 249 (1989).

[124] A. Jablonski, Efficiency of anti-stokes fluorescence in dyes, Nature **131**, 839 (1933).

[125] J. Zimmermann, A. Zeug, and B. Roder, A generalization of the Jablonski diagram to account for polarization and anisotropy effects in time-resolved experiments, Phys. Chem. Chem. Phys. **5**, 2964 (2003).

[126] C. Tang, Two-layer organic photovoltaic cell, Appl. Phys. Lett. **48**, 183 (1986).

[127] M. Hiramoto, H. Fujiwara, and M. Yokoyama, Three-layered organic solar cell with a photoactive interlayer of codeposited pigments, Appl. Phys. Lett. **58**, 1062 (1991).

[128] P. Peumans, S. Uchida, and S. R. Forrest, Efficient bulk heterojunction photovoltaic cells using small-molecular-weight organic thin films, Nature **425**, 158 (2003).

[129] R. Schueppel, K. Schmidt, C. Uhrich, K. Schulze, D. Wynands, J. L. Bredas, B. Maennig, M. Pfeiffer, K. Leo, E. Brier, E. Reinold, H.-B. Bu, and P. Baeuerle, Tailored heterojunctions for efficient thin-film organic solar cells: a photoinduced absorption study, Proc. SPIE **6656**, 66560G (2007).

[130] R. Schueppel, K. Schmidt, C. Uhrich, K. Schulze, D. Wynands, J. L. Brédas, E. Brier, E. Reinold, H.-B. Bu, P. Baeuerle, B. Maennig, M. Pfeiffer, and K. Leo, Optimizing organic photovoltaics using tailored heterojunctions: A photoinduced absorption study of oligothiophenes with low band gaps, Phys. Rev. B **77**, 085311 (2008).

[131] B. Maennig, *Organische p-i-n Solarzellen*, Doktorarbeit, 2004.

[132] J. Drechsel, B. Maennig, F. Kozlowski, M. Pfeiffer, K. Leo, and H. Hoppe, Efficient organic solar cells based on a double p-i-n architecture using doped wide-gap transport layers, Applied Physics Letters **86**, 244102 (2005).

[133] R. Schueppel, R. Timmreck, N. Allinger, T. Mueller, M. Furno, C. Uhrich, K. Leo, and M. Riede, Controlled current matching in small molecule organic tandem solar cells using doped spacer layers, J. Appl. Phys. **107**, 044503 (2010).

[134] Y. Hsiao, W. Whang, S.-C. Suen, J. Shiu, and C. Chen, Morphological control of CuPc and its application in organic solar cells, Nanotechnology **19**, 415603 (2008).

[135] P. E. Burrows, S. R. Forrest, L. S. Sapochak, J. Schwartz, P. Fenter, T. Buma, V. S. Ban, and J. L. Forrest, Organic vapor phase deposition: a new method for the growth of organic thin films with large optical non-linearities, Journal of Crystal Growth **156**, 91 (1995).

[136] H. Wang, F. Zhu, J. Yang, Y. Geng, and D. Yan, Weak Epitaxy Growth Affording High-Mobility Thin Films of Disk-Like Organic Semiconductors, Adv. Mater. **19**, 2168 (2007).

[137] B. Yu, L. Huang, H. Wang, and D. Yan, Efficient Organic Solar Cells Using a High-Quality Crystalline Thin Film as a Donor Layer, Adv. Mater. **22**, 1017 (2010).

[138] M. Hiramoto, Design of nanostructure for photoelectric conversion by vertical organic superlattice, Electronics and Communications in Japan, Part 2 **89**, 13 (2006).

[139] Y. Kim, S. Cook, S. M. Tuladhar, S. A. Choulis, J. Nelson, J. R. Durrant, D. D. C. Bradley, M. Giles, I. McCulloch, C.-S. Ha, and M. Ree, A strong regioregularity effect in self-organizing conjugated polymer films and high-efficiency polythiophene:fullerene solar cells, Nat Mater **5**, 197 (2006).

[140] R. Gysel, N. Cates, M. McGehee, A. Mayer, and M. Toney, Molecular self-ordering in organic solar cell materials, SPIE Newsroom (2009).

[141] M. Campoy-Quiles, T. Ferenczi, T. Agostinelli, P. G. Etchegoin, Y. Kim, T. D. Anthopoulos, P. N. Stavrinou, D. D. C. Bradley, and J. Nelson, Morphology evolution via self-organization and lateral and vertical diffusion in polymer:fullerene solar cell blends, Nat Mater **7**, 158 (2008).

[142] J. J. Dittmer, R. Lazzaroni, P. Leclère, P. Moretti, M. Granström, K. Petritsch, E. A. Marseglia, R. H. Friend, J. L. Brédas, H. Rost, and A. B. Holmes, Crystal network formation in organic solar cells, Solar Energy Materials and Solar Cells **61**, 53 (2000).

[143] H. Hoppe, M. Niggemann, C. Winder, J. Kraut, R. Hiesgen, A. Hinsch, D. Meissner, and N. Sariciftci, Nanoscale Morphology of Conjugated Polymer/Fullerene-Based Bulk- Heterojunction Solar Cells, Adv. Funct. Mater. **14**, 1005 (2004).

[144] X. Yang, J. Loos, S. C. Veenstra, W. J. H. Verhees, M. M. Wienk, J. M. Kroon, M. A. J. Michels, and R. A. J. Janssen, Nanoscale Morphology of High-Performance Polymer Solar Cells, Nano Letters **5**, 579 (2005).

[145] W. Ma, C. Yang, X. Gong, K. Lee, and A. Heeger, Thermally Stable, Efficient Polymer Solar Cells with Nanoscale Control of the Interpenetrating Network Morphology, Adv. Funct. Mater. **15**, 1617 (2005).

[146] G. Li, V. Shrotriya, Y. Yao, and Y. Yang, Investigation of annealing effects and film thickness dependence of polymer solar cells based on poly(3-hexylthiophene), J. Appl. Phys. **98**, 043704 (2005).

[147] N. Kim, I. H. Oh, S. Yoon, C. E. Lee, J. Y. Choi, B. H. Youn, C. Y. Jang, and J. Kim, Efficient Organic Photovoltaic Cells with Nano-Domain Control

of the Interpenetrating Network Morphology Through Post-Thermal Treatment, Journal of the Korean Physical Society **55**, 2654 (2009).

[148] Y. Zhao, Z. Xie, Y. Qu, Y. Geng, and L. Wang, Solvent-vapor treatment induced performance enhancement of poly(3-hexylthiophene):methanofullerene bulk-heterojunction photovoltaic cells, Appl. Phys. Lett. **90**, 043504 (2007).

[149] C. Y. Kwong, A. B. Djurisic, P. C. Chui, K. W. Cheng, and W. K. Chan, Influence of solvent on film morphology and device performance of poly(3-hexylthiophene):TiO2 nanocomposite solar cells, Chemical Physics Letters **384**, 372 (2004).

[150] F. Zhang, K. Jespersen, C. Björström, M. Svensson, M. Andersson, V. Sundström, K. Magnusson, E. Moons, A. Yartsev, and O. Inganäs, Influence of Solvent Mixing on the Morphology and Performance of Solar Cells Based on Polyfluorene Copolymer/Fullerene Blends, Adv. Funct. Mater. **16**, 667 (2006).

[151] S. Cook, A. Furube, and R. Katoh, Mixed Solvents for Morphology Control of Organic Solar Cell Blend Films, Jpn. J. Appl. Phys. **47**, 1238 (2008).

[152] S. Barrau, V. Andersson, F. Zhang, S. Masich, J. Bijleveld, M. R. Andersson, and O. InganaÌˆs, Nanomorphology of Bulk Heterojunction Organic Solar Cells in 2D and 3D Correlated to Photovoltaic Performance, Macromolecules **42**, 4646 (2009).

[153] A. Keawprajak, P. Piyakulawat, C. Saekung, and U. Asawapirom, Effects of Film Preparation on the Morphology and Performance of Organic Solar Cells, Journal of Microscopy Society of Thailand **1**, 134 (2009).

[154] G. Li, V. Shrotriya, J. Huang, Y. Yao, T. Moriarty, K. Emery, and Y. Yang, High-efficiency solution processable polymer photovoltaic cells by self-organization of polymer blends, Nat Mater **4**, 864 (2005).

[155] K. Suemori, T. Miyata, M. Yokoyama, and M. Hiramoto, Three-layered organic solar cells incorporating a nanostructure-optimized phthalocyanine:fullerene codeposited interlayer, Applied Physics Letters **86**, 063509 (2005).

[156] M. Hiramoto, K. Suemori, and M. Yokoyama, Photovoltaic properties of ultramicrostructure-controlled organic Co-deposited films, Jpn. J. Appl. Phys. Pt. 1 **41**, 2763 (2002).

[157] M. Vogel, J. Strotmann, B. Johnev, A. C. Lux-Steiner, and K. Fostiropoulos, Influence of nanoscale morphology in small molecule organic solar cells, Thin Soild Films **511**, 367 (2006).

[158] J. S. Kim, Y. Lee, J. H. Lee, J. H. Park, J. K. Kim, and K. Cho, High-Efficiency Organic Solar Cells Based on End-Functional-Group-Modified Poly(3-hexylthiophene), Adv. Mater. **22**, 1355 (2010).

[159] J. Drechsel, A. Petrich, M. Koch, S. Pfuetzner, R. Meerheim, S. Scholz, J. Drechsel, K. Walzer, M. Pfeiffer, and K. Leo, Influence of Material Purification by Vacuum Sublimation on Organic Optoelectronic Device Performance, SID Symposium Digest of Technical Papers **37**, 1692 (2006).

[160] W. Tress, A. Petrich, M. Hummert, M. Hein, K. Leo, and M. Riede, Imbalanced mobilities causing S-shaped IV curves in planar heterojunction organic solar cells, Appl. Phys. Lett. **98**, 063301 (2011).

[161] W. Tress, S. Pfuetzner, K. Leo, and M. Riede, Open circuit voltage and IV curve shape of ZnPc:C_{60} solar cells with varied mixing ratio and hole transport layer, J. Photon. Energy **1**, 011114 (2011).

[162] W. Shockley, The Theory of P-n Junctions In Semiconductors and P-n Junction Transistors, Bell System Technical Journal **28**, 435 (1949).

[163] R. Marks, J. Halls, D. Bradley, R. Friend, and A. Holmes, The photovoltaic response in poly(p-phenylene vinylene) thin-film devices, J. Phys. - Condens. Matter **6**, 1379 (1994).

[164] P. Peumans, A. Yakimov, and S. R. Forrest, Small molecular weight organic thin-film photodetectors and solar cells, J. Appl. Phys. **93**, 3693 (2003).

[165] G. F. Burkhard, E. T. Hoke, S. R. Scully, and M. D. McGehee, Incomplete Exciton Harvesting from Fullerenes in Bulk Heterojunction Solar Cells, Nano Letters **9**, 4037 (2009).

[166] S. H. Park, A. Roy, S. Beaupre, S. Cho, N. Coates, J. S. Moon, D. Moses, M. Leclerc, K. Lee, and A. J. Heeger, Bulk heterojunction solar cells with internal quantum efficiency approaching 100%, Nat Photon **3**, 297 (2009).

[167] K. Emery and C. Osterwald, Solar cell efficiency measurements, Solar Cells **17**, 253 (1986).

[168] *Standard ASTM E 948-05:Test Method for Electrical Performance of PV Cells using Reference Cells under Simulated Sunlight.*, American Society for Testing and Materials, West Conshohocken, USA, 2005.

[169] *Standard and IEC and 60904-1:Photovoltaische Einrichtungen - Teil 1: Messen der photovoltaischen Strom-/Spannungskennlinien.*, DIN Deutsches Institut für Normung, Beuth Verlag, Berlin, 2007.

[170] C. Gueymard, Parameterized transmittance model for direct beam and circumsolar spectral irradiance, Solar Energy **71**, 325 (2001).

[171] C. Gueymard, D. Myers, and K. Emery, Proposed reference irradiance spectra for solar energy systems testing, Solar Energy **73**, 443 (2002).

[172] K. A. Emery, C. R. Osterwald, T. W. Cannon, D. R. Myers, J. Burdick, T. Glatfelter, W. Czubatyj, and J. Yang, Methods for Measuring Solar Cell Efficiency Independent of Reference Cell or Light Source, Proc. 18th IEEE PV Spec. Conf. , 623 (1985).

[173] V. Shrotriya, G. Li, Y. Yao, T. Moriarty, K. Emery, and Y. Yang, Accurate measurement and characterization of organic solar cells, Advanced Functional Materials **16**, 2016 (2006).

[174] H. Singh and M. Srivastava, Fullerenes: Synthesis, Separation, Characterization, Reaction Chemistry, and Applications - A Review, Energy Sources, Part A: Recovery, Utilization, and Environmental Effects **17**, 615 (1995).

[175] A. W. Jensen, S. R. Wilson, and D. I. Schuster, Biological applications of fullerenes, Bioorganic & Medicinal Chemistry **4**, 767 (1996).

[176] S. Bosi, T. Da Ros, G. Spalluto, and M. Prato, Fullerene derivatives: an attractive tool for biological applications, European Journal of Medicinal Chemistry **38**, 913 (2003).

[177] M. A. Dahlen, The Phthalocyanines A New Class of Synthetic Pigments and Dyes, Industrial & Engineering Chemistry **31**, 839 (1939).

[178] H. W. Kroto, J. R. Heath, S. C. O'Brien, R. F. Curl, and R. E. Smalley, C_{60}: Buckminsterfullerene, Nature **318**, 162 (1985).

[179] K. S. Novoselov, A. K. Geim, S. V. Morozov, D. Jiang, Y. Zhang, S. V. Dubonos, I. V. Grigorieva, and A. A. Firsov, Electric Field Effect in Atomically Thin Carbon Films, Science **306**, 666 (2004).

[180] W. Krätschmer and D. R. Huffman, Fullerites: New forms of crystalline carbon, Carbon **30**, 1143 (1992).

[181] R. Mitsumoto, T. Araki, E. Ito, Y. Ouchi, K. Seki, K. Kikuchi, Y. Achiba, H. Kurosaki, T. Sonoda, H. Kobayashi, O. V. Boltalina, V. K. Pavlovich, L. N. Sidorov, Y. Hattori, N. Liu, S. Yajima, S. Kawasaki, F. Okino, and H. Touhara, Electronic Structures and Chemical Bonding of Fluorinated Fullerenes Studied by NEXAFS, UPS, and Vacuum-UV Absorption Spectroscopies, The Journal of Physical Chemistry A **102**, 552 (1998).

[182] D. M. N. M. Dissanayake, R. A. Hatton, T. Lutz, C. E. Giusca, R. J. Curry, and S. R. P. Silva, A PbS nanocrystal-C_{60} photovoltaic device for infrared light harvesting, Appl. Phys. Lett. **91**, 133506 (2007).

[183] D. Gao, M. G. Helander, Z.-B. Wang, D. P. Puzzo, M. T. Greiner, and Z.-H. Lu, C_{60}:LiF Blocking Layer for Environmentally Stable Bulk Heterojunction Solar Cells, Adv. Mater. **22**, 5404 (2010).

[184] W. Zhao and A. Kahn, Charge transfer at n-doped organic-organic heterojunctions, J. Appl. Phys. **105**, 123711 (2009).

[185] R. Lof, M. van Veenendahl, B. Koopmans, H. Jonkman, and G. Sawatzky, Band gap, exitons, and coulomb interaction in solid C_{60}, Phys. Rev. Lett. **68**, 3924 (1992).

[186] W. Brütting, M. Bronner, M. Götzenbrugger, and A. Opitz, Ambipolar Blends of Cu-Phthalocyanine and Fullerene: Charge Carrier Mobility, Electronic Structure and their Implications for Solar Cell Applications, Macromol. Symp. **268**, 38 (2008).

[187] F. Li, M. Pfeiffer, A. Werner, K. Harada, K. Leo, N. Hayashi, K. Seki, X. Liu, and X.-D. Dang, Acridine orange base as a dopant for n doping of C_{60} thin films, J. Appl. Phys. **100**, 023716 (2006).

[188] K. Itaka, M. Yamashiro, J. Yamaguchi, M. Haemori, S. Yaginuma, Y. Matsumoto, M. Kondo, and H. Koinuma, High-Mobility C_{60} Field-Effect Transistors Fabricated on Molecular- Wetting Controlled Substrates, Adv. Mater. **18**, 1713 (2006).

[189] T. Birendra Singh, H. Yang, B. Plochberger, L. Yang, H. Sitter, H. Neugebauer, and N. S. Sariciftci, Characterization of highly crystalline C_{60} thin films and their field-effect mobility, phys. stat. sol. (b) **244**, 3845 (2007).

[190] S. Kobayashi, T. Takenobu, S. Mori, A. Fujiwara, and Y. Iwasa, C_{60} thin-film transistors with high field-effect mobility, fabricated by molecular beam deposition, Science and Technology of Advanced Materials **4**, 371 (2003).

[191] A. Skumanich, Optical absorption spectra of carbon 60 thin films from 0.4 to 6.2 eV, Chemical Physics Letters **182**, 486 (1991).

[192] S. Yoo, W. J. Potscavage Jr., B. Domercq, S.-H. Han, T.-D. Li, S. C. Jones, R. Szoszkiewicz, D. Levi, E. Riedo, S. R. Marder, and B. Kippelen, Analysis of improved photovoltaic properties of pentacene/C_{60} organic solar cells: Effects of

exciton blocking layer thickness and thermal annealing, Solid-State Electronics **51**, 1367 (2007).

[193] F. Monestier, J.-J. Simon, P. Torchio, L. Escoubas, B. Ratier, W. Hojeij, B. Lucas, A. Moliton, M. Cathelinaud, C. Defranoux, and F. Flory, Optical modeling of organic solar cells based on CuPc and C_{60}, Appl. Opt. **47**, C251 (2008).

[194] P. Simon, B. Maennig, and H. Lichte, Conventional Electron Microscopy and Electron Holography of Organic Solar Cells, Adv. Funct. Mater. **14**, 669 (2004).

[195] D. Alloway and N. Armstrong, Organic heterojunctions of layered perylene and phthalocyanine dyes: characterization with UV-photoelectron spectroscopy and luminescence quenching, Applied Physics A: Materials Science & Processing **95**, 209 (2009).

[196] W. Gao and A. Kahn, Electronic structure and current injection in zinc phthalocyanine doped with tetrafluorotetracyanoquinodimethane: interface versus bulk effects, Organic Electronics **3**, 53 (2002).

[197] S. Olthof, W. Tress, R. Meerheim, B. Lussem, and K. Leo, Photoelectron spectroscopy study of systematically varied doping concentrations in an organic semiconductor layer using a molecular p-dopant, J. Appl. Phys. **106**, 103711 (2009).

[198] I. Kim, H. M. Haverinen, Z. Wang, S. Madakuni, Y. Kim, J. Li, and G. E. Jabbour, Efficient Organic Solar Cells Based on Planar Metallophthalocyanines, Chemistry of Materials **21**, 4256 (2009).

[199] W. Gao and A. Kahn, Controlled p-doping of zinc phthalocyanine by coevaporation with tetrafluorotetracyanoquinodimethane: A direct and inverse photoemission study, Appl. Phys. Lett. **79**, 4040 (2001).

[200] J. Blochwitz, T. Fritz, M. Pfeiffer, K. Leo, D. M. Alloway, P. A. Lee, and N. R. Armstrong, Interface electronic structure of organic semiconductors with controlled doping levels, Organic Electronics **2**, 97 (2001).

[201] H. R. Kerp and E. E. van Faassen, Photovoltaic yield from exciton dissociation in organic dye layers, Phys. Chem. Chem. Phys. **1**, 1761 (1999).

[202] E. A. Lucia and F. D. Verderame, Spectra of polycrystalline phthalocyanines in the visible region, J. Chem. Phys. **48**, 2674 (1968).

[203] C. Schünemann, C. Elschner, A. Levin, M. Levichkova, K. Leo, and M. Riede, Zinc phthalocyanine – Influence of substrate temperature, film thickness, and kind of substrate on the morphology, Thin Solid Films **519**, 3939 (2011).

[204] S. Senthilarasu, R. Sathyamoorthy, and S. Kulkarni, Substrate temperature effects on structural orientations and optical properties of ZincPthalocyanine (ZnPc) thin films, Materials Science and Engineering: B **122**, 100 (2005).

[205] K. Fehse, S. Olthof, K. Walzer, K. Leo, R. L. Johnson, H. Glowatzki, B. Broker, and N. Koch, Energy level alignment of electrically doped hole transport layers with transparent and conductive indium tin oxide and polymer anodes, J. Appl. Phys. **102**, 073719 (2007).

[206] C.-W. Chen, T.-Y. Cho, C.-C. Wu, H.-L. Yu, and T.-Y. Luh, Fuzzy-junction organic light-emitting devices, Appl. Phys. Lett. **81**, 1570 (2002).

[207] J. Kido and T. Matsumoto, Bright organic electroluminescent devices having a metal-doped electron-injecting layer, Appl. Phys. Lett. **73**, 2866 (1998).

[208] M. Y. Chan, C. S. Lee, S. L. Lai, M. K. Fung, F. L. Wong, H. Y. Sun, K. M. Lau, and S. T. Lee, Efficient organic photovoltaic devices using a combination of exciton blocking layer and anodic buffer layer, Journal of Applied Physics **100**, 094506 (2006).

[209] Y. Wang, N. Herron, V. Grushin, D. LeCloux, and V. Petrov, Highly efficient electroluminescent materials based on fluorinated organometallic iridium compounds, Appl. Phys. Lett. **79**, 449 (2001).

[210] S. Scholz, Q. Huang, M. Thomschke, S. Olthof, P. Sebastian, K. Walzer, K. Leo, S. Oswald, C. Corten, and D. Kuckling, Self-doping and partial oxidation of metal-on-organic interfaces for organic semiconductor devices studied by chemical analysis techniques, J. Appl. Phys. **104**, 104502 (2008).

[211] S. Pfuetzner, J. Meiss, A. Petrich, M. Riede, and K. Leo, Thick C_{60}:ZnPc bulk heterojunction solar cells with improved performance by film deposition on heated substrates, Appl. Phys. Lett. **94**, 253303 (2009).

[212] S. H. Kim, J. Jang, and J. Y. Lee, Relationship between indium tin oxide surface treatment and hole injection in C_{60} modified devices, Appl. Phys. Lett. **89**, 253501 (2006).

[213] K. Schulze, C. Uhrich, R. Schuppel, K. Leo, M. Pfeiffer, E. Brier, E. Reinold, and P. Baeuerle, Efficient vacuum-deposited organic solar cells based on a new low-bandgap oligothiophene and fullerene C_{60}, Advanced Materials **18**, 2872 (2006).

[214] H. Seifert, Externe Quanteneffzienz von organischen Solarzellen, Diplomarbeit, Technische Universität Dresden, 2008.

[215] M. B. Casu, Y. Zou, S. Kera, D. Batchelor, T. Schmidt, and E. Umbach, Investigation of polarization effects in organic thin films by surface core-level shifts, Phys. Rev. B **76**, 193311 (2007).

[216] S. Olthof, *Photoelectron Spectroscopy on Doped Organic Semiconductors and Related Interfaces*, Doktorarbeit, Technische Universität Dresden, 2010.

[217] M. Hein, Bestimmung der Ladungsträgerbeweglichkeit in organischen Materialien für organische Solarzellen, Diplomarbeit, Technische Universität Dresden, 2010.

[218] P. Eaton and P. West, *Atomic Force Microscopy*, Oxford University Press, New York City, 2010.

[219] Allen and Frank, The Cambridge Structural Database: a quarter of a million crystal structures and rising, Acta Crystallographica Section B **58**, 380 (2002), Cambridge Structural Database (CSD), Release 2009, Cambridge Crystallographic Data Centre (CCDC), UK.

[220] M. Riede, C. Uhrich, R. Timmreck, J. Widmer, D. Wynands, M. Levichkova, M. Furno, G. Schwartz, W. Gnehr, M. Pfeiffer, and K. Leo, Optimization of organic tandem solar cells based on small molecules, Photovoltaic Specialists Conference (PVSC), 35th IEEE , 000513 (2010).

[221] E. Centurioni, Generalized matrix method for calculation of internal light energy flux in mixed coherent and incoherent multilayers, Appl. Opt. **44**, 7532 (2005).

[222] W. Tress, K. Leo, , and M. Riede, Influence of hole transport layers and donor materials on open circuit voltage and shape of IV curves of organic solar cells, Advanced Functional Materials **21**, 2140 (2011).

[223] J. Staudigel, M. Stossel, F. Steuber, and J. Simmerer, A quantitative numerical model of multilayer vapor-deposited organic light emitting diodes, J. Appl. Phys. **86**, 3895 (1999).

[224] W. F. Pasveer, J. Cottaar, C. Tanase, R. Coehoorn, P. A. Bobbert, P. W. M. Blom, D. M. de Leeuw, and M. A. J. Michels, Unified Description of Charge-Carrier Mobilities in Disordered Semiconducting Polymers, Phys. Rev. Lett. **94**, 206601 (2005).

[225] L. J. A. Koster, E. C. P. Smits, V. D. Mihailetchi, and P. W. M. Blom, Device model for the operation of polymer/fullerene bulk heterojunction solar cells, Phys. Rev. B **72**, 085205 (2005).

[226] L. J. A. Koster, V. D. Mihailetchi, and P. W. M. Blom, Bimolecular recombination in polymer/fullerene bulk heterojunction solar cells, Appl. Phys. Lett. **88**, 052104 (2006).

[227] A. Pivrikas, N. S. Sariciftci, G. Juška, and R. Österbacka, A review of charge transport and recombination in polymer/fullerene organic solar cells, Prog. Photovolt: Res. Appl. **15**, 677 (2007).

[228] M. M. Wienk, J. M. Kroon, W. J. H. Verhees, J. Knol, J. C. Hummelen, P. A. van Hal, and R. A. J. Janssen, Efficient Methano[70]fullerene/MDMO-PPV Bulk Heterojunction Photovoltaic Cells, Angewandte Chemie International Edition **42**, 3371 (2003).

[229] S. Pfuetzner, J. Meiss, A. Petrich, M. Riede, and K. Leo, Improved bulk heterojunction organic solar cells employing C_{70} fullerenes, Appl. Phys. Lett. **94**, 223307 (2009).

[230] G. Orlandi and F. Negri, Electronic states and transitions in C_{60} and C_{70} fullerenes, Photochem. Photobiol. Sci. **1**, 289 (2002).

[231] A. Graja and J.-P. Farges, Optical spectra of C_{60} and C_{70} complexes: their similarities and differences, Adv. Mater. Opt. Electron. **8**, 215 (1998).

[232] S. Leach, M. Vervloet, A. Desprès, E. Bréheret, J. P. Hare, T. John Dennis, H. W. Kroto, R. Taylor, and D. R. M. Walton, Electronic spectra and transitions of the fullerene C_{60}, Chemical Physics **160**, 451 (1992).

[233] M. M. Mandoc, L. J. A. Koster, and P. W. M. Blom, Optimum charge carrier mobility in organic solar cells, Appl. Phys. Lett. **90**, 133504 (2007).

[234] A. J. Ikushima, T. Kanno, S. Yoshida, and A. Maeda, Valence and conduction band edges of metal-phthalocyanines and carrier behavior, Thin Solid Films **273**, 35 (1996).

[235] C. Brabec, U. Scherf, and V. Dyakonov, *Organic Photovoltaics: Materials, Device Physics, and Manufacturing Technologies*, Wiley-VCH Verlag GmbH, 2008.

[236] B. Kippelen and J.-L. Bredas, Organic photovoltaics, Energy Environ. Sci. **2**, 251 (2009).

[237] C. I. Wu, Y. Hirose, H. Sirringhaus, and A. Kahn, Electron-hole interaction energy in the organic molecular semiconductor PTCDA, Chemical Physics Letters **272**, 43 (1997).

[238] M. Kröger, S. Hamwi, J. Meyer, T. Riedl, W. Kowalsky, and A. Kahn, P-type doping of organic wide band gap materials by transition metal oxides: A case-study on Molybdenum trioxide, Organic Electronics **10**, 932 (2009).

[239] R. R. Lunt, N. C. Giebink, A. A. Belak, J. B. Benziger, and S. R. Forrest, Exciton diffusion lengths of organic semiconductor thin films measured by spectrally resolved photoluminescence quenching, J. Appl. Phys. **105**, 053711 (2009).

[240] A. Lewis, A. Ruseckas, O. P. Gaudin, G. Webster, P. Burn, and I. Samuel, Singlet exciton diffusion in MEH-PPV films studied by exciton-exciton annihilation, Organic Electronics **7**, 452 (2006).

[241] High Performance Carbon Nano Materials Bucky USA, http://buckyusa.com/, accessed 03.11.2010.

[242] H.-N. Li, H. Yang, X.-X. Wang, J.-F. Ni, P. Wang, L. Meng, X.-B. Wang, I. Kurash, H.-J. Qian, J.-O. Wang, and Z.-Y. Liu, Electronic structure of C_{84} film studied by photoemission measurement and first-principles calculation, Journal of Physics: Condensed Matter **21**, 265502 (2009).

[243] A. L. Balch, A. S. Ginwalla, J. W. Lee, B. C. Noll, and M. M. Olmstead, Partial Separation and Structural Characterization of C_{84} Isomers by Crystallization of $(\eta^2\text{-}C_{84})Ir(Co)Cl(P(C_6H_5)_3)_2$, Journal of the American Chemical Society **116**, 2227 (1994).

[244] T. J. S. Dennis, T. Kai, T. Tomiyama, and H. Shinohara, Isolation and characterisation of the two major isomers of [84]fullerene (C_{84}), Chem. Commun. , 619 (1998).

[245] J. Crassous, J. Rivera, N. S. Fender, L. Shu, L. Echegoyen, C. Thilgen, A. Herrmann, and F. Diederich, Chemistry of C_{84}: Separation of Three Constitutional Isomers and Optical Resolution of D_2-C_{84} by Using the “Bingel–Retro-Bingel” Strategy, Angewandte Chemie International Edition **38**, 1613 (1999).

[246] H. S. Cho, T. K. Ahn, S. I. Yang, S. M. Jin, D. Kim, S. K. Kim, and H. D. Kim, Singlet excited state (S_1) of higher fullerenes C_{76} and C_{84}: correlation between lifetime and HOMO-LUMO energy gap, Chemical Physics Letters **375**, 292 (2003).

[247] F. B. Kooistra, V. D. Mihailetchi, L. M. Popescu, D. Kronholm, P. W. M. Blom, and J. C. Hummelen, New C_{84} derivative and its application in a bulk heterojunction solar cell, Chemistry of Materials **18**, 3068 (2006).

[248] K. Suemori, T. Miyata, M. Hiramoto, and M. Yokoyama, Enhanced Photovoltaic Performance in Fullerene:Phthalocyanine Codeposited Films Deposited on Heated Substrate, Jpn. J. Appl. Phys. **43**, L1014 (2004).

[249] K. Sakai and M. Hiramoto, Efficient Organic p-i-n Solar Cells Having Very Thick Codeposited i-Layer Consisting of Highly Purified Organic Semiconductors, Molecular Crystals and Liquid Crystals **491**, 284 (2008).

[250] M. Wojdyla, B. Derkowska, Z. Lukasiak, and W. Bala, Absorption and photoreflectance spectroscopy of zinc phthalocyanine (ZnPc) thin films grown by thermal evaporation, Materials Letters **60**, 3441 (2006).

[251] D.-J. Liu, R. L. B. Selinger, and J. D. Weeks, Representing molecular shape and interactions: A reduced intermolecular potential for copper phthalocyanine, J. Chem. Phys. **105**, 4751 (1996).

[252] V. P. Antropov, O. Gunnarsson, and O. Jepsen, Coulomb integrals and model Hamiltonians for C_{60}, Phys. Rev. B **46**, 13647 (1992).

[253] M. Fendrich, T. Wagner, M. Stöhr, and R. Möller, Hindered rotation of a copper phthalocyanine molecule on C_{60} : Experiments and molecular mechanics calculations, Phys. Rev. B **73**, 115433 (2006).

[254] M. M. Mandoc, F. B. Kooistra, J. C. Hummelen, B. de Boer, and P. W. M. Blom, Effect of traps on the performance of bulk heterojunction organic solar cells, Appl. Phys. Lett. **91**, 263505 (2007).

[255] J. H. Lee, S. Cho, A. Roy, H.-T. Jung, and A. J. Heeger, Enhanced diode characteristics of organic solar cells using titanium suboxide electron transport layer, Appl. Phys. Lett. **96**, 163303 (2010).

[256] M. Hoffmann, K. Schmidt, T. Fritz, T. Hasche, V. M. Agranovich, and K. Leo, The lowest energy Frenkel and charge-transfer excitons in quasi-one-dimensional structures: application to MePTCDI and PTCDA crystals, Chemical Physics **258**, 73 (2000).

[257] H.-B. Bürgi, R. Restori, and D. Schwarzenbach, Structure of C_{60}: partial orientational order in the room-temperature modification of C_{60}, Acta Crystallographica Section B **49**, 832 (1993), Inorganic Crystal Structure Database (ICSD) code 73661.

[258] A. Hoshino, Y. Takenaka, and H. Miyaji, Redetermination of the crystal structure of [alpha]-copper phthalocyanine grown on KCl, Acta Crystallographica Section B **59**, 393 (2003), CCDC code 219250.

[259] P. Erk, H. Hengelsberg, M. F. Haddow, and R. van Gelder, The innovative momentum of crystal engineering, CrystEngComm **6**, 474 (2004), CCDC code 241066.

[260] R. W. Vook, Forbidden Reflections in Electron Diffraction Patterns of Evaporated Tin Films, J. Appl. Phys. **32**, 2474 (1961).

[261] A. Jain and K. Vijayan, Forbidden reflections from the aramid PPT A-A novel correlation with stacking faults, Bull. Mater. Sci. **27**, 47 (2004).

[262] PDF, Powder diffraction file (PDF), Release 2001, International Centre for Diffraction Data, 2001.

[263] ICSD, Inorganic Crystal Structure Database (ICSD), Version 1.4.2, Release 2007. Karlsruhe: National Institute of Standards and Technology (NIST) and Fachinformationszentrum Karlsruhe (FIZ), 2007.

[264] W. Kraus and G. Nolze, POWDER CELL - a program for the representation and manipulation of crystal structures and calculation of the resulting X-ray powder patterns, Journal of Applied Crystallography **29**, 301 (1996).

[265] S. van Smaalen, V. Petricek, J. L. de Boer, M. Dusek, M. A. Verheijen, and G. Meijer, Low-temperature structure of solid C_{70}, Chemical Physics Letters **223**, 323 (1994).

[266] I. Rusakova, A. Hamed, and P. H. Hor, TEM Study of C_{70} Polycrystalline Films, Journal of Materials Research **9**, 2814 (1994).

[267] S. Kazaoui and N. Minami, Intermolecular charge transfer excitons in C_{70} as compared with C_{60} films, Synthetic Metals **86**, 2345 (1997).

[268] I. Bruder, A. Ojala, C. Lennartz, S. Sundarraj, J. Schöneboom, R. Sens, J. Hwang, P. Erk, and J. Weis, Theoretical and experimental investigation on the influence of the molecular polarizability of novel zinc phthalocyanine derivatives on the open circuit voltage of organic hetero-junction solar cells, Solar Energy Materials and Solar Cells **94**, 310 (2010).

[269] S. Pfuetzner, C. Mickel, J. Jankowski, M. Hein, J. Meiss, C. Schuenemann, C. Elschner, A. A. Levin, B. Rellinghaus, K. Leo, and M. Riede, The influence of substrate heating on morphology and layer growth in C_{60}:ZnPc bulk heterojunction solar cells, Organic Electronics **12**, 435 (2011).

[270] S. Braun, M. P. de Jong, W. Osikowicz, and W. R. Salaneck, Influence of the electrode work function on the energy level alignment at organic-organic interfaces, Appl. Phys. Lett. **91**, 202108 (2007).

[271] M. Hermenau, S. Scholz, K. Leo, and M. Riede, Total charge amount as indicator for the degradation of small molecule organic solar cells, Solar Energy Materials and Solar Cells **95**, 1278 (2011).

[272] S. H. Park, J. G. Jeong, H.-J. Kim, S.-H. Park, M.-H. Cho, S. W. Cho, Y. Yi, M. Y. Heo, and H. Sohn, The electronic structure of C_{60}/ZnPc interface for organic photovoltaic device with blended layer architecture, Appl. Phys. Lett. **96**, 013302 (2010).

[273] A. Opitz, M. Bronner, W. Brutting, M. Himmerlich, J. A. Schaefer, and S. Krischok, Electronic properties of organic semiconductor blends: Ambipolar mixtures of phthalocyanine and fullerene, Appl. Phys. Lett. **90**, 212112 (2007).

[274] M.-S. Liao and S. Scheiner, Electronic structure and bonding in metal phthalocyanines, Metal=Fe, Co, Ni, Cu, Zn, Mg, J. Chem. Phys. **114**, 9780 (2001).

Acknowledgements

Now it's time to express my gratitude to all who contributed to the success of this thesis.

First of all I thank Prof. Karl Leo for the opportunity to work on this topic, for the liberties working on the topics, and the possibility to attend conferences and workshops. Without his support and the excellent experimental infrastructure of the institute, this would not have been possible.

This also applies to Dr. Moritz Riede, supervisor and leader of the organic solar cells group at the IAPP. With his support, essential advice and guidance: "keep the red thread throughout your thesis", he contributed to the success of this work.

I thank Prof. Masahiro Hiramoto for the opportunity to work in his lab as visiting student, for his hospitality, and his willingness to review this thesis.

This work was funded by the Bundesministerium für Bildung und Forschung in the framework of the OPEG project (...)

For the support and discussions concerning measurements at the different charaterization tools and facilities, I'd like to thank:

...Annette Petrich and Tina Träger for material sublimation,

...the Lesker team (Caroline Walde, Andreas Bunk, Danny Jenner, Jan Förster, Tobias Günther, and Sandro Egert) for producing Lesker wafers,

...Carsten Wolf for technical support of the Maus 1 & 2 & 3 (aka ESK),

...Max Tietze and Dr. Selina Olthof for UPS/XPS measurements,

...Jens Jankowski and Moritz P. Hein for mobility measurements,

...Wolfgang Tress for electrical simulations,

...Ellen Kern for SEM measurements,

...Christine Mickel and Dr. Bernd Rellinghaus for TEM measurements,

...Prof. Lothar Dunsch for mass spectroscopy measurements,

...the organic solar cell and OLED group for fruitful scientific discussions,

and those who I might have forgotten to mention here.

Many thanks to Dr. Jan Meiß and Dean Slack who did proof reading.

Thanks to those who contributed to the funny and sporty activities in addition the scientific work at the IAPP:

...the organizers of the Organic Days every year,

...the colleagues from the IAPP with their huge participation at the Team Challenge Dresden 2009 and 2010,

...especially to my colleagues Torben Menke, Jan Meiss, and René Kullock which made it happen to win the Team Challenge Dresden and the Campuslauf in 2009 in the student ranking in our team ”IAPP Express”,

...Robert Brückner as member in the team IAPP Express at Chemnitz Stadtlauf 2010,

...the participants at Dresden Stadtlauf Halbmarathon: René Kullock, Jan Meiß, Sandro Egert, Torben Menke, and Karl Leo,

...the participants at the Moritzburg Triathlon in 2009 and 2010: Sandro Egert, Torben Menke, Jan Meiß, and Moritz Riede,

...Johannes Haase, Maik Langner, Hannah Ziehlke, Daniel Kasemann, Robert Brückner, and Jan Meiß for the scientific and non-scientific discussions and activities (games of darts after lunch) in our office (Kompetenz-Kern-König-Bau),

and many many more....

Now, I’d like to thank my family, my twin brother André (he is no physicist, and it’s good that way $\ddot\smile$), and his wife Claudi for their support and social meetings. Thanks to my friends for funny and eventful acivities and come togethers beside work. At last I thank my girlfriend Janine (aka Maus) for her great support in all circumstances, her sympathy, perseverance, and love. Thank you.

Erklärung

Hiermit versichere ich, dass ich die vorliegende Arbeit ohne unzulässige Hilfe Dritter und ohne Benutzung anderer als der angegebenen Hilfsmittel angefertigt habe. Die aus fremden Quellen direkt oder indirekt übernommenen Gedanken sind als solche kenntlich gemacht. Die Arbeit wurde bisher weder im Inland noch im Ausland in gleicher oder ähnlicher Form einer anderen Prüfungsbehörde vorgelegt.

Steffen Pfützner Dresden, 08. August 2011